Deliverable 6.1

D6.1 Integration of RISE Innovations in the Fields of OELF, RLA and SHM

Deliverable information	
Work package	WP6 Pilot and demonstration sites for RISE technologies and methods
Lead	GFZ
Authors	Cecilia I. Nievas (GFZ) Helen Crowley (EUCENTRE) Yves Reuland (IBK-ETH) Graeme Weatherill (GFZ) Georgios Baltzopoulos (UNINA) Kirsty Bayliss (UEDIN, former affiliation) Eleni Chatzi (IBK-ETH) Eugenio Chioccarelli (UNIRC, formerly UNINA) Philippe Guéguen (UGA) Iunio Iervolino (UNINA) Warner Marzocchi (UNINA) Mark Naylor (UEDIN) Mabel Orlacchio (UNINA, former affiliation) Jelena Pejovic (GF-UCG) Nikola Popovic (GF-UCG) Francesco Serafini (UEDIN) Nina Serdar (GF-UCG)
Reviewers	Bozidar Stojadinovic (IBK-ETH)
Approval	Management Board
Status	Final
Dissemination level	Public
Delivery deadline	28.02.2023
Submission date	28.02.2023
Intranet path	DOCUMENTS/DELIVERABLES/Deliverable_6.1.pdf

This project has received funding from the European Union's Horizon 2020 research and innovation programme under grant agreement No 821115

Table of contents

Summary

This report presents the work carried out in RISE Task 6.1 to demonstrate how different developments of the RISE project in the fields of operational earthquake loss forecasting (OELF), rapid loss assessment (RLA) and structural health monitoring (SHM) can work together for the dynamic assessment of seismic damage and losses. The open-source software named Real-Time Loss Tools was developed not only to make this task possible but also with the objective of creating a tool that the research community could use to explore all the aspects of this integration and develop strategies for future scalability and operationalisation.

This demonstration activity focuses on showcasing what would have been calculated during the 2009 L'Aquila and 2016-2017 Central Italy earthquake sequences if a RLA and an event-based OELF system capable of accounting for damage accumulation had been implemented and operational at the time. With the aim of bringing in the SHM component and keeping the proof of concept manageable, a fictitious building stock combining aggregate numbers of buildings and three individual monitored structures that have been studied within RISE (but are located in different countries) has been used. Outputs consist of expected damage states, economic losses, injuries and deaths after each earthquake that effectively occurs and due to each subsequently-generated 24-hour seismicity forecast.

The report first explains the processing algorithm of the Real-Time Loss Tools and discusses each component that feeds the models and calculations (both from a scientific and software input perspective), and then moves to a detailed step-by-step walk through the case studies and, finally, the concluding remarks.

1. Introduction

The RISE project has enabled developments in a large number of scientific aspects of seismic risk reduction, whose stand-alone value has been shown in several other deliverables for the project and their associated journal publications. The present deliverable is the culmination of the work carried out in Task 6.1 to demonstrate how several of these developments can work together for the dynamic assessment of seismic damage and losses. It is essentially a proof of concept based on a series of case-studies from two well-known seismic sequences, the 2009 L'Aquila and 2016-2017 Central Italy sequences, and an open-source software named Real-Time Loss Tools[1] that was developed for this purpose.

While the proof of concept and organisation of this report are described in detail at the end of this introductory chapter (section 1.5), the following lines are dedicated to an overview of the main fields that this work brings together and some of the work carried out within RISE in each of them: rapid loss assessment (RLA), operational earthquake forecasting (OEF), its natural extension to loss calculations, that is, operational earthquake loss forecasting (OELF), and structural health monitoring (SHM).

1.1 Rapid Loss Assessment (RLA)

When an earthquake occurs, there are many remote sensors that record data from the event: waveforms recorded by seismic instruments are used to locate the hypocentre and magnitude of the earthquake and to assess the strong ground shaking at the surface of the earth; people and buildings feel the shaking and observe or record the impact that it has on them. All of these data can be used to rapidly estimate, in the minutes, hours or days following an earthquake, the impact that the earthquake has on the surrounding people, buildings and infrastructure. In the first few minutes following an earthquake, a simple qualitative assessment (e.g., no impact, minor impact, major impact) is often sufficient to understand the magnitude of the event, and this is referred to as Rapid Impact Assessment (e.g., Lilienkamp et al., 2023). In the following hours, however, it becomes important to understand the impact in terms of quantitative losses (e.g., number of collapsed buildings, number of fatalities or homeless people, direct economic loss) and this estimation is referred to as Rapid Loss Assessment (RLA). This fast assessment of the impact of the earthquake provides first order estimates of the losses which can be continually updated as more information and data arrive from the remote sensors.

It can often take days or even months for the true toll of an earthquake to be measured and reported. Stakeholders such as early responders, governments, and the insurance industry all need to have an estimate of the potential magnitude of the losses much earlier than this, so that they can plan and better manage the recovery phase after the earthquake. For example:

- Early responders such as civil protection agencies need to know which areas have been most hit, and the scale of collapsed buildings, so that they can send the right teams and equipment to search for trapped survivors. They will also need an estimate of the number of homeless people, so they can prepare emergency shelter.

- Governments may need to allocate funding for the rescue and recovery efforts, either nationally or as part of international aid, when the event has occurred in another country.

- Insurers need to plan for post-earthquake damage assessments to manage the potential insurance claims (e.g., Pittore et al., 2015).

Whilst these initial rapid estimates of loss are statistical (i.e., they can only provide a distribution of the expected damage and loss, rather than identify specific buildings that will be damaged) and

[1] https://git.gfz-potsdam.de/real-time-loss-tools/real-time-loss-tools

they contain a number of uncertainties, they nevertheless provide useful, actionable information for these communities.

For over 13 years, the U.S. Geological Survey (USGS) has been running a global rapid loss assessment service called PAGER (Prompt Assessment of Global Earthquakes for Response: Earle et al., 2009).The USGS's PAGER system uses ShakeMaps, which provide a rapid estimate of ground shaking in an area struck by an earthquake, together with global exposure and empirical vulnerability models to assess the losses from earthquakes. More information on the details of RLA is provided in the RISE Good Practice Report "European Rapid Earthquake Loss Assessment"[2].

Within the RISE project, thanks to the developments in Task 4.1, a European ShakeMap is now online[3] and exposure models for 44 European countries, at a resolution required for scenario analyses, together with the associated and vulnerability models have been made available[4]. A new prototype scientific service that allows the damage and losses to be assessed for any ShakeMap in the European ShakeMap system (the ESRM20 Rapid earthquake Loss Assessment code) has now also been released thanks to efforts in the RISE project, and as documented in Deliverable D6.5 (Crowley et al., 2023).

1.2 Operational Earthquake Forecasting (OEF)

The frequent occurrence of deadly earthquake events highlights the importance of delivering reliable and skilful earthquake forecasts over different time windows (from days to decades) to support rational actions of risk reductions and enhancing preparedness and resilience. For this purpose, the International Commission for Earthquake Forecasting for Civil Protection, nominated by the Italian government after the Mw 6.1 earthquake occurred in L'Aquila (Italy) on 6 April 2009 (Jordan et al., 2011), recommended the development of an Operational Earthquake Forecasting (OEF) system, which comprises procedures for gathering and disseminating authoritative information about the time dependence of seismic hazards, in order to help communities prepare for potentially destructive earthquakes. Specifically, OEF provides timely earthquake (probabilistic) forecasts over time-space-intensity windows of interest for stakeholders (e.g., government agencies and departments).

OEF systems have already been implemented in several forecasting applications worldwide, such as in Italy, New Zealand and the United States (Marzocchi et al., 2014; Gerstenberger et al., 2014; Michael et al., 2020). In principle, OEF should deliver a continuous flow of information to avoid violating the so-called hazard/risk separation principle (Jordan et al., 2014). So far, this feature is in place only in the Italian OEF system (*OEF-Italy*), whereas in most cases OEF information is released upon specific subjective requests.

OEF-Italy is composed by an ensemble of three different clustering models, ETAS-LM, ETES, STEP-LG that are described in Marzocchi et al. (2014) and references therein. Each model is weighted according to its forecasting skill, specifically, weights are proportional to the inverse of the logarithmic score of each model and normalized to 1. The system produces weekly forecasts of earthquake occurrence (M4+, M5.5+) in each cell of the Collaboratory for the Study of Earthquake Predictability (CSEP) grid (Taroni et al., 2018), and ground shaking macroseismic intensity (VI+, VII+, and VIII+). The graphical interface of the model allows the end user to define the area of interest to get the overall probability.

Several new earthquake forecasting models and innovations have been produced as part of Task 3.3 of the RISE project, as is briefly described in section 3.1.

[2] http://rise-eu.org/dissemination/good-practices/European-rapid-earthquake-loss-assessment/
[3] http://shakemapeu.ingv.it/
[4] https://gitlab.seismo.ethz.ch/efehr/esrm20

1.3 Operational Earthquake Loss Forecasting (OELF)

Operational Earthquake Loss Forecasting is the natural extension of OEF into the risk domain, and is thus one step closer to the decision-making process, as it connects directly with the potential consequences in terms of damage and losses that could be associated with the forecasted seismicity. Only a few countries in the world have systems that produce operational earthquake forecasts (e.g., Italy, the United States, New Zealand, Japan) and it is only Italy that takes it to the OELF level by means of the MANTIS-K system (Iervolino et al., 2015).

Using the earthquake rates provided by the *OEF-Italy* system , i.e., the expected number per unit time (*Δt*, equal to one week) of earthquakes above magnitude 4, originating at each point-like seismic source *{x,y}*, *λ(t,x,y)*, MANTIS-K calculates the expected value of earthquakes per unit time that, in a given area (e.g., a municipality) identified by coordinates *{w,z}*, makes the building of a structural typology of interest, *k*, reach some performance levels of interest, that is, $PL^k = pl_j$.. In fact, it is assumed that a finite number, say *n*, of performance levels can be used to discretize the damage conditions of the structure: pl_1 identifies the undamaged state, pl_n the conventional collapse, pl_j, with *j=2, …, n-1*, the intermediate damage condition between the undamaged and the collapse state (increasing *j*, the level of damage increases). The sought rate of earthquakes causing a building of the structural typology *k*, located in *{w,z}*, on a soil class indicated as θ, to reach pl_j is $\lambda^k_{PL=pl_j}(t,w,z,\theta)$ and can be computed via Equation (1):

$$\lambda^k_{PL=pl_j}(t,w,z,\theta) = \iint_{x\ y} \lambda(t,x,y) \cdot \int_{im=0}^{+\infty} P\left[PL^k = pl_j \middle| im\right] \cdot \int_{m=0}^{+\infty} f_{IM|M,R,\theta}(m,r,\theta) \cdot f_M(m) \cdot dm \cdot dx \cdot dy \tag{1}$$

where *M* is the magnitude of the earthquake, *R* is the distance between the point-like seismic source *{x,y}* and the site of interest *{w,z}*; $f_M(M)$ is the probability density function of the magnitude of the earthquakes (assumed to be independent and identically distributed among sources); $f_{IM|M,R,\theta}(m,r,\theta)$ is the probability density function (pdf) of the intensity measure, *IM*, at the site *{w,z}* conditional to *M=m*, *R=r*, and the soil class θ (or possibly other covariates); $P\left[PL^k = pl_j \middle| im\right]$ is the probability that a structure of the *k*-th structural typology reaches pl_j given that IM=im at the construction site (such a probability is assumed independent from θ). $P\left[PL^k = pl_j \middle| im\right]$ can be retrieved from the so-called fragility functions for the structural typology of interest. Finally, the integrals over *x* and *y* in Equation (1) are extended to comprehend all the sources within a maximum distance from the *{w,z}* site; such a distance usually depends on the adopted ground motion propagation models providing $f_{IM|M,R,\theta}(m,r,\theta)$.

If the local soil conditions are uncertain, the random variable representing the soil class at the site of the buildings of the structural typology can be considered defining its probability mass function, $P[\theta_q]$, with *q=1, …, Q*, where *Q* is the number of soil classes. In such a case, the rate of earthquakes taking to pl_j a building randomly selected among those of the structural typology *k* and located in *{w,z}*, i.e., $\lambda^k_{PL=pl_j}(t,w,z)$ can be computed via Equation (2):

$$\lambda^k_{PL=pl_j}(t,w,z) = \sum_{q=1}^{Q} P\left[\theta_q\right] \cdot \lambda^k_{PL=pl_j}(t,w,z,\theta_q) \tag{2}$$

In the same hypotheses discussed in Iervolino et al. (2015), if the number of buildings of the *k*-th structural typology at *{w,z}* site is available, $N_B^k(w,z)$, the expected number of buildings reaching pl_j in *(t,t+Δt)*, that is $N_{B,plj}{}^k(t+\Delta t,w,z)$, can be approximately computed via Equation (3):

$$N^k_{B,pl_j}(t+\Delta t,w,z) \approx N^k_B(w,z) \cdot \lambda^k_{PL=pl_j}(t,w,z) \cdot \Delta t \tag{3}$$

An upgraded version of the OELF system, named MANTIS v2.0, was formulated and tested as part of RISE Task 4.2 to account for the evolution, over time, of the structural damage conditions. In MANTIS v2.0, loss forecasting accounts for the possible structural damage accumulation due to the occurrence of more than one earthquake in the forecasting period. Moreover, the upgraded system is able to estimate the possible damage due to the occurred earthquakes and, consequently, forecast the performance level of buildings that, at the time of computation, are already at an intermediate performance level (see Deliverable D4.3, Chioccarelli et al., 2022, for further details).

1.4 Structural Health Monitoring (SHM)

Recent advances in sensor development have resulted in an increasing availability of sensing hardware at low cost, thus making permanent installations of sensors a realistic outlook, even for conventional buildings that form the largest portion of the existing building stock. Structural health monitoring (SHM) offers the tools to analyse such a permanent inflow of sensor data and retrieve information regarding the structural state (health) of the structure. Among its many applications, SHM can be used to infer damage based on accelerations recorded in the buildings, or predict structural response within the first seconds of ground shaking for building-specific earthquake early warning (EEW) applications.

The rapid processing of dynamic sensor data (i.e., acceleration time series) enables near-real-time estimates of the damage state. Damage-sensitive features (DSFs) can be derived from the measured time series to assess the presence and severity of damage (Reuland et al., 2023). The contrasting of monitoring-derived DSFs against thresholds, which can be data-driven or model-defined, allows to tag a building via labels that reflect discrete damage states (Sivori et al., 2022). Damage-state probabilities can be formulated in a manner similar to classical fragility functions that link the probability of exceeding damage-states to intensity measures (IMs). Following the fragility functions formulation, IMs which only contain information about the ground-motion, are replaced with DSFs, thus contributing with monitoring-derived information on the state of the structure.

Monitoring data can further contribute to reducing the pre-earthquake uncertainties in the material and model parameters of engineering models that are used to derive fragility functions involved in traditional rapid loss assessment (Martakis et al., 2021). Within the RISE project, multiple buildings were measured during planned demolition to demonstrate such uncertainty reduction and evaluate the influence of the amplitude of shaking on DSFs (Martakis et al., 2022). The added value of weak-to-moderate earthquake data for structural response analysis was evaluated using data recorded in the Grenoble City Hall as part of the RISE project as well (Astorga and Guéguen, 2023). Finally, the ever-increasing computational power has enabled the use of machine-learning approaches to classify buildings into damage-state categories after earthquakes. While absence of historic data to train such classifiers may pose a challenge for such applications, domain adaptation has been shown to be a powerful tool to apply simulation-based classifiers to real data, thus providing a robust way to combine multiple DSFs that goes beyond SHM-based fragility functions (Martakis et al., 2023) and reduces the computational burden of previous post-earthquake updating schemes (Reuland et al., 2019a, 2019b).

Though not within the scope of the work presented herein (and reported elsewhere), several institutions within the RISE project have worked on the development of building-specific EEW systems. Iaccarino et al. (2021) explored the feasibility of predicting the structural drift from the first seconds of P-wave signals for such an application. A Japanese dataset was used to calibrate models based on machine-learning and to study their capability to predict structural drifts. The study showed that by implementing a residuals analysis, the main sources of drift variability could be identified. The models trained on the Japanese dataset were later applied to a US dataset, and it was found that exporting EEW models across regions worsened the prediction variability, but

also that the problem can be strongly mitigated by including correction terms as a function of earthquake magnitude. At the same time, Safak et al. (2022) developed within RISE Tasks 4.5 and 6.1 an EEW structural safety model for an instrumented building in Istanbul (RISE Deliverable 4.6). The model links the ground motions observed at distant stations with those observed at the base of the building, and established thresholds for the latter that would cause critical response for the safety of the building.

1.5 Proof of concept and organisation of this report

With the purpose of demonstrating how different developments of the RISE project can work together for the dynamic assessment of seismic damage and losses, in Task 6.1 we focused on assembling a proof of concept to show the interaction and links between all these different components. The open-source software named Real-Time Loss Tools[5] was developed not only to make this task possible but also with the objective of creating a tool that the research community could use to explore all the aspects of this integration and develop strategies for future scalability and operationalisation. To our knowledge, this is the first such open-source tool, and we believe it may facilitate discussions regarding interfaces, deployment challenges and the need for scientific developments to bridge gaps between different research focuses.

The Real-Time Loss Tools have been designed to carry out rapid loss assessments (RLA) and event-based operational earthquake loss forecasts (OELF) incorporating probabilities of damage states based on structural health monitoring (SHM) methods, calculating cumulative damage by means of state-dependent fragility models, calculating expected economic losses and human casualties (injuries and deaths) and updating the number of occupants in the buildings, by taking into account the time of the day of the earthquake as well as whether people are allowed back (due to inspection and repair times) and are able to do so (due to their own health status). The tools work in this way by recursively calling OpenQuake (Pagani et al., 2014; Silva et al., 2014) and updating the exposure model and other relevant input files. To the authors' knowledge, this code contains the first attempt to update numbers of occupants in buildings in RLA and OELF calculations during an ongoing earthquake sequence. We believe these tools provide a useful demonstration of how the scenario calculators of the OpenQuake engine can be used in a time-dependent manner, and hope that this might lead to future developments of the engine that will enable more efficient modelling of the dynamics of risk, in particular during a sequence of earthquakes.

The Real-Time Loss Tools use the following inputs stemming from the RISE project:

- Short-term seismicity forecasts: Output forecasts from any OEF model can be used, as long as their output is a series of realisations of earthquakes, each of which is characterised at least by epicentral location, moment magnitude, UTC date and time of occurrence. For this proof of concept, the output of the *ETAS.inlabru* model developed as part of RISE Task 3.3 has been used (Serafini et al., 2023; Naylor et al., 2023; Bayliss et al., 2022; Bayliss et al., 2020).

- SHM-based probabilities of damage for monitored buildings: Probabilities of damage from any estimation method can be used. For this proof of concept, the output of the method developed by Reuland et al. (2021, 2022b) within RISE Task 4.4, which is based on damage-sensitive features (Reuland et al., 2023) developed for a pair of sensors per building, was used.

- State-dependent fragility models for Italian structural typologies developed by Orlacchio (2022) within RISE Task 4.2, which take as a starting point the state-independent fragility models of the European Seismic Risk Model 2020 (ESRM20; Crowley et al., 2021a), which were finalised in RISE Task 4.1.

[5] https://git.gfz-potsdam.de/real-time-loss-tools/real-time-loss-tools

- Knowledge on the dynamic behaviour of two real buildings: a hotel in Budva, Montenegro, studied by the University of Montenegro (GF-UCG, RISE external partner) and the Grenoble City Hall, France, studied by the University of Grenoble Alps (UGA).

- Knowledge on the dynamic behaviour of a theoretical building representative of typical Swiss residential structures, studied by IBK-ETH.

The concept of the Dynamic Exposure Model developed by Schorlemmer et al. (2020, 2023) within RISE Task 2.7 (Deliverable D2.13) is used for this proof of concept as well. In this model, building exposure is defined in terms of a series of individual buildings whose footprints are retrieved from OpenStreetMap (OSM) and quadtree-formulated tiles of zoom level 18 (around 100-m side in central-southern Europe) that group buildings expected to exist in the tile but not yet represented in OSM. The model itself is not used, as this proof of concept is based on a fictitious building portfolio, due to the fact that we are working with a combination of Italian building types, existing buildings in Montenegro and France, and a theoretical Swiss building, all of which we assume to be located in the same site. These last three buildings are represented with their individual footprints, and nine tiles with aggregate numbers of buildings of different Italian building types are used as the remaining exposure in this work. The three individual buildings are instrumented and monitored and allow us to incorporate the SHM component to the proof of concept.

Given the recent trend in the OEF community to transition from generating seismicity forecasts in terms of earthquake rates to outputting large numbers of stochastic realisations of seismicity (i.e., full catalogues of possible earthquakes), the Real-Time Loss Tools depart from the closed-form rate-based analytical formulation of MANTIS-K (Iervolino et al., 2015) and MANTIS v2.0 (Chioccarelli et al., 2022) (see section 1.3) and instead carry out operational earthquake loss forecasts in an event-based manner, by means of a stochastic generation of ruptures for the earthquakes in the input seismicity forecast, similarly to what was done by Papadopoulos et al. (2020) in the context of probabilistic seismic risk assessment.

This proof of concept represents what would have been calculated during the 2009 L'Aquila and 2016-2017 Central Italy earthquake sequences if a RLA and event-based OELF system (referred to simply as OELF in the remainder of this document) of this kind had been implemented and operational at the time. For both the RLA and OELF calculations we focus on earthquakes with moment magnitude Mw 5.0 and above, for lower computational demand and ease of visualisation of the results; it is nevertheless clear that earthquakes of smaller magnitudes are capable of causing damage as well (see, for example, Nievas et al., 2020). As these sequences did not actually affect the three monitored buildings, non-linear time-history analyses (NLTHAs) have been used to simulate what their SHM sensors would have recorded (provided they were all fully functioning at the time of the earthquakes). The need, therefore, for accelerograms to run these NLTHAs motivated us to select study sites where seismological stations had effectively recorded the two earthquake sequences. This led to the identification of three and four sites for the L'Aquila and Central Italy sequences, respectively, and we thus modelled seven cases in which the same exposure model (composed by the nine tiles and three buildings) was moved around to the seven different locations. Figure 1 shows the location of these sites. The two sequences were chosen to represent a case in which most of the damage occurred in the first large shock (L'Aquila) and a case in which damage increased gradually or with different shocks in the sequence, also depending on the location (Central Italy). Only one case of L'Aquila and two cases of Central Italy are finally presented in detail in this report.

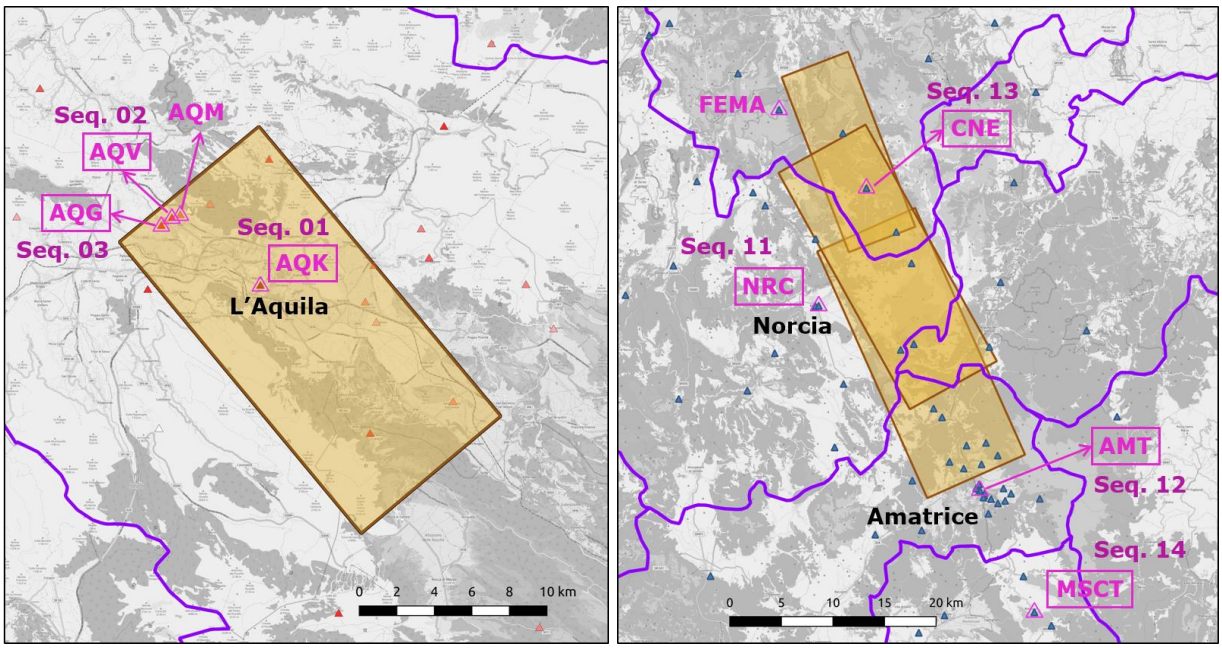

Figure 1 Seismological stations (triangles) and sites selected from the 2009 L'Aquila (left) and 2016-2017 Central Italy (right) earthquake sequences. The seven sites are labelled "Seq. XX" and by marking the station name with a rectangle. Rupture planes from the Italian Accelerometric Archive (ITACA; Russo et al., 2022) for the larger-magnitude shocks are shown in light orange. Background: OpenStreetMap.

The report starts by explaining the functioning of the processing algorithm (the Real-Time Loss Tools that were developed) in Chapter 2. Chapter 3 describes each of the components of the model and workflow, focusing not only in the specifics of this proof of concept but also on the general concepts behind them. Chapter 4 describes in detail the input files needed for the Real-Time Loss Tools, with the purpose of facilitating future applications and use of the software. Chapter 5 walks step-by-step through the running of the proof of concept, demonstrating how the different components fit together. The report finishes with Chapter 6, in which we discuss our observations along this process.

2. Processing algorithm

The Real-Time Loss Tools[6] developed as part of RISE Task 6.1 carry out a series of state-dependent calculations for RLA and OELF incorporating inputs from SHM and updating the number of occupants in the buildings as a function of the history of damage and injury. In a nutshell, they do so by recursively calling OpenQuake[7] (Pagani et al., 2014; Silva et al., 2014) while updating its input files, and keeping track at every point in time of the damage states of buildings and the number of people unable to return to the buildings they usually occupy. The tools output numbers of buildings in different damage states and/or probabilities of a building to reach a given damage state, economic losses, injuries and deaths, all this after any earthquake in the sequence and after each seismicity forecast. While they illustrate how different components feed into each other and fit together, they are not an operational deployment but a research tool made openly available to the community.

In order to run the Real-Time Loss Tools, the user needs to specify a sequence of as many RLA and OELF calculations as they desire by means of an input CSV file (see section 4.9) that points at specific input files with earthquake catalogues and/or parameters. This is schematically shown in Figure 2 by means of the first two decision rhombuses: the programme runs until there are no more catalogue files to process, and follows an RLA or OELF workflow according to what is indicated in the triggering CSV file. This means that calculations for a whole earthquake sequence can currently

[6] https://git.gfz-potsdam.de/real-time-loss-tools/real-time-loss-tools

[7] The Real-Time Loss Tools have been developed based on v3.15 of the OpenQuake engine.

only be done *a posteriori* (i.e., after the whole earthquake sequence has occurred) or can be manually triggered at will (e.g., after each large earthquake) by the user whenever desired. In a full-scale operational system, however, there would be a component of the software in charge of triggering calculations according to some pre-defined criterion instead of the CSV file used by the Real-Time Loss Tools. For example, operational earthquake forecast (OEF) calculations are triggered in Italy at least once a day and whenever an earthquake with local magnitude M_L of 3.5 and above occurs (Marzocchi et al., 2014).

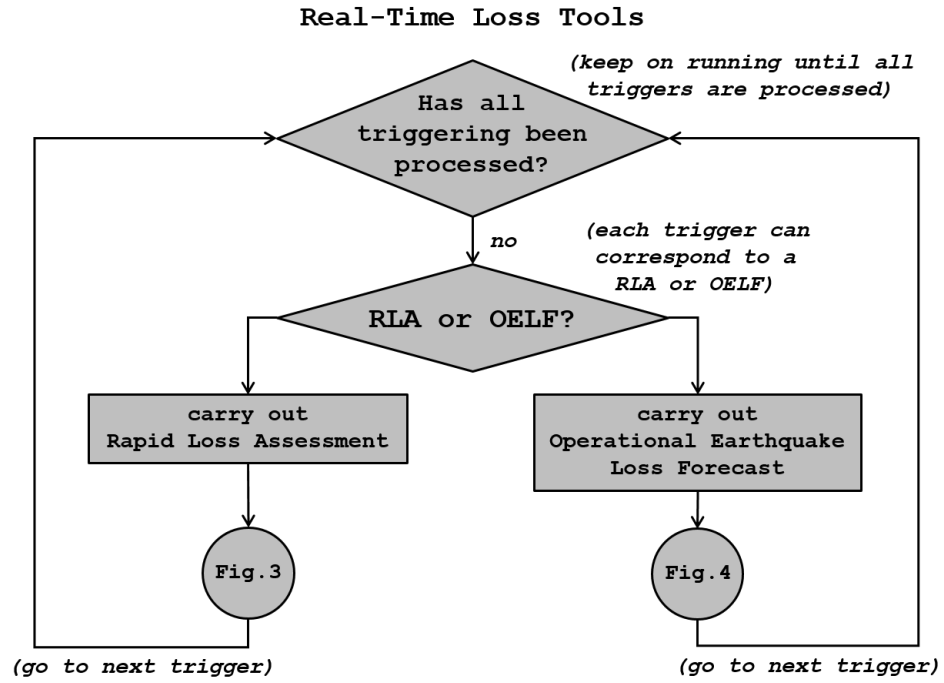

Figure 2 General overview of the processing algorithm of the Real-Time Loss Tools.

The RLA and OELF paths share many common steps, given that, conceptually, an OELF calculation can be thought of as running a very large number of RLA calculations one after the other. A fundamental difference between the two is that the RLA routine updates the current "real" exposure model, i.e. the model that is intended to represent what has happened in the real world after the event has occurred, while the OELF routine does not because it is a forecast that may or may not occur (please note that the use of "real" here does not imply "observed" or assessed by an engineer). Another relevant difference is that SHM-based damage estimates only feed into RLA calculations but not OELF ones, simply because the RLA earthquakes have occurred and could be recorded by the corresponding sensors in the monitored buildings while the OELF earthquakes have not, and there is thus no sensor data to input into the algorithm.

As shown in Figure 3, the RLA calculation starts by calculating the local time of occurrence of the earthquake (which is originally input in UTC, which is the time standard used by earthquake networks and ShakeMap systems, and then converted to the local time) and by updating the number of occupants in the buildings based on the time of the day and whether previous earthquakes have caused occupants to be injured and/or displaced. The time of the day is taken into account by means of coefficients that are used to multiply what we denominate "census" occupants, that is, occupants associated with a building irrespective of the time of the day, their health status or the damage state of the building. These coefficients are provided as input in the configuration file for day, night and transit times (see section 3.4.3).

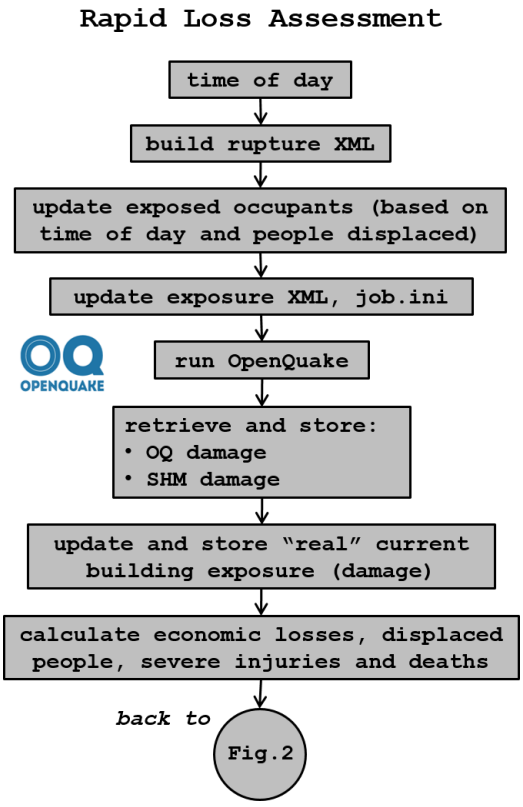

Figure 3 Overview of the processing algorithm of the Real-Time Loss Tools for Rapid Loss Assessment (RLA).

Once the number of occupants is defined, a series of updates to input files for OpenQuake is carried out, including the building of the rupture associated with the earthquake, and a scenario damage calculation is run with OpenQuake using state-dependent fragility models that take into account the current damage state of the building just before the new earthquake hits. Damage results in terms of probabilities and/or number of buildings in different damage states are retrieved from this OpenQuake calculation. If SHM-based damage results (see chapter 3.6) are available for some buildings, these override those obtained from OpenQuake for those buildings. OpenQuake calculations are carried out for all buildings irrespective of whether they are instrumented or not because it is possible that sensors do not work properly at the time an earthquake occurs, or the quality of the recording is too poor to allow processing with the purpose of estimating damage. In a full-scale implementation there would be a part of the software in charge of retrieving these SHM-based results and/or placing them where the Real-Time Loss Tools can find them. In this proof of concept the SHM-based results are passed on as a CSV file.

Damage results stemming from post-earthquake inspections (either rapid green-yellow-red tagging or thorough inspections) could be incorporated into the workflow in the same way as in the case of SHM-based results. The code could be designed either in terms of a hierarchy of preference (e.g. inspection results preferred over SHM-based results, which are in turn preferred over classic rapid loss assessment results that use ground motion-based fragility models), or to carry out weighted averages of different sources of damage information as per user-defined weights. The current version of the Real-Time Loss Tools does not have this option, but the user can input inspection-based damage results as if they were SHM results if desired. Future versions of the software could take a step further and use the inspection-based or SHM-based probabilities of damage to constrain the estimates of damage of unmonitored or uninspected buildings, as suggested by Bodenmann et al. (2021).

The resulting probabilities of each asset in the exposure model being classified under a certain damage state are used to update the exposure model in terms of damaged buildings, and redistrib-

ute the replacement costs and theoretical census occupants (i.e. irrespective of previous earthquakes or time of the day). This is represented in the second-to-last box of the RLA routine in Figure 3. Finally, the economic losses are calculated based on the current probabilities of each damage state for each asset in the exposure model in combination with an economic consequence model. Being based on cumulative damage states, these economic losses are also cumulative. The injuries and deaths are also calculated based on the current probabilities of each damage state for each asset in the exposure model in combination with a human consequence model, and the timelines for people to be allowed and able to return back to their buildings is also calculated and stored. The algorithm then moves on to processing the next trigger.

The OELF calculation starts by looking at a seismicity forecast and building ruptures associated with the earthquakes in the forecast (see section 3.2), as shown in Figure 4. The seismicity forecast is composed of a large number of stochastic realisations of seismicity that we name stochastic event sets (SES), following the nomenclature used by OpenQuake. In a full-scale implementation there would be a part of the software in charge of triggering the generation of a seismicity forecast and/or retrieving its resulting catalogues, but in this proof of concept the latter are passed on as CSV files.

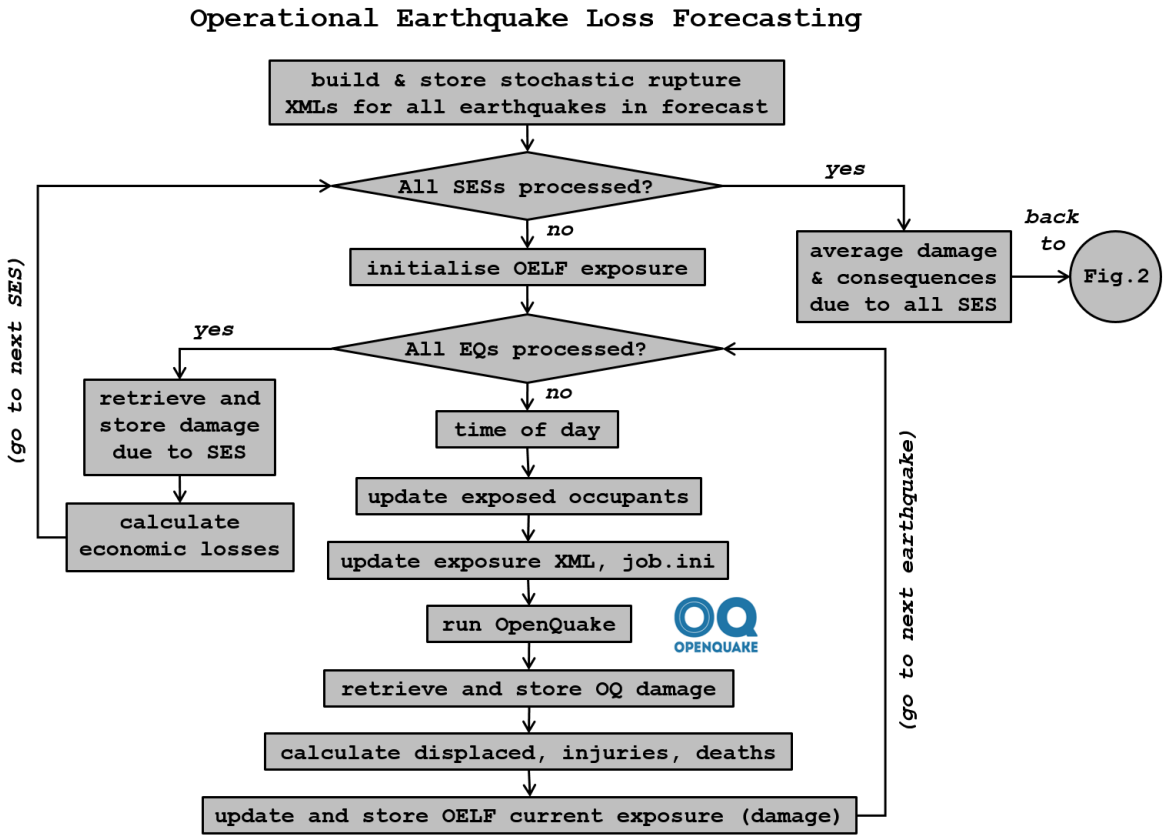

Figure 4 Overview of the processing algorithm of the Real-Time Loss Tools for Operational Earthquake Loss Forecasting (OELF).

The seismicity forecast is initially filtered according to a minimum magnitude and maximum distance to the exposed assets defined in the configuration, so as to not build ruptures that will not be used. Earthquakes identified as having too small magnitudes or occurring too far away are still taken into account for the calculation, assuming they cause no damage. Ideally the criteria used to assume that earthquakes do not cause damage (and thus do not need full damage calculations to be run) should be based on engineering parameters of greater relevance to seismic risk than earthquake magnitude itself (e.g., Bommer and Crowley, 2017); however, the number of earthquakes to be run in an OELF calculation can be very large and we preferred to provide this option in the Real-Time Loss Tools albeit in an oversimplified way. The creation of fully operational RLA and OELF systems requires that efficient and accurate ways of defining a useful criterion be investigated.

The OELF calculation loops through each stochastic event set (SES) and, within each SES, through each earthquake, as shown in Figure 4. The exposure model is initialised at the beginning of each SES by being retrieved from the current "real" exposure, that is, the exposure model that represents the damage probability status of buildings in the real world and is updated by the RLA calculations when earthquakes actually happen. Within a SES, damage builds up and the OELF exposure model associated with this SES is updated, analogously to what happens in a RLA calculation. In this sense, the calculation of the local time of the day, updating of the occupants in the building and running the scenario damage with OpenQuake is the same as for RLA, with the difference that no results from SHM are considered.

While the OELF economic losses can be calculated at the end of each SES based on the final damage status of the assets (for that SES), the human casualties and their associated timelines for people to be allowed/able to return need to be calculated for each earthquake. As it is likely that people may not be allowed to return within the time horizon for which an OELF calculation is carried out (e.g., a day or a week since the last significant real earthquake), a flag is implemented in the Real-Time Loss Tools that allows for the updating of occupants to be bypassed when running an OELF as a function of the input number of days needed for inspection/repair/health recovery and the time since the last real earthquake. Damage states, economic losses and human casualties are averaged out for all stochastic event sets and the resulting expected values are output as the results of the OELF calculation.

The final output of each RLA and OELF calculation is generated by building ID. A building ID can refer to an individual building (e.g., one of the three monitored buildings in this proof of concept) or an aggregation of buildings (e.g., one of the tiles in this proof of concept) (see section 3.4.2). For each RLA calculation, the outputs are:

- probability of an individual building resulting in each damage grade of the (user-defined) scale (if the building ID refers to an individual building with one building class) or number of buildings resulting in each damage grade (if the building ID refers to an aggregation of buildings of different classes);

- expected economic losses for each building ID, in terms of both absolute values and loss ratios (with respect to their total replacement cost), calculated combining the probabilities of all damage states with their corresponding expected loss ratio (as per the input economic consequence model);

- expected human casualties for each building ID, classified by (user-defined) levels of severity, in terms of both absolute values and loss ratios (with respect to the total number of census occupants), calculated combining the probabilities of all damage states with their corresponding expected loss ratio (as per the input human consequence model).

The outputs for each OELF calculation are the same as for a RLA, averaging out the results for individual stochastic event sets. Future implementations could expand these outputs to include measures of the uncertainty in the results; these might be particularly relevant in the case of OELF outputs.

When a series of triggers are run within the same call of the Real-Time Loss Tools (i.e. using a triggering CSV file indicating to run RLA and/or OELF for each input catalogue), the user has the option to generate summary outputs that group the results from all RLA and all OELF calculations.

The strategy to calculate cumulative damage and losses due to a series of earthquakes associated with different stochastic event sets implemented in the Real-Time Loss Tools is slightly different from that used by Papadopoulos and Bazzurro (2020), who, for each building, sampled a damage state for each earthquake and, if larger than the previously obtained damage state, sampled an economic loss ratio (considering uncertainty in the consequence model), which was kept if larger

than the previously obtained loss ratio (due to the previous earthquakes) or otherwise discarded. In our implementation we keep the probabilities of each damage state all throughout the earthquake sequence and calculate the expected economic (and human) loss ratio due to the final probabilities obtained at the end.

Finally, it is worth pointing out that the algorithm outlined above is not the only way that damage estimations from SHM techniques can be incorporated into loss assessments. In this sense it is worth mentioning the work of Trevlopoulos et al. (2020), who demonstrated the derivation of state-dependent fragility models in terms of period elongation (a feature related to inelastic deformation that is easily retrievable from sensor data) that can be used with ground motion data as input to estimate the probability of the building's period resulting in a certain range, which can be separately associated with a damage state (i.e. the ranges of period elongation act effectively as the damage scale). The use of such fragility curves and a Markov chain process allows for state vectors to be updated at any time in the sequence with real measurements of the period elongation of the building. This is slightly different from the approach followed in this proof of concept, as SHM data is herein incorporated by initially deriving building(-class)-specific fragility models in which SHM-based damage-sensitive features are the independent variable and the damage scale is the same as that used in fragility models based on ground motion intensity. In other words, the present approach results in probabilities of damage grades as a function of a recorded SHM-based parameter, while the approach of Trevlopoulos et al. (2020) results in probabilities of ranges of period elongation as a function of ground motion intensities, which must then be associated with damage states separately. The advantage of the method of Trevlopoulos et al. (2020) is that it can be implemented within an OELF (because the independent variable is ground motions and the dependent variable is the probability of period elongations of a certain magnitude), while our implementation can only update damage states during a RLA calculation, thus only affecting the initial state of the OELF calculation and not the calculation in itself. At the same time, the advantage of running an OELF calculation with a workflow of the kind (i) ground motions to probability of period elongation plus (ii) period elongation to probability of damage, over the use of traditional fragility models that move directly from ground motions to probability of damage should be investigated.

2.1 Keeping track of damage states

In order to be able to use state-dependent fragility models and calculate cumulative damage, the Real-Time Loss Tools keep track of the damage state of buildings by updating the exposure model after each new earthquake is run. As only expected values of damage and loss are output, the original number of buildings in a tile associated with a certain number of building classes is distributed across damage states after being affected by an earthquake, as shown in the example in Figure 5. In the case of individual buildings (i.e. non-aggregated individual entities), the distributed "numbers" of buildings are effectively the probabilities of each damage grade. The damage state of the building (or aggregate of buildings) is stored in the exposure CSV file as part of the string that contains the building class, which can be found in the column labelled as *taxonomy*. Following the simplified building classes of Figure 5, the strings "CLASS_A/DS0", "CLASS_A/DS1" and so on would be the ones in the *taxonomy* column (see section 4.4). These same strings would then be sought in the exposure-vulnerability mapping CSV file used by OpenQuake and/or the fragility model directly, to identify the set of fragility curves for a building of "CLASS_A" given that the building is currently already in DS0, DS1, etc. (see section 4.5).

Assuming an initial undamaged condition (though this is not a requirement), each original building class in the initial exposure model splits into as many damage states as present in the fragility models, if the ground motion intensity results in all damage states being produced (i.e. zeroes are not stored in the exposure model). In OpenQuake terms, this "splitting" results in the creation of new assets, each of which occupies a row of the exposure CSV file. We thus define the use of the term "*building_id*" to refer either to an individual building or a geographic aggregation of buildings (e.g., "TILE_1" in Figure 5), the term "*original_asset_id*" to refer to a specific building class of a specific building_id (i.e. IDs associated with each "CLASS_A" and "CLASS_B" for "TILE_1" in Figure

5), and the term "*asset_id*" to refer to the ID of a particular asset in the OpenQuake sense of the word, which implies one specific row of the exposure model and in our case refers to a specific combination of *building_id*, *original_asset_id* and damage state.

When the updated exposure model is subject to a second earthquake, all assets that resulted in DS4 due to the first earthquake can only remain in DS4, while all assets that resulted in DS3 due to the first earthquake can either remain in DS3 or get further damaged into DS4, and so on. A basic sanity check of the cumulative damage calculation is that the number of buildings in DS4 can only increase (or remain the same) and the number of buildings in DS0 can only decrease (or remain the same), while the total number of buildings stays the same.

At each step of the update, the replacement cost and number of occupants (both theoretical census occupants and occupants for that specific earthquake at the corresponding time of the day and accounting for previous injuries and deaths) are distributed proportionally to the splitting in terms of numbers of buildings. In other words, replacement costs and numbers of occupants are assigned by multiplying the original undamaged values by the probability of occurrence of each damage state. Following the example of Figure 5, the total replacement cost and census occupants of "CLASS_A/DS0" in the initial undamaged state, which correspond to 8.6 buildings, get distributed proportionally across 0.851, 1.296, ... and 5.184 buildings. In this sense, the Real-Time Loss Tools assume that costs and occupants are given for each asset and not in terms of a unit of building (which is an option in OpenQuake itself but has not been propagated to the Real-Time Loss Tools). Once the replacement costs have been distributed as described, the economic consequence model is used to calculate losses. The calculation of injuries and deaths requires some additional considerations, which are described in the following section.

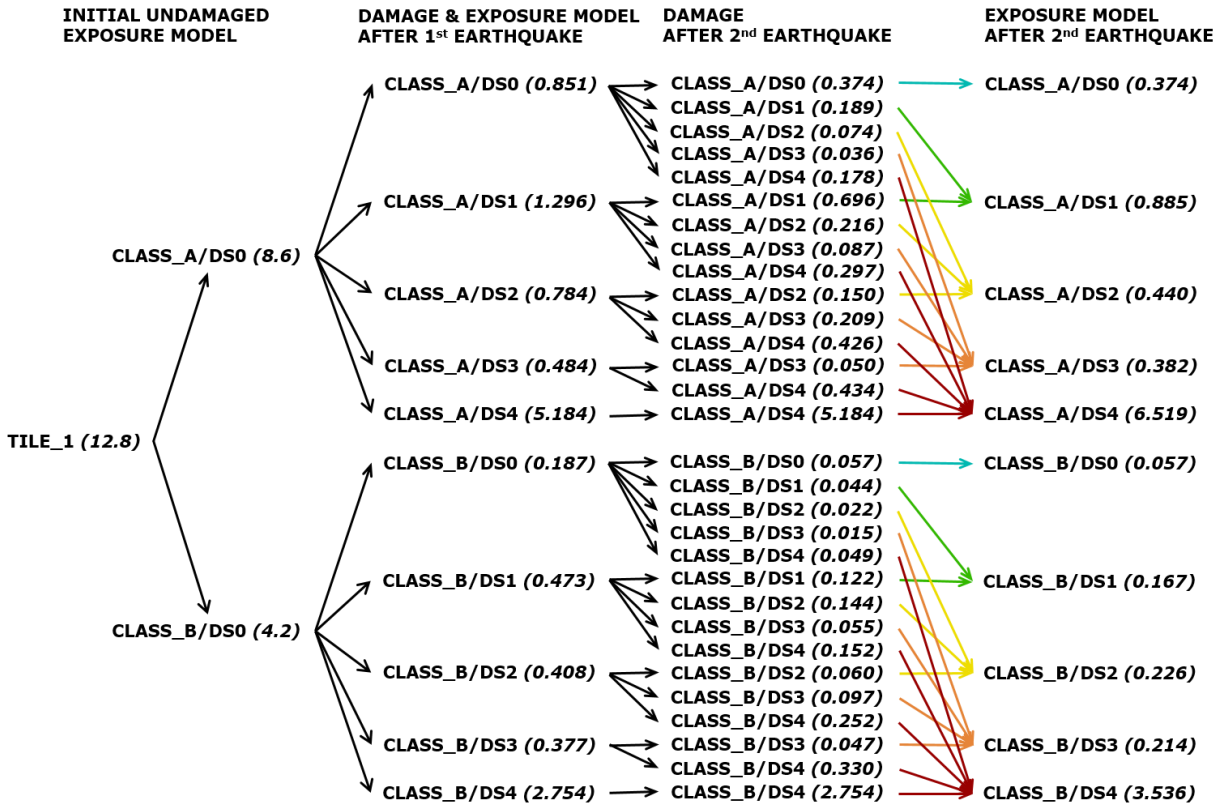

Figure 5 Example of the update of damage states in the exposure model for one tile with buildings of two different classes. Numbers in parentheses are numbers of buildings.

While in the short-term (and perhaps even the middle-term) it can only be expected that the damage state of buildings only evolves towards worse conditions, this is no longer true once we start looking into the repairing or replacing of buildings in the longer timeframe of post-earthquake recovery. The Real-Time Loss Tools currently focus on the short-term, but a full-scale implementation

should allow for the possibility that buildings get repaired and that new buildings get erected to replace fully damaged ones. This is one of the points in which the Real-Time Loss Tools and the present deliverable cross paths with the OpenQuake Recovery and Rebuilding Effort (OQ-REE) plug-in developed as part of RISE Task 4.3 (Deliverable 4.4; Reuland et al., 2022a). The possibility of bringing the two together into an integrated state-dependent model that includes recovery (e.g., Iervolino and Giorgio, 2015, 2022) could be explored in the future.

2.2 Updating the number of occupants

The effect of previous earthquakes on the number of people able to occupy buildings is incorporated into the calculation in a novel way that, to the authors' knowledge, has not been previously implemented. When a RLA is carried out, the number of people injured to different degrees of severity is calculated (bottom box of the RLA routine in Figure 3, second-to-last box of the OELF routine in Figure 4). This step occurs after the exposure model has been updated with the new damage states and the number of occupants has been distributed proportionally as well (as explained in the previous section).

Whether these injured people can return or not to the buildings they normally occupy depends on several factors, of which the Real-Time Loss Tools focus on two main ones: firstly, whether the building can be occupied in itself, depending on its damage status and whether it has been evacuated or not for inspection, and, secondly, whether the health of the people is such that they can leave hospital (and are not deceased). These two factors are represented in the Real-Time Loss Tools as expected numbers of days needed for inspection and repair (as a function of the damage state of the building), and numbers of days that people are expected to spend in hospital (as a function of the severity of their injuries). These numbers of days are counted with respect to the point in time at which the earthquake occurs.

When a RLA (or damage assessment due to one earthquake within an OELF) is carried out, two timelines of future occupancy are calculated based on these numbers of days. One of the timelines represents the number of people "still away" from the buildings they usually occupy, as a function of time. In the Real-Time Loss Tools, one timeline is calculated per earthquake and per *original_asset_id*, and is stored as an individual CSV file. As schematically shown in Figure 6, the total number of people still unable to return to their buildings at any point in time (e.g. the occurrence of a third earthquake in the example figure) are retrieved from all timelines of all past earthquakes.

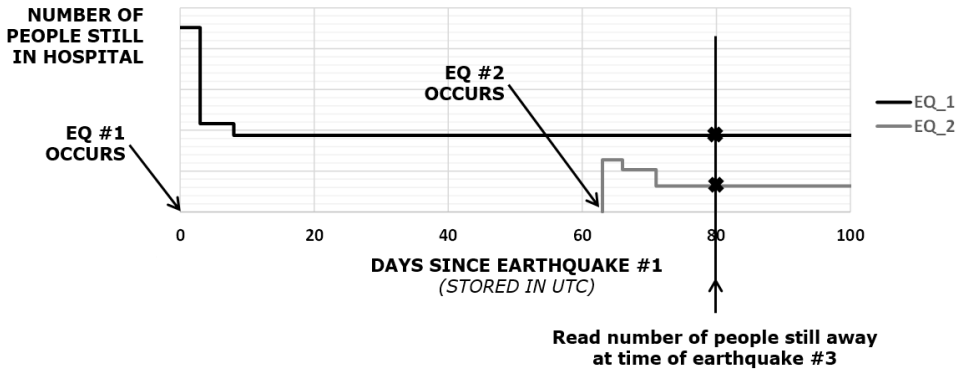

Figure 6 Schematic timeline of number of people still away due to injuries/death caused by two earthquakes.

The second timeline calculated by the Real-Time Loss Tools represents a step function indicating the moment in time in which people are allowed to return to their buildings, and it is calculated per earthquake and per damage state, as schematically depicted in Figure 7, and is stored as a CSV file as well. The step function takes a value of zero when people are not allowed back in and a value of 1 when they are allowed. This factor is named "occupancy factor" within the Real-Time Loss Tools.

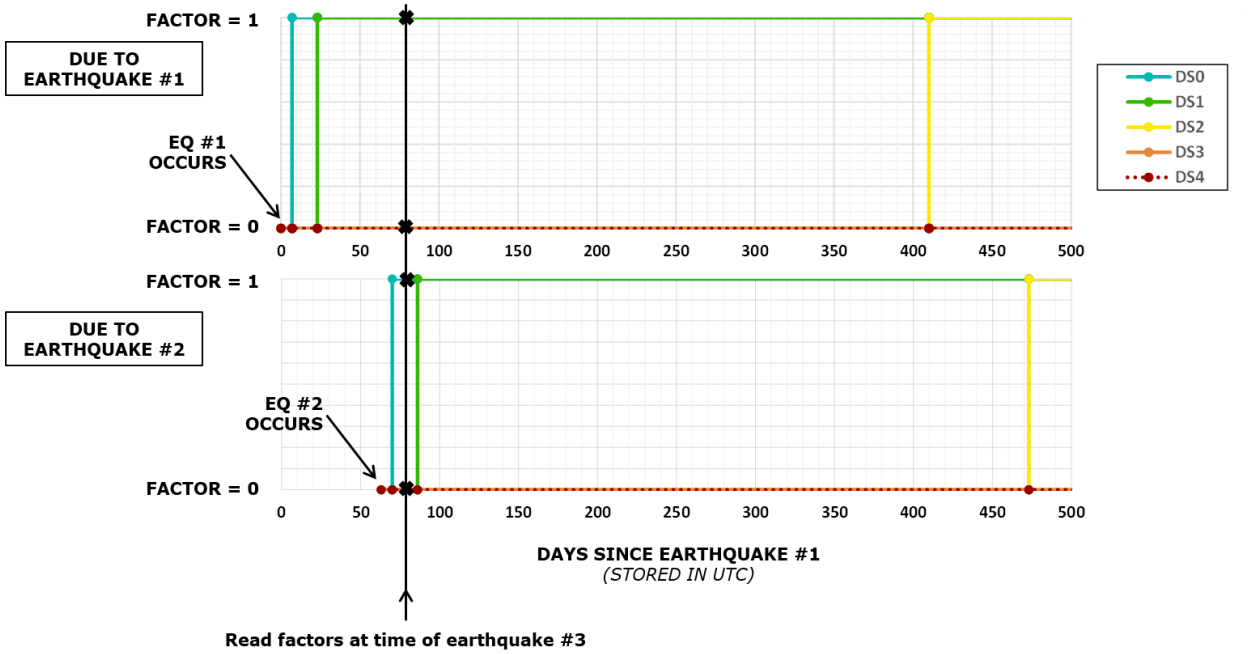

Figure 7 Schematic timeline of binary occupancy factors indicating whether people are allowed (1) or not (0) back to the buildings which they usually occupy, due to damage caused by two earthquakes.

When a new earthquake calculation is carried out, previous timelines due to all previous earthquakes are sought. The date and time in which the "current" earthquake occurs is first used to retrieve the step functions showing if people are allowed back to the buildings. If all factors are zero (nobody us allowed back into any building), the calculation ends there because there is no need to know how many people are still unable to return due to their own health. If at least one of the factors is different from zero, the number of people still away (Figure 6) is retrieved for each *original_asset_id*, and the number of occupants on the date and time of the current earthquake is calculated (also per *original_asset_id*) as:

$$occupants\ at\ time\ of\ day_{current} = F_{time\ of\ day} \cdot F_{occupancy} \cdot \left[census_{original} - still\ away\right] \quad (4)$$

where $F_{time\ of\ day}$ is the factor associated with the day, night or transit times of the day, $F_{occupancy}$ is the 0-1 binary factor that depends on the current damage state of the building (e.g. Figure 7), $census_{original}$ is the number of census occupants, and *still away* is the number of people whose health status does not allow them to return to the building (Figure 6).

The updating of the number of occupants by the Real-Time Loss Tools is a simplified version of what could, in the future, be a more rigorous calculation. Ideally we would like to keep track of all the paths of damage that each *original_asset_id* can follow. Looking at Figure 5, each of the damage states listed under "damage after 2nd earthquake" is associated with a number of injuries of different severities and a respective probability of occurrence (the probability of the *original_asset_id* being in that damage state). Each of those damage situations would lead to their own future timeline of possible damage and further injuries, always spreading the tree further with branches of damage states equal to or worse than the previous one. However, expanding the branching at every earthquake quickly leads to a significant increase in computational demand, as the number of *asset_id* associated with the same *original_asset_id* keeps on increasing. It is for this reason that the last column of Figure 5 groups together all current damage states (e.g., DS1) irrespective of the path it took the building to get to those damage states (e.g., DS0 after the first earthquake but DS1 after the second one, vs DS1 after both the first and second earthquakes). It is also for this reason that the updating of occupants is carried out at the level of the *original_asset_id*, calculating a total expected number of injured people still away due to all possible damage states, and arriving at a

current expected number of occupants, which is distributed across different damage states in proportion to the probabilities of the damage states themselves. It is thinking in the direction of this more rigorous calculation that the occupancy factors are stored for each earthquake (Figure 7), even though in the current calculations it is the last damage state that is defining the calculation. Further efforts could focus on evaluating the feasibility of keeping track of the damage paths.

The more we move into the future, the more other factors might begin to affect these timelines, as people can move away, severely damaged buildings can be re-built with the capacity to host different numbers of people, etc. In other words, the more we move into the future the more we start thinking in terms of post-earthquake recovery modelling in all of its dimensions, a matter that has been investigated in more detail as part of RISE Task 4.3 (Deliverable 4.4; Reuland et al., 2022a) (see section 3.9.1).

3. Components

3.1 Seismicity forecast

3.1.1 A new generation of Operational Earthquake Forecasting models

The field of earthquake forecasting is continuously evolving as new methods and innovative techniques are developed or adopted from other areas of expertise. Several institutions have worked within RISE Task 3.3 to produce a new generation of earthquake forecasting models, resulting in a large set of models having different degrees of innovation. In particular, the models and achievements of the task can be grouped in different classes that are summarised as follows (see also RISE Deliverable 3.3, Marzocchi et al., 2022):

- The tweaking of the existing best performing OEF models, which correspond to different flavours of the Epidemic-type aftershock sequence (ETAS) model.

- The development of a more refined clustering ETAS model that includes the innovative description of a time memory that is not included in classical ETAS models.

- A flavour of simplified/basic versions of clustering models that are still able to capture the essence of the earthquake clustering, while being, at the same time, easy and flexible enough to be used in regions where the earthquake catalogues make difficult to set up more complex models (e.g., regions that do not have good and long instrumental catalogues, or wide and inhomogeneous regions like Europe). Not less important, this kind of model may also represent a good reference model to be applied in any experiment carried out by CSEP, in order to have a homogeneous reference from which the information gain of each model can be measured.

- Innovative time-independent and time-dependent models that are based on the Bayesian INLABRU philosophy; in other words, non-parametric Bayesian data-driven earthquake spatial and temporal models.

- An innovative model that takes into account one of the most important problems in delivering reliable earthquake forecasts: the time variability of the completeness magnitude. In fact, it is well known that after a large earthquake (which is the time when the model should be more useful), the magnitude of completeness markedly increases. If not properly addressed, this issue may result in a severe underestimation of the forecasting model, in particular after a major event.

- An innovative testable time-dependent model entirely based on continuum mechanics, which accounts for the physics of the rate and state and the coulomb failure function. The

novelty of this model is that it accounts for the slip distribution on the source fault to describe the nearby stress heterogeneities that were one of the main reasons for the poor forecasting performances of this kind of model in the past.

A noteworthy feature of this new generation of earthquake forecasting models is that their outputs are a large number of stochastic realisations of seismicity (i.e., synthetic catalogues), instead of earthquake rates, which had been customary in the past. This overcomes the need to make assumptions on the statistical distributions associated with earthquake occurrence and the spatial correlation of rates in neighbouring cells in order to be able to calculate probabilities, which are now calculated numerically instead.

3.1.2 Specific details for the present application in Italy

For this proof of concept, the *ETAS.inlabru* method[8] developed by the University of Edinburgh within the RISE project has been used to produce the short-term seismicity forecasts. *ETAS.inlabru* is a Bayesian method for fitting temporal, spatial and spatial temporal ETAS model to seismicity data where the spatial model can include a wide range of marked point, marked polygon and raster covariates and a latent field within a linear predictor. Generally, it is more efficient than MCMC methods as it approximates the posterior distribution of a transformation of the parameters to be Gaussian with a mean and standard deviation that can be deterministically calculated using the Integrated Nested Laplace Approximation (INLA). This ensures complete reproducibility of the results. The posteriors returned by inlabru include the full covariance structure and samples of ETAS parameters are drawn from the joint posterior distribution of the parameters. Forecasts are generated by drawing 10,000 samples from the joint posteriors and then each parameters set is used to generate a synthetic catalogue. Therefore, a forecast for a pre-determined period of time is summarised by a collection of 10,000 synthetic catalogues for that period. The ability to sample from the joint distribution of the parameters ensures that the epistemic uncertainty around the parameters value are accounted for in the forecasts. The model used to generate the forecasts is a classic spatio-temporal ETAS model with spatially varying background rate and isotropic spatial kernel. The background rate is assumed to be the product between a productivity parameter and a function of the spatial location such that the integral of the background rate over the spatial domain is equal to the productivity parameter. The logarithm of the spatial variation of the background rate is assumed to be a Gaussian process with Matern covariance function and is estimated independently from the ETAS parameters. The magnitude distribution is independent from space and time and is assumed to follow a tapered Gutenberg-Richter law with b-value of 1 and a corner magnitude equal to 7.0. The posterior distribution of all parameters is estimated retrospectively using data from 2009-01-01 00:00:00 to 2010-01-01 00:00:00 and from 2016-01-01 00:00:00 to 2018-01-01 00:00:00 for the 2009 Aquila and 2016 Amatrice sequences respectively. The Homogenized Instrumental Seismic Catalog (HORUS) of Italy (Lolli et al., 2020) has been used for this application. For more details of the technical implementation see Serafini et al. (2023), Naylor et al. (2023), and Bayliss et al. (2020, 2022).

The *ETAS.inlabru* method is not implemented as part of the Real-Time Loss Tools. The seismicity forecasts are produced independently of the latter and passed on as input in the form of text or CSV files (see section 4.1). In this sense, the Real-Time Loss Tools can take input from any OEF model.

In order to generate the forecasts for this proof of concept, a polygon encompassing around 200 km in all directions from the areas affected by the 2009 L'Aquila and 2016-2017 Central Italy was defined, as shown in Figure 8, which also depicts the epicentres of all stochastic event sets in the forecasts. As can be observed, there are clusters of seismicity not only around the areas of interest in this work.

[8] https://github.com/edinburgh-seismicity-hub/spatio_temporal_ETAS_for_OEF

Figure 9 and Figure 10 show the distribution of magnitudes for each individual forecast (exported Mw 3.99+). As can be observed, using a corner magnitude of 7.0 in a tapered Gutenberg-Richter law leads to a few earthquakes with Mw larger than 7.0 being generated, the largest of all having a magnitude of 8.5. While these values are not fully compatible with what is usually observed in extensional settings of this kind (Neely and Stein, 2021), we did not remove the stochastic event sets that contained them as it was observed that the mean loss values obtained were not extreme despite their contributions. However, the handling of magnitudes larger than could be expected from the tectonic environment in the context of a full-scale operational earthquake loss forecasting system requires further consideration.

For details on the times at which the forecasts were generated, please refer to section 5.1.

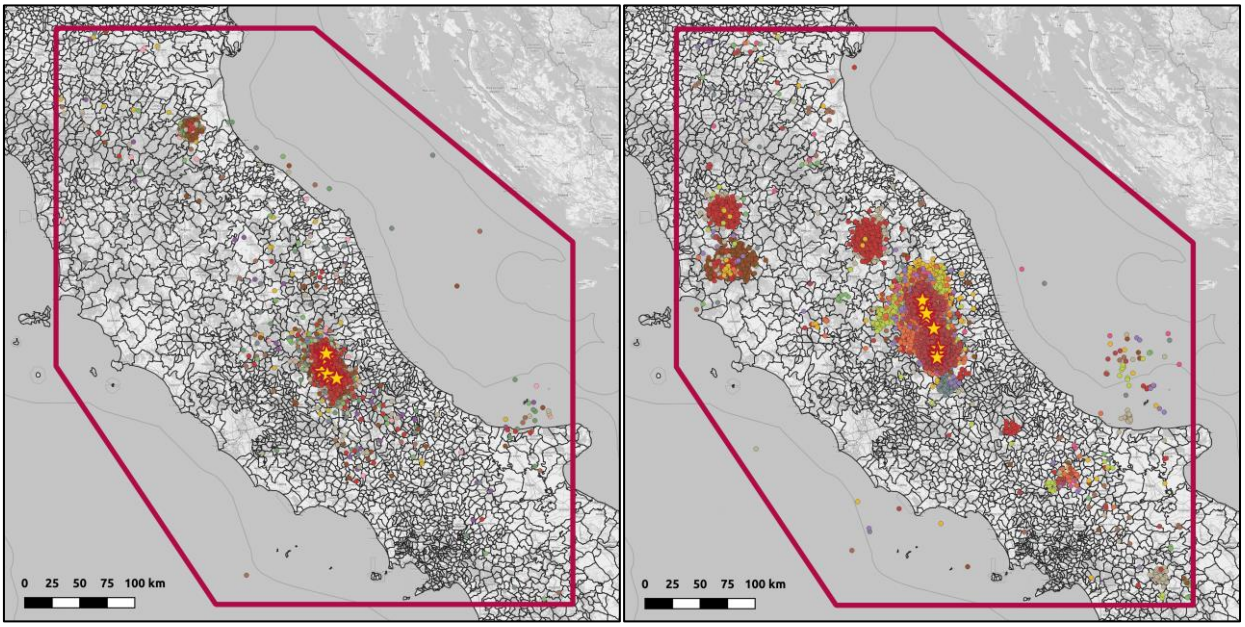

Figure 8 Earthquakes from all daily forecasts (of 10,000 realisations each) generated for the 2009 L'Aquila (left) and 2016-2017 Central Italy sequences (right) (exporting threshold: Mw 3.99). Yellow starts indicate real earthquakes of the two sequences with Mw 5.5 and above.

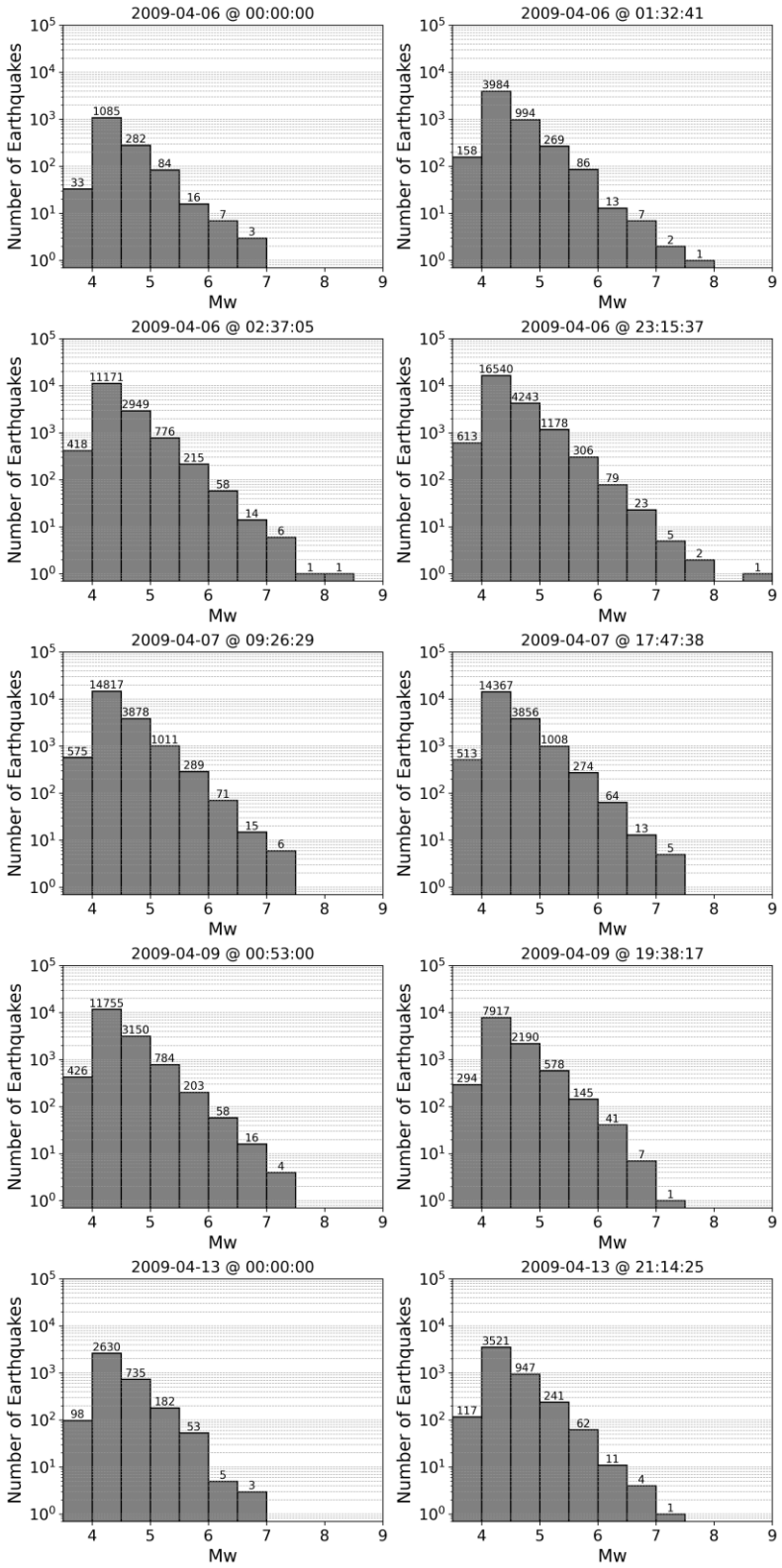

Figure 9 Number of earthquakes per magnitude bin for each of the daily forecasts (of 10,000 realisations each) generated for the 2009 L'Aquila sequence (exporting threshold: Mw 3.99).

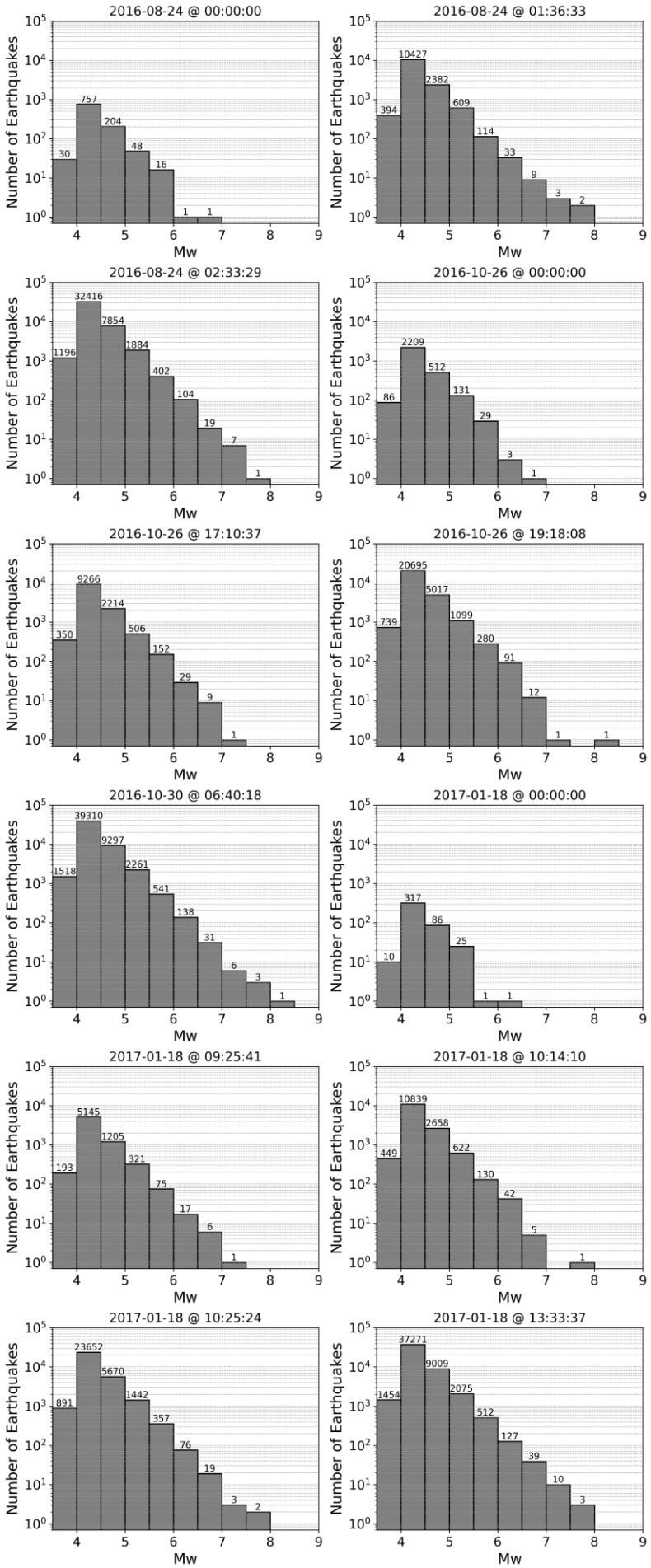

Figure 10 Number of earthquakes per magnitude bin for each of the daily forecasts (of 10,000 realisations each) generated for the 2016-2017 Central Italy sequence (exporting threshold: Mw 3.99).

3.2 Generation of earthquake ruptures

The connection between a seismicity forecast and the corresponding estimate of damage is via the characterisation of ground motion at the locations of the building exposure (or nearby sites where site conditions are known/defined). Empirical ground motion models (GMMs) are used for this purpose, as they describe the resulting probability distribution of ground motions given an earthquake's source properties, its distance from the site, and the local soil characteristics of each site in question. While seismicity forecasts that take the form of synthetic catalogues typically provide, for each simulated earthquake, an estimate of its epicentre, time and magnitude, modern GMMs require a more detailed description of the rupture. Their scaling of source-to-site distance with earthquake size and distance usually assume that the source is represented by a three-dimensional finite rupture, whose area increases exponentially with magnitude.

In the databases of strong motions from which the GMMs are calibrated, 3D finite rupture models for large and/or well-recorded events are taken from detailed seismological source inversions, the results of which are often published in the scientific literature or made available in compilations of finite-fault rupture models, e.g., SRCMOD (Mai & Thingbaijam, 2014). For a*pplication* of GMMs, however, we need to characterise the finite-fault properties of ruptures that have not yet occurred or, in the case of RLA, of ruptures that have occurred but for which the seismological source inversions have not yet been undertaken and no rupture model is yet available. Different approaches can be found in the literature to account for rupture finiteness in ground motion prediction in the absence of a known rupture surface. These include both the "equivalent distances" approaches, which use empirical formulae to convert point source distances (e.g., distance from the site to the epicentre $[R_{EPI}]$ or from the site to the hypocentre $[R_{HYPO}]$) to magnitude-dependent finite fault distances (e.g., shortest distance from the site to the rupture surface $[R_{RUP}]$, the surface projection of the rupture plane, i.e. the "Joyner-Boore" distance $[R_{JB}]$, etc.), or the use of "virtual faults", which are synthetic 3D fault planes whose positions, size and orientations may depend on local tectonics. Both approaches have their advantages and disadvantages, and the choice of approach depends on the context of the application, the choice of GMM and the tectonic information available for the region in question. In the current study we need to consider how to define finite rupture distances for two specific contexts: rapid loss assessment (RLA) and operational earthquake loss forecasting (OELF).

3.2.1 Rupture generation for Rapid Loss Assessment

RLA requires prediction of ground motions at sites of interest within seconds to minutes following an event, which may in some cases be conditioned upon observations of ground motions at recording stations where available. Here the rupture orientations can have a significant influence on the predicted losses in the near-field region of the fault, particularly where the expected rupture length may be on the order of tens, or even hundreds, of kilometres. For well recorded events, particularly those of larger magnitude, 3D finite rupture models derived from seismological inversions will eventually be produced by seismologists. These require the seismologist to process the waveforms needed for the inversion, to undertake the inversion itself, and to interpret the results in the corresponding tectonic context. In the best cases this process can yield preliminary estimates of the rupture plane within a few hours of the event, but these may be refined multiple times as new seismological data become available or a picture of the complexity of the rupture plane emerges. This is the mechanism implemented, for example, in the USGS ShakeMap system[9], whereby multiple versions are developed in the hours and days following a large event. For rapid prediction of ground motion (i.e., seconds to minutes after the event) the definition of a simpler planar approximation to the rupture surface is the main objective.

[9] https://earthquake.usgs.gov/data/shakemap/

Beginning with the assumption that for RLA following a notable earthquake the magnitude itself will be moderate to large, an effective means of defining an expected R_{JB} from R_{EPI}, magnitude (M) and distributions of known rupture properties is proposed by Thompson & Worden (2018):

$$E\left[R_{JB}\middle|R_{EPI},M\right]=\int_{-\infty}^{\infty}\int_{\delta_{min}}^{\delta_{max}}\int_{0}^{L}\int_{0}^{W_S}\int_{0}^{2\pi}R_{JB}(\theta,x,y,\delta,\epsilon)\times P(\theta)P(x)P(y)P(\delta)P(\epsilon)\,d\theta\,dx\,dy\,d\delta\,d\epsilon \tag{5}$$

Where θ and δ are the fault strike and dip, with probability distributions $P(\theta)$ and $P(\delta)$ respectively, x and y are the strike-normal and strike-parallel distances of the hypocentre within the rupture plane, with probability distributions $P(x)$ and $P(y)$ respectively. L is the fault length (km), which is determined via a magnitude to rupture-length scaling relation of the form $L=f(M)+\epsilon\cdot\sigma_L$, where ϵ is the number of standard deviations above or below the median length. W_S is the surface projection of the rupture width defined from $W_S=W\cos(\delta)$, orientation (θ and δ) and hypocenter position (x and y). Effectively, this approach integrates over a set of source-to-site distances corrected for finite rupture dimension L and W_S, and finds the expected Joyner-Boore distance given the probabilities of each and assuming a planar fault rupture. For most of these variables the probability distributions are uniformly distributed such that $\theta=\mathcal{U}(0,2\pi)$, $\delta=\mathcal{U}(\delta_{min},\delta_{max})$, $x=\mathcal{U}(0,W_S)$ and $y=\mathcal{U}(0,L)$, while $\epsilon=\mathcal{N}(0,1)$. Equation (5) can be extended to apply to expected rupture distance, $E[R_{RUP}|R_{EPI},M]$, by introducing an additional integral to account for the distribution of depth to the top of rupture (Z_{TOR}):

$$E[R_{RUP}|R_{EPI},M]=\int_{0}^{z}\int_{-\infty}^{\infty}\int_{\delta_{min}}^{\delta_{max}}\int_{0}^{L}\int_{0}^{W_S}\int_{0}^{2\pi}R_{RUP}(\theta,x,y,\delta,\epsilon,Z_{TOR})\times P(\theta)P(x)P(y)P(\delta)P(\epsilon)P(Z_{TOR})\,d\theta\,dx\,dy\,d\delta\,d\epsilon\,dZ_{TOR} \tag{6}$$

Where z is constrained by rupture length, width and seismogenic thickness in the region of the earthquake. Uncertainty in the prediction of ground motion arising from the distribution of distances ($\mathrm{Var}[R_{JB}|R_{EPI},M]$ and $\mathrm{Var}[R_{RUP}|R_{EPI},M]$) should be propagated into the standard deviation of the ground motion model using standard error propagation.

The equivalent distance approach has some appealing characteristics in terms of computational efficiency and the flexibility to adopt different probability distributions or impose different limits on the uniform distributions where tectonic information in a region may permit doing so. The formulations in equations (5) and (6) represent the least informative cases in which no information about rupture orientation is available. Once a focal mechanism has been determined for the event then the number of potential orientations is restricted to two likely candidate planes. Likewise, the orientations of large earthquakes on (or very close to) known major fault structures could be reasonably constrained to agree with those of the fault structures themselves. Where the equivalent distance approach is limited, however, is that it cannot easily be extended to consider other metrics of source-to-site distance such as strike-normal distance to the up-dip projection of the rupture plane (R_{JB}) or strike-parallel distance to the surface projection of the rupture plane (R_{Y0}); distance metrics that are becoming more widely used for predicting near-fault ground motion amplification effects such as hanging wall scaling and directivity. While the equivalent distances $E[R_{JB}|R_{EPI},M]$ and $E[R_{RUP}|R_{EPI},M]$ do not refer to a specific rupture plane, one cannot necessarily determine a physically-consistent suite of near-fault distance metrics. For GMMs currently applied in Europe, such near-fault amplification factors are seldom modelled explicitly; however, this is likely to change in the near future.

Though the integrals shown in equations (5) and (6) do not necessarily require characterisation of virtual faults, the virtual faults approach to finite rupture distance characterisation originates from the same framework. With virtual faults we generate a large number of fault surfaces, representing the uncertainties in the aforementioned properties ($\theta,\delta,x,y,\epsilon,Z_{TOR}$) either by sampling their respective distributions or enumerating discrete approximations to the distributions (as prob-

ability mass functions). For each virtual fault, the corresponding finite fault distances are calculated and the resulting expectation and variance determined from the set of faults. This is analogous to the equivalent distance approach and has the same advantages that the distributions and their ranges can be refined and reduced where information is available to do so. The additional advantage is that by generating the faults directly, it is possible to retrieve a preferred rupture plane (or subset of planes) either by i) identifying that which produces R_{JB} and R_{RUP} closest to $E[R_{JB}]$ and/or $E[R_{RUP}]$ across range of sites of relevance, and/or ii) minimise the misfit of the expected GMM to observed data as strong motion records become available. From this preferred rupture plane one can determine other distance metrics for near-fault scaling directly, and the rupture itself can be input into existing calculation software such as the USGS ShakeMap (Worden et al., 2020) and/or OpenQuake-engine (Pagani et al., 2014). The main limitation of the virtual faults approach is the potential computational cost of re-computing distances for large numbers of ruptures; however, the distance calculations can be easily parallelised, and good results can be found by retrieving the preferred virtual fault plane using a lower resolution grid or small subset of target sites.

One important development in the field of rapid assessment of ground shaking following an event is the FinDer algorithm (Böse et al., 2012, 2018). This is an efficient approach for rapid determination of the rupture *as a line source* by minimising the misfit between expected and observed PGA using binary template matching, which can yield good estimates of the rupture length and orientation within a few seconds of the data being recorded. The line source does not necessarily remove all the uncertainties captured in the integrals in equations (5) and (6), as dip, down-dip hypocentre position and top-of-rupture depth remain unconstrained. It can, however, significantly reduce the major uncertainties due to rupture strike, length, and along-strike hypocentre position. This can be easily integrated into both the equivalent distance and virtual fault approaches, and the remaining unconstrained properties potentially refined further based on regional geological and seismological information.

3.2.2 Generating ruptures in synthetic catalogues for OELF

The translation of the synthetic catalogues from effective two-dimensional point sources to three dimensional finite ruptures also requires the integration of more information to constrain the scaling of the finite fault dimensions with magnitude, their depth in the Earth's crust, their orientation, and their style-of-faulting. This is common to RLA; however, the sheer number of earthquakes needed for OELF, combined with the predominance of low magnitude events, render the full distance distribution approaches used for RLA impractical to apply at scale. Instead, rather than using a suite of virtual faults for each event in the synthetic catalogue to characterise the full distribution of source-to-site distances for each location, we sample a single virtual fault per event from distributions provided for the region in which the event occurs. As the vast majority of events will be small-to-moderate magnitude (M ≤ 5), the specific rupture characteristics will have a weaker influence on the ground motion as source-to-site distances are already systematically larger due to the smaller rupture surface. Even those GMMs with specific near-fault scaling terms will tend to taper these to zero for smaller magnitudes, minimising the influence further. In the minority of cases that the synthetic catalogues may produce larger events, the uncertainty in location has a far greater influence than that of other rupture properties. In this case it is mostly sufficient to capture only the predominant orientation and finite dimension of the ruptures, which should be already defined in the local distributions of θ, δ and rupture rake (ψ), along with the magnitude to distance or magnitude to rupture area (A) scaling relation ($A = f(M, \psi) + \epsilon\sigma_D$). This should ensure consistency of the properties of the simulated rupture planes with those of the local scale tectonics.

In the proposed framework for OELF being applied in the Real-Time Loss Tools we require a zonation of rupture property distributions, which divides a region into specific zones (polygons) and provides for each zone the following information: i) Magnitude to rupture area scaling relation, ii) a preferred rupture aspect ratio (i.e. $\nu = L/W$), iii) earthquake hypocentre depth distribution $f(h_D)$,

iv) upper and lower seismogenic depths, and v) a distribution of rupture nodal plane properties, $f(\theta, \delta, \psi)$. Fortunately, this information is something that is commonly provided in distributed seismicity source models for PSHA, particularly those undertaken using the OpenQuake-engine software. Though a regionalisation of rupture properties does not necessarily have to originate from the PSHA source model, the use of such source models provides a convenient consistency in the treatment of finite faults between national/regional scale hazard assessments and OELF systems.

The generation of stochastic ruptures for OELF in the current application is summarised as follows. For each earthquake in the synthetic catalogues used to represent the OEF we are provided with an epicentre, a magnitude and an event time. If no depth information is provided for the synthetic event (which is commonly the case) we sample from the hypocentre depth distribution for the zone in which the epicentre falls. In the OpenQuake formulation, this takes the form of a probability mass function such that $f(h_D) = P(h_D = d_1, d_2, \dots, d_{Nd})$, i.e., a discrete set of depths and their corresponding probabilities (shown in Figure 11). There is no theoretical reason to prevent $f(h_D)$ from taking the form of a continuous distribution; however, most PSHA software represent it as a discrete set of depths and weights. With the hypocentre now defined, we then generate the finite rupture. First, we need to sample the rupture nodal plane properties (θ, δ, ψ) from the distribution $f(\theta, \delta, \psi)$, which is again represented as a probability mass function $f([\theta, \delta, \psi]) = P([\theta, \delta, \psi] = [\theta, \delta, \psi]_1, [\theta, \delta, \psi]_2, \dots, [\theta, \delta, \psi]_{NP})$, also shown in Figure 11. We then determine the rupture area from the magnitude-to-area scaling relation ($\log A\ (km^2) = f(M, \psi) + \epsilon \cdot \sigma_A$), and thus the rupture length (L) and down-dip width (W) from the aspect ratio ν. The hypocentre is assumed to be located in the centre of the rupture plane, thus $P(y) = 1$ for $y = L/2$ and 0 otherwise, and $P(x) = 1$ for $x = W/2$ and 0 otherwise. Using the hypocentre location, the rupture dimensions and the rupture orientation we then construct an *initial* rupture plane for the earthquake.

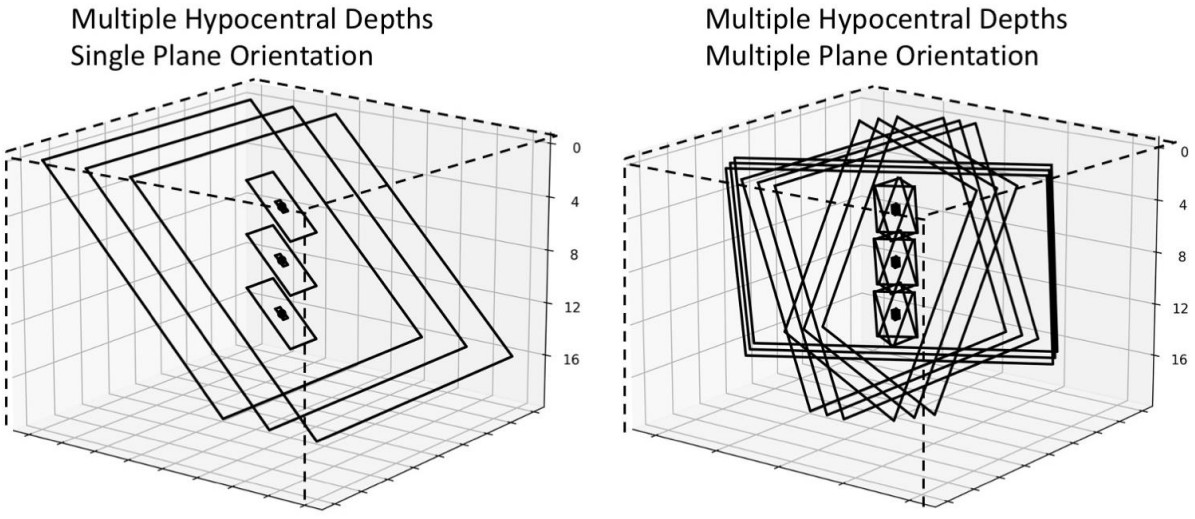

Figure 11 Illustration of hypocentral depth distributions (left) and nodal plane distributions (right) for generation of synthetic ruptures in OELF in the form of probability mass functions: $P(h_D = 4\ km, 8\ km, 12\ km)$ and $P([\theta, \delta, \psi] = [0,\ 60, -90], [60, 60, -90], [120, 60, -90])$.

If the upper and lower edges of the rupture are contained within the upper and lower seismogenic depths respectively, no further adjustment is applied. The initial rupture is then assigned to the synthetic event and the process will move to the next event. If the vertical extent of the rupture width is less than the seismogenic thickness of the zone, the rupture is translated down- or up-dip accordingly to ensure that it is contained within the zone. When this happens the *absolute* location of the hypocentre does not change but its relative position within the rupture plane (x) will shift, meaning that the hypocentre is no longer in the centroid of the rupture. If the vertical extent of the rupture width initially exceeds the seismogenic thickness defined for the zone, the rupture will be rescaled such that its width is constrained by the seismogenic thickness, but its length will increase in order to conserve the sampled rupture area. After rescaling, the rupture will then be assigned to the earthquake and the process will move on to the next event. In this process we effectively break the aspect ratio to allow longer ruptures while conserving both the

seismogenic thickness of the crust and the rupture area to magnitude scaling. This assumption is consistent with observations of rupture aspect ratio scaling for larger magnitude events and the physics of rupture generation.

The outcome of the process returns a corresponding rupture plane for each event in the synthetic catalogue, which can then be exported into a set of OpenQuake-engine rupture model XML files. Further refinements to the process can be applied, and there may be a case for adopting an approach for larger earthquakes that follows the virtual rupture approach proposed for RLA, especially given that such events are comparatively rare in the data set. We have not done so in the current application, however. There may also be scope to incorporate dependencies in the rupture properties for successive events in a sequence, rather than sampling each independently. In the current form, however, this process is compatible with any existing uniform source zone model, which can be input into the software in the OpenQuake-engine XML format.

3.2.3 Specific details for the present application in Italy

The two case-study applications focus on the 2009 L'Aquila and the 2016-2017 Central Italy sequences. For the larger earthquakes in the sequences, finite-fault rupture planes have been determined from seismological inversion and are available through the Italian Accelerometric Archive (ITACA) website[10] (Russo et al., 2022). While the resulting OpenQuake-engine rupture mode XML files could have been directly pre-computed and input to the Real-Time Loss Tools, the software was coded to explicitly include the need for an algorithm to generate/retrieve such rupture properties, so as to highlight the relevance of this step. In its current implementation, a function simply translates the ITACA rupture properties into the OpenQuake XML format assuming normal faulting (which is the case in this study). Although we have presented in section 3.2.1 how finite fault ruptures can be determined for large earthquakes in RLA, this is not the focus of the case study application here. Instead, we focus on the OELF applications, for which the methodology in section 3.2.2 is applied.

The Real-Time Loss Tools developed in this work have initially focused on implementation zonation of rupture properties using uniform area sources models provided in the OpenQuake-engine seismogenic source model XML format. This provides for each source zone the fixed polygon geometry, upper and lower seismogenic depths, rupture aspect ratio and choice of magnitude-area scaling relation. It also defines the hypocentral depth distributions and rupture nodal plane distributions as probability mass functions. For Italy we have two recent PSHA models available that could provide uniform area source zonations for our purpose: i) the 2020 European Seismic Hazard Model (ESHM20; Danciu et al., 2021) and ii) the MPS 19 National Seismic Hazard Model for Italy (Meletti et al., 2021). Though the former could be considered for European scale operation, evaluation of the sources contained therein revealed that the distributions of depth and rupture orientation had been collapsed to single values, in many cases forming north-south striking vertical dipping ruptures. This collapsing of the distributions was undertaken to improve efficiency of the ESHM20 calculations and was shown to have a minimal impact on PSHA. However, this collapsing does make the ESHM20 model poorly suited for the purpose intended here. Instead, we adopt a specific uniform area source model from the MPS19 source model logic tree, namely MA4, which is described in detail in Visini et al. (2022).

The MA4 model defines 50 sources covering Italy and the surrounding territory. For all sources the magnitude to rupture area scaling relation used is that of Wells & Coppersmith (1994), while the initial aspect ratio, ν, is fixed to 1.0 throughout. Upper and lower seismogenic depth is specified for each source along with probability mass function for hypocentral depth and nodal planes. The latter have been determined for each zone from analysis of local scale geology and available earthquake focal mechanisms. For three zones a depth-dependent nodal plane distribution is defined such that earthquakes below a dividing depth layer assume a different distribution from

[10] https://itaca.mi.ingv.it

those above the layer. This results in the zone being split into two separate zones, each with the same polygon geometry but different depth and nodal plane distributions. Where events in the synthetic catalogues for OELF have associated depth information, they are assigned the distributions of the corresponding depth layer for the purpose of generating ruptures. If only the epicentre is provided (which is the case in the present proof of concept), then a decision must be made as to which depth layer the event should be assigned. For this purpose, we randomly sample the choice of depth layer, weighted according to the relative rate of seismicity λ_M with M ≥ 4.5 of each of the two layers from the magnitude recurrence model. This has been added as a general functionality, meaning that depth-dependent rupture properties can be supported by the tools if the user wishes to specify them. The area source model is shown in Figure 12 along with an illustration of a rupture set generated for an OEF synthetic catalogue.

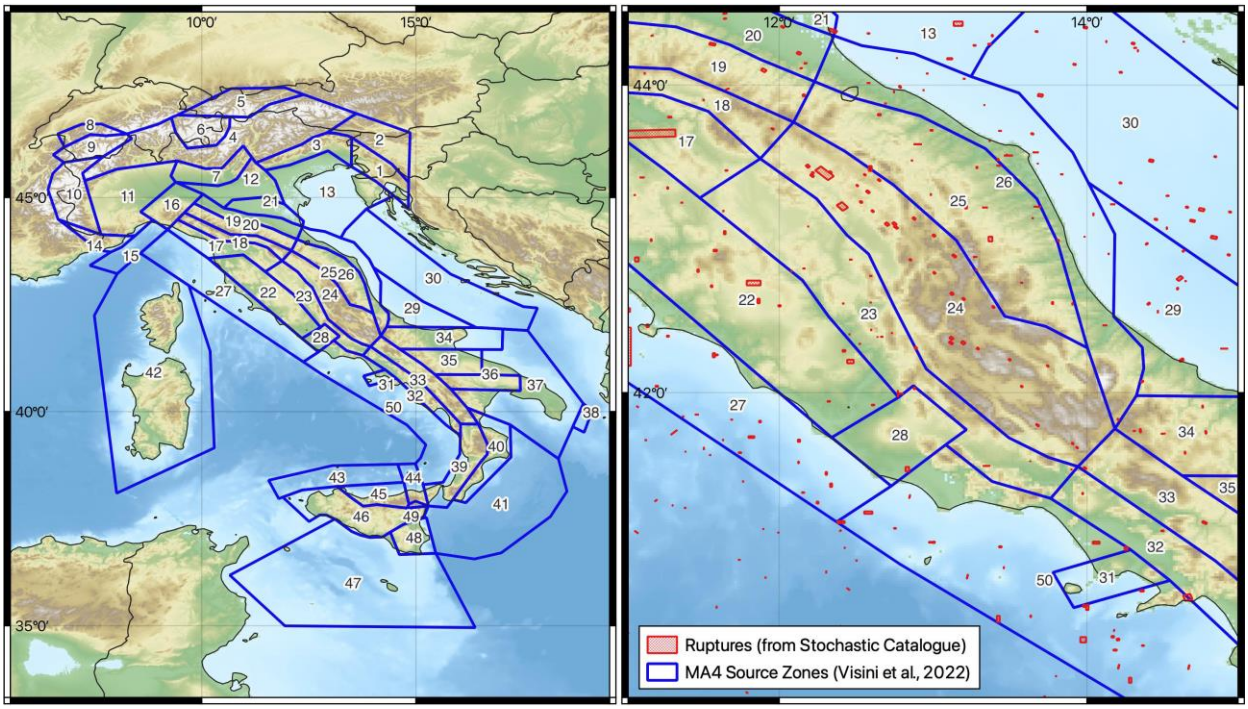

Figure 12 MA4 seismic source zone model (Visini et al., 2022) (left) and an example of a stochastically generated finite rupture set for Central Italy developed from a synthetic earthquake catalogue (right).

3.3 Ground motions

3.3.1 Generation of ground motion fields for RLA and OELF

The generation of ground motion fields for rapid loss assessment and operational earthquake loss forecasting is not any different from any other seismic hazard or risk modelling application, and requires attention to the classic ground motion components:

- selection of a ground motion model (GMM) or a set of ground motion models combined by means of a logic tree;
- consideration of spatial and inter-period correlation of the variability;
- definition of a site model to characterise soil conditions.

As the Real-Time Loss Tools use OpenQuake to calculate the ground motions and resulting damage, all possibilities, requirements and constraints of OpenQuake regarding these three components apply for the Real-Time Loss Tools as well.

One additional component that can be incorporated in the case of rapid loss assessments is the use of ground motion values measured by seismological stations and/or inferred from macroseismic

intensities calculated from the responses of citizens to online questionnaires to constrain and condition the ground motion fields, as is done by the USGS ShakeMap software (Worden et al., 2010, 2018). The current version of the Real-Time Loss Tools does not make use of such ShakeMaps as an input into the RLA (as is instead considered in the European system described in RISE Deliverable 6.5, Crowley et al., 2023), though this would be possible as the OpenQuake engine can run scenario loss calculations using ShakeMaps as an input (see Silva and Horspool, 2019), as further discussed in Deliverable 6.5. Alternatively, rather than use the ShakeMaps from existing systems (e.g. those in the U.S., Europe, Italy, Switzerland), which are tied to specific networks of seismological stations or online questionnaires, the Real-Time Loss Tools could effectively develop its own ShakeMaps, incorporating also data coming from instrumented buildings. This feature would become particularly interesting in a future in which large numbers of buildings may be instrumented at their base and other levels for the purpose of constant monitoring; the large volume of data would help to drastically reduce the uncertainty in the calculated ground motions. The current version of the Real-Time Loss Tools does not have this capability, and neither does v3.15 of the OpenQuake engine for which it is coded. The newest version of OpenQuake (v3.16), which has been just released on 17 February 2023, includes this capability as an experimental feature; the Real-Time Loss Tools can be easily updated to be able to take in the required input files with measured ground motions and pass it on to OpenQuake.

3.3.2 Specific details for the present application in Italy

The ground motion model of Lanzano et al. (2019), which was developed specifically for Italy, was used for this proof of concept. The intensity measure calculated was average spectral acceleration (AvgSA) based on the 23 periods used by Orlacchio (2022) in the derivation of the state-dependent fragility models, as explained in section 3.5.2, which are 0.04, 0.07, 0.1, 0.15, 0.2, 0.25, 0.3, 0.35, 0.4, 0.45, 0.5, 0.6, 0.7, 0.8, 0.9, 1.0, 1.25, 1.5, 1.75, 2.0, 2.25, 2.5, and 2.75 seconds. The inter-period correlation of the spectral ordinates was accounted for in OpenQuake by means of the Jayaram and Baker (2009) model.

For the characterisation of local soil conditions, the 30-arcsec resolution V_{S30}[11] model of Weatherill et al. (2022) developed for the European Seismic Risk Model 2020 (Crowley et al., 2021a) was used (Figure 13). When provided with a site model and an exposure model, OpenQuake calculates the ground motions at the points of the site model that are nearest neighbours to the locations of the exposure model. When looking in detail at the specific available coordinates around the exposure model used for this proof of concept (e.g., Figure 14), it became apparent that all components of exposure would be assigned to one or two points of the site model, at most. On top of this, the use of AvgSA as the intensity measure meant that no spatial correlation of ground motions could be accounted for, as no publicly available spatial correlation model for AvgSA exists yet. For this reason, we decided to interpolate the values of V_{S30} to the centroid of the nine tiles using inverse distance weighting of the model of Weatherill et al. (2022), as shown in Figure 14 for the case of the exposure being located in the town of Norcia.

This modelling decision is the equivalent of considering full spatial correlation for the location of the nine tiles and three buildings of this proof of concept. While this is not fully accurate, it is not unreasonable to expect a large correlation for a building portfolio that covers such a small geographic area, like the one used herein. Moreover, keeping the 30-arcsec model would have led to full correlation as well in the cases in which all exposure locations had the same closest neighbour. However, in cases in which two nearest neighbours existed, there would have been the risk of using extremely different values of ground motion for two sub-sets of the exposure locations, which would be more unrealistic (or at least with an accuracy impossible to define, given the resolution of the original exposure model).

[11] Average shear wave velocity in the top 30 meters.

For each earthquake run, be it within a RLA or OELF calculation, 1,000 realisations of ground motion (and, consequently, 1,000 realisations of damage probabilities) were calculated to capture the aleatory variability of the ground motion model.

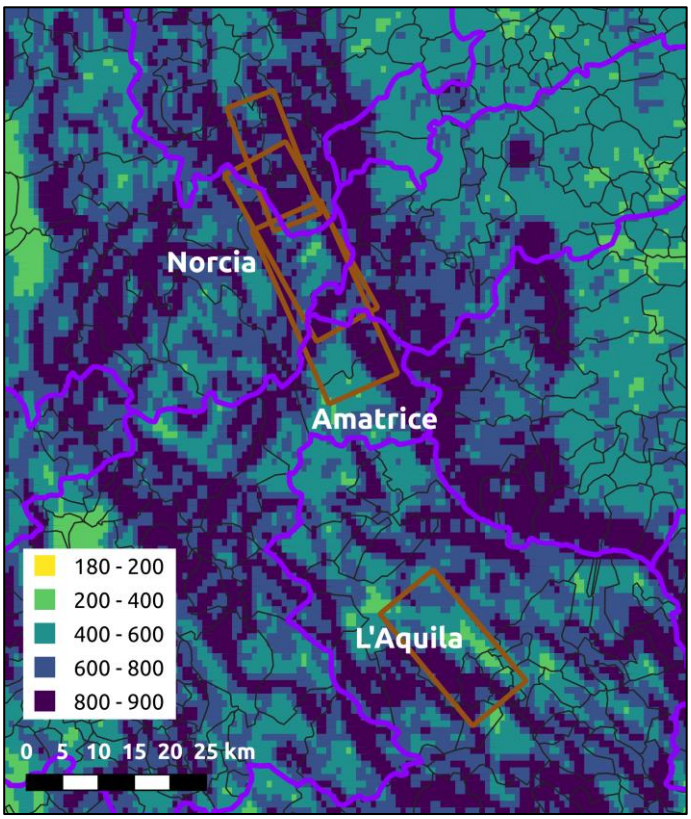

Figure 13 Model of average shear wave velocity in the top 30 m (V_{S30}) of Weatherill et al. (2022) for ESRM20 (Crowley et al., 2021a), in m/s.

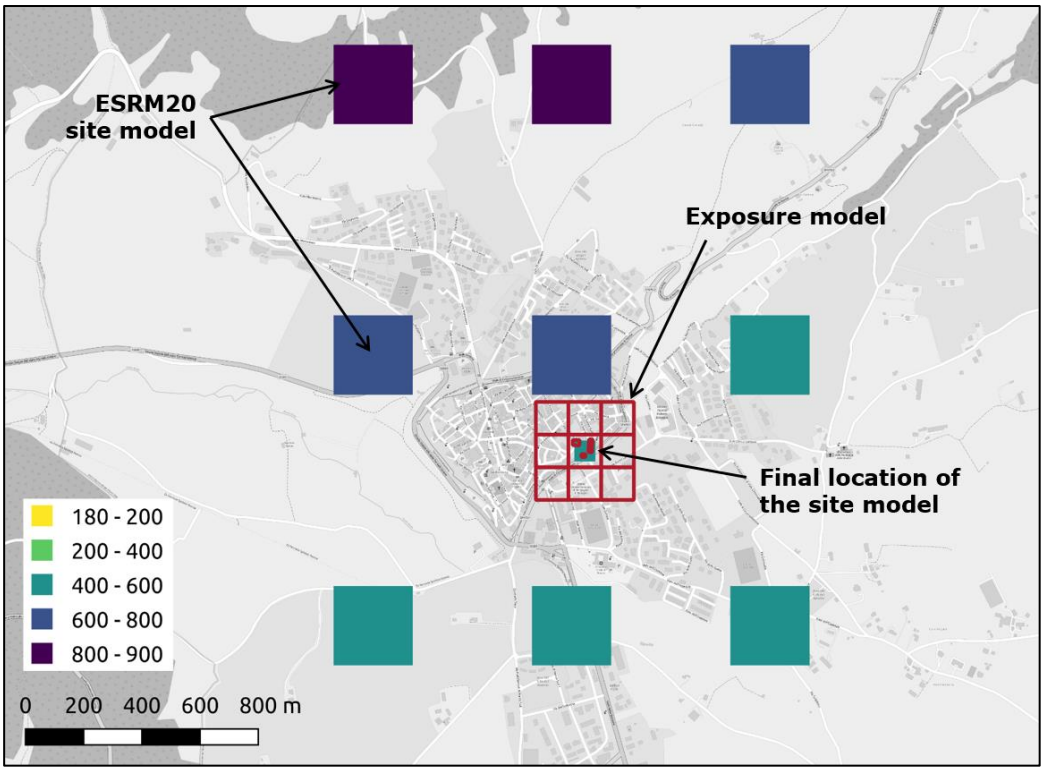

Figure 14 Model of average shear wave velocity in the top 30 m (V_{S30}) of Weatherill et al. (2022) for ESRM20 (Crowley et al., 2021a), in m/s, around the town of Norcia. Background: OpenStreetMap.

3.4 Exposure model

3.4.1 Exposure models for dynamic damage/loss assessments

Exposure models for regional applications have traditionally been created with a top-down approach, starting from statistical data available at some degree of aggregation, usually population census data and commercial/industrial statistics in terms of a country's administrative units. Such an approach has been followed, for example, for the creation of exposure models for South America (Yepes-Estrada et al. 2017) and Europe (ESRM20; Crowley et al., 2020, 2021a), and finds its roots in the fact that it is virtually impossible to carry out building-by-building physical surveys in large areas (countries, continents) without governmental support and investment. Proposals have been made, nevertheless, to combine exposure models resulting from top-down approaches with in-situ survey data collected for smaller regions (e.g., Pittore et al., 2020), allowing risk modellers not only to incorporate ground-truth observations to a model of a reality that may have remained relatively static, but also to capture changes in the ground-truth in time.

This last aspect of the variability of exposure in time has been the focus of attention of Task 2.7 in the RISE project, within which a Dynamic Exposure Model for Europe has been developed (Deliverable D2.13; Schorlemmer et al., 2020, 2023), which continuously retrieves data from OpenStreetMap (OSM) and combines it with a distribution onto zoom-level 18 quadtiles of the ESRM20 exposure model (Crowley et al., 2020) that takes into account an estimate of the completeness of OSM on each tile (i.e., whether all buildings that exist in reality are represented in OSM). The resulting model is thus a combination of individual buildings whose footprints are retrieved from OSM and quadtree-formulated tiles of zoom level 18 (around 100-m side in central-southern Europe) that group buildings expected to exist in the tile but not yet represented in OSM (which are calculated comparing the expected numbers of buildings from the distribution of ESRM20 against those already in OSM). This approach results in a continuous feeding of the model with new data, which can either stem from new data incorporated to OSM regarding existing buildings, or data on new buildings.

The existence of an exposure model capable of hosting information on individual buildings is fundamental for the incorporation of SHM data which is, by nature, compiled at a building-by-building level. Dynamic properties of buildings such as fundamental frequencies of vibration as well as fragility models based on damage sensitive features derived from recorded sensor data (see section 3.6) can be appropriately stored in databases or any other file structure that allows easy retrieval when attempting to carry out a rapid loss assessment or an operational earthquake loss forecast. Even traditional fragility models based on ground motion intensity measures can be refined and calibrated based on knowledge on the dynamic properties of monitored buildings (e.g., Perrault et al., 2013), enabling the risk modeller to switch from building class-derived fragilities to building-specific ones. Such fragility models need not necessarily be stored *within* the exposure model per se; what is needed is a clear storage system and a link between the two to be able to retrieve both exposure and fragility models when necessary.

Apart from the incorporation of newly-built structures, a fundamental aspect in which an exposure model can and should be dynamic is in the capacity to store the current health (or damage) status of the building(s). Existing damage may stem not only from that caused by previous earthquakes within a sequence but also from lack of maintenance and deterioration associated with weathering (e.g., Iervolino et al., 2016). The damage status can be a specific damage state in a scale, or probabilities of each damage state, and needs to be stored in direct association with their corresponding buildings in either case. In the case of individual buildings, probabilities of damage remain probabilities, but in the case of aggregations of buildings in a tile or an administrative unit these translate into expected numbers of buildings of each building class in each damage state. The repairing or replacing of a building that has been damaged after an earthquake (or any other hazard) can be thought of as the ultimate change in a building's health status. A continuous

RLA/OELF system should have a means of updating the exposure model to reflect the longer-term effects of post-earthquake recovery on the building stock.

Focus so far has been placed on the study of the fragility/vulnerability of buildings, as they are the simplest to study and assess, but exposure refers to buildings' occupants as well, and so does its dynamic component. Ideally one would wish to have models that describe the number of occupants in a building at different times of the day, on different days of the week, and at different times of the year. The ESRM20 exposure model (Crowley et al., 2021a) classifies building occupants according to the time of the day. These are calculated by multiplying the "census" number of occupants, that is, the number of occupants that results from dividing all people into the available number of buildings, by coefficients associated with day, night and transit times. The coefficients used by ESRM20 are a modified version of the PAGER population distribution model (Jaiswal and Wald, 2010). Future versions of ESRM20 will incorporate the seasonal variability of occupancy based on the Global Human Settlement Layer's ENACT 2011 Population Grid (Schiavina et al., 2020; Batista e Silva et al., 2020).

3.4.2 Specific details for the present application

This proof of concept uses the concept of the Dynamic Exposure Model developed by Schorlemmer et al. (2020, 2023) just described, by focusing on three monitored buildings that are represented by their individual footprints and nine tiles with aggregate numbers of buildings. However, the formulation of the proof of concept and the Real-Time Loss Tools themselves work with any sort of resolution of the exposure model. The format is that of the OpenQuake exposure CSV files (see section 4.4).

The three monitored buildings included in the exposure are a theoretical typical Swiss residential unreinforced masonry building, a 15-storey reinforced concrete shear-wall hotel in Budva, Montenegro, and the 13-storey reinforced concrete shear-wall tower of the Grenoble City Hall, France. More details on these buildings, such as their characteristics (real or assumed), any numerical modelling efforts that have been undertaken, as well as existing monitoring activities and associated analyses are provided in the following subsections. It is noted that assumptions on replacement costs and numbers of occupants of these two real buildings are based on ball-park estimates, and fragility models derived for them are based on very simplified models. Moreover, neither of the two are located in Italy and are therefore exposed to a different seismic hazard. As a consequence, the results obtained within this proof of concept are not to be interpreted as statements on the vulnerability or safety of these real buildings.

Figure 15 depicts the nine tiles and the number of buildings of different classes contained in them, as well as the footprints of the three monitored buildings, all located within tile 5 (the central one). All building classes in the tiles are Italian masonry or reinforced concrete residential structures for which Orlacchio (2022) developed state-dependent fragility models as part of RISE Task 4.2. The footprints of the Budva hotel and the Grenoble city hall were retrieved from OpenStreetMap and rotated so that the principal axes of the buildings were aligned with the directions in which the accelerograms were run to simulate the effect of earthquakes (see section 3.7).

This "generic" exposure model was translated to the seven different locations considered initially for this study (i.e., stations marked with rectangles in Figure 1), so that the central tile contained the seismological station used to retrieve the ground motion records. The tiles were not arbitrary but corresponded to real quadtree-formulated tiles of zoom level 18, defined in the EPSG:3857 projection (as used by the Dynamic Exposure Model for Europe, RISE Deliverable D2.13; Schorlemmer et al., 2020, 2023).

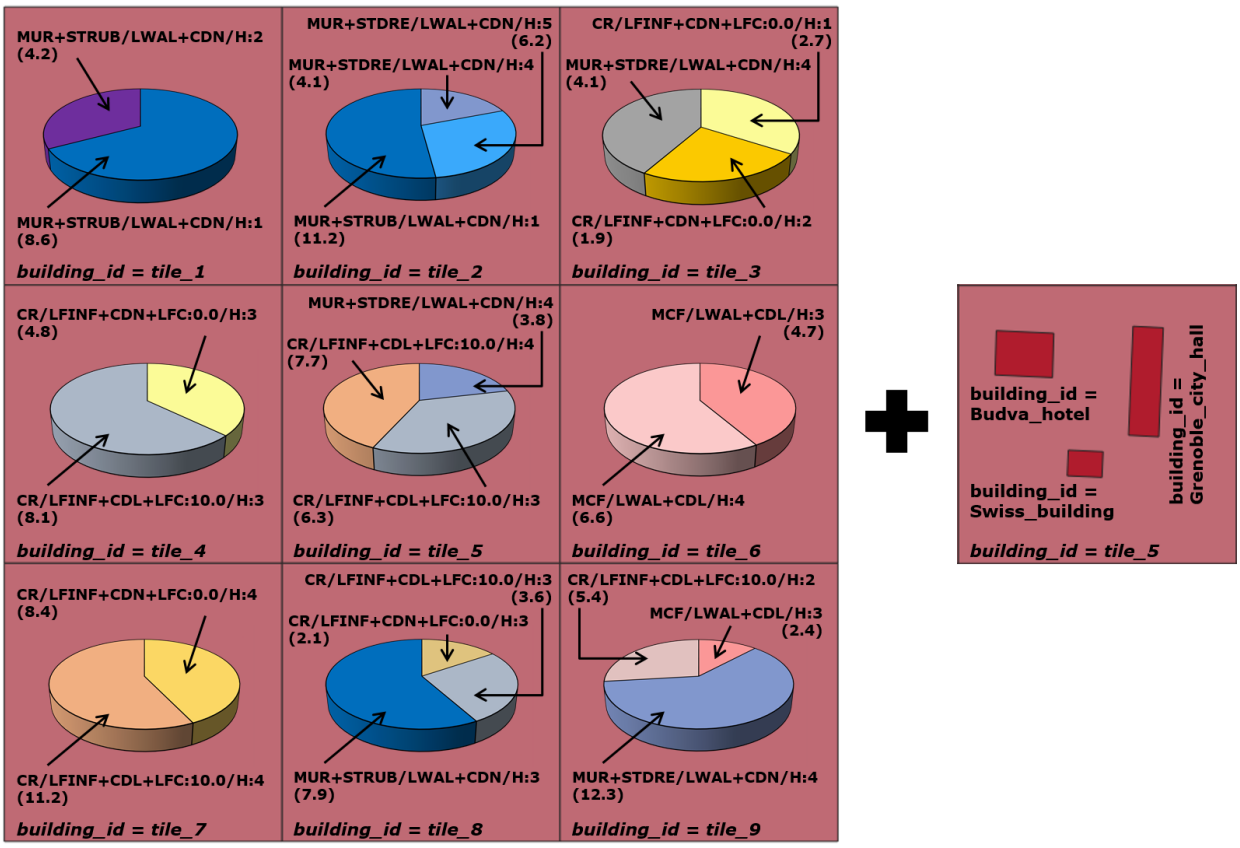

Figure 15 Exposure model used for this proof of concept: tiles (left) and individual monitored buildings (right). Building classes in terms of GEM Building Taxonomy v3 (Silva et al., 2022). Number of buildings indicated in parentheses.

3.4.2.1 Typical Swiss residential building

Based on typical geometries and construction practices in Switzerland, a representative residential building has been modelled (see Figure 16). The stiffness of the building mainly results from the façade walls and a stiff reinforced-concrete slab rigidly links the walls at floor level. The basement floor has smaller openings and has therefore higher stiffness and strength. Thus, the building effectively corresponds to a three-floor unreinforced masonry (URM) building.

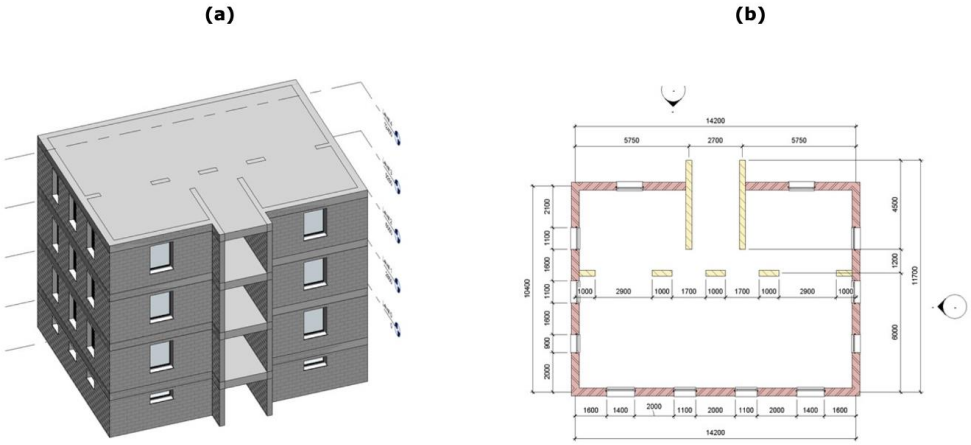

Figure 16 Render (left) and plan view (right) of the fictitious typical Swiss URM building.

The building is modelled in OpenSees (McKenna et al., 2000) using macro-elements that have been developed for unreinforced masonry buildings (Vanin et al., 2020a, 2020b). These three-dimensional elements combine shear and bending failure and can even be used to model out-of-plane

failures. However, given the stiff connection of the walls to the floors, out-of-plane failure is ignored in this case. The predicted pushover (PO) curve, using a triangular load pattern, is shown in Figure 17 (left). First, the spandrels fail (at around 3 mm), thus reducing the stiffness of the structural system without compromising the transfer of vertical loads. Failure is reached at a roof-level displacement of 29 mm, when a wall on the first floor fails in shear. Using the N2-method, the PO curve is transformed into a bilinear capacity curve (see Figure 17b). Given the importance of the initial slope of the curve for dynamic properties – which are essential in the formulation of DSFs for SHM – the bilinear curve is defined using the initial slope of the PO curve, until the failure of spandrels.

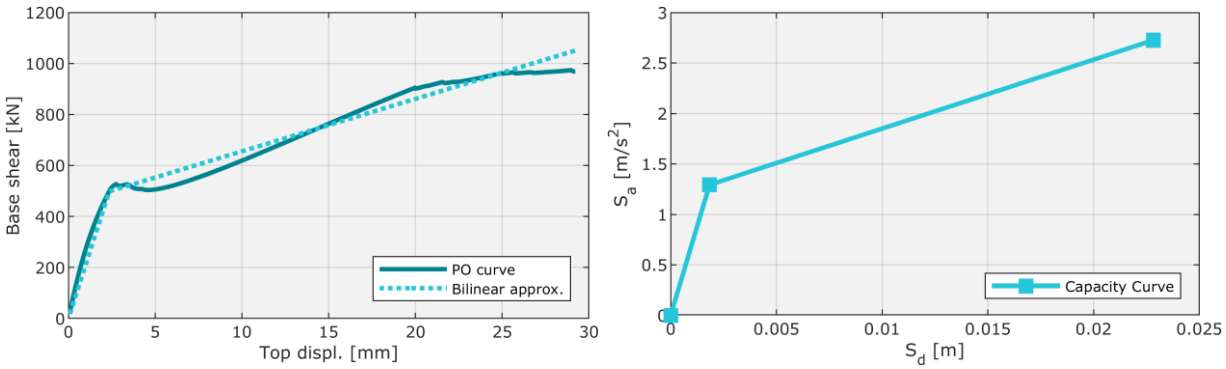

Figure 17 Results of the static nonlinear (pushover) analysis and the bilinear approximation (left) and the corresponding bilinear capacity curve for nonlinear time-history analysis with a SDoF model.

The result of the nonlinear time-history analyses is illustrated for the 2019-2017 Central Italy sequence in Figure 18. The maximum top displacement is compared with damage thresholds, established on the basis of the yield displacement defining the capacity curve (see Figure 17). In addition, the number of walls that remained linear-elastic (referred to as "healthy") are compared with the number of walls that have been damaged (first stiffness degrades and then, when the maximum shear force is reached the strength degrades).

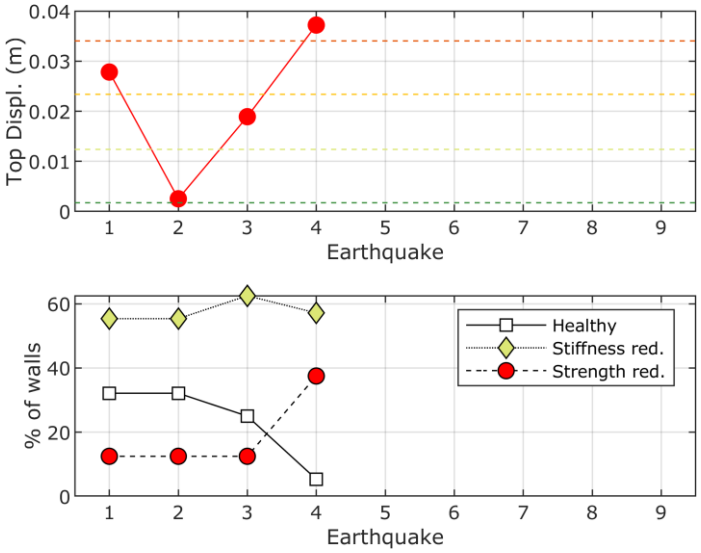

Figure 18 Damage prediction for the typical Swiss masonry building during the 2016-2017 Central Italy earthquake sequence. Maximum transient top-displacement is compared with DS thresholds (top) and the number of damaged walls is evaluated (bottom). During the fourth earthquake of the sequence the building reaches failure.

3.4.2.2 Hotel in Budva, Montenegro

The Budva hotel consists of 19 storeys, i.e., two underground garage storeys, a basement, ground level, a mezzanine, thirteen usable floors and a roof (i.e., 15 storeys above ground in total). Based on standard MEST EN 1998-1, used for building design at the location, the values of design PGA are 0.34 g and 0.15 g for the return period of 475 and 95 years, respectively. The height of the building is 55.9m, of which 13.4m are below ground level. The base of the building has a rectangular shape of approximately 21.2 x 16.7 m. Non-structural walls are made out of bricks and gypsum boards. Plans of the characteristic floor below and above ground level are shown in Figure 19. The thicknesses of the designed walls are 0.20 m, 0.25 m, 0.30 m and 0.40 m. The building is founded on a slab with a thickness of 1.20 m. Floor slabs are cast-in-place reinforced concrete and have a thickness of 0.15 m. Frames have negligible stiffness compared to the walls, which makes the structural system of the building a system with ductile walls. The design ductility class is medium (DCM). The concrete class is C30/37, and the rebar reinforcement class is B500B. Structural elements have been designed for dead, live and seismic loads. Seismic analysis has been conducted using multimodal spectral analysis according to MEST EN 1998-1, where masses of dead loads and 30% live loads with an eccentricity of 5% have been used.

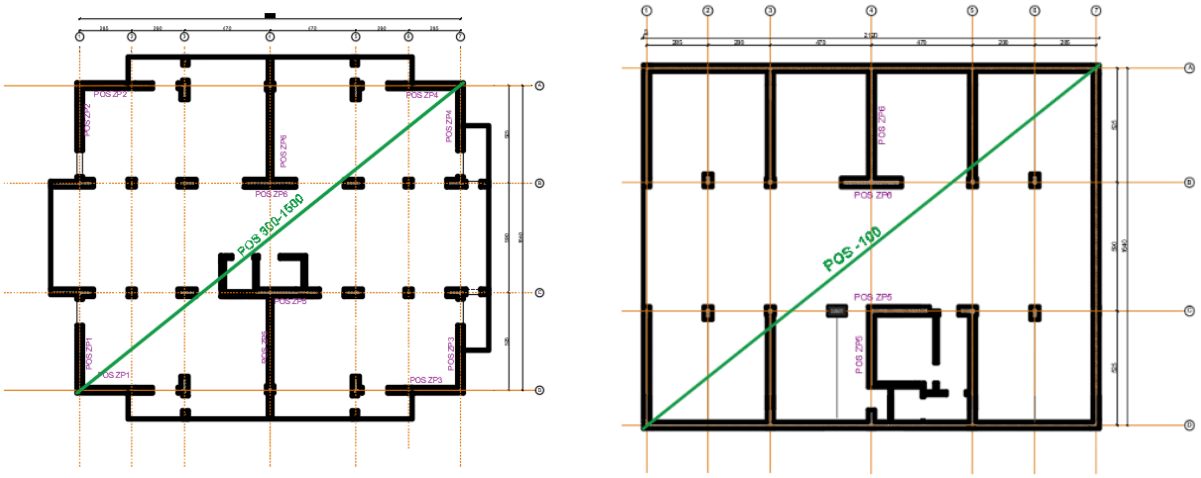

Figure 19 Floor plan of floors above (left) and below (right) ground level.

A non-linear model of the building was done using the CSI PERFORM 3D software. Modelled structural elements are walls, floor slabs and the foundation slab. Slabs are modelled as rigid diaphragms, with accompanying mass of dead loads and 30% of live loads. Walls are modelled as fibre elements, except garage walls, which are modelled as elastic elements, in line with the literature's recommendations (CSI, Powell, 2007). The walls are modelled using two components which are acting in parallel. The first component contains vertical reinforcement fibres (representing the reinforcement on the wall faces) and concrete fibres of negligible strength and Young's modulus to not interfere with the behaviour of the concrete fibres from the second component. The second component contains bending reinforcement (placed at the corners of the wall) and concrete fibres. Concrete of the boundary elements is modelled with confined concrete characteristics, while web concrete is modelled with unconfined concrete characteristics. Shear behaviour is considered elastic, where the shear D/C ratio is examined. Out of plane behaviour of the walls is modelled as elastic without considering P-Δ effects. Columns and beams are not modelled since the stiffness of the frames is negligible against that of the walls. Fibres of both reinforcement and concrete are modelled with bilinear stress-strain relationships. Modal analysis showed that the fundamental periods of vibration in two principal planar directions are T_x=1.832 s and T_y=1.527 s. The non-linear model is shown in Figure 20.

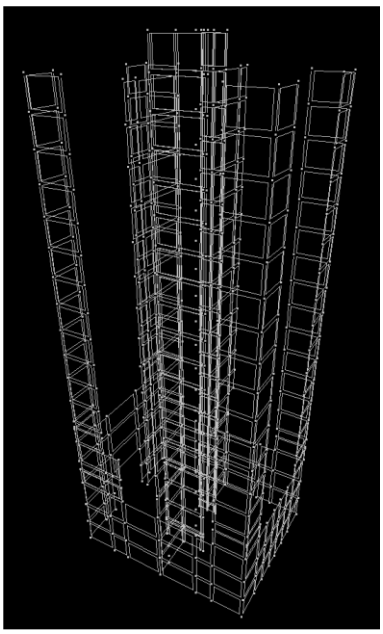

Figure 20 Nonlinear model of the Budva hotel in Perform 3D.

With respect to seismic action, in studies undertaken outside of the RISE project, the building has been checked to evaluate the non-collapse (NC) requirement and damage limitation (DL) requirement by conducting non-linear time-history analyses (NLTHAs). In order to account for uncertainties in soil effects, a total of 56 earthquake records were selected. Earthquakes were grouped into eight groups of seven earthquake records for each planar direction and each soil type (A, B, C and D). Several limit states have been defined and analysed: the shear capacity limit state for NC requirements, limit states for deformations (concrete core crash and reinforcement yielding and wall capacity rotations) for both NC and DL requirements and the limit state of inter-storey drifts in both planar directions only for DL requirements check. NC requirements were checked for an earthquake intensity corresponding to a 475-year return period, while the return period of 95 years was used to examine damage limitation requirements. Selected groups of earthquake records were scaled to these two intensity levels using REXEL v 3.5 software (in line with EN 1998-1 provision). In order to evaluate the NC and DL requirements, the behaviour of the building was checked by obtaining maximum values of demand/capacity (D/C) ratios from each NLTHA and obtaining its mean values for each group of earthquake records. D/C ratios for concrete crushing were calculated based on maximal values of confined concrete strain obtained using EN 1992-1-1 provisions. The yielding of longitudinal reinforcement was checked through D/C ratios based on the value of reinforcement yielding strain equal to 0.00234. Rotation capacities have been assigned both according to FEMA 356 and EN 1998-3. Capacity for inter-storey drifts has been assigned according to EN 1998-1 from the damage limitation requirement for the non-structural brittle elements (0.05 values adopted).

The results of the latter analyses showed that considering mean values for each group of records, the D/C ratio for wall rotation did not exceed 1, ranging from 0.43 to 0.7, meaning that NC requirements are satisfied. Also, mean values of the D/C ratio (ranging from 0.3 to 0.59) showed that concrete crushing strains are under the limit values and mean tension strains have exceeded the yield point. That behaviour is desirable and expected because it represents the ductile nonlinear behaviour of structural walls. Yielding is observed mainly on higher floors. Requirements that prevent brittle failure (shear stress D/C ratios) are also checked, and the results show that the shear capacity is not exceeded.

With the objective of preventing limitations of building usage due to damage and disproportionately high repair costs, DL requirements were checked as well. Based on the obtained mean of D/C values for concrete and reinforcement strains lower than 1, yielding of reinforcement and concrete crushing is prevented. The mean values of inter-storey D/C ratios are below 1.00 (ranging from 0.53 to 0.94) for each group of records, meaning that the DL requirement is fulfilled from

this point of view. Capacity values for wall rotations for DL requirements were calculated based on the values proposed in FEMA 356 for Immediate Occupancy and taken with the value of 0.003 rad. Analyses showed that this value had not been reached.

Based on the above results, the considered building in Budva satisfies both non-collapse and damage limitation requirements. Detailed results can be found in Popovic and Pejovic (2023).

The possibility of evaluating the damage level of the building based on its dynamic properties measured after an earthquake was examined, with focus on the elongation of the natural period of vibration due to plastic deformation as the dynamic parameter. This is justified considering that along with induced structural damages, the decline of stiffness leads to a more flexible structure, and thus the vibration period increases. The effect of the elongation period can be expressed through the relationship $\Delta T=T_{in}/T_{el}$ (Katsanos and Sextos, 2015), where T_{el} is the fundamental elastic vibration period, and T_{in} is the vibration period after damage caused by the earthquake.

In the case of the Budva building, four damage levels were considered: slight damage, medium damage, significant damage and collapse. These damage states can be described through several damage indexes. Here Park-Ang index (DIPA) is used. The values of Park-Ang indices were calculated for each of the 58 NLTHAs conducted (scaled intensity level equal to the 475-year return period). Based on the work of Aghagholizadeh and Massumi (2016), we assumed the following relation between DIPA and the four damage levels considered: for slight damage DIPA <0.2, medium damage 0.2< DIPA <0.4, values of DIPA >0.4 are related to significant damage while collapse state is assumed when DIPA >1. At the same time, from each NLTHA, T_{in} was determined based on the floor acceleration at the building top, and the ΔT was derived.

Figure 21 shows the relationship between the elongation period (ΔT) and the DIPA. In order to define the relationship between the damage index and the elongation period parameter, two regression curves were fitted to the NLTHA results. Our results show that when the vibration period increases by 13%, it can be considered that the structure has entered the medium damage level until the increase reaches about 50%. After an increase higher than 50% and up to 90%-95%, the structure can be considered to exhibit significant damage. For the increase of vibration period over 90%-95%, it can be assumed that the structure has reached the collapse state.

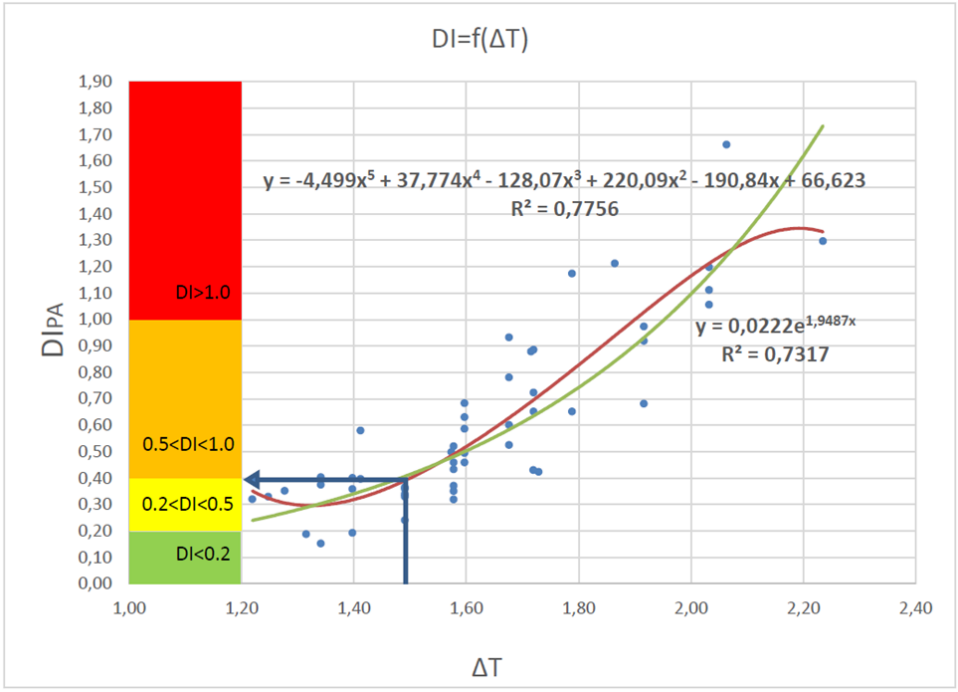

Figure 21 Relation between Park-Ang index and period elongation (ΔT) obtained for the Budva hotel by means of NLTHAs.

For the damage-dependent fragility function developed for this building (see section 3.5.3), a modal pushover analysis using the CSI PERFORM 3D model described above has also been undertaken, in both directions of the building. The weaker direction pushover (Figure 22) was used, though similar levels of ultimate base shear were obtained in both directions.

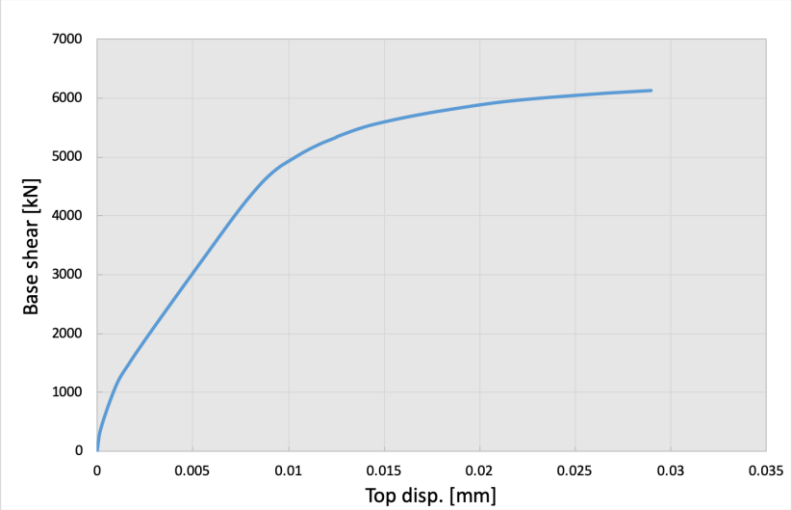

Figure 22 Model pushover curve in the weaker direction of the Budva hotel.

A number of tri-axial MEMS accelerometers developed by QuakeSaver[12] have been installed in the Budva hotel as part of the RISE project. Data from these sensors are not used in this work, though, as the proof of concept focuses on past earthquakes that have occurred in Italy. However, this (together with the Grenoble City Hall about to be described) is an example of an actual monitored building whose processed recorded response could feed into the framework presented herein.

3.4.2.3 Grenoble City Hall, France

The Grenoble city hall is a 13-story reinforced concrete structure built in 1967, with a plan section of 44m x 13m (L, T, respectively), and a height of 52 m above the ground. The inter-story height is regular between the third and twelfth floors (3.2m) and larger for the first (4.68m) and second floors (8m), above which a 23m span pre-stressed slab is supported by two inner cores. These cores, consisting of reinforced concrete shear walls, surround the stairwells and lifts and are located on two opposite sides of the building. The foundation system consists of deep piles anchored in a rigid underlying layer of sand and gravel. The building dates from before the introduction of the seismic building code, and so it was not built according to earthquake design rules. Since 2004, the building has been the subject of modal analysis and ambient vibration-based monitoring studies (e.g., Michel et al., 2010, Michel and Guéguen, 2010; Mikael et al., 2013), numerical modelling and engineering applications calibrated to experimental data (e.g., Desprez et al., 2015), and data-driven studies to analyse specific behaviours, such as soil-structure interaction (Guéguen et al., 2017) and rotation (Guéguen et al., 2020). The resonance modes of the structure are thus known to be 1.16 Hz and 1.22 Hz in the longitudinal and transverse directions, respectively, with a torsional mode at 1.44 Hz.

The National Building Array Program (NBAP) in France was launched in 2004 by the French Accelerometric Network (RAP-RESIF, 2023; Péquegnat et al., 2008). RAP-RESIF manages the network of accelerometer stations primarily dedicated to recording strong motion at sites of engineering interest, i.e., with stations in noisy urban areas. The NBAP decided from the outset to apply the standards of the seismic community and the RAP-RESIF roadmap for data collection and distribution: (1) the instruments had to be sufficiently sensitive for the level of seismicity in France; (2) the data had to be fully described in terms of seismological parameters (magnitude, localization, time of occurrence)

[12] https://docs-9ca1bd.quakesaver.net/sensors/qs-mems.html

and instrumental response (commonly called metadata) so as to be reusable by anyone; and (3) the data had to be openly accessible online.

The NBAP started in 2004 by installing six 24-bit dataloggers at Grenoble's City Hall building, coupled to 3C Kinemetrics Episensor accelerometers with a high dynamic range of 155 dB (with 1g clip level and flat frequency response above 200Hz to DC), at the top (FDSN station code RA.OGH4 to 6) and bottom (FDSN station code RA.OGH1 to 3) of the building (Figure 23). The channels are oriented along the main axes of the structure (FDSN channel codes HN1 for the transverse T direction-azimuth N60, HN2 for the longitudinal L direction-azimuth N330, and HNZ for the vertical). After a first period in triggered mode, the overall acquisition system was updated in 2008 to continuous mode, and integrated in 2012 into the SeiscomP detection and location system (Weber et al., 2007) implemented by the Alpine Seismicity Monitoring Service (SISmalp, 2023), hosted at the Earth Science Institute (ISTerre) in Grenoble. This service operates the regional component of the French Seismological and Geodetic Network (RESIF, https://www.resif.fr) in charge of national coordination of observation and data distribution via the RESIF-DC data centre (Péquegnat et al., 2021; RESIF-DC, 2023). By 2019, a seventh station (FDSN station code RA.OGH7) had been integrated into the CHB array at mid-height, and a multi-parameter weather station (e.g., wind speed, temperature, humidity, etc.) completed the setup (FDSN station Code RA.OGH8) (Figure 23). While the weather channels are sampled at 10 min, the sampling rate adopted for the accelerometer channels was 125 Hz until 2018, then 100 Hz until now. All RAP-RESIF data are transmitted via ADSL to the RESIF-DC data centre in miniSEED format and available online via webservice (RESIF.RAP, 1995).

Figure 23 View of the city hall building in Grenoble and description of the monitoring array. The two stations highlighted in black (OGH1 and OGH4) are those used in this study.

Amplitude-frequency noise models for seismic building monitoring in a weak-to-moderate seismic region

Given the abundance of monitored data for the Grenoble City Hall building, but which cannot be used in the case study presented herein, as an additional activity for this deliverable, a study has been undertaken of the amplitude-frequency noise models from the high-quality accelerometric monitoring of this building and the benefits of seismic building monitoring policies in weak-to-moderate seismic regions. First, accelerometric data from one continuous year were used to derive broadband noise models for the bottom and top of the building. The noise models were compared with (1) the noise sensitivity of the high-gain accelerometer installed in the building and low-cost sensor sensitivity models; (2) the typical earthquake response curves given by Clinton and Heaton (2002); and (3) the earthquakes recorded in the Northern Alps (Figure 24). This study highlights threshold values for signal-to-noise ratio (≥3 or 9dB) recordings as a function of magnitude and distance for weak-to-moderate earthquakes. We presented a preliminary cost-benefit analysis of instrumentation for such regions according to seismic hazard and instrumentation quality. For weak-to-moderate seismic regions like the Grenoble area, the capability of high-dynamic accelerometers

to record low-amplitude ground motions and building responses is confirmed and encouraged to enable high quality observation of building response over a broad range of frequencies. Bearing in mind that full-scale building test data are of greater interest for improving our understanding of building response than even the most sophisticated models, the recording of weak-to-moderate earthquakes in buildings must be broadened using high dynamic instruments to obtain more comprehensive and advanced results. A detailed analysis can be found in Guéguen et al. (2023).

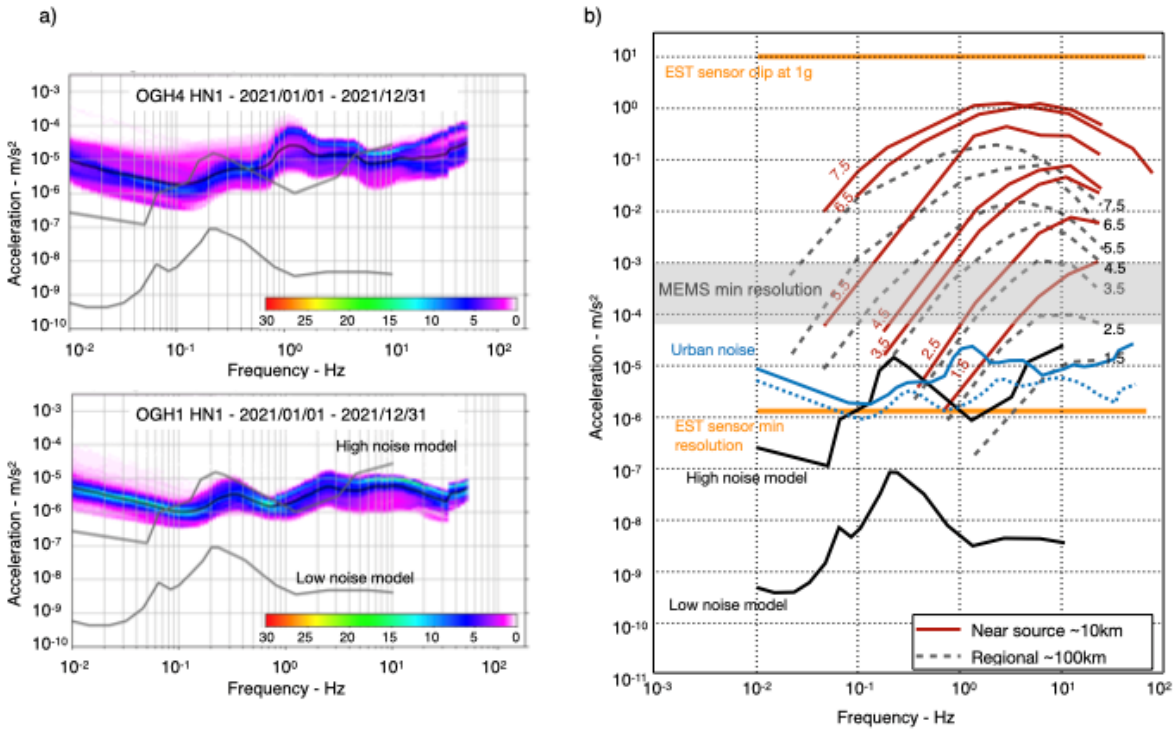

Figure 24 Noise models for the Grenoble city area. a) Mean PSD of observed horizontal amplitudes at the OGH4 (top) and OGH1 (bottom) stations of the city hall building array throughout 2021. b) Comparison of the CHB instrument response (orange lines), Grenoble's urban noise (blue lines) and the high-noise and low-noise models (Peterson, 1993) (bold black lines). For reference, dashed black and red curves show the response for various sized earthquakes at two distances (local: 10km; regional: 100km) derived from Clinton and Heaton (2002). The grey zone represents MEMS noise resolution (synthesis from Holland, 2003; Cochran et al., 2009; Lin et al., 2021).

On the value of weak-to-moderate earthquake data recorded in buildings

The seismic network installed in the Grenoble City Hall building in France has registered weak to moderate earthquakes for 18 years. As an additional activity for this deliverable, we evaluated the added value of weak-to-moderate earthquake data for structural response analysis. The building response was analysed in terms of intensity measures and engineering demand parameters, and compared to strong earthquake data recorded in one Japanese building (Figure 25). Evidence of non-linear response was observed, represented by a shift in fundamental frequency triggered at low strain-amplitudes and strain-rates values. A low strain-rate threshold in the order of $10^{-11}s^{-1}$ was observed to activate non-linearities, confirming the link between loading rates and structural state. Finally, a continuous transition of the behaviour was observed between weak-to-moderate (France) to moderate-to-strong (Japan) earthquakes data, highlighting some hidden physical processes activated in different buildings during earthquakes. We conclude then on the strong need for building testing in moderate-to-weak seismic prone regions for the development and calibration of realistic models for the prediction of the earthquake response and the vulnerability and risk assessment of existing buildings. A detailed analysis can be found in Astorga and Guéguen (2023).

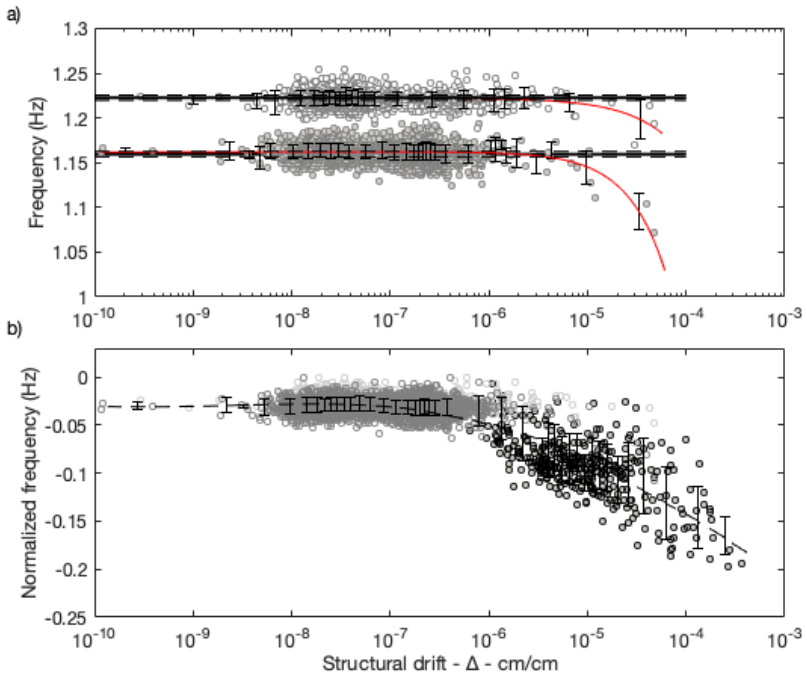

Figure 25 Variations of the normalized fundamental frequency as a function of drift values, Δ (a) for the City-Hall Building Grenoble in the two horizontal direction, and (b) comparison between CHB Grenoble (gray) and ANX building Japan (black) for weak-to-strong data.

3.4.3 Replacement cost, occupants

For the Italian building classes aggregated into tiles, the replacement costs and number of occupants were retrieved from the corresponding building classes in the ESRM20 exposure model (Crowley et al., 2020), assuming an urban setting and averaging out values across the whole Italian territory.

Something similar was done for the case of the Swiss building, except that average values from the ESRM20 exposure model were combined with national statistics as well, and the actual floor area of the building was considered (instead of assuming average floor areas).

In the case of the three monitored buildings, replacement costs and number of occupants were defined combining average values from the ESRM20 exposure model (Crowley et al., 2020) with national statistics and international statistics (European Court of Auditors, 2018; Swiss Federal Statistical Office, 2022; Ville de Grenoble, 2021), which were particularly useful in the case of the Grenoble city hall, as public/governmental buildings are not covered by ESRM20. Table 1 shows the final replacement costs and number of occupants assigned. It is highlighted that these values come from models and assumptions and are not intended as a statement on the real replacement cost or number of occupants of those buildings.

Table 1 Replacement costs and number of "census" occupants (irrespective of the time of the day) assigned to the three monitored buildings in this proof of concept. Values are based on models and assumptions and are not to be interpreted as statements.

Building	Replacement cost	"Census" occupants
Swiss building	1,300,000 EUR	10
Budva hotel	8,000,000 EUR	36
Grenoble city hall	25,000,000 EUR	450

The question of the presence of tourists in the Budva hotel or visitors/public in the Grenoble city hall at the time of the earthquake(s) is a relevant matter for the modelling of human exposure. Non-permanent occupants of buildings take particular significance in the case of commercial or public buildings but have less of an impact on residential building classes. The modelling of the displacement of people is already complex under normal conditions, and the occurrence of an earthquake adds even more complexity. While it would be possible to think of estimating a number of tourists that may occupy a hotel at a certain point in time, the longer-term "return" of tourists after a first earthquake shock becomes harder to define (e.g., would injured tourists return to the hotel or go back to their location of residence, would more tourists come to a hotel in an area that has just been affected by an earthquake, etc). Similarly, how a governmental building like the Grenoble city hall would be used (if usable) after a first earthquake of a sequence is a strategic decision of the authorities which might lead, for example, to larger numbers of people if the building hosts post-earthquake response activities. As all these complexities were beyond the scope of the present work, the number of occupants of the Budva hotel and the Grenoble city hall are intended to only represent "standard" numbers of employees of both buildings and do not include tourists or visitors.

The number of occupants at different times of the day (day, night and transit) were calculated from the number of census occupants by means of the coefficients used in the European Seismic Risk Model 2020 (ESRM20; Crowley et al., 2021a), which are a modified version of the PAGER population distribution model (Jaiswal and Wald, 2010). These coefficients are country specific and distinguish between residential and non-residential building classes. The coefficients for Italy were used herein.

3.5 State-dependent ground motion-based fragility models

3.5.1 General overview

Certain risk assessment methods, able to model damage accumulation (e.g., Iervolino et al., 2016; Yeo and Cornell, 2009), require a set of fragility curves for each structure. These curves provide the probability of the structure transitioning between any pair of damage states from intact conditions to failure, and are thus named *state-dependent* fragility functions. More specifically, state-dependent fragilities provide the probability that the structure reaches or exceeds damage state DS_j, with $j=2,\ldots,n$, given the occurrence of a ground motion with intensity measure *IM* and the damage state DS_i, with $i=1,\ldots,n-1$ and $j>i$, which has already been attained by the structure when the earthquake occurs, $P[DS_j \mid DS_i, IM=z]$. We speak of ground motion-based fragility models in this section to distinguish them from the structural health monitoring-based fragility models that are described in section 3.6, the former using a measure of ground motion as the intensity measure, while the latter are based on measures of the response of a building.

State-of-the-art analytical derivation of classical structural fragility entails subjecting the numerical model of the structure to numerous nonlinear dynamic analyses, for example, incremental dynamic analysis (IDA) (Vamvatsikos and Cornell, 2001, 2004), which consists in collecting the non-linear responses of an (initially undamaged) structure to a set of records, each one progressively scaled in amplitude to represent different levels of seismic intensity. For the evaluation of state-dependent fragility curves, an extended version of IDA has been suggested (e.g., Ryu et al., 2011; Goda 2012; Ruiz-García 2012; Raghunandan et al., 2015; Goda 2015; Baltzopoulos et al., 2018; Nazari et al., 2015), referred to here as back-to-back or B2B-IDA. According to this method, the structural model is first subjected to a set of records, representing a first seismic event hitting the structure at its intact state and causing it to reach a first damage state DS_i. Each record of the set is scaled in amplitude to the lowest value of *IM* that causes the structure to reach the damage state DS_i. Thus, at the end of each record a different realisation of the damaged structural model is produced. Subsequently, each realisation of the structural model in DS_i is subjected to another (or the same) set of accelerograms simulating an aftershock. Each record of the second set is scaled until the damaged structure reaches the more severe damage state DS_j. The state-dependent fragility can then be derived by collecting the scaled intensities of all records in the

second set, possibly fitting a parametric model based on those results, as will be discussed in more detail in the following paragraphs.

The derivation of fragility curves via IDA can be particularly demanding from a computational point of view and this has motivated the development of simplified procedures for analytical fragility development, based on static nonlinear analysis (*pushover* analysis). These methods consist in substituting the complex numerical model with an equivalent inelastic single-degree-of-freedom (SDoF) system, whose definition is based on the pushover curve of the original structure. Because the number of required dynamic analyses is increased by orders of magnitude in the case of B2B-IDA, the need of simplified procedures to derive state-dependent fragility is even more pressing (Luco et al., 2004). In this context, a pushover-based methodology was developed as part of RISE Task 4.2 by Orlacchio (2022) for the assessment of state-dependent fragility curves for multi-story moment-resisting frame structures that not only uses *equivalent* SDoF models to simplify the fragility assessment, but also seeks to further reduce the computational cost by eschewing the need for the first step dynamic analysis needed to bring the structure to the initial damage state DS_i, using instead instances of the damaged structural configuration obtained from a predictive model via Monte-Carlo simulation. This model enables the generation of a series of realizations of the pushover backbones representing the structure's ESDoF approximation when it is in the given initial damage state of interest, DS_i. Other studies have suggested that IDA-based approaches for state-dependent fragility estimation should be employed with due consideration to the criteria for the definition of discrete damage states (Baraschino et al., 2022).

3.5.2 State-dependent fragility models for Italian building classes

Within RISE Task 4.2, the ESDoF and IDA-based methodology was implemented for the development of state-dependent fragility curves for structural typologies of the European building stock. European existing structural typologies were identified in accordance with the building classification employed initially within the Horizon 2020 SERA project (Romão et al., 2019) and ultimately in the ESRM20 (Crowley et al., 2021a): this classification was based on an updated version of the GEM building taxonomy (Brzev et al., 2013; Silva et al., 2022). This taxonomy defines buildings considering four main characteristics: primary construction material (e.g., reinforced concrete, unreinforced masonry, steel, etc.); typology of the lateral load resisting system (e.g., wall, moment frame, infilled frame, etc.); height expressed in terms of number of stories; seismic capacity-related properties (e.g., ductility and/or design lateral force), which depend on the evolution of seismic design in the country (e.g., Petruzzelli and Iervolino, 2021; Crowley et al., 2021b). For each resulting typology, a backbone representative of the ESDoF system was defined in terms of displacements, δ, and ratio of the reacting force over the mass of the structure, F/m. In fact, for reinforced concrete structural typologies, a set of backbones were defined via a probabilistic approach developed to account for the building-to-building variability within each typology. Moreover, in the same project, the average backbone was also delivered: the displacement-acceleration coordinates of each point of the average curve are evaluated as the geometric mean of the corresponding points defining the capacity curves of the set. Such a geometric mean is independently obtained for the abscissas and the ordinates.

Hereafter, the considered building typologies are those associated with reinforced concrete and masonry buildings comprised in the Italian residential building stock. Each typology was analysed referring to the backbone; in the cases of reinforced concrete typologies, the average curve was considered.

3.5.2.1 Italian reinforced concrete (RC) structures

The Italian RC existing residential buildings are represented by eighteen structural typologies, each of them identified by a code that summarizes its characteristics (see Table 2). The first two letters of the code are CR and refer to reinforced concrete. Then, the code reports the lateral load

resisting system that, for all the Italian buildings, is infilled frame structures (LFINF). The level of seismic code design is identified as CDN if it is null, or CDL if it is low; the seismic design lateral force coefficient (LFC) is 0.0 in case of CDN and 5.0 or 10.0 in case of CDL. Finally, the number of stories varies between one and six and is indicated as H:1 to H:6.

For each building typology, the average capacity curve is defined by four points in terms of δ and F/m, that correspond to: the yielding threshold, $\{\delta_1, F_1/m\}$; the displacement associated with the maximum reacting force, i.e., the capping point, $\{\delta_2, F_2/m\}$; the displacement associated with slope variation in the post-elastic behaviour (e.g., the loss of all the infilled masonries contribution to lateral stiffness), $\{\delta_3, F_3/m\}$; the ultimate displacement value, $\{\delta_4, F_4/m\}$. Table 2 reports the numerical values of the points defining the backbones for all the Italian RC structural typologies.

Table 2 Backbone parameters for each Italian RC structural typology.

#	Structural typology	δ_1 (mm)	δ_2 (mm)	δ_3 (mm)	δ_4 (mm)	F_1/m (g)	F_2/m (g)	F_3/m (g)	F_4/m (g)
1	CR/LFINF+CDN+LFC:0.0/H:1	1.66	8.81	62.19	95.55	0.292	0.363	0.196	0.174
2	CR/LFINF+CDN+LFC:0.0/H:2	2.93	13.49	55.10	85.81	0.137	0.171	0.112	0.068
3	CR/LFINF+CDN+LFC:0.0/H:3	4.97	23.68	66.78	98.01	0.102	0.128	0.087	0.046
4	CR/LFINF+CDN+LFC:0.0/H:4	7.26	36.21	81.86	107.56	0.082	0.102	0.072	0.037
5	CR/LFINF+CDN+LFC:0.0/H:5	10.07	47.12	93.84	123.07	0.076	0.094	0.069	0.034
6	CR/LFINF+CDN+LFC:0.0/H:6	13.64	61.89	112.27	140.66	0.071	0.089	0.066	0.030
7	CR/LFINF+CDL+LFC:5.0/H:1	1.93	8.89	50.17	88.93	0.334	0.417	0.233	0.226
8	CR/LFINF+CDL+LFC:5.0/H:2	3.27	13.30	56.22	83.02	0.140	0.174	0.110	0.072
9	CR/LFINF+CDL+LFC:5.0/H:3	5.39	21.32	64.44	88.56	0.106	0.132	0.084	0.052
10	CR/LFINF+CDL+LFC:5.0/H:4	8.22	29.76	68.47	89.48	0.091	0.114	0.077	0.041
11	CR/LFINF+CDL+LFC:5.0/H:5	11.16	33.90	68.98	90.43	0.086	0.107	0.072	0.037
12	CR/LFINF+CDL+LFC:5.0/H:6	14.76	40.63	71.79	91.27	0.086	0.107	0.075	0.036
13	CR/LFINF+CDL+LFC:10.0/H:1	1.93	8.92	51.02	89.81	0.331	0.413	0.233	0.233
14	CR/LFINF+CDL+LFC:10.0/H:2	3.38	13.93	56.00	87.02	0.143	0.178	0.113	0.075
15	CR/LFINF+CDL+LFC:10.0/H:3	6.27	22.93	66.02	102.85	0.128	0.160	0.103	0.078
16	CR/LFINF+CDL+LFC:10.0/H:4	9.44	28.44	68.02	99.88	0.112	0.140	0.092	0.062
17	CR/LFINF+CDL+LFC:10.0/H:5	12.54	31.73	72.74	111.23	0.103	0.128	0.082	0.055
18	CR/LFINF+CDL+LFC:10.0/H:6	16.19	40.83	76.37	100.12	0.102	0.128	0.086	0.054

For each typology, five damage states were considered ranging from no damage (DS0) to near-collapse (DS4); all of them were defined on the basis of Villar-Vega et al. (2017) and Lagomarsino et al. (2006). The engineering demand parameter (EDP) adopted for the identification of the damage states is the (absolute value of the) maximum transient inelastic response in terms of displacement. DS1, i.e., slight damage, is considered reached when the maximum displacement equals or exceeds 75% of δ_2, whereas the DS4 threshold corresponds to the ultimate displacement capacity of the structure, δ_4. The thresholds of DS2 and DS3 are evenly spaced between the first and last damage state thresholds and are reached at the displacements equal to $0.5 \cdot \delta_2 + 0.33 \cdot \delta_4$ and $0.25 \cdot \delta_2 + 0.67 \cdot \delta_4$, respectively.

Figure 26a shows a generic backbone curve and the damage states thresholds whereas in Figure 26b the eighteen backbones associated with RC structures are reported. As shown, two subsets of curves can be identified in Figure 26b: they are representative of one-story and more-than-one-story (from two to six) RC buildings, respectively. More specifically, the curves with the highest values of F/m correspond to one-story structures among which one has an absent level of seismic design whereas the other two have low code level with design lateral force equal to 5% and 10% of the building weight, respectively. The one-story buildings have vibration periods of about 0.15s whereas the structures with more than one story have periods ranging from 0.29s to 0.88s.

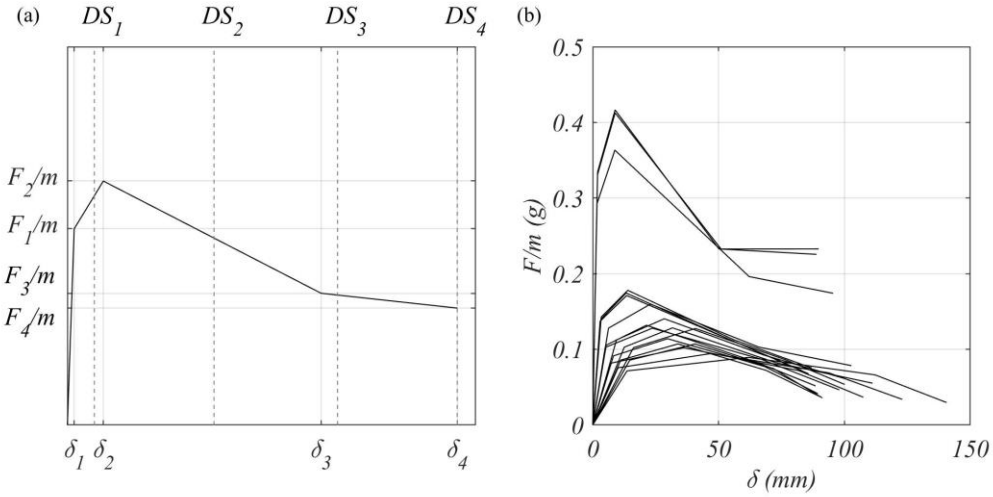

Figure 26 Backbone and damage state thresholds for a generic Italian RC typology (a), backbones of the eighteen Italian RC residential structural typologies (b).

3.5.2.2 Italian masonry structures

The Italian masonry structures portfolio is represented by a set of fifteen wall masonry structures: ten unreinforced masonry (MUR) buildings, and five confined masonry structures (MCF). The MUR structures are classified based on the masonry material in rubble stone masonry (STRUB), dressed stone masonry (STDRE) and masonry with clay bricks (CL99). The lateral load resisting system is characterized by wall (LWALL) and all the MUR structures have a null level of seismic code design (CDN) whereas MCF are characterized by low-code seismic design (CDL). The number of stories varies between one and five (from H:1 to H:5).

For each masonry building typology, the backbone is defined by three points in the terms of δ, *F/m* coordinates, those are: $\{\delta_1, F_1/m\}$, $\{\delta_2, F_2/m\}$, $\{\delta_3, F_3/m\}$. The values of the parameters defining the backbones of each structural typology are reported in Table 3.

Table 3 Backbone parameters for each Italian masonry structural typology.

#	Structural typology	δ_1 (mm)	δ_2 (mm)	δ_3 (mm)	F_1/m (g)	F_2/m (g)	F_3/m (g)
1	MUR+STRUB/LWAL+CDN/H:1	0.30	2.00	10.00	10.00	0.195	0.390
2	MUR+STRUB/LWAL+CDN/H:2	0.60	5.00	20.00	20.00	0.112	0.224
3	MUR+STRUB/LWAL+CDN/H:3	0.89	7.00	31.00	31.00	0.081	0.162
4	MUR+STRUB/LWAL+CDN/H:4	1.19	10.00	41.00	41.00	0.064	0.129
5	MUR+STRUB/LWAL+CDN/H:5	1.49	12.00	51.00	51.00	0.054	0.108
6	MUR+CL/LWAL+CDN/H:3	1.00	8.00	34.00	34.00	0.082	0.164
7	MUR+CL/LWAL+CDN/H:4	1.33	11.00	46.00	46.00	0.065	0.131
8	MUR+CL/LWAL+CDN/H:5	1.66	13.00	57.00	57.00	0.055	0.109
9	MUR+STDRE/LWAL+CDN/H:4	1.26	10.00	43.00	43.00	0.068	0.136
10	MUR+STDRE/LWAL+CDN/H:5	1.58	13.00	54.00	54.00	0.057	0.114
11	MCF/LWAL+CDL/H:1	0.000	0.004	0.017	0.017	0.470	0.940
12	MCF/LWAL+CDL/H:2	0.001	0.007	0.034	0.034	0.235	0.470
13	MCF/LWAL+CDL/H:3	0.001	0.011	0.050	0.050	0.157	0.313
14	MCF/LWAL+CDL/H:4	0.002	0.014	0.067	0.067	0.118	0.235
15	MCF/LWAL+CDL/H:5	0.002	0.018	0.084	0.084	0.094	0.188

Five damage states are defined, from DS0 through to DS4. Consistently with those already described for RC structures, DS1 is reached when the maximum displacement equals or exceeds 75% of δ_2, whereas the near-collapse threshold corresponds to the ultimate displacement capacity of the structure, that is, in this case, δ_3. The thresholds of the intermediate damage states, DS2 and DS3, are reached at the displacements equal to $0.5 \cdot \delta_2 + 0.33 \cdot \delta_3$ and $0.25 \cdot \delta_2 + 0.67 \cdot \delta_3$, respectively. The generic backbone curve associated with masonry structures is depicted in Figure 27a together with the damage state thresholds; the backbones of the fifteen Italian masonry building typologies are shown in Figure 27b. The unreinforced masonry structures classes are plotted as solid lines whereas those of the confined masonry buildings are in dashed lines. Both the unreinforced masonry buildings and the confined masonry structures have periods of vibration between 0.13s and 0.69s.

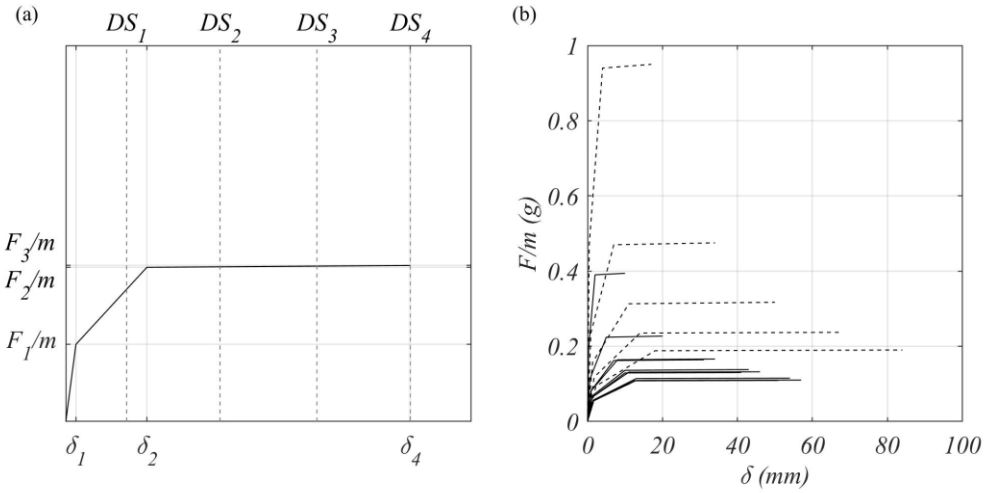

Figure 27 Backbone and damage state thresholds for a generic Italian masonry typology (a), backbones of the fifteen Italian masonry residential structural typologies (b).

3.5.2.3 Development of the state-dependent fragility models

The ESDoF systems associated with the backbones described in the previous sections were characterised by a pinched hysteretic behaviour exhibiting degradation of both strength and (unloading and reloading) stiffness under cyclic loading. An example of the cyclic response is shown in Figure 28. The hysteretic behaviour was modelled in the OpenSees software (Open System for Earthquake Engineering Simulation, McKenna et al., 2000) via the "Pinching4" material (Martins and Silva, 2021).

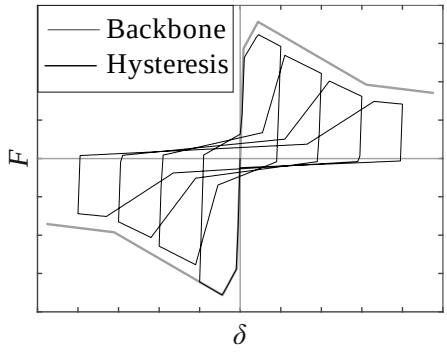

Figure 28 Example of backbone curve and cyclic response of an inelastic SDoF system with pinched hysteretic behaviour and cyclic strength and stiffness degradation.

The chosen viscous damping ratio for RC concrete structural typologies is the same adopted in the SERA project, which is 5%. On the other hand, the adopted viscous damping ratio for masonry structures is chosen in accordance with the paper of Guerrini et al. (2017) in which the nonlinear dynamic response of several ESDoF systems, representative of masonry buildings, is investigated.

In the cited paper, among other parameters, the viscous damping ratio for flexural dominated, shear dominated, and a combination of the two systems are reported. Resulting viscous damping ratios range between 3% and 5% and a ratio equal to 4.1% is computed when the flexural and the shear dominated systems are combined (assuming the two systems in parallel). The same value of 4.1% was adopted for all the masonry structural typologies.

Fragility functions (i.e., for the undamaged structure) and state-dependent fragility functions were evaluated using IDA20 and back-to-back IDA, respectively (Orlacchio et al., 2021; Orlacchio, 2022). Applying the IM-based approach to the results of IDA and back-to-back IDA, fragility functions and state-dependent fragility functions were computed. This approach consists in finding the realisations of the seismic intensity leading the structure, from DS_i, to equal or exceed a certain damage state threshold, DS_j. The considered intensity measure is the geometric mean of spectral accelerations Sa_{avg} (Baker and Cornell, 2006) evaluated, according to Equation (7), considering the twenty-three periods of the ground motion prediction equation of Bindi et al. (2011), defined in a range between 0.0s and 2.75s.

$$Sa_{avg}(T_1, T_2, \dots, T_{23}) = \sqrt[23]{Sa(0.0s) \cdot \dots \cdot Sa(2.75s)} \tag{7}$$

Figure 29 and Figure 30 show, as an example, the set of state-dependent fragility models obtained for an Italian reinforced concrete and masonry building class, respectively.

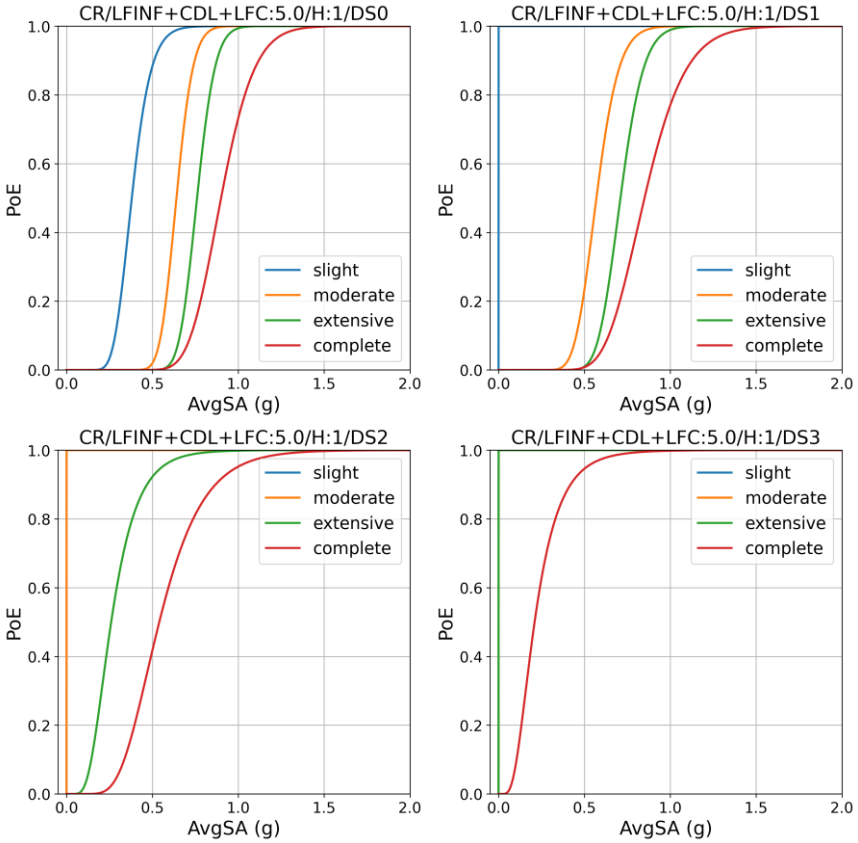

Figure 29 Set of state-dependent fragility models developed by Orlacchio (2022) for the Italian CR/LFINF+CDL+LFC:5.0/H:1 building class.

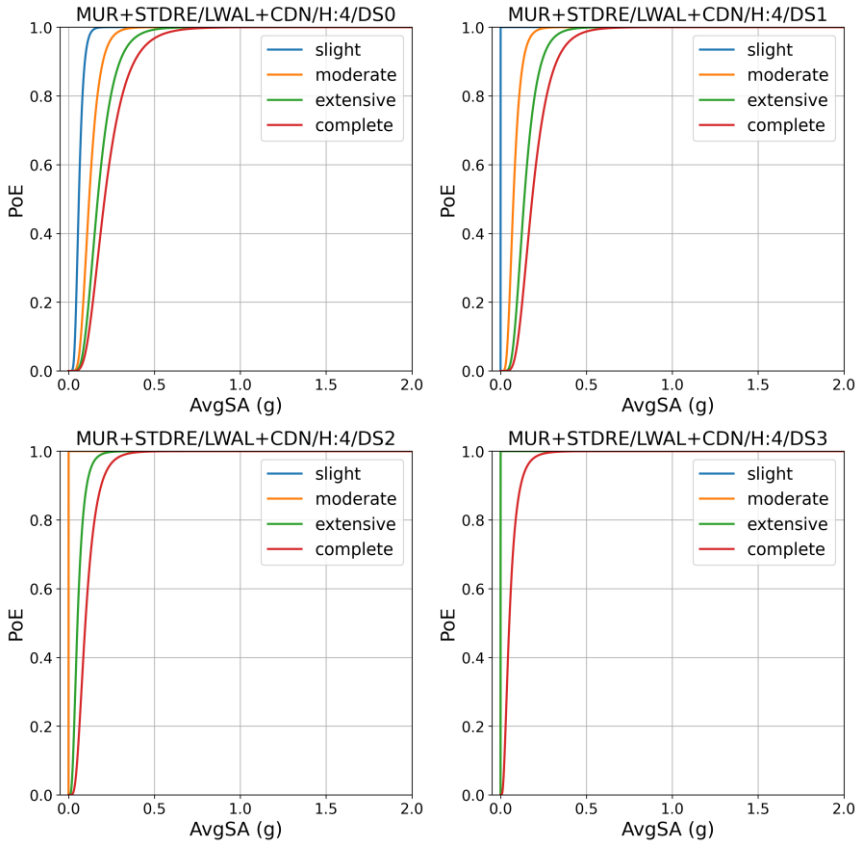

Figure 30 Set of state-dependent fragility models developed by Orlacchio (2022) for the Italian MUR+STDRE/LWAL+CDN/H:4 building class.

3.5.3 State-dependent fragility models for the three monitored buildings

The full state-dependent fragility methodology described above has not been applied to the three monitored buildings, but instead simplified methods have been investigated. With more time and resources, it would of course be possible to apply the full methodology, but it was decided that it would be useful to include also a demonstration of simpler methods herein, which could be applied to get a reasonable approximation of the influence of accumulated damage on the fragility of buildings.

In order to produce state-dependent fragility models for the Budva hotel (see section 3.4.2.2), the simplified approach referred to in Section 3.5.1 has been employed; this method is based on pushover curves of the damaged structural configuration obtained from a predictive model via Monte-Carlo simulation (Orlacchio, 2022). Instead, for the other two monitored buildings (i.e. the Grenoble City Hall, Section 3.4.2.3 , and the Swiss residential building, Section 3.4.2.1), fragility models for the undamaged buildings have first been developed, and then the ratios between the median AvgSa from the damage-dependent fragility functions for each damage state obtained for the Budva hotel were applied.

For the Budva hotel, a pushover curve was obtained with the nonlinear model (see Figure 22) and transformed to the capacity curve of the ESDoF system (in terms of spectral acceleration versus spectral displacement). For the Grenoble City Hall a capacity curve was obtained from the modelling efforts undertaken in previous projects (Desprez et al., 2011); the capacity curve along the short direction was used. For the Swiss residential building, the capacity curve shown in Figure 17 was used. Fragility functions for the undamaged buildings (i.e. "/DS0") were then produced by modelling the ESDoF systems in the OpenSees software via the "Pinching4" material with the same numerical parameters employed for the Italian masonry and reinforced concrete buildings

in Section 3.5.2.3 , making use of GEM's Vulnerability Modeller's Toolkit (see Martins et al., 2021). The same intensity measure (AvgSa) described previously has been used.

As mentioned previously, for the Budva hotel, pushover curves for the buildings given an initial damage state (from DS1 to DS3) were obtained with the methodology of Orlacchio (2022), and are shown in Figure 31. The same methodology as employed for the fragility functions for the undamaged buildings was used to produce the damage-dependent fragility functions, leading to the final set of models shown in Figure 32.

Figure 33 and Figure 34 show the final set of models for the Grenoble City Hall and the Swiss building, respectively.

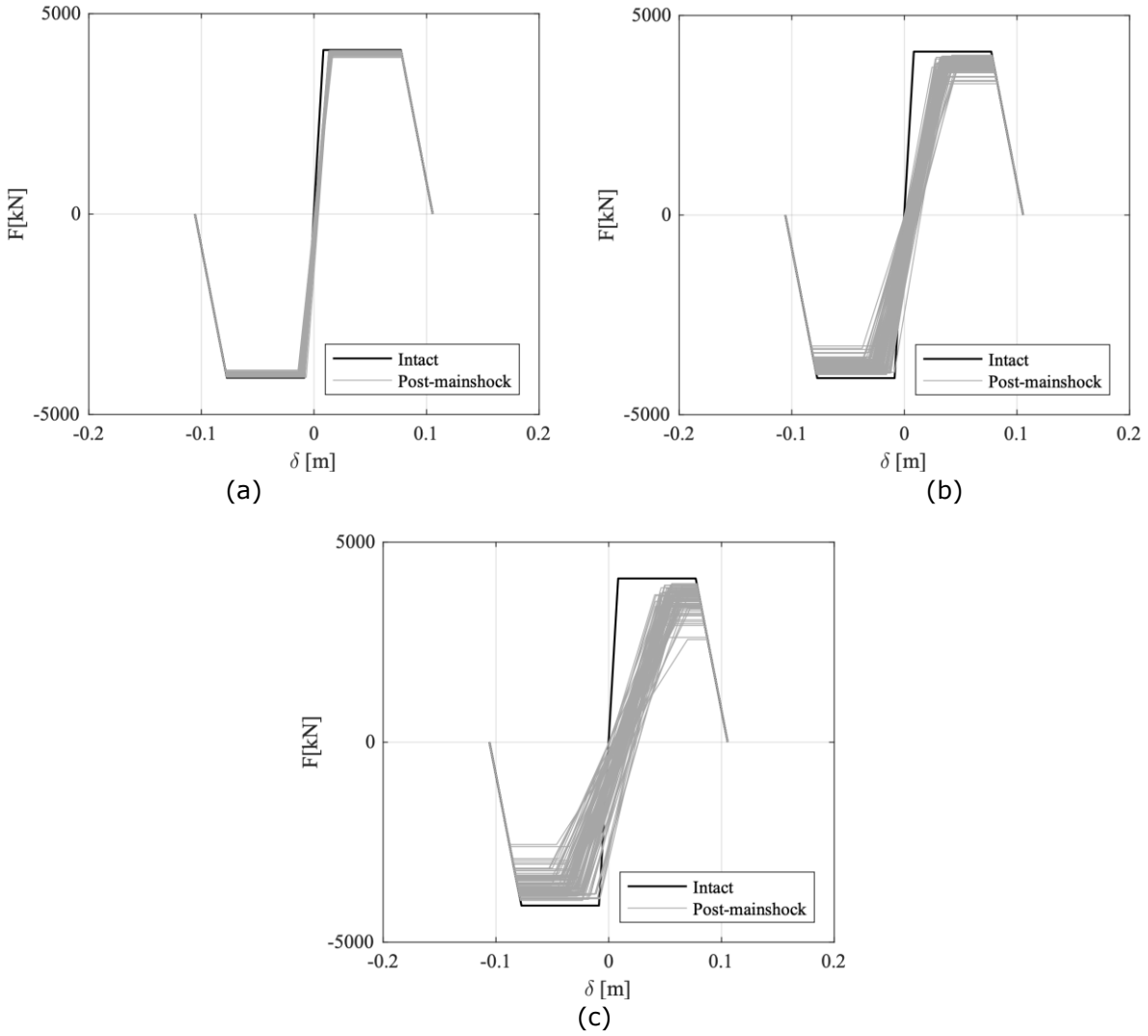

Figure 31 Pushover curves for the Budva hotel given an initial damage state (a) DS1, (b) DS2 and (c) DS3. 'Intact' refers to the undamaged building, where 'post-mainshock' refers to the building that has been previously damaged to a given damage state during a mainshock earthquake.

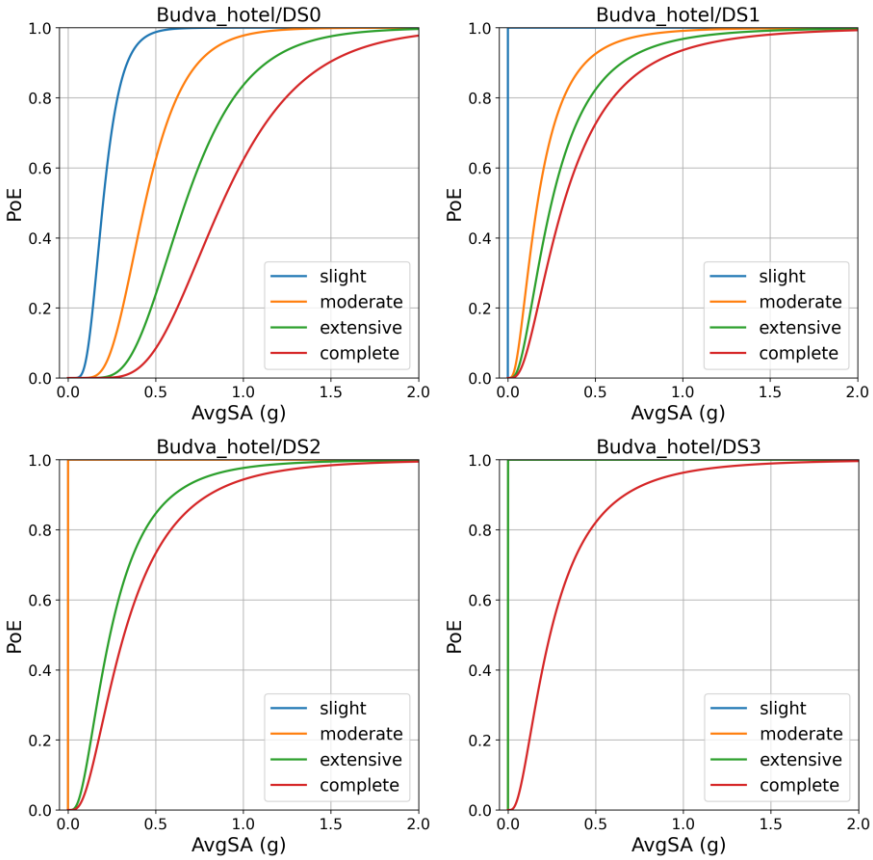

Figure 32 Set of state-dependent fragility models developed for the Budva hotel.

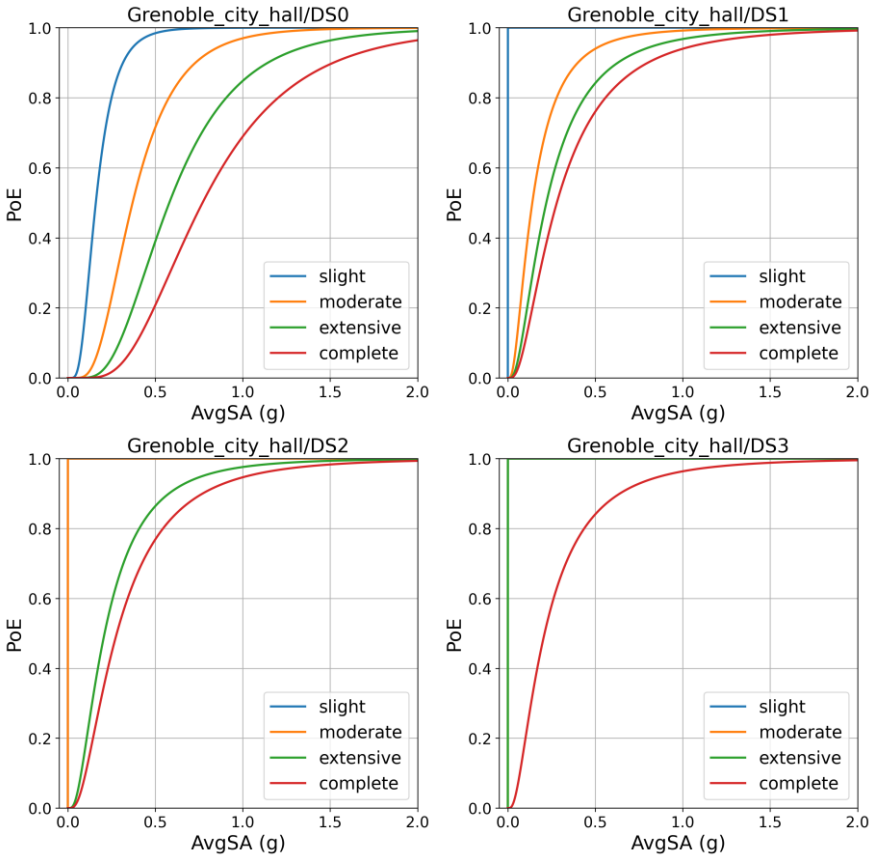

Figure 33 Set of state-dependent fragility models developed for the Grenoble City Hall.

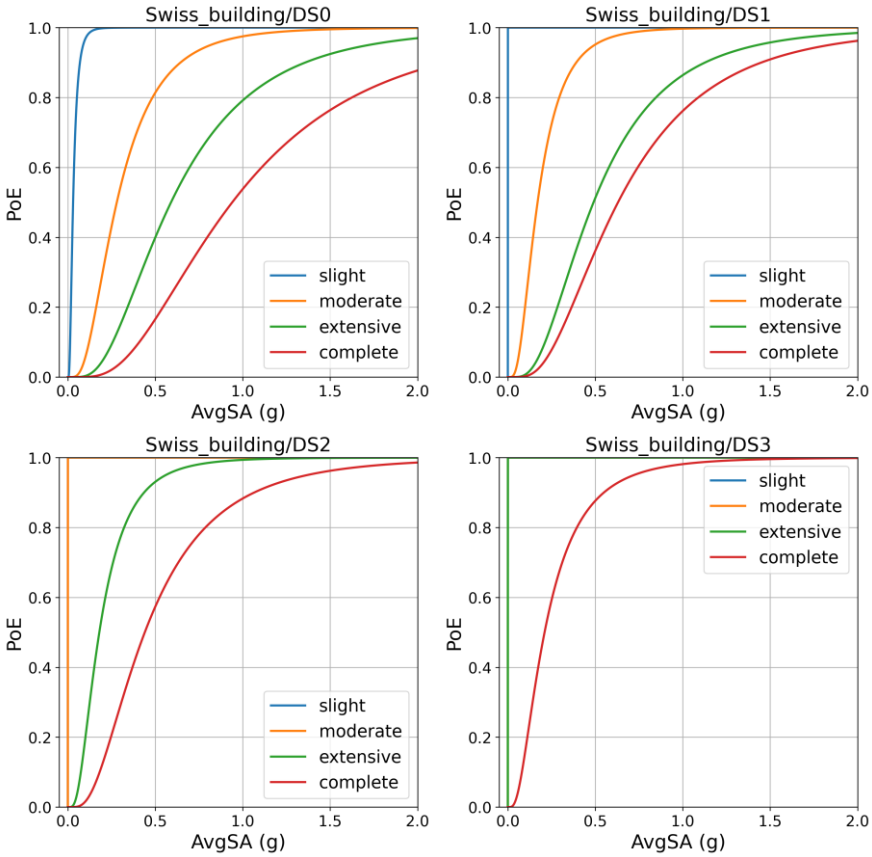

Figure 34 Set of state-dependent fragility models developed for the Swiss building.

3.6 SHM-based fragility models

3.6.1 General method

While typical ground motion-based fragility models involve intensity measures that only characterise the earthquake excitation, the increased availability of dynamic sensors (such as those investigated and developed in WP2 of the RISE project) empowers the inclusion of the measured building behaviour during earthquakes into fragility models. Engineering models for seismic response prediction and damage estimation typically involve displacements and reaction forces, both of which are challenging to measure with sufficient precision and at reasonable expense for large building stocks. Therefore, permanent seismic monitoring of buildings in earthquake-prone regions relies mostly on acceleration measurements. SHM offers the tools to extract damage-sensitive features (DSFs) from recorded time-history data.

SHM-based fragility models are derived in a similar manner to their ground motion-based counterparts: a building is modelled to predict the DSFs characterizing the nonlinear response during a set of ground-motion records (see Figure 35). These pre-defined fragility models are then compared with the DSF extracted from the real building during a strong ground motion to derive the probability to fall within a given damage state. Monitoring data is also available from the real building during normal operations and can be used to define a healthy range of DSFs (see Figure 35). Regardless of the fragility model, DSFs that fall within this reference state can be considered healthy as the behaviour does not deviate from healthy reference data.

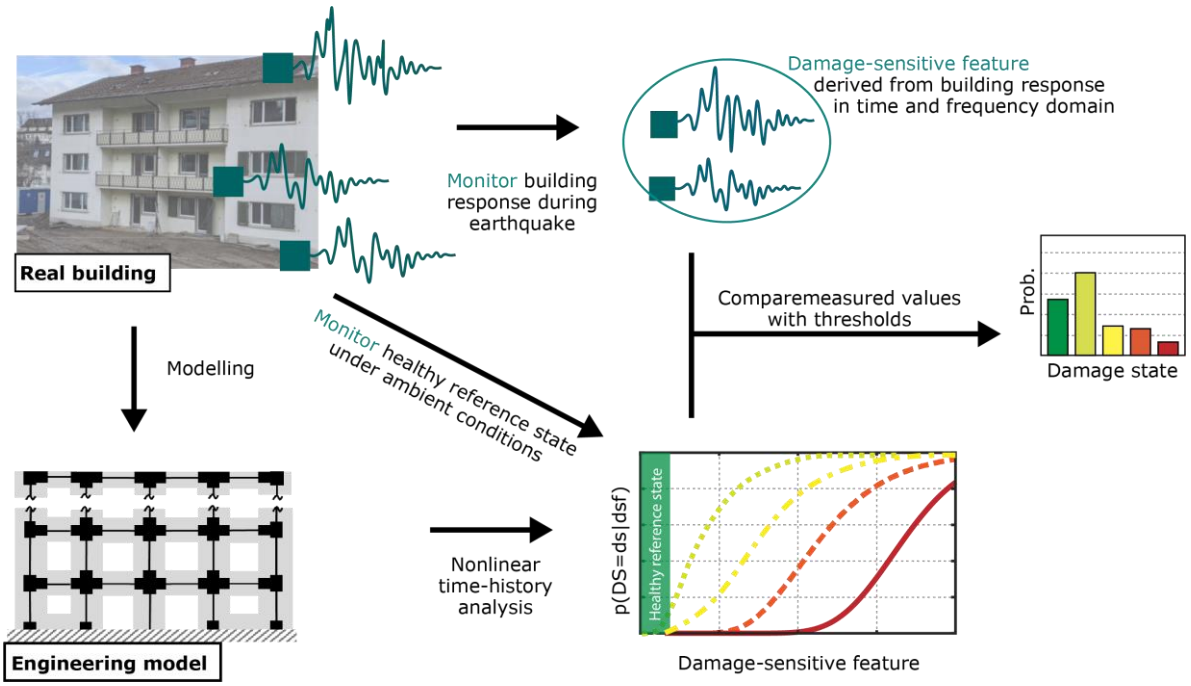

Figure 35 Use of dynamic SHM data for rapid post-earthquake damage assessment using pre-computed fragility models that are based on DSFs.

Multiple DSFs can be extracted from the dynamic structural response and subsequently used to characterize the building state (Reuland et al., 2023), most notably the natural frequency of a building may indicate onset of damage and therefore serve in rapid post-earthquake assessment (Goulet et al., 2015; Trevlopoulos & Guéguen, 2016). For this proof of concept, three DSFs, formulated for a pair of sensing nodes (one at the top of the building and one at the base of the building) are considered:

- Based on transmissibility as a quantity that is correlated to damage, T_{cnt} is a DSF that tracks relative changes of the centroid of the transmissibility with respect to a healthy reference state. The transmissibility between the input sensor (at the ground) and the output sensor (at the top of the building) is sensitive to damage, due to the fact that a reduction in stiffness (due to damage) in turn provokes a reduction in the frequency of fundamental modes of the substructure defined by the input-output sensor pair.

- A second DSF exploits the time-frequency representation offered by the wavelet transform and enables tracking correlation in the time domain for separate frequency bands. A decrease in the correlation of the wavelet coefficients below the frequency bandwidth of a particular structural mode may indicate nonlinearity. Indeed, when the structure behaves linearly, an almost perfect correlation is observed outside the frequency values that correspond to the local structural modes (Goggins et al., 2007). When the frequency values of structural modes decrease due to damage, then the correlation in the bandwidth below the initial frequency in turn decreases and this behavior is encoded as a DSF termed WLC (wavelet-based linear correlation).

- Finally, a direct stiffness proxy, K_{prx}, approximates the reaction force, which is defined as the acceleration at the output sensor (at the top of the building) and the displacement obtained as the relative displacement at the output sensor with respect to the input sensor. Displacements are approximated using numerical integration. Thus, changes in the stiffness proxy, K_{prx}, deliver a direct damage indicator and, when comparing against the values from healthy reference data, this DSF provides a direct measure of stiffness loss. In order to mitigate known limitations and uncertainties induced by numerical integration schemes, prior wavelet-based filtering is performed to reduce noise effects and increase precision.

For more detailed information about DSFs, readers are referred to the RISE Deliverable 4.5 (Reuland et al., 2022b) and the related publication (Reuland et al., 2023).

3.6.2 Specific details for the three buildings of the present application

In Figure 36, an example of an SHM-based fragility model is provided for the typical Swiss masonry building. Based on the simulated dynamic time-history of the model (see Section 3.4.2.1), the relationship between the DSF and an informative EDP (in this case maximum transient top displacement) can be derived (Figure 36a). The DSF represented in Figure 36 corresponds to the WLC, a metric of correlation in the time domain of a limited frequency bandwidth between a pair of sensors. Then, fragility functions can be derived in a similar manner to ground motion-based fragility functions (Martins and Silva, 2021), as shown in Figure 36b.

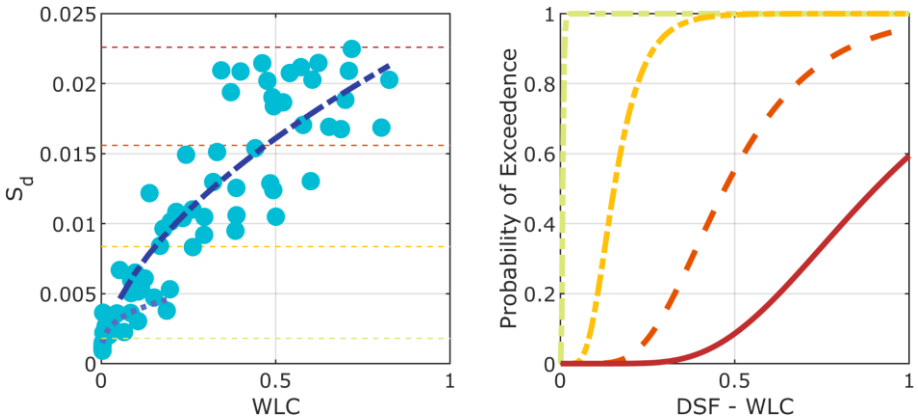

Figure 36 Example of the derivation of a SHM-based fragility function. From the fitted DSF-EDP relation (left) cumulative probability density functions for increasing damage-states are derived (right).

Leveraging upon permanently installed accelerometers, the real building response to a damaging earthquake can be measured. However, given the absence of data from real buildings, numerical simulations with engineering models are used to produce building responses to two seismic sequences. As an example, two DSFs resulting from the response of the simulated Swiss masonry building to the 2016-2017 Central Italy sequence are shown in Figure 37. The two DSFs correspond to the WLC and the K_{prx}. When comparing the DSF of each earthquake (black line) with the maximum transient displacement (indicated together with the damage state of the building in Figure 18), a good correlation is observed.

In absence of repair works, the damage-state of a structure cannot improve over time. Therefore, it is suggested to consider the highest DSF previously observed to derive DS probabilities. This approach is indicated with a grey line in Figure 37. DSFs can be formulated to track the absolute damage – accumulated from the pristine damage state until the current state – or the relative increment in damage between two earthquakes in a sequence (see RISE Deliverable 4.5; Reuland et al., 2022b). However, given the model simulations correspond to undamaged buildings, this goes beyond the scope of this report.

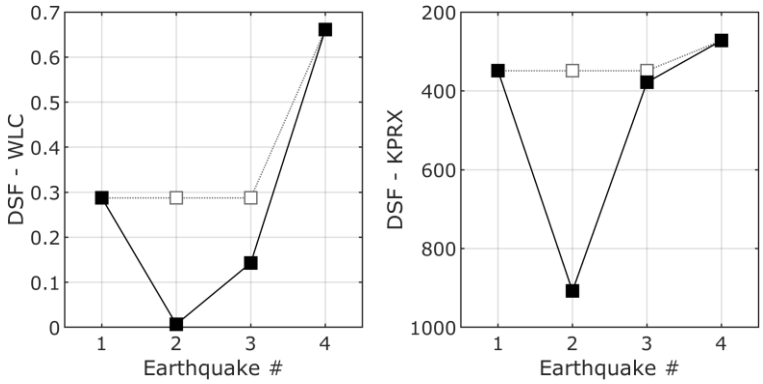

Figure 37 Derivation of two DSFs from the dynamic data measured by two sensors (one at the base and one at the top of the building) during the first four earthquakes of the 2016-2017 Central Italy sequence.

As an example, the DS probabilities predicted using the fragility curves formulated with respect to all three DSFSs are shown for the Swiss masonry building at location 13 (Figure 1) after the second earthquake of the 2016-2017 Central Italy sequence are shown in Figure 38. The probabilities stemming from the three single DSFs do not yield the same results, underlining the need for a robust combination of multiple DSFs. In this case, the combination is done by averaging the predictions from the three DSFs. However, more advanced techniques based on machine learning may be used for combining multiple DSFs (Martakis et al., 2023). The derivation of multiple DSFs from one sensor pair augments the amount of information, without adding additional need for sensors. Therefore, in this study, the three DSFs, T_{cnt}, K_{prx} and WLC, are systematically combined. Figure 39 shows the predicted damage-state probabilities for the 2016-2017 Central Italy sequence (also at location 13) after combination of all three DSFs. While the first earthquake produces severe damage, which is predicted, even if much scatter exists between DS2-4, collapse (which is attained during the fourth earthquake) is correctly picked up.

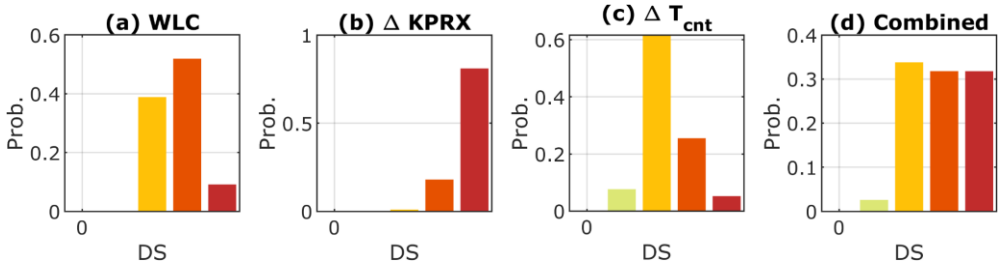

Figure 38 Predicted probabilities of DS for the typical Swiss masonry building at location 13 during the second earthquake of the 2016-2017 Central Italy sequence. The probabilities are assigned based on individual DSFs: WLC (a), K_{prx} (b), and T_{cnt} (c). Then, the three predictions are combined, by averaging the predicted probabilities

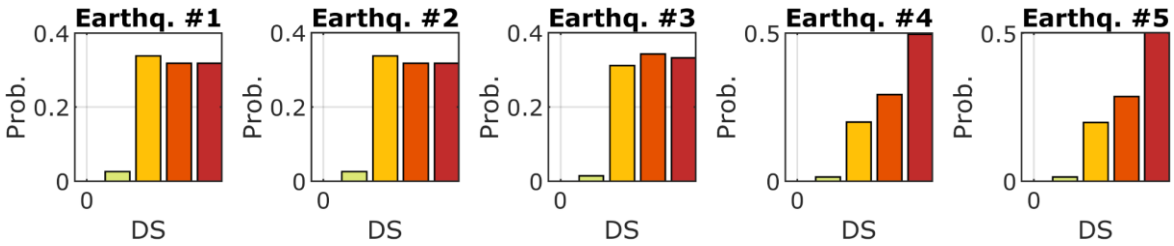

Figure 39 Predicted probabilities of DS for the typical Swiss masonry building at location 13 during the first five earthquakes of the 2016-2017 Central Italy sequence. The probabilities are assigned based on averaging the three DSFs that are extracted from a pair of sensors – one at the base and one at the top of the building

3.7 Estimation of damage probabilities using SHM

3.7.1 General overview

In a full-scale implementation, instrumented buildings would be monitored by means of an operational structural health monitoring system that would calculate damage sensitive features, either continuously or when triggered (e.g., by the detection of an earthquake), and use them to retrieve probabilities of damage from the previously defined SHM-based fragility models (see section 3.6).

A relevant challenge in such an implementation is the effect that weather conditions, amplitude of shaking and occupancy can have on DSFs. This effect can either mask actual damage or, on the contrary, lead to false alarms. Statistical tools or approaches based on machine learning can be deployed to address this issue, with several potential objectives.

A first objective consists in quantifying the undesirable effects on the DSFs in a learning phase. Subsequently, the learned relation between DSFs and environmental and operational conditions

can be included into the condition-based decision algorithm, in the case of damage-triggered alarms (e.g. Guéguen and Tiganescu, 2018), or to the continuous monitoring of buildings (Bogoevska et al., 2017). Some applications of an operational system exist already for two buildings monitored by the French RAP-RESIF network (the City Hall building in Grenoble and Tour Ophite in Lourdes), which will be updated to incorporate results obtained as part of the RISE project.

A second objective consists in detecting damage and identifying fragility and safety immediately after extreme events, which requires calibrating the variations of DSFs for each damage level and finding the best combination of DSFs for a certain estimate. Physics-based simulation models and robust treatment of uncertainties may be used for this task (Reuland et al., 2019a).

Finally, a third objective, based on the strategy of transfer learning for domain adaptation (i.e., using the knowledge obtained from one machine learning application to another one in which the data domain changes), would consist in transferring the relationship between DSFs and damage including the above-mentioned undefinable effects learned on a building to all the buildings of the class for a full-scale implementation. This objective needs the model adaptation to each building of the class according to specific constructive features and may also start from simulations (Martakis et al., 2023). This also may contribute to the building testing based fragility assessment for post-earthquake inspections by assessing abnormal response from a single post-event measurement.

3.7.2 Simulation of SHM by means of non-linear time-history analyses

For this proof of concept, we have simulated the recording of earthquake shaking by the three instrumented buildings by means of non-linear time-history analyses (NLTHA) using real accelerograms retrieved from the Italian Accelerometric Archive (ITACA) website (Russo et al., 2022). Having decided to focus the rapid loss assessment calculations on earthquakes with moment magnitude of 5.0 and above, the 2009 L'Aquila sequence was composed of eight earthquakes and the 2016-2017 Central Italy sequence was composed of nine earthquakes.

For the three sites selected for the 2009 L'Aquila sequence show in Figure 1, the following records have been used:

- Sequence 01: all eight earthquakes from station AQK, located in the town of L'Aquila.
- Sequence 02: seven out of eight earthquakes from station AQV, but the second earthquake was retrieved from nearby station AQM (it was not available from AQV).
- Sequence 03: seven out of eight earthquakes from station AQG, but the third earthquake was retrieved from nearby station AQV (it was not available from AQG).

For the four sites selected for the 2016-2017 Central Italy sequence show in Figure 1, the following records have been used:

- Sequence 11: all nine earthquakes from station NRC, located in the town of Norcia.
- Sequence 12: all nine earthquakes from station AMT, located in the town of Amatrice.
- Sequence 13: the first two earthquakes were recorded by station FEMA, located in the free field, while the other seven earthquakes were retrieved from CNE, located in the town of Castelsantangelo sul Nera (the first two earthquakes were not available from CNE).
- Sequence 14: all nine earthquakes from station MSCT, located in the town of Mascioni.

For the case of the Budva hotel, the east-west component of the accelerograms was applied along the X axis shown in Figure 40, while the north-east component was applied along the Y axis. The NLTHAs were run using the PERFORM 3D software, and results obtained along the X axis, which is the weaker direction of the building, were used, in agreement with what was done for the derivation of the ground motion-based fragility models (see sections 0 and 3.5.3)

The Grenoble City Hall was represented by an ESDoF system characterised by its capacity curve along the short direction (Desprez et al., 2011), labelled Y in Figure 40, not only for the running of NLTHAs to simulate the effect of the earthquake sequences but also for the derivation of the ground motion-based and SHM-based fragility models.

The Swiss building was modelled in OpenSees as described in section 3.4.1, and NLTHAs were conducted bi-directionally, as shown in Figure 40. The building was oriented with the longer direction in the East-West direction. The damage states have been attributed only based on the maximum transient displacement at the roof level, although significant damage to the spandrels has been observed prior to reaching DS1. This full-order model was also used to simulate pre-earthquake white-noise excitation, which is required to derive DSFs as relative changes between the healthy reference state and the damaged state (Reuland et al., 2023).

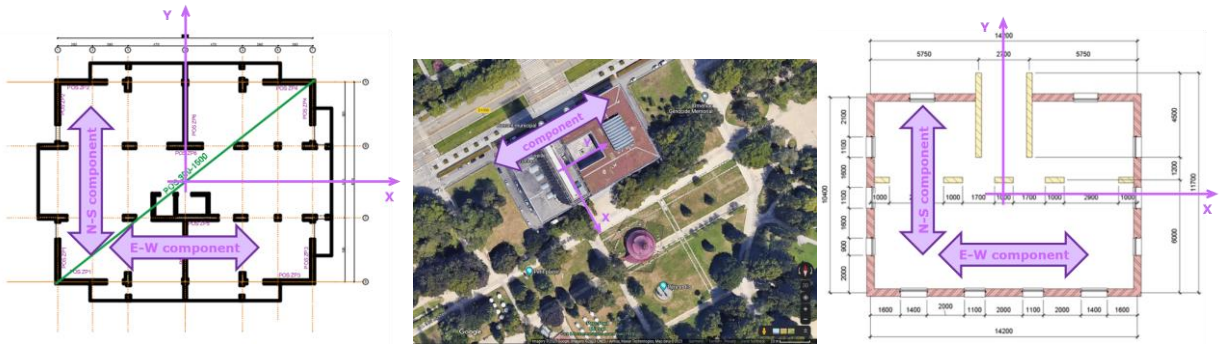

Figure 40 Axes and orientations for the NLTHAs for the three monitored buildings: the Budva hotel (left), the Grenoble City Hall (centre), and the Swiss building (right).

While the variation of ground motions at different orientations is of relevance for determining the seismic demand on a building (e.g., Hong and Goda, 2007; Shahi and Baker, 2014; Nievas and Sullivan, 2018), considering the effects of directionality was beyond the scope of this proof of concept, particularly because in a real SHM application the orientation of the recordings would be as per the relative orientation of the sensors with respect of the building, which will be known. It cannot be overemphasised that this step of running NLTHAs is needed in this proof of concept to simulate earthquake action that was not really experienced by these buildings.

3.8 Economic and human consequence models

Damage-loss or consequence models, which provide damage ratios for each damage state in the fragility functions (DS1, DS2, DS3 and DS4), have been used to assess the economic losses. The following damage ratios (which represent the ratio of cost of repair to cost of replacement) have been adopted: 0.05 (DS1: slight damage), 0.15 (DS2: moderate damage), 0.6 (DS3: extensive damage), 1.0 (DS4: complete damage). These values have been used in ESRM20 and are based on a review of recent European damage-loss models (Cosenza et al., 2018; Di Ludovico et al., 2021; De Martino et al., 2017; Erdik, 2021; Akkar, 2021; Tyagunov et al., 2006).

For the human casualties, the injury classification scale reported in HAZUS (FEMA, 2003) has been employed, as summarised below:

- Injury severity level 4: instantaneously killed or mortally injured.
- Injury severity level 3: injuries that pose an immediate life threatening condition.
- Injury severity level 2: injuries that require use of medical technology (e.g. x-rays, surgery), but are not expected to be life threatening.
- Injury severity level 1: injuries that require basic medical aid (in the field).

The indoor casualty rates for reinforced concrete frames and unreinforced masonry buildings provided in HAZUS, with the modifications employed for the Portuguese case study in the LESSLOSS project (Spence, 2007), have been adopted herein and combined with the model for fatalities in ESRM20, as summarised in Table 4 and Table 5 below. The collapse rates required to assess the probability of collapse given DS4 are given for each typology in the ESRM20 fatality model (Crowley et al., 2021a). For injury severity 4 (i.e. fatalities) given collapse, the ESRM20 uses a number of factors obtained from both past observations and expert judgement, including: the likelihood that a completely damaged building will collapse to the extent that it could cause loss of life (currently taken as an average of 1.0% based on the data from recent earthquakes: Antonios Pomonis, personal communication), a collapse factor (which is based on expert judgement and varies from 0.5 to 5 as a function of the building class), the probability of entrapment given collapse (Reinoso et al. 2017), and the probability of loss of life given entrapment (Reinoso et al. 2017).

Table 4 Indoor casualty rates (i.e. percentage of occupants) that would be expected to reach each severity level given the damage state for reinforced concrete frame buildings.

Injury Severity	DS1	DS2	DS3	DS4 (no collapse)	DS4 (collapse)
Injury severity 1	0.05	0.2	1	5	50
Injury severity 2	0.005	0.02	0.1	1	10
Injury severity 3	0	0	0.001	0.01	2
Injury severity 4	0	0	0.001	0.01	ESRM20 model

Table 5 Indoor casualty rates (i.e. percentage of occupants) that would be expected to reach each severity level given the damage state for unreinforced masonry buildings.

Injury Severity	DS1	DS2	DS3	DS4 (no collapse)	DS4 (collapse)
Injury severity 1	0.05	0.4	2	10	50
Injury severity 2	0.005	0.04	0.2	2	10
Injury severity 3	0	0.001	0.002	0.02	2
Injury severity 4	0	0.001	0.002	0.02	ESRM20 model

3.9 Timelines for damage inspection, repair and hospitalisations

3.9.1 General concept

The updating of the number of occupants in a building during an ongoing seismic sequence requires knowledge on the constraints and conditions that will exist after each earthquake for people to be able to return to the buildings they normally occupy. This matter is one aspect within the broader scope of post-earthquake recovery, for which a model and associated plug-in for OpenQuake (OQ-RRE) was developed as part of RISE Task 4.3 (Deliverable 4.4; Reuland et al., 2022a), following the iRe-CoDeS framework (Interdependent Resilience Compositional Demand/Supply quantification; Blagojevic et al., 2021; Didier et al., 2018). As Reuland et al. (2022a) describe, the timeline of the recovery process is influenced by a large number of factors, many of which can vary significantly for different countries and regions, and for which only very limited quantifiable

data exists. For this reason, the modelling of the return of occupants to buildings has been developed in the Real-Time Loss Tools in a simplified manner, taking into account a selected number of variables involved. It is our hope that future developments of the Real-Time Loss Tools and the OpenQuake Recovery and Rebuilding Effort (OQ-RRE) software lead to a full integration of all these aspects of earthquake resilience.

In the Real-Time Loss Tools we consider the ability of a person to return to the buildings they usually occupy to be a function of two aspects that can be separated from one another: the health status of the person, and the need for inspection and repair of potentially damaged buildings. The first one is associated with the level of injury sustained by a person (the most extreme being death) and the amount of time it would take for a person with that level of injury to be discharged from hospital, if they need medical care other than that which can be provided on site by paramedical professionals. The second one is associated with the time it takes for buildings to be inspected and repaired (if necessary) after an earthquake has occurred, and depends not only on the damage state of the building but also on local policies and decisions made by the authorities in the aftermath of a damaging event (Reuland et al., 2022a). For example, the inspection of buildings might be carried out upon request by the building owner, or it might be indicated for a large region, irrespective of what the perceived damage states of the buildings are.

3.9.2 Specific details for the present application

While the number of days that a person spends in hospital or that it takes for a building to be inspected/repaired is clearly variable (Reuland et al., 2022a) the Real-Time Loss Tools use only expected values.

For the definition of number of days a person with different levels of injury (see definition in section 3.8) is expected to spend in hospital, the following assumptions were made:

- Injury severity level 4: these are instant deaths or mortal injuries, and thus no possibility of return can be considered (simulated by using a very large number of days in the code).
- Injury severity level 3: average 8 days spent in hospital, which results from rounding up the Italian average of 7.5 days for hospital stays that require acute care, according to statistics from the Organisation for Economic Cooperation and Development (OECD, 2023). Average values for a large number of European countries range from 5 till 7.
- Injury severity level 2: average 3 days spent in hospital, which results from rounding down the Italian average of 3.3 days for hospital stays due to childbirth (OECD, 2023), which we take as a proxy for mild injuries in lieu of more specific statistics.
- Injury severity level 1: zero days spent in hospital.

The number of days that it takes to inspect and repair buildings suffering from different damage states adopted for this proof of concept is shown in Table 6. Several factors were considered for their definition, including not only existing literature on the matter and the work of Reuland et al. (2022a) as part of RISE Task 4.3, but also the implications for the two earthquake sequences considered in the present work. It is known that after the main shock of the 2009 L'Aquila sequence most people did not return to buildings either because the damage was too widespread or because of fear. This means that the numbers selected needed to be such that this reality were represented, and it is the case given the small intervals between successive earthquakes (see section 5.1).

For the case of the 2016-2017 Central Italy sequence, Dolce and Di Bucci (2018) express that the third and fourth earthquakes ($M_w \geq 5$) in the sequence did not produce further casualties because "*most of the local population had been yet arranged in safe, temporary lodging*" and that the fifth earthquake (the strongest event in the sequence) produced no casualties either, largely aided by the time of the day at which it occurred, around 20 minutes before the time surveys and activities carried out by first responders (associated with the previous earthquakes) were planned to start.

However, given the larger gaps in time in between earthquakes (August 2016, October 2016, January 2017), the smaller numbers of 7 days to inspect and 0 and 15 days to repair buildings in damage states 0 and 1 were selected (Table 6), so that at least a small proportion of the occupants had the chance to be reinstated in the buildings so as to show how the updating of occupants works in the Real-Time Loss Tools. As will be seen in chapter 5, this decision leads to small numbers of additional casualties only.

Table 6 Expected numbers of days needed for inspection and repair of buildings suffering from different damage states used for this proof of concept.

Damage State	Inspection	Repair	Total
DS0	7	0	7
DS1	7	15	22
DS2	45	365	410
DS3	45	1,095	1,140
DS4	45	1,095	1,140

As the Real-Time Loss Tools add up the number of days needed for inspection and repair, the use of 45 days for inspection of damage states 2 through 4 is inconsequential, because it gets added to 365 (one year) and 1,095 (3 years), and neither of the two sequences considered herein are that long (and, once more, longer periods into the future bring additional uncertainty from other factors of the recovery process not accounted for herein). These large numbers (1 and 3 years) are aligned with the timelines described by Dolce and Di Bucci (2018), who speak of 24 hours to 6-12 months needed for post-earthquake damage and safety assessments and "years" to repair, as well as the satellite and street-level imagery that can be observed on Google Maps and Google Street View for the affected area (e.g., Amatrice) many years after the events.

4. Software Input

This chapter focuses on the input files needed to run the Real-Time Loss Tools for this proof of concept, following the order in which the individual components and their conceptual background have been discussed in chapter 3. The actual files used are available on GitLab[13].

Figure 41 shows the file structure needed to run the Real-Time Loss Tools and indicates the subsections of this chapter that deal with each sort of input. As the Real-Time Loss Tools run OpenQuake to calculate ground motion fields and damage, some of the input files are the same as would be needed to run standard OpenQuake calculations, while many others are specific to the Real-Time Loss Tools.

[13] https://git.gfz-potsdam.de/real-time-loss-tools/rise-d6-1-data-files

Section	main_path
Section 4.9	**|__ config.yml**
Section 4.9	**|__ triggering.csv**
Section 4.1	**|__ catalogues**
	| |__ cat_01.csv
	| |__ …
	|__ current
Section 4.9	**|** |__ job.ini
Section 4.4	**|** |__ exposure_model.xml
Section 4.4	**|__ exposure_models**
	| |__ oelf
	|	|__ *(empty)*
	| |__ rla
	|	|__ *(empty)*
	| |__ exposure_model_undamaged.csv
Section 4.2	**|__ ruptures**
	| |__ oelf
	|	|__ *(empty)*
	| |__ rla
	|	|__ source_parameters.csv
	| |__ source_model.xml
Section 4.6	**|__ shm**
	| |__ damage_results_shm.csv
	|__ static
Section 4.7	**|** |__ consequences_economic.csv
Section 4.7	**|** |__ consequences_injuries_severity_Y.csv
Section 4.5	**|** |__ exposure_vulnerability_mapping.csv
Section 4.5	**|** |__ fragility_model.xml
Section 4.3	**|** |__ gmpe_logic_tree.xml
Section 4.8	**|** |__ recovery_damage.csv
Section 4.8	**|** |__ recovery_injuries.csv
Section 4.3	**|** |__ site_model.csv
	|__ openquake_output
	| |__ *(empty)*
	|__ output
	|__ *(empty)*

Figure 41 File structure within *main_path* needed to run the Real-Time Loss Tools. The list on the left indicates the sections of this chapter where each input file is explained.

4.1 Seismicity forecast and actual seismicity

The Real-Time Loss Tools require that each running trigger be associated with a catalogue file with certain parameters associated to the earthquakes to be processed.

In the case of RLA and for this proof of concept, for which the finite-fault rupture planes have been retrieved from the Italian Accelerometric Archive (ITACA) website (Russo et al., 2022), the catalogue CSV files contain the following fields:

- **longitude**: longitude of the hypocentre;
- **latitude**: latitude of the hypocentre;

- **magnitude**: moment magnitude;
- **datetime**: date and time of occurrence, in UTC and in standard ISO 8601 format (i.e., YYYY**-**MM**-**DD**T**HH**:**MM**:**SS);
- **depth**: hypocentral depth, in km;
- **catalog_id**: an identifier (for internal purposes, if desired);
- **event_id**: identifier of the event, to be used to retrieve finite-fault rupture parameters (see section 4.2).

In our proof of concept we use the ITACA event ID. Table 7 below shows an example of a catalogue file for RLA purposes.

Table 7 Example of the input catalogue CSV file for the first large earthquake in the 2016-2017 Central Italy sequence.

longitude	latitude	magnitude	datetime	depth	catalog_id	event_id
13.2335	42.6983	6.0	2016-08-24T01:36:32	8.1	CIT	EMSC-20160824_0000006

In the case of OELF, the Real-Time Loss Tools require that the catalogue CSV files contain the following fields (e.g., Table 8):

- **longitude** (can be named "**Lon**" as well): longitude of the hypocentre;
- **latitude** (can be named "**Lat**" as well): latitude of the hypocentre;
- **magnitude** (can be named "**Mag**" as well): moment magnitude;
- **datetime** (can be named "**Time**" as well): date and time of occurrence, in UTC and in standard ISO 8601 format (i.e., YYYY**-**MM**-**DD**T**HH**:**MM**:**SS);
- **catalog_id** (can be named "**Idx.cat**" as well): ID of the realisation of seismicity (stochastic event set) that this earthquake belongs to.

Optional fields are:

- **depth**: hypocentral depth, in km;
- **event_id**: unique identifier of the earthquake within a stochastic event set.

Table 8 Example of an OELF input catalogue CSV file.

longitude	latitude	datetime	magnitude	catalog_id
13.194844	42.927584	2016-08-24T12:19:01	4.41	30
13.209671	42.953998	2016-08-24T03:56:41	4.17	72
13.224407	42.672478	2016-08-24T08:12:32	4.41	140
13.106070	42.771073	2016-08-24T08:59:22	4.38	158
13.168614	42.621428	2016-08-24T04:49:58	5.03	213
13.125766	42.653852	2016-08-24T07:27:05	4.02	213
13.091322	42.628619	2016-08-24T09:58:24	4.31	213
13.095957	42.633398	2016-08-24T15:53:24	4.52	213
13.048759	42.607241	2016-08-24T21:18:36	4.09	213
13.190763	42.943432	2016-08-24T05:57:05	4.15	218
13.123646	42.710244	2016-08-24T03:50:10	4.07	219
13.131355	42.873699	2016-08-24T05:41:11	4.04	301
13.089598	42.837544	2016-08-24T02:56:43	4.68	336
13.029475	42.837803	2016-08-24T07:02:15	4.23	336
13.038191	42.840566	2016-08-24T08:07:24	4.01	336
13.187590	42.552217	2016-08-24T22:00:27	4.65	360
13.196402	42.791988	2016-08-24T15:09:48	4.96	385
13.174792	42.850683	2016-08-24T00:19:20	4.04	404

RLA catalogues must contain only one earthquake (= one row) per CSV file, as the Real-Time Loss Tools will ignore any additional rows. OELF catalogues can contain any number of earthquakes/rows. The way the catalogue files are read is controlled by the *type_analysis* column of the *triggering.csv* file (see section 4.9). How many stochastic event sets of an OELF input catalogue CSV file are run is controlled in the configuration file (*config.yml*, see section 4.9).

All catalogue files are located under *main_path/catalogues* and listed in *main_path/triggering.csv*.

4.2 Earthquake ruptures

The Real-Time Loss Tools search for finite-fault rupture parameters associated with the earthquakes for which a RLA is run in a file called *source_parameters.csv* located under *main_path/ruptures/rla*. The search is carried out based on the **event_id** indicated in the catalogue CSV file (see section 4.1). Following the nomenclature used by the Italian Accelerometric Archive (ITACA; Russo et al., 2022), *source_parameters.csv* contains the following fields (for all RLA earthquakes named in *triggering.csv*):

- **event_id**: identifier of the event, as in the corresponding catalogue CSV file.
- **Mw**: moment magnitude;
- **nucleation_lon**, **nucleation_lat**, **nucleation_depth**: longitude, latitude and depth (in km) of the hypocentre;
- **LL_lon**, **LL_lat**: longitude and latitude of the lower-left corner of the rupture plane;
- **UR_lon**, **UR_lat**: longitude and latitude of the upper-right corner of the rupture plane;
- **LR_lon**, **LR_lat**: longitude and latitude of the lower-right corner of the rupture plane;
- **UL_lon**, **UL_lat**: longitude and latitude of the upper-left corner of the rupture plane;
- **Z_top**: depth to the top of the rupture (in km);
- **Strike**: strike of the rupture plane;
- **Dip**: dip of the rupture plane;
- **Rake**: rake of the rupture plane.

Once these parameters are retrieved, the Real-Time Loss Tools create the associated rupture XML file to be passed as input to OpenQuake.

For the case of OELF, the Real-Time Loss Tools will search for the source model in the OpenQuake-engine seismogenic source model format[14] with the name indicated in the configuration file (see section 4.9). The XML file is to be located under *main_path/ruptures*. Then, the Real-Time Loss Tools will proceed with the stochastic generation of ruptures and their associated rupture XML files.

4.3 Ground motions

The ground motion logic tree is input as an XML file (*gmpe_logic_tree.xml*) following the OpenQuake format[15]. When using average spectral acceleration (AvgSA) as the intensity measure, the periods used to define it are defined in this file as well. Figure 42 shows the contents of the XML file used for this proof of concept.

[14] https://docs.openquake.org/oq-engine/master/manual/hazard.html#source-typologies
[15] https://docs.openquake.org/oq-engine/master/manual/hazard.html#defining-logic-trees

```
<?xml version="1.0" encoding="UTF-8"?>

<nrml xmlns:gml="http://www.opengis.net/gml"
      xmlns="http://openquake.org/xmlns/nrml/0.4">
    <logicTree logicTreeID='lt1'>

            <logicTreeBranchSet uncertaintyType="gmpeModel" branchSetID="bs1"
                        applyToTectonicRegionType="Active Shallow Crust">

                  <logicTreeBranch branchID="b1">
                    <uncertaintyModel>
                        [GenericGmpeAvgSA]
                        gmpe_name = "LanzanoEtAl2019_RJB_OMO"
                        avg_periods = [0.04, 0.07, 0.1, 0.15, 0.2, 0.25, 0.3, 0.35, 0.4, 0.45, 0.5,
                                       0.6, 0.7, 0.8, 0.9, 1.0, 1.25, 1.5, 1.75, 2.0, 2.25, 2.5, 2.75]
                        corr_func = "baker_jayaram"
                    </uncertaintyModel>
                    <uncertaintyWeight>1.0</uncertaintyWeight>
                  </logicTreeBranch>

            </logicTreeBranchSet>

    </logicTree>
</nrml>
```

Figure 42 Ground motion model XML file used for this proof of concept.

The site model is input as a CSV file (*site_model.csv*) following the OpenQuake format. The parameters required vary depending on the ground motion prediction equations (GMPEs) specified in the ground motion logic tree (*gmpe_logic_tree.xml*). For the GMPE used for this proof of concept, the site model was defined as shown in Table 9.

Table 9 Site model CSV file used for this proof of concept.

lon	lat	vs30	vs30measured
13.33672	42.37326	416.09	0
13.40126	42.34484	476.42	0
13.34358	42.37731	520.54	0
13.28728	42.63244	418.46	0
13.15269	42.89458	837.61	0
13.35045	42.52627	534.73	0
13.09639	42.79288	566.34	0

Additional parameters associated with the calculation of ground motion fields in OpenQuake are defined in the *job.ini* file (see section 4.9). Both *gmpe_logic_tree.xml* and *site_model.csv* are placed under *main_path/static*.

4.4 Exposure model

The initial exposure model is input as a combination of a CSV file (*exposure_model_undamaged.csv*) and an XML file (*exposure_model.xml*) following the OpenQuake format. The most relevant contents of the exposure model are defined in the CSV file, in which each row corresponds to a building or set of buildings associated with a particular location and building class (general OpenQuake definition). Apart from the mandatory fields needed for OpenQuake, the Real-Time Loss Tools require that a **building_id** and **original_asset_id** be defined, as each row corresponds to an **original_asset_id**, which is a specific combination of a **building_id** and a building class. If a **building_id** refers to an individual building, then each **original_asset_id** refers to a building class with a specific probability of being that of the building (specified in the field **number**). If the **building_id** refers to a set of buildings (e.g. those in a tile), each **original_asset_id** refers to a building class with an associated number of buildings (specified in the field **number** as well). Another difference with

respect to the standard exposure file for OpenQuake is the need to specify the current damage state of the building as part of the string that defines the building class (under the *taxonomy* column, see below). The initial exposure model may consist of already damaged structures.

The columns in the exposure CSV file are as follows:

- **id**: unique identifier to be used by OpenQuake (OpenQuake requires the label "id", but the Real-Time Loss Tools thinks of it as **asset_id** to be more specific);
- **lon**, **lat**: longitude and latitude of the original asset (e.g. centroid of an individual building or a tile);
- **taxonomy**: building class, specifying the damage state as the last parameter, using a slash to concatenate it to the rest of the building class string (e.g. class_A/DS0, class_A/DS1, etc);
- **number**: number of buildings of this **original_asset_id** (i.e., of this **building_id** and building class), or probability of this building class corresponding to this **original_asset_id**;
- **structural**: total replacement cost of all buildings or fractions of buildings specified in **number**;
- **census**: number of occupants in all buildings or fractions of buildings specified in **number**, irrespective of the time of the day;
- **occupancy**: occupancy associated with certain parameters to assign the number of occupants at different times of the day (names need to coincide with those specified under *time_of_day_occupancy* in the configuration file (see section 4.9);
- **building_id**: unique identifier for this individual building or aggregation unit (e.g., tile);
- **original_asset_id**: unique identifier for this combination of **building_id** and building class.

Table 10 shows an example of the contents of the exposure CSV file. Additional columns may be added for post-processing aggregation purposes (e.g. names and IDs of administrative units).

Table 10 Extract of the CSV file of one of the undamaged exposure models used for this proof of concept.

id	lon	lat	taxonomy	number	structural	census	occupancy	building_id	original_asset_id
exp_1	13.285904	42.633454	MUR+STRUB/LWAL+CDN/H:1/DS0	8.6	1495409.9	24.5098	residential	tile_1	exp_1
exp_2	13.285904	42.633454	MUR+STRUB/LWAL+CDN/H:2/DS0	4.2	963819.3	15.8469	residential	tile_1	exp_2
exp_3	13.287277	42.633454	MUR+STDRE/LWAL+CDN/H:4/DS0	4.1	3148508.4	55.9639	residential	tile_2	exp_3
exp_4	13.287277	42.633454	MUR+STDRE/LWAL+CDN/H:5/DS0	6.2	5951448.7	105.7855	residential	tile_2	exp_4
exp_5	13.287277	42.633454	MUR+STRUB/LWAL+CDN/H:3/DS0	11.2	3981068.2	67.6642	residential	tile_2	exp_5

Final results obtained by the Real-Time Loss Tools are output in terms of the **building_id** to the *main_path/output* folder. Intermediate OpenQuake results are output in terms of **asset_id** to the *main_path/openquake_output* folder. While **building_id** and **original_asset_id** consistently refer to the same building/s and building classes along the whole run, the values of **asset_id** may change. This is not directly visible to the user that only focuses on the results in the *main_path/output* folder. Figure 43 shows the components of the exposure model used for this proof of concept and illustrates the relation between **building_id**, **original_asset_id** and **asset_id**. As an example, *building_id = tile_2* is associated with three different *original_asset_id*, namely *exp_3*, *exp_4* and *exp_5*, each of which represents a number of buildings of different building classes. In the case of *building_id = tile_6* only two *original_asset_id* are needed and for *building_id = shm_Swiss* just one *original_asset_id* is sufficient.

The exposure XML file follows the OpenQuake format[16]. Figure 44 shows the contents of the file used for this proof of concept. As can be seen, the time of the day of the earthquake (under "occupancyPeriods") is not specified. This is because the Real-Time Loss Tools update this file each time to use the time of the day of the earthquake being run (day, night, or transit).

[16] https://docs.openquake.org/oq-engine/master/manual/risk.html#exposure-models

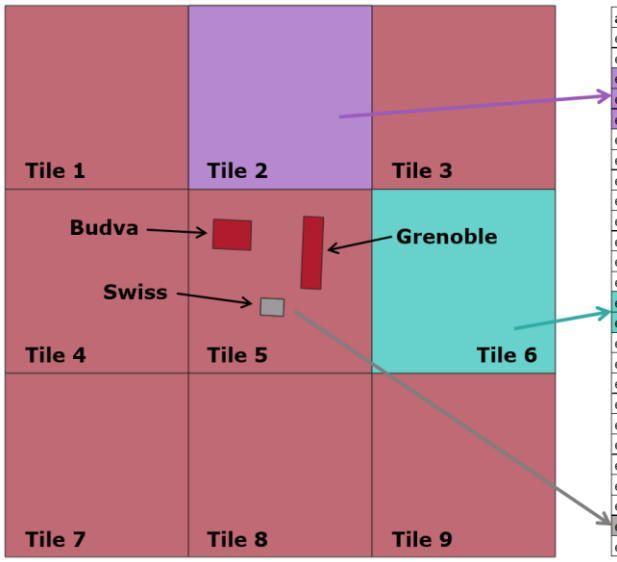

asset_id	lon	lat	taxonomy	number	building_id	original_asset_id
exp_1	13.3999	42.3459	MUR+STRUB/LWAL+CDN/H:1/DS0	8.6	tile_1	exp_1
exp_2	13.3999	42.3459	MUR+STRUB/LWAL+CDN/H:2/DS0	4.2	tile_1	exp_2
exp_3	13.4013	42.3459	MUR+STDRE/LWAL+CDN/H:4/DS0	4.1	tile_2	exp_3
exp_4	13.4013	42.3459	MUR+STDRE/LWAL+CDN/H:5/DS0	6.2	tile_2	exp_4
exp_5	13.4013	42.3459	MUR+STRUB/LWAL+CDN/H:3/DS0	11.2	tile_2	exp_5
exp_6	13.4026	42.3459	CR/LFINF+CDN+LFC:0.0/H:1/DS0	2.7	tile_3	exp_6
exp_7	13.4026	42.3459	CR/LFINF+CDN+LFC:0.0/H:2/DS0	1.9	tile_3	exp_7
exp_8	13.4026	42.3459	CR/LFINF+CDL+LFC:10.0/H:1/DS0	3.3	tile_3	exp_8
exp_9	13.3999	42.3448	CR/LFINF+CDN+LFC:0.0/H:3/DS0	4.8	tile_4	exp_9
exp_10	13.3999	42.3448	CR/LFINF+CDL+LFC:10.0/H:3/DS0	8.1	tile_4	exp_10
exp_11	13.4013	42.3448	MUR+STDRE/LWAL+CDN/H:4/DS0	3.8	tile_5	exp_11
exp_12	13.4013	42.3448	CR/LFINF+CDL+LFC:10.0/H:3/DS0	6.3	tile_5	exp_12
exp_13	13.4013	42.3448	CR/LFINF+CDL+LFC:10.0/H:4/DS0	7.7	tile_5	exp_13
exp_14	13.4026	42.3448	MCF/LWAL+CDL/H:3/DS0	4.7	tile_6	exp_14
exp_15	13.4026	42.3448	MCF/LWAL+CDL/H:4/DS0	6.6	tile_6	exp_15
exp_16	13.3999	42.3438	CR/LFINF+CDN+LFC:0.0/H:4/DS0	8.4	tile_7	exp_16
exp_17	13.3999	42.3438	CR/LFINF+CDL+LFC:10.0/H:4/DS0	11.2	tile_7	exp_17
exp_18	13.4013	42.3438	CR/LFINF+CDN+LFC:0.0/H:3/DS0	2.1	tile_8	exp_18
exp_19	13.4013	42.3438	CR/LFINF+CDL+LFC:10.0/H:3/DS0	3.6	tile_8	exp_19
exp_20	13.4013	42.3438	MUR+STRUB/LWAL+CDN/H:3/DS0	7.9	tile_8	exp_20
exp_21	13.4026	42.3438	MCF/LWAL+CDL/H:3/DS0	2.4	tile_9	exp_21
exp_22	13.4026	42.3438	MUR+STDRE/LWAL+CDN/H:4/DS0	12.3	tile_9	exp_22
exp_23	13.4026	42.3438	CR/LFINF+CDL+LFC:10.0/H:2/DS0	5.4	tile_9	exp_23
exp_24	13.4009	42.3451	Budva_hotel/DS0	1	shm_Budva	exp_24
exp_25	13.4012	42.3447	Swiss_building/DS0	1	shm_Swiss	exp_25
exp_26	13.4015	42.3450	Grenoble_city_hall/DS0	1	shm_Grenoble	exp_26

Figure 43 Extract of one of the exposure CSV files used for this proof of concept and its relation with the physical space.

```
<?xml version="1.0" encoding="UTF-8"?>
<nrml xmlns="http://openquake.org/xmlns/nrml/0.4" xmlns:gml="http://www.opengis.net/gml">
  <exposureModel category="buildings" id="exposure" taxonomySource="GEM taxonomy">
    <description>exposure model</description>
    <conversions>
      <costTypes>
        <costType name="structural" type="aggregated" unit="EUR"/>
      </costTypes>
    </conversions>
    <occupancyPeriods>time</occupancyPeriods>
    <tagNames>occupancy id_3 name_3 id_1 name_1 id_2 name_2 building_id</tagNames>
    <assets>exposure_model_current.csv</assets>
  </exposureModel>
</nrml>
```

Figure 44 Exposure model XML file used for this proof of concept.

It is noted that the naming of the column of the CSV file that contains the replacement costs is dictated by the "loss category" assigned to the fragility models in the fragility XML file (see section 4.5), and is to be specified in the exposure XML file as well (as shown in Figure 44). Total replacement costs are being assigned to structural fragility models because no non-structural fragility models or fragility models for contents are being used (their existence is limited).

The *exposure_model_undamaged.csv* file is located under *main_path/exposure_models* and the *exposure_model.xml* file is located under *main_path/current*.

4.5 State-dependent ground motion-based fragility models

Fragility models can be input to OpenQuake either in a continuous or a discrete fashion. As all the models used for this proof of concept are defined in terms of the CDF of a log-normal distribution, the fragility models were input as continuous curves defined in terms of means and standard deviations of the lognormal CDFs, by means of XML files (e.g. Figure 45).

A key characteristic of state-dependent fragility models is that they are only defined for damage states equal to or more severe than the initial damage state, simply because a building cannot go back in terms of damage unless repaired. In order to simulate this in the input XML file for OpenQuake, a very small value of mean and standard deviation (1E-10) were used to define the curves for damage states smaller than the initial damage state. In Figure 45 it can be observed how all

curves (for slight, moderate, extensive and complete damage) are defined with non-zero-like values for the building class "CR/LFINF+CDL+LFC:5.0/H:3/DS0", which is undamaged, but the curve for slight damage is defined by these small values of 1E-15 for the same class in an initial damage state of DS1, i.e. "CR/LFINF+CDL+LFC:5.0/H:3/DS1". Such a "hack" results in curves that look like step functions, albeit being defined mathematically by a lognormal CDF. As an example, Figure 46 shows the whole set of curves associated with building class "CR/LFINF+CDL+LFC:5.0/H:3" for different initial damage conditions. As an alternative to this "hack", the user could choose to define the fragility models by means of discrete functions (instead of continuous log-normal functions), as this option is supported by OpenQuake.

```
<?xml version="1.0" ?>
<nrml xmlns="http://openquake.org/xmlns/nrml/0.5">
<fragilityModel assetCategory="buildings" id="fragility_model" lossCategory="structural">
<description>State-dependent fragility model Orlacchio (2022) PhD Thesis</description>
<limitStates>slight moderate extensive complete</limitStates>
<fragilityFunction format="continuous" id="CR/LFINF+CDL+LFC:5.0/H:3/DS0" shape="logncdf">
<imls imt="AvgSA" maxIML="5" minIML="1e-15" noDamageLimit="1e-15"/>
<params ls="slight" mean="0.1768" stddev="0.0505"/>
<params ls="moderate" mean="0.3253" stddev="0.1033"/>
<params ls="extensive" mean="0.4253" stddev="0.1535"/>
<params ls="complete" mean="0.4605" stddev="0.1764"/>
</fragilityFunction>
<fragilityFunction format="continuous" id="CR/LFINF+CDL+LFC:5.0/H:3/DS1" shape="logncdf">
<imls imt="AvgSA" maxIML="5" minIML="1e-15" noDamageLimit="1e-15"/>
<params ls="slight" mean="1E-10" stddev="1E-10"/>
<params ls="moderate" mean="0.2463" stddev="0.0943"/>
<params ls="extensive" mean="0.3721" stddev="0.1343"/>
<params ls="complete" mean="0.4424" stddev="0.1793"/>
</fragilityFunction>
<fragilityFunction format="continuous" id="CR/LFINF+CDL+LFC:5.0/H:3/DS2" shape="logncdf">
<imls imt="AvgSA" maxIML="5" minIML="1e-15" noDamageLimit="1e-15"/>
<params ls="slight" mean="1E-10" stddev="1E-10"/>
```

Figure 45 Fragility model XML file used for this proof of concept (only initial lines shown).

When defining state-dependent fragility models for use in OpenQuake in the fashion just described, special attention should be paid to OpenQuake parameters that set lower bounds of ground motions below which the buildings are assumed to be undamaged. These are *minIML* and *noDamageLimit*, within the fragility XML file, and *minimum_intensity*, within the job.ini. While useful with state-independent fragility models, setting a *minimum_intensity* of, say, 1E-5, results in OpenQuake assuming that ground motions below 1E-5 lead to undamaged assets, even if the assets were already in a different damage state, which is clearly undesirable. In this proof of concept, 1E-15 was used for *minIML* and *noDamageLimit*, within the fragility XML file, and no *minimum_intensity* was set in the job.ini file.

The CSV used by OpenQuake for mapping building classes as defined in the exposure model to building classes as defined in the fragility model is trivial for this proof of concept (see Table 11), as all building classes of the exposure model have their associated fragility models, but it can easily be used in a non-trivial fashion if needed. An example application of a non-trivial exposure-vulnerability mapping file would be if the user desires to run the Real-Time Loss Tools using damage-independent fragility models. In such a case, the exposure-vulnerability mapping should direct the building classes with initial damage states different from undamaged to the fragility models of the initially undamaged condition. This "hack" was used as part of RISE Task 4.6 to carry evaluate the gains of using state-dependent fragility models in the context of a multi-criteria decision analysis; see RISE Deliverable 4.7; Mena Cabrera et al., 2023).

As can be seen in the examples in Figure 45 and Table 11, the current damage state of the structure is part of the string that defines the name of the building class. OpenQuake seeks for fragility models with IDs as specified in the *taxonomy* column of the exposure CSV file in the mapping CSV file (if provided) and/or the fragility XML file directly.

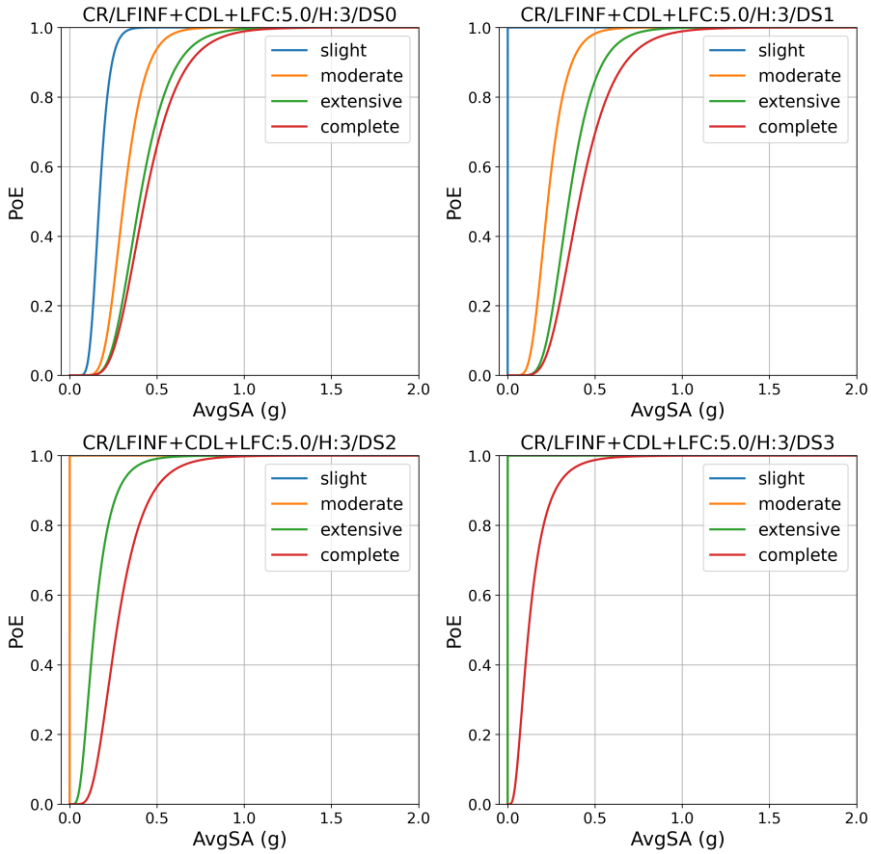

Figure 46 Fragility model for building class CR/LFINF+CDL+LFC:5.0/H:3, with different initial damage states (DS0=slight, DS1=moderate, DS2=extensive and DS3=complete).

Table 11 Exposure-vulnerability (or fragility, in this case) mapping CSV file used for this proof of concept (only initial lines shown).

taxonomy	conversion	weight
CR/LFINF+CDL+LFC:10.0/H:1/DS0	CR/LFINF+CDL+LFC:10.0/H:1/DS0	1
CR/LFINF+CDL+LFC:10.0/H:2/DS0	CR/LFINF+CDL+LFC:10.0/H:2/DS0	1
CR/LFINF+CDL+LFC:10.0/H:3/DS0	CR/LFINF+CDL+LFC:10.0/H:3/DS0	1
CR/LFINF+CDL+LFC:10.0/H:4/DS0	CR/LFINF+CDL+LFC:10.0/H:4/DS0	1
CR/LFINF+CDN+LFC:0.0/H:1/DS0	CR/LFINF+CDN+LFC:0.0/H:1/DS0	1
CR/LFINF+CDN+LFC:0.0/H:2/DS0	CR/LFINF+CDN+LFC:0.0/H:2/DS0	1
CR/LFINF+CDN+LFC:0.0/H:3/DS0	CR/LFINF+CDN+LFC:0.0/H:3/DS0	1
CR/LFINF+CDN+LFC:0.0/H:4/DS0	CR/LFINF+CDN+LFC:0.0/H:4/DS0	1
MCF/LWAL+CDL/H:3/DS0	MCF/LWAL+CDL/H:3/DS0	1
MCF/LWAL+CDL/H:4/DS0	MCF/LWAL+CDL/H:4/DS0	1
MUR+STDRE/LWAL+CDN/H:4/DS0	MUR+STDRE/LWAL+CDN/H:4/DS0	1
MUR+STDRE/LWAL+CDN/H:5/DS0	MUR+STDRE/LWAL+CDN/H:5/DS0	1
MUR+STRUB/LWAL+CDN/H:1/DS0	MUR+STRUB/LWAL+CDN/H:1/DS0	1
MUR+STRUB/LWAL+CDN/H:2/DS0	MUR+STRUB/LWAL+CDN/H:2/DS0	1
MUR+STRUB/LWAL+CDN/H:3/DS0	MUR+STRUB/LWAL+CDN/H:3/DS0	1
CR/LFINF+CDL+LFC:10.0/H:1/DS1	CR/LFINF+CDL+LFC:10.0/H:1/DS1	1
CR/LFINF+CDL+LFC:10.0/H:2/DS1	CR/LFINF+CDL+LFC:10.0/H:2/DS1	1

Both the fragility XML and the mapping CSV files are located under *main_path/static* and are called within the job.ini input file for OpenQuake (see section 4.9).

4.6 Estimation of damage probabilities using SHM

The Real-Time Loss Tools read damage probabilities obtained by means of structural health monitoring techniques as one *damage_results_shm.csv* file in which each row corresponds to one **building_id** and damage state, and each column corresponds to an earthquake in the sequence, as shown in Table 12. In a full-scale implementation, results would come independently for each earthquake instead (as the earthquake occurs and the SHM calculations are run).

Table 12 Example of a *damage_results_shm.csv* file with three monitored buildings and eight earthquakes.

building_id	dmg_state	IT-2009-0009	IT-2009-0032	IT-2009-0084	IT-2009-0095	IT-2009-0102	IT-2009-0121	IT-2009-0140	IT-2009-0174
building_1	no_damage	0.4	0.27	0.2	0.15	0.1	0.07	0.06	0.06
building_1	dmg_1	0.3	0.2	0.23	0.18	0.15	0.13	0.12	0.11
building_1	dmg_2	0.2	0.4	0.35	0.32	0.27	0.25	0.25	0.24
building_1	dmg_3	0.08	0.1	0.15	0.22	0.28	0.32	0.33	0.34
building_1	dmg_4	0.02	0.03	0.07	0.13	0.2	0.23	0.24	0.25
building_2	no_damage	0.4	0.27	0.2	0.15	0.1	0.07	0.06	0.06
building_2	dmg_1	0.3	0.2	0.23	0.18	0.15	0.13	0.12	0.11
building_2	dmg_2	0.2	0.4	0.35	0.32	0.27	0.25	0.25	0.24
building_2	dmg_3	0.08	0.1	0.15	0.22	0.28	0.32	0.33	0.34
building_2	dmg_4	0.02	0.03	0.07	0.13	0.2	0.23	0.24	0.25
building_3	no_damage	0.4	0.27	0.2	0.15	0.1	0.07	0.06	0.06
building_3	dmg_1	0.3	0.2	0.23	0.18	0.15	0.13	0.12	0.11
building_3	dmg_2	0.2	0.4	0.35	0.32	0.27	0.25	0.25	0.24
building_3	dmg_3	0.08	0.1	0.15	0.22	0.28	0.32	0.33	0.34
building_3	dmg_4	0.02	0.03	0.07	0.13	0.2	0.23	0.24	0.25

To run the Real-Time Loss Tools without input from SHM, the file *damage_results_shm.csv* still needs to exist and contain only the first row, i.e. "building_id, dmg_state, earthquake_id_1, …, earthquake_id_N".

The *damage_results_shm.csv* file is located under *main_path/shm*.

4.7 Economic and human consequence models

The consequence models for both economic and human impacts share a common CSV format in which each row corresponds to a building class present in the exposure model and each column corresponds to a damage state, and the values shown are percentages (0-100%) of the total exposed replacement cost or occupants. The Real-Time Loss Tools requires one *consequences_economic.csv* file and as many *consequences_injuries_severity_X.csv* files as levels of injury are indicated under *injuries_scale* in the configuration file (see section 4.9), with X being equal to each of the levels. Table 13 shows examples of such files. All consequence CSV files are placed under *main_path/static*.

Table 13 Example of a *consequences_economic.csv* file (left) and a *consequences_injuries_severity_X.csv* file (right).

Taxonomy	DS0	DS1	DS2	DS3	DS4
CR/LFINF+CDN+LFC:0.0/H:1	0	5	15	60	100
CR/LFINF+CDN+LFC:0.0/H:2	0	5	15	60	100
CR/LFINF+CDN+LFC:0.0/H:3	0	5	15	60	100
CR/LFINF+CDN+LFC:0.0/H:4	0	5	15	60	100
CR/LFINF+CDN+LFC:0.0/H:5	0	5	15	60	100
CR/LFINF+CDN+LFC:0.0/H:6	0	5	15	60	100
CR/LFINF+CDL+LFC:5.0/H:1	0	5	15	60	100
CR/LFINF+CDL+LFC:5.0/H:2	0	5	15	60	100
CR/LFINF+CDL+LFC:5.0/H:3	0	5	15	60	100
CR/LFINF+CDL+LFC:5.0/H:4	0	5	15	60	100
CR/LFINF+CDL+LFC:5.0/H:5	0	5	15	60	100

Taxonomy	DS0	DS1	DS2	DS3	DS4
CR/LFINF+CDN+LFC:0.0/H:1	0	0.05	0.2	1	6.35
CR/LFINF+CDN+LFC:0.0/H:2	0	0.05	0.2	1	6.35
CR/LFINF+CDN+LFC:0.0/H:3	0	0.05	0.2	1	6.35
CR/LFINF+CDN+LFC:0.0/H:4	0	0.05	0.2	1	6.35
CR/LFINF+CDN+LFC:0.0/H:5	0	0.05	0.2	1	6.35
CR/LFINF+CDN+LFC:0.0/H:6	0	0.05	0.2	1	6.35
CR/LFINF+CDL+LFC:5.0/H:1	0	0.05	0.2	1	5.9
CR/LFINF+CDL+LFC:5.0/H:2	0	0.05	0.2	1	5.9
CR/LFINF+CDL+LFC:5.0/H:3	0	0.05	0.2	1	5.9
CR/LFINF+CDL+LFC:5.0/H:4	0	0.05	0.2	1	5.9
CR/LFINF+CDL+LFC:5.0/H:5	0	0.05	0.2	1	5.9

4.8 Timelines for damage inspection and hospitalisations

The number of days needed for inspection and repair of buildings in different damage states is input through a *recovery_damage.csv* file, while the number of days spent in hospital or until a person with different severities of injury is able to return to the building/s they usually occupy is input through a *recovery_injuries.csv* file. Examples of both are shown in Table 14.

Table 14 Contents of the *recovery_damage.csv* file (left) and the *recovery_injuries.csv* file (right) used for this proof of concept.

dmg_state	N_inspection	N_repair
DS0	7	0
DS1	7	15
DS2	45	365
DS3	45	1095
DS4	45	1095

injuries_scale	N_discharged
1	0
2	3
3	8
4	36500

A very large number of *N_discharged* days can be used for extreme severity of injury representing instantaneous death or mortal injuries. In the example of Table 14, 36,500 days (≈ 100 years) are assigned to injuries of severity 4 for this purpose.

It is possible to force the Real-Time Loss Tools to not carry out the update of occupants (i.e. to always consider all original occupants irrespective of damage and injury) by filling in the two tables with zeroes.

Both CSV files are placed under *main_path/static*.

4.9 Configuration and running controls

The overall configuration and control over the running of the Real-Time Loss Tools is guided by three files: *config.yml*, *triggering.csv*, and OpenQuake's *job.ini*. Only *config.yml* and *job.ini* would be needed in an operational implementation, as the triggering of calculations (RLA or OELF) would be handled by the overall architecture of the software (e.g., when an accelerometric network detects an earthquake).

The *triggering.csv* is thus very simple and consists of a CSV file with two columns:

- **catalogue_filename**: name of the catalogue CSV file (each of the files contained in *main_path/catalogues*, see section 4.1);
- **type_analysis**: type of analysis to run with the corresponding catalogue, either RLA (rapid loss assessment) or OELF (operational earthquake forecasting). When RLA is indicated, only the first row of the catalogue (apart from the column names) is read.

Table 15 shows an example of a *triggering.csv* file. The *triggering.csv* file is placed under *main_path*.

Table 15 Example of a *triggering.csv* file.

catalogue_filename	type_analysis
forecast_before_01.csv	OELF
real_earthquake_01.csv	RLA
forecast_after_01.csv	OELF
real_earthquake_02.csv	RLA
forecast_after_02.csv	OELF
forecast_at_arbitrary_time.csv	OELF
real_earthquake_03.csv	RLA
forecast_after_03.csv	OELF

The configuration *config.yml* file, placed directly under *main_path*, contains the following parameters:

- **description_general**: General description, used by OpenQuake to describe each job run.

- **main_path**: Path to the main running directory, assumed to have the needed file structure (Figure 41).

- **oelf_source_model_filename**: Name of the source model XML file needed to create the ruptures to run OELF calculations, assumed to be located under *main_path/ruptures* (see section 4.2).

- **state_dependent_fragilities**: *True* if the fragility models used to run OpenQuake are state-dependent (as for this proof of concept), *False* otherwise (the *False* option was used as part of RISE Task 4.6 to carry evaluate the gains of using state-dependent fragility models in the context of a multi-criteria decision analysis; see RISE Deliverable 4.7; Mena Cabrera et al., 2023).

- **mapping_damage_states**: Nested parameters linking the names of damage states as output by OpenQuake and as labelled in the fragility model. The parameter keys are the names of damage states as output by OpenQuake and the values are the names of damage states as labelled in the fragility model. It is assumed that the damage states are input in order of severity, from least severe to most severe. For this proof of concept, this parameter is shown in Figure 47:

```
mapping_damage_states:
  no_damage: DS0
  dmg_1: DS1
  dmg_2: DS2
  dmg_3: DS3
  dmg_4: DS4
```

Figure 47 Parameter *mapping_damage_states* as defined for this proof of concept.

- **oelf**: Parameters used to run Operational Earthquake Loss Forecasting (OELF):
  - **min_magnitude**: Minimum magnitude to carry out a damage and loss assessment while running OELF (5.0 in this proof of concept). Earthquakes in the OELF catalogues are assumed to produce zero damage.

  - **max_distance**: Maximum epicentral distance between earthquake source and site to run the earthquake (200 km in this proof of concept). Earthquakes in the OELF

catalogues located farther away from the exposure sites than this distance are assumed to produce zero damage.

- **continuous_ses_numbering**: If *True* (as in this proof of concept), the software will assume there are as many stochastic event sets as indicated in **ses_range** (see below), with an increment of 1. If *False*, the Real-Time Loss Tools simply reads the IDs of the stochastic event sets from the OELF catalogue. *True* is used when the OELF CSV catalogue does not include all realisations of seismicity because of a minimum magnitude threshold being used to write the file (i.e., stochastic event sets might be missing because they did not contain any earthquake with magnitude larger than the threshold set to write the file). Such stochastic event sets are assumed to exist but cause no damage when *continuous_ses_numbering* is set to *True*.

- **ses_range**: Start and end number of the ID of the stochastic event sets, given as a list separated by comma and space (", "), used if *continuous_ses_numbering* is set to *True*. In this proof of concept, *ses_range: 1, 10000*.

- **rupture_generator_seed**: Optional seed (positive non-zero integer) to set for the random number generator controlling the stochastic rupture simulations, so that results are reproducible. A seed of 1976 was used for this proof of concept.

- **rupture_region_properties**: Optional set of properties to control the generation and scaling of ruptures according to the tectonic region. One set with the following parameters is set for each tectonic region:
  - **msr**: Choice of Magnitude Scaling Relation (must be supported by OpenQuake)
  - **area_mmax**: Earthquake magnitude to cap the scaling of the rupture area. Magnitudes greater than this will have rupture areas fixed to that corresponding to this *area_mmax* magnitude. This parameter avoids unrealistic ruptures from being generated when the input OELF seismicity catalogues contain very large magnitudes.
  - **aspect_limits**: Lower and upper limits on the randomly sampled aspect ratio of the ruptures.
  - **default_usd**: Default upper seismogenic depth (km) if not specified in the source model.
  - **default_lsd**: Default lower seismogenic depth (km) if not specified in the source model.

  Figure 48 shows the parameters of *rupture_region_properties* used for this proof of concept.

```
rupture_region_properties:
  Volcanic Shallow:
    msr: WC1994
    area_mmax: 7.0
    aspect_limits: 1.0, 1.5
    default_usd: 0.0
    default_lsd: 10.0
  Active Shallow Crust:
    msr: Leonard2014_Interplate
    area_mmax: 7.75
    aspect_limits: 1.0, 1.5
    default_usd: 0.0
    default_lsd: 25.0
```

Figure 48 Parameter *rupture_region_properties* as defined for this proof of concept.

- **injuries_scale**: Scale of severity of injuries, given as a list separated by comma and space (", "). For this proof of concept, *injuries_scale = 1, 2, 3, 4*.

- **injuries_longest_time**: Maximum number of days since the time of an earthquake that will be used to calculate the number of occupants in the future, irrespective of the number of days indicated in *recovery_damage.csv* or *recovery_damage.csv* (see section 4.8). For this proof of concept, 730 days were used.

- **time_of_day_occupancy**: Factors by which the census number of occupants is multiplied to obtain the people in the building at a certain time of the day. It needs to be sub-divided into occupancy cases with names as specified in the *occupancy* field of the exposure CSV file (see section 4.4), each of which containing a factor for *day* (10 am to 6 pm), *night* (10 pm to 6 am) and *transit* (6 am to 10 am, and 6 pm to 10 pm) times. Figure 49 shoes the values used for this proof of concept, which correspond to those for Italy in the exposure model for ESRM20 (Crowley et al., 2021a).

```
time_of_day_occupancy:
  residential:
    day: 0.242853
    night: 0.9517285
    transit: 0.532079
  commercial:
    day: 0.4982155
    night: 0.0436495
    transit: 0.090751
```

Figure 49 Parameter *time_of_day_occupancy* as defined for this proof of concept.

- **timezone**: Local time zone in the format of the IANA Time Zone Database[17], used to convert from UTC time to local time, for the purpose of determining the time of the day of the earthquake and, as a consequence, the number of occupants. For this proof of concept, *timezone = "Europe/Rome"*.

- **store_intermediate**: If *True*, intermediate results/calculations including intermediate exposure models and damage states are stored.

- **store_openquake**: If *True*, OpenQuake HDF5 files will be stored and jobs will be kept in OpenQuake's database. If *False*, these will be erased after the damage results are retrieved.

- **post_process**: Parameters controlling the post-processing of results:

    - **collect_csv**: If *True*, individual damage and loss results (due to each RLA earthquake and each OELF catalogue) are collected under one RLA and one OELF CSV file.

OpenQuake's *job.ini* file, placed under *main_path/current*, is updated in each run but contains a series of parameters that are kept the same all along. Figure 50 shows the contents of *job.ini*.

[17] https://www.iana.org/time-zones

```
[general]
description = State-depdendent job.ini
calculation_mode = scenario_damage
ses_seed = 159

[exposure]
exposure_file = exposure_model.xml
taxonomy_mapping_csv = ../static/exposure_vulnerability_mapping_state_dependent.csv
time_event = time

[fragility]
structural_fragility_file = ../static/fragility_model.xml

[Rupture information]
rupture_model_file = ../ruptures/rla/rupture.xml
rupture_mesh_spacing = 0.5

[Site conditions]
site_model_file = ../static/site_model.csv

[Calculation parameters]
gsim_logic_tree_file = ../static/gmpe_logic_tree.xml
truncation_level = 3
maximum_distance = 200.0
number_of_ground_motion_fields = 1000
```

Figure 50 Contents of *job.ini*.

The parameters of the *job.ini* file are the following:

- **[general]**
  - **description**: It can contain any string, as it will be replaced by the contents of *description_general* from the config.yml file.
  - **calculation_mode**: It must be *scenario_damage*.
  - **ses_seed**: A value of 159 was used for this proof of concept for the purpose of reproducibility.
- **[exposure]**
  - **exposure_file**: Path and filename to the exposure XML file (see section 4.4). It must be *exposure_model.xml*.
  - **taxonomy_mapping_csv**: Path and filename to the exposure-vulnerability mapping CSV (see section 4.5). It must be *../static/exposure_vulnerability_mapping.csv* (the name of the CSV file can be different).
  - **time_event**: It can contain any string, as it will be replaced by the time of the day associated with each earthquake to be run.
- **[fragility]**
  - **structural_fragility_file**: Path and filename to the fragility XML file (see section 4.5). It must be *../static/fragility_model.xml*.
- **[Rupture information]**
  - **rupture_model_file**: Path and filename to the rupture XML file (see section 4.2). It can contain any string, as it will be replaced by the name and location of each rupture XML file to be used to run OpenQuake.
  - **rupture_mesh_spacing**: Spacing (km) used to discretise the rupture plane. In this proof of concept a value of 0.5 km was used.
- **[Site conditions]**
  - **site_model_file**: Path and filename to the site model CSV file (see section 4.3). It must be *../static/site_model.csv*.
- **[Calculation parameters]**
  - **gsim_logic_tree_file**: Path and filename to the ground motion logic tree XML file (see section 4.3). It must be *../static/gmpe_logic_tree.xml*.

- **truncation_level**: Number of standard deviations to consider for sampling ground motions from the ground motion prediction equation. For this proof of concept a value of 3 was used.
- **maximum_distance**: Maximum epicentral distance (km) between earthquake source and site. All sites further away from this distance are ignored by OpenQuake. For this proof of concept a value of 200 km was used.
- **number_of_ground_motion_fields**: Number of stochastic realisations of ground motion to be generated for each earthquake. For this proof of concept a value of 1,000 was used.
- **minimum_intensity**: Minimum ground motion intensity at a site for damage to be calculated. For this proof of concept and for any application that uses state-dependent fragility/vulnerability models, the *minimum_intensity* parameter should not be used (i.e. skip it in the *job.ini* file; see comments in section 4.5).

The behaviour of the Real-Time Loss Tools when other input parameters accepted by OpenQuake are included in the *job.ini* file has not been tested.

5. Step-by-step through the case-studies

5.1 Definition of scenarios

This proof of concept focuses on two main case scenarios, the 2009 L'Aquila and the 2016-2017 Central Italy earthquake, and a series of three and four locations for each of them, marked with black dots in Figure 51. For a matter of simplicity and with the objective of making the case studies simpler to follow, we focused the rapid loss assessment calculations on earthquakes with moment magnitude (reported in the Italian Accelerometric Archive, ITACA; Russo et al., 2022) of 5.0 and above, which results in eight and nine earthquakes for L'Aquila and Central Italy, respectively. These earthquakes are listed in Table 16 and Table 17, and their epicentres are shown as stars in Figure 51.

Table 16 Earthquakes with Mw ≥ 5 of the 2009 L'Aquila sequence (according to ITACA).

EQ #	ITACA event ID	Date (UTC)	Time (UTC)	Lon.	Lat.	Depth (km)	Mw
1	IT-2009-0009	6 April 2009	01:32:40	13.4193	42.3140	8.2	6.1
2	IT-2009-0032	6 April 2009	02:37:04	13.3280	42.3600	8.7	5.1
3	IT-2009-0084	6 April 2009	23:15:36	13.3850	42.4630	9.7	5.1
4	IT-2009-0095	7 April 2009	09:26:28	13.3870	42.3360	9.6	5.1
5	IT-2009-0102	7 April 2009	17:47:37	13.4860	42.3030	17.1	5.5
6	IT-2009-0121	9 April 2009	00:52:59	13.3510	42.4890	11.0	5.4
7	IT-2009-0140	9 April 2009	19:38:16	13.3500	42.5040	9.3	5.2
8	IT-2009-0174	13 April 2009	21:14:24	13.3770	42.4980	9.0	5.0

Table 17 Earthquakes with Mw ≥ 5 of the 2016-2017 Central Italy sequence (according to ITACA).

EQ #	ITACA event ID	Date (UTC)	Time (UTC)	Lon.	Lat.	Depth (km)	Mw
1	EMSC-20160824_0000006	24 Aug 2016	01:36:32	13.2400	42.7000	7.3	6.0
2	EMSC-20160824_0000013	24 Aug 2016	02:33:29	13.1507	42.7922	8.0	5.3
3	EMSC-20161026_0000077	26 Oct 2016	17:10:36	13.1243	42.8747	8.1	5.4
4	EMSC-20161026_0000095	26 Oct 2016	19:18:06	13.1192	42.9211	5.7	5.9
5	EMSC-20161030_0000029	30 Oct 2016	06:40:18	13.1620	42.8182	6.8	6.5
6	EMSC-20170118_0000027	18 Jan 2017	09:25:42	13.2768	42.5450	10.0	5.1
7	EMSC-20170118_0000034	18 Jan 2017	10:14:12	13.2849	42.5465	10.4	5.5
8	EMSC-20170118_0000037	18 Jan 2017	10:25:26	13.2770	42.5033	9.4	5.4
9	EMSC-20170118_0000119	18 Jan 2017	13:33:37	13.2747	42.4733	9.5	5.0

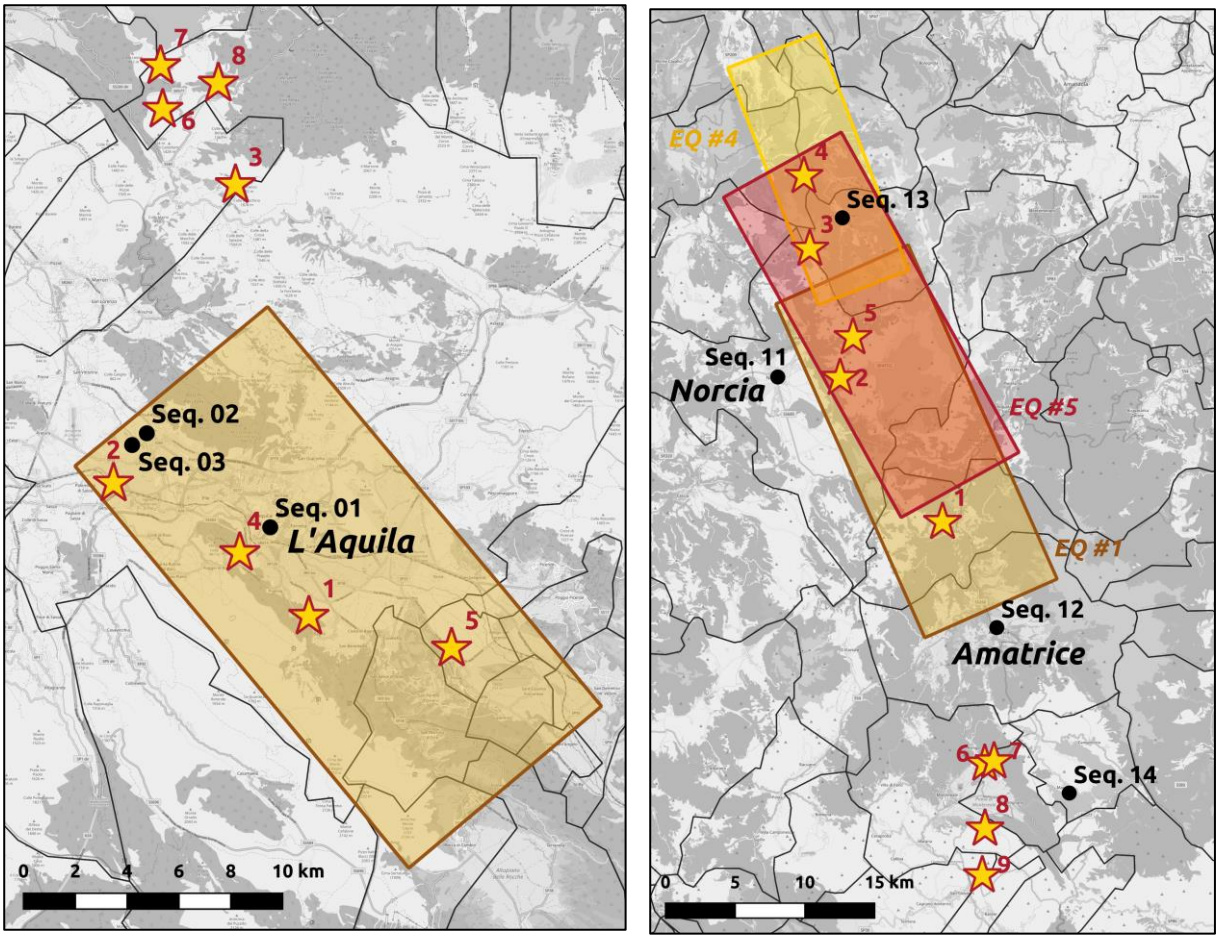

Figure 51 Earthquakes with moment magnitude Mw equal to or greater than 5.0 (as per the Italian Accelerometric Archive) of the 2009 L'Aquila (left) and 2016-2017 Central Italy (right) earthquake sequences (numbered stars), together with the seven selected sites (black dots labelled "Seq. XX") and rupture planes of the largest shocks from the Italian Accelerometric Archive (ITACA; Russo et al., 2022). Background: OpenStreetMap.

A 24-hour seismicity forecast was generated at 00:00 hour of the day in which the first shock of interest listed in Table 16 and Table 17 occurred, namely 6 April 2009 and 24 August 2016, and right after each of the shocks in the tables. Additionally, forecasts were generated at 00:00 of 13 April 2009 (L'Aquila), 26 October 2016 and 18 January 2017 (Central Italy), in view of the larger amount of time in between real earthquakes of Mw 5.0 and above. A rapid loss assessment was run for each of the earthquakes in Table 16 and Table 17 and a loss forecast was run for each 24-hour seismicity forecast. The timelines of RLA and OELF calculations are depicted in Figure 52 and

Figure 53. For each earthquake run, either of a RLA or OELF calculation, 1,000 realisations of ground motion (and, consequently, 1,000 realisations of damage probabilities) were calculated.

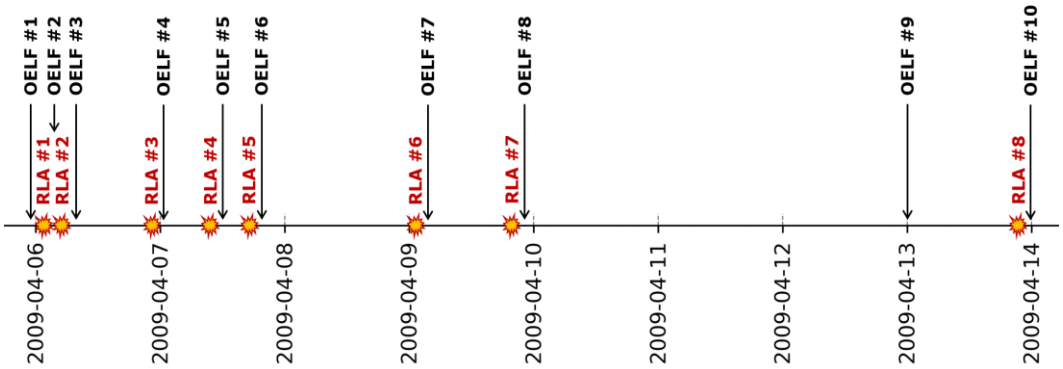

Figure 52 Timeline of RLA and OELF calculations carried out in this proof of concept for the 2009 L'Aquila sequence.

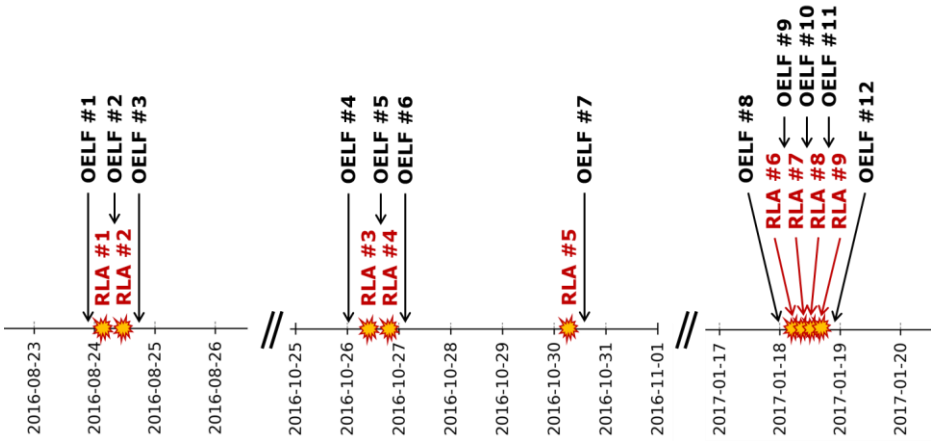

Figure 53 Timeline of RLA and OELF calculations carried out in this proof of concept for the 2016-2017 Central Italy sequence.

Series of real accelerograms were retrieved for each of the seven locations to simulate the action of the earthquakes on the three monitored buildings, as explained in section 3.7. The different locations used for each sequence (L'Aquila, Central Italy) differ from one another in terms of:

- site properties,
- distance with respect to each real earthquake rupture,
- distance with respect to each forecasted earthquake,
- building of the ruptures for the seismicity forecasts,
- ground motion variability sampled when generating the 1,000 ground motion fields,
- the accelerograms that represent the action on the three monitored buildings.

This step-by-step demonstration of the calculations and the way in which the different components are integrated focuses on three of these seven case-studies: location 01 of the 2009 L'Aquila sequence (in the town of L'Aquila itself, section 5.2), and locations 12 (in the town of Amatrice, section 5.3) and 14 (in the town of Mascioni, section 5.4) of the 2016-2017 Central Italy sequence. Some brief observations on all seven cases are presented in section 5.5, while section 5.6 covers a discussion on running times and the OELF minimum magnitude threshold.

5.2 Case-study 1: 2009 L'Aquila sequence at location 01

The running of this case-study starts with a 1-day seismicity forecast generated at 00:00:00 UTC[18] on 6 April 2009, that is, a bit over an hour and a half before the main shock. As can be observed in Figure 54, a concentration of seismicity in what would become the rupture of the main shock (brown rectangle) is forecast, including one Mw 6.5 and a couple of Mw 5.8 in close proximity to the Mw 6.1 main shock. However, as these are only a handful of the 10,000 realisations of seismicity that the forecast produces (see full magnitude distribution in the left plot of Figure 55), the mean expected economic loss ratio calculated starting from the assumption of an undamaged building portfolio is 0.06%, and only 64 out of the 10,000 stochastic event sets produce losses larger than zero (running OELF for earthquakes with Mw ≥ 5).

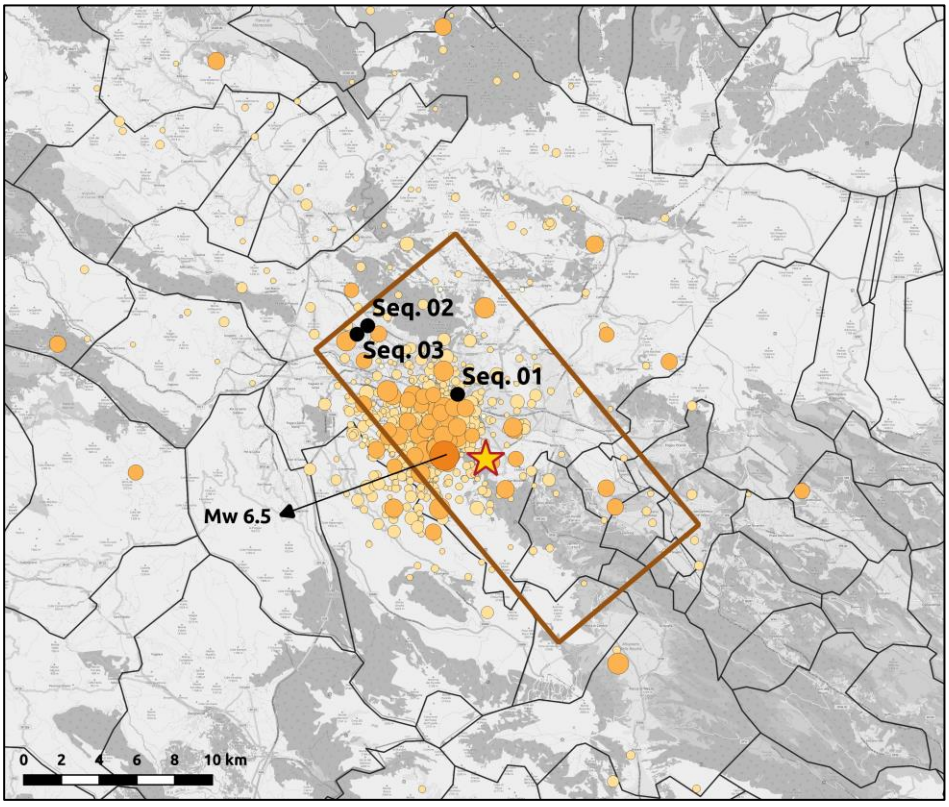

Figure 54 One-day seismicity forecast (10,000 realisations, Mw ≥ 3.99) around the town of L'Aquila generated at 00:00:00 of 6 April 2009, around 92 minutes before the Mw 6.1 main shock (yellow star, rupture in brown). Background: OpenStreetMap.

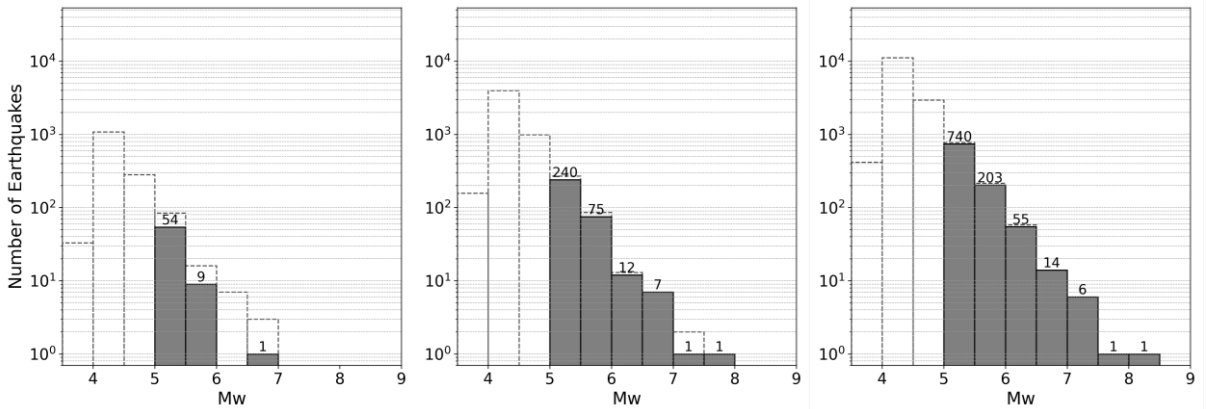

Figure 55. Number of earthquakes per magnitude bin of the daily forecast generated at 00:00 UTC (left), after the main shock (centre) and after the second shock (right) of 6 April 2009. Dotted bars show the complete forecasts (Mw≥3.99) while filled bars show the forecasts filtered for the running of OELF calculations at location 01 (Mw≥5.0, 200 km maximum epicentral distance).

[18] All dates and times are UTC unless expressed otherwise.

Damage and losses do occur when the first earthquake of Mw ≥ 5 takes place: the Mw 6.1 main shock of 6 April 2009 at 01:32:40 UTC. Starting from an undamaged initial state, 116.5 out of 137.5 (84.7%) buildings modelled in the nine tiles of the exposure model are expected to suffer from some degree of damage, while 21.0 (15.3%) are expected to remain intact. The distribution per tile and damage state is shown in Figure 56. The damage scale used is the same as in the European Seismic Risk Model 2020 (ESRM20, Crowley et al., 2021a): no damage (DS0), slight damage (DS1), moderate damage (DS2), extensive damage (DS3), and complete damage (DS4). It is noted that DS4 is not a synonym of collapse and only a small fraction of completely damaged buildings would be expected to collapse, while the majority would be in need of demolition and replacement.

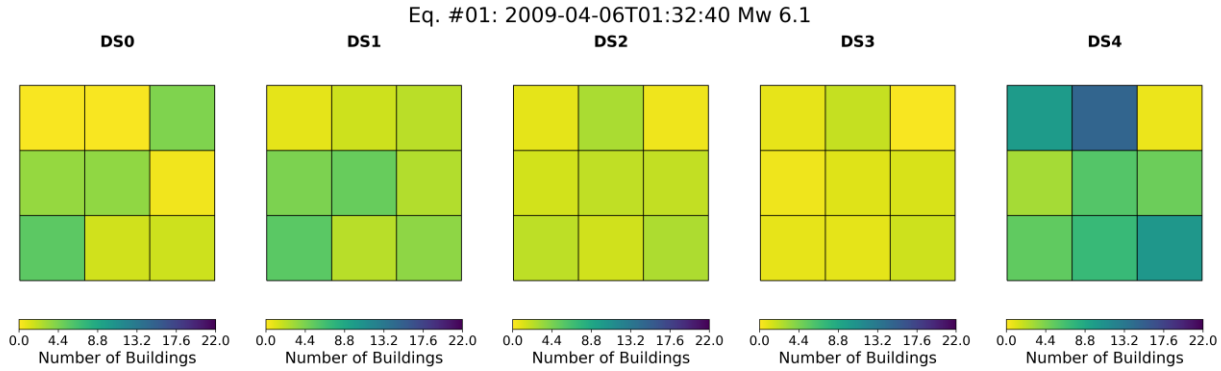

Figure 56 Expected number of buildings per damage state in each exposure tile at location 01 due to the Mw 6.1 2009 L'Aquila main shock.

Transforming the above into probabilities of observing each damage grade and including the three monitored buildings results in Figure 57. The total aggregate number of buildings per damage state (and their associated percentages with respect to the total building stock) are depicted in Figure 58, in which it becomes clear that a very large proportion (45%) of the buildings is expected to be completely damaged to the extent that a full replacement is needed.

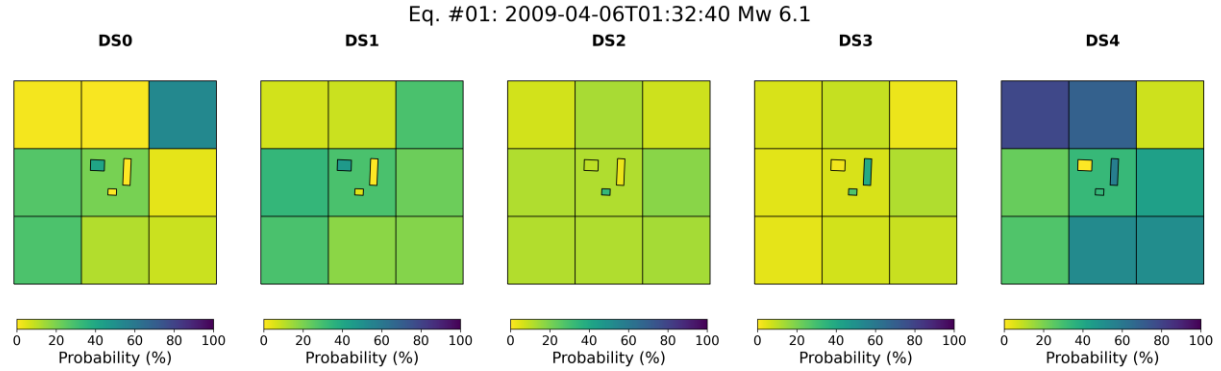

Figure 57 Expected probabilities of each damage state for each exposure tile and monitored building at location 01 due to the Mw 6.1 2009 L'Aquila main shock.

The probabilities of damage for the three instrumented buildings stem from the SHM-based fragilities described in section 3.6. Having modelled the response of these buildings when subject to accelerograms of the L'Aquila main shock recorded at seismic station AQK, the three damage sensitive features were derived as would be the case if the building response to a real earthquake is monitored.

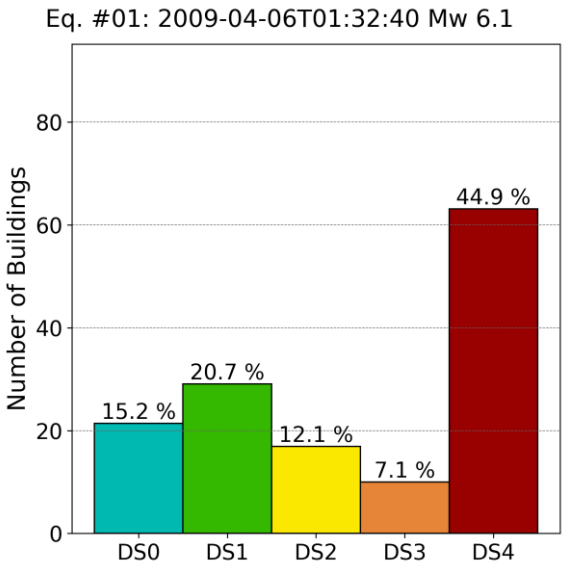

Figure 58 Expected aggregate number of buildings and probabilities per damage state at location 01 due to the Mw 6.1 2009 L'Aquila main shock.

These expected damage states lead to an expected total absolute loss of around 64 million EUR, which is 53.8% of the total value of all buildings in the exposure model. The distribution of these economic losses across different tiles and buildings is shown in Figure 59. The spatial patterns of damage, absolute losses and loss ratios (i.e. ratio of loss to full value of the building stock) are different because losses depend not only on damage but also on the total number of buildings and their individual replacement costs (see, for example, how the top-left tile presents a larger economic loss ratio than other tiles but a lower absolute economic loss than many).

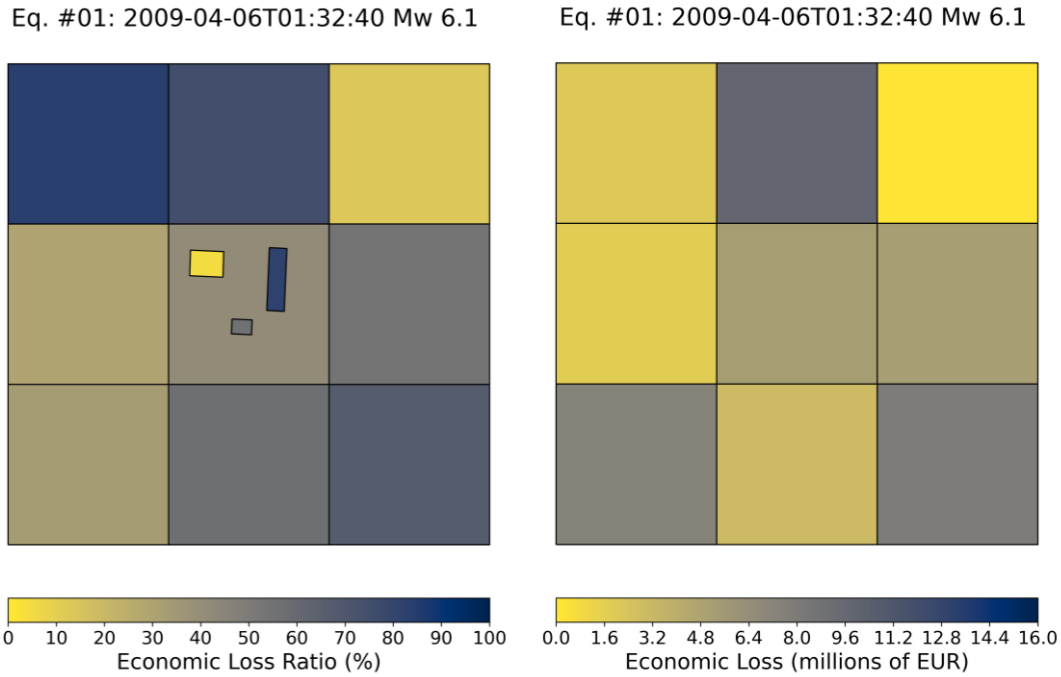

Figure 59 Expected economic loss ratios (left) and economic loss in EUR (right, only tiles) due to the Mw 6.1 2009 L'Aquila main shock.

In terms of human casualties, 56.59 people (3.03 % of the census occupants) are expected to suffer from injuries of severity 1, which require only basic medical aid in the field, while 11.11 0.45 and 7.12 people (0.60%, 0.02% and 0.38% of the census occupants, respectively) are expected to suffer from injuries of severity 2 (non-life-threatening but requiring medical technology), 3 (immediately life-threatening) and 4 (instantaneously killed or mortally injured). As depicted in Figure 60,

larger human casualty ratios (ratio between expected number of injuries of a certain severity and the total number of census occupants) are expected in tiles with a larger proportion of masonry structures than in those populated mostly with reinforced concrete moment-resisting frames (cf. Figure 15). Number of injured people are not necessarily integers due to the fact that these are numerical outputs of a model and they represent an expected value in a statistical sense.

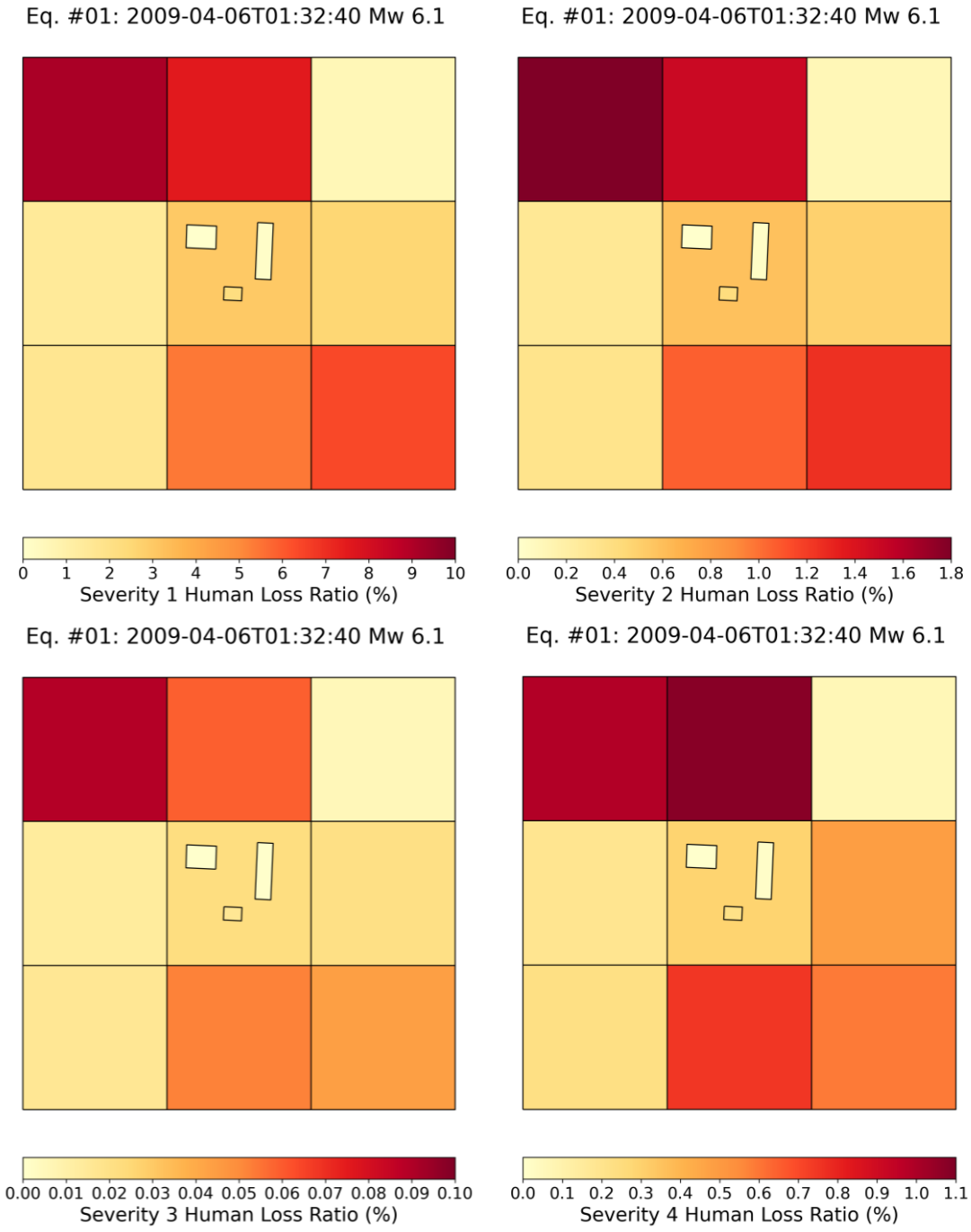

Figure 60 Expected ratios of census occupants injured with different severity levels due to the Mw 6.1 2009 L'Aquila main shock.

As soon as this main shock occurs, a seismicity forecast is produced for the coming 24 hours (though any reference period of interest can be used). Figure 61 shows the epicentres around L'Aquila while the full magnitude distribution is depicted in the central plot of Figure 55. The mean expected cumulative economic loss due to these 10,000 realisations of seismicity is around 64.5 million EUR, which is 54.1% of the total value of all buildings in the exposure model and represents only a 0.34% increase with respect to the expected economic loss after the main shock. However, individual stochastic sets of seismicity predict up to 114 million EUR of economic loss, which is 95.5% of the total

value of the building stock, with the 99th percentile of OELF economic losses being around 78 million EUR (65.4%). These results are depicted in Figure 62. The filled red dot represents the losses expected due to the Mw 6.1 main shock, and the loss forecast for the subsequent 24 hours is represented with the empty red dot and dashed lines, at the end of the 24-hour period. Also depicted in Figure 62 are the losses predicted by the end of the day of 6 April 2009 before the main shock took place. As the time span of the seismicity forecast is 24 hours, no additional human casualties are predicted due to the update in the number of occupants in the buildings after the main shock and the minimum seven days for inspection defined in Table 6.

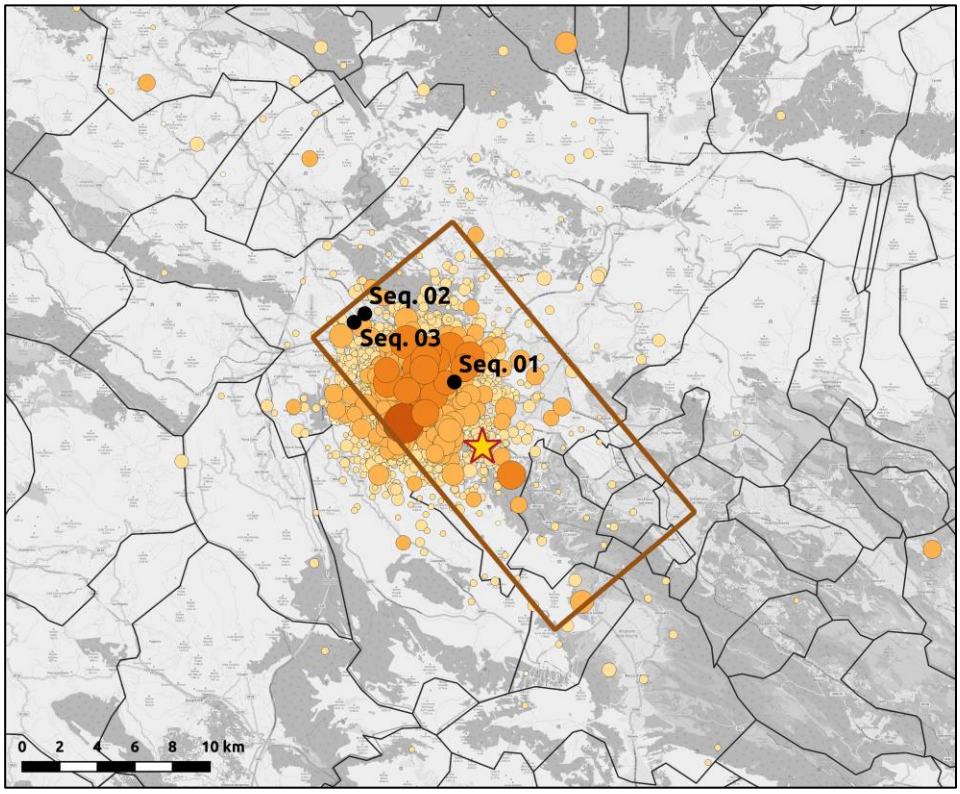

Figure 61 One-day seismicity forecast (10,000 realisations, Mw ≥ 3.99) around the town of L'Aquila generated right after the Mw 6.1 main shock of 6 April 2009 (yellow star, rupture in brown). Background: OpenStreetMap.

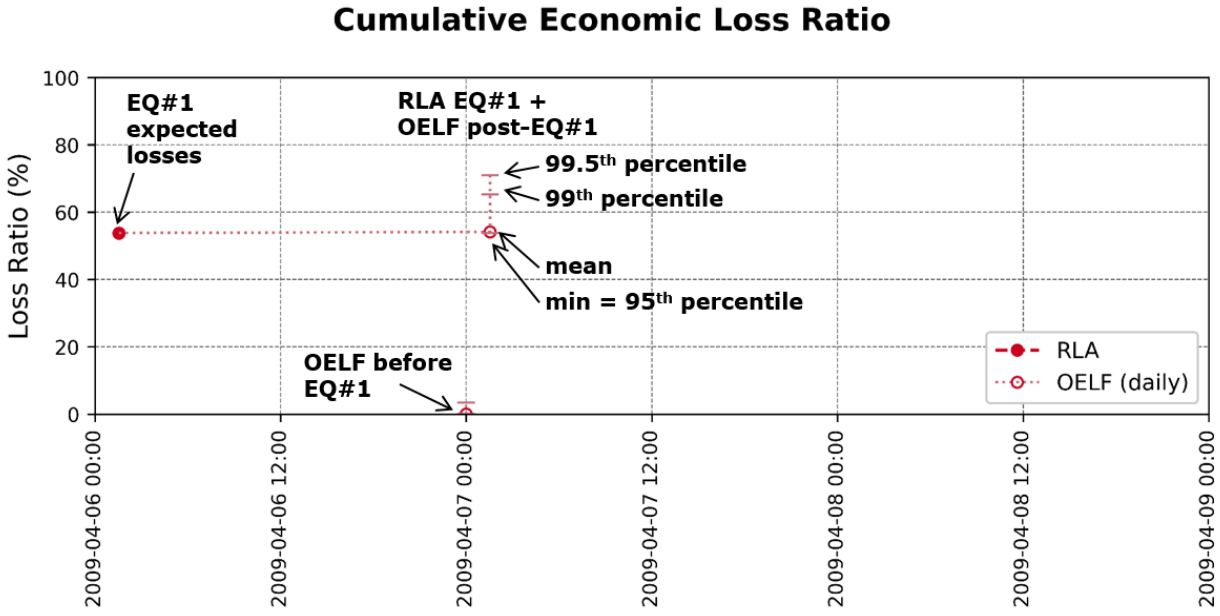

Figure 62 Cumulative economic loss ratios for the whole portfolio after the Mw 6.1 2009 L'Aquila main shock (RLA) and subsequent 24-hour seismicity forecast (OELF, depicted at the end of the 24-hour period).

It is noted that we are using the term "main shock" in these descriptions because the proof of concept is based on a past earthquake sequence for which the perspective of time has allowed seismologists to identify the main shock as such. However, this would not necessarily be the terminology used in a live application of a fully operational system, unless an algorithm able to predict whether any specific earthquake is expected to be the main shock of its sequence is implemented as well (e.g., Gulia and Wiemer, 2019). It is noted, nevertheless, that the very concept of a main shock is debatable, particularly in cases like the 2016-2017 Central Italy sequence, on which we focus in the coming sub-sections.

As the second shock of interest (Mw 5.1) hits on 6 April 2009 at 02:37 UTC (see Table 16), the overall expected proportion of damaged buildings raises from 84.8 % (Figure 58) to 85.7%, while the proportion of buildings in DS4 raises by 5.5% from 44.9% to 50.4% (Figure 63). As shown in Figure 64, the spatial pattern of damage probabilities does not change much with respect to that observed after the main shock (cf. Figure 57). The probabilities of damage for the three instrumented buildings stem once more from the SHM-based fragilities described in section 3.6.

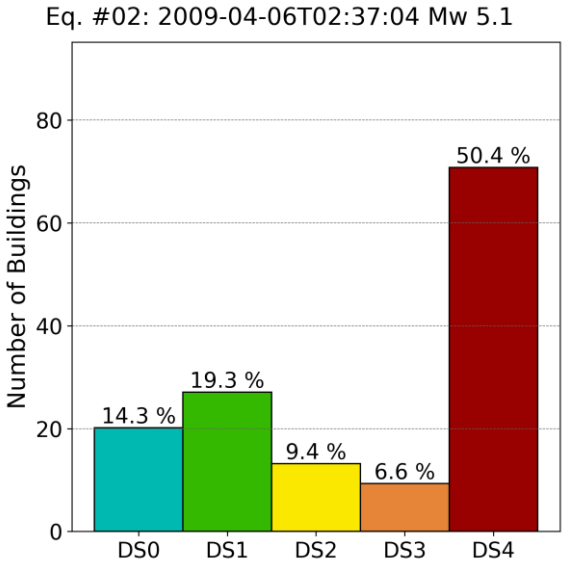

Figure 63 Expected cumulative aggregate number of buildings and probabilities per damage state at location 01 after the second shock of interest (Mw 5.1) of the 2009 L'Aquila sequence.

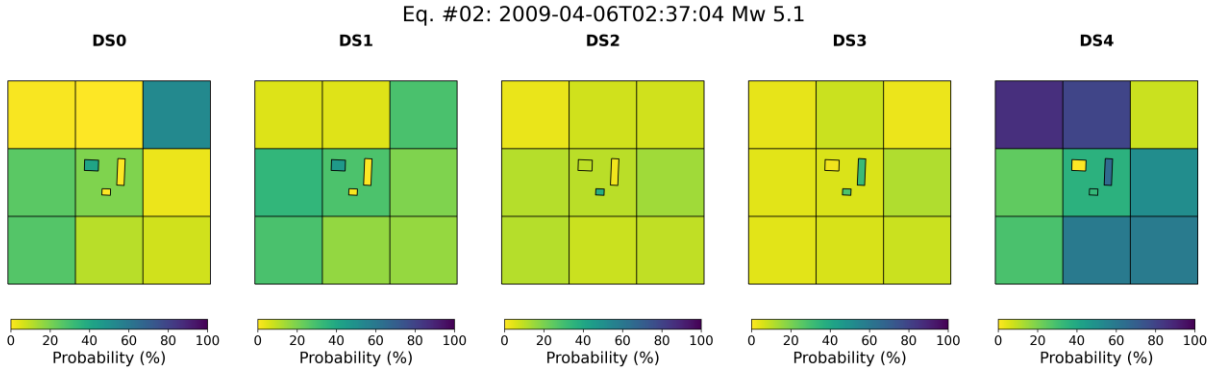

Figure 64 Expected cumulative probabilities of each damage state for each exposure tile and monitored building at location 01 after the second shock of interest (Mw 5.1) of the 2009 L'Aquila sequence.

These expected damage states lead to an expected total absolute loss of around 69.0 million EUR, which is 57.9% of the total value of all buildings in the exposure model and represents an increase of 4.1% with respect to the loss expected after the Mw 6.1 shock. The expected human casualties do not change after this second shock or indeed any of the eight events for which RLA calculations were carried out, as the number of occupants remains zero after the first shock for the rest of the

sequence, due to the short time intervals in between different earthquakes when compared against the minimum of 7 days set as needed for inspection of all buildings, including those without damage (see Table 6).

Just like before, a seismicity forecast is produced for the coming 24 hours and expected losses are calculated (see plot on the right of Figure 55). Expected human casualties do not increase for the same reasons just mentioned, but expected mean economic losses do amount to 69.9 million EUR, i.e. 58.7% of the total value of the building stock. Building up on Figure 62, Figure 65 shows these economic loss projections in time and in relation with the last "real" (as opposed to forecast) earthquake for which a RLA calculation was run. There is no connection between the two OELF empty dots because each OELF calculation refers to the last RLA expected losses. The 99th percentile of OELF economic losses rises up to 88.5 million EUR (74.3%).

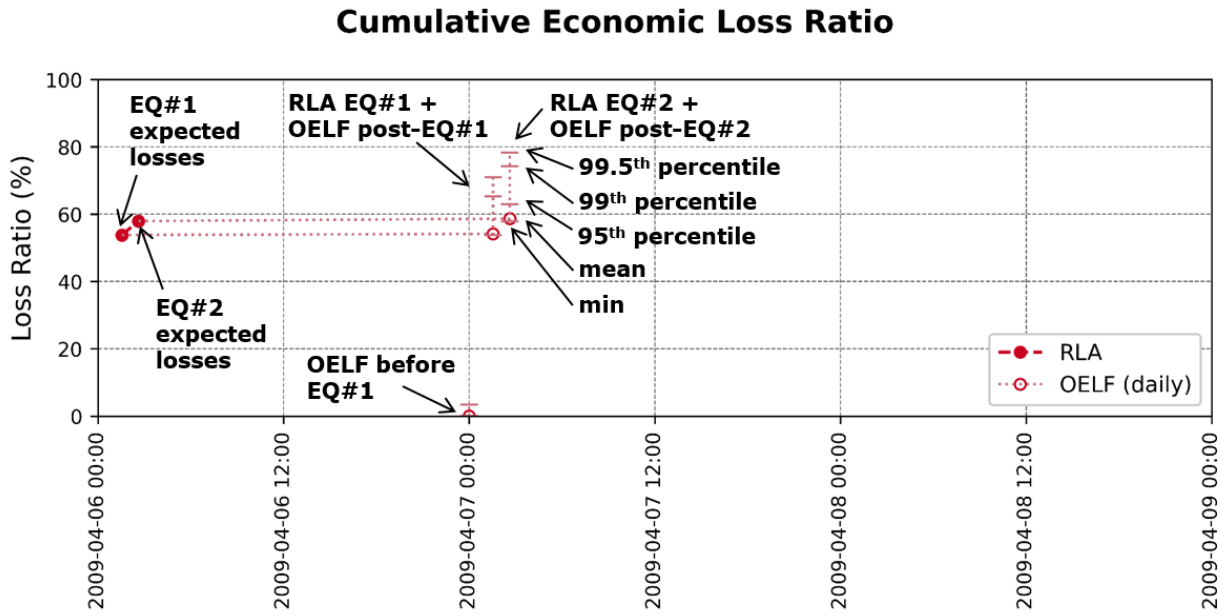

Figure 65 Cumulative economic loss ratios for the whole portfolio after the Mw 6.1 2009 L'Aquila main shock and Mw 5.1 second shock (RLA), and subsequent 24-hour seismicity forecasts (OELF, depicted at the end of the 24-hour periods).

The same sort of calculations are repeated after each of the earthquakes in Table 16 and their subsequent 24-hour seismicity forecasts. As shown in Figure 66, damage continues to increase in significant percentages until after the fifth earthquake, while the three remaining ones only contribute marginally to the overall final scenario. This is consistent with the larger distance between their respective epicentres and the location of the building stock (see Figure 51).

The accumulation of damage predicted by the SHM-based fragility models is very different for the three monitored buildings, as shown in Figure 67. Damage to the Budva hotel is not expected to evolve at all during the sequence. Damage to the Grenoble City Hall also seems dominated by the main shock, though an increase in the probability of DS4 from 57% to 65% is observed after the second shock. The Swiss building seems to be the most affected by the sequence, as the initial 34% probability of DS4 becomes almost certain DS4 after the fifth earthquake.

Figure 68 through Figure 70 are the continuation of Figure 62 and Figure 65 and show how the expected economic loss ratio evolves after each real earthquake and so do their associated 24-hour forecasts, with the final picture being presented in Figure 71. It is noted that the expected mean economic losses after each OELF carried out after the first four earthquakes appear as small in comparison to what actually follows in the sequence, due to the small likelihood of larger magnitude earthquakes. This observation led nevertheless to a check over the impact of the selection of the minimum earthquake magnitude used to run OELFs. As will be explained in section 0, our analysis shows that these seemingly low forecast losses are not attributable to this decision.

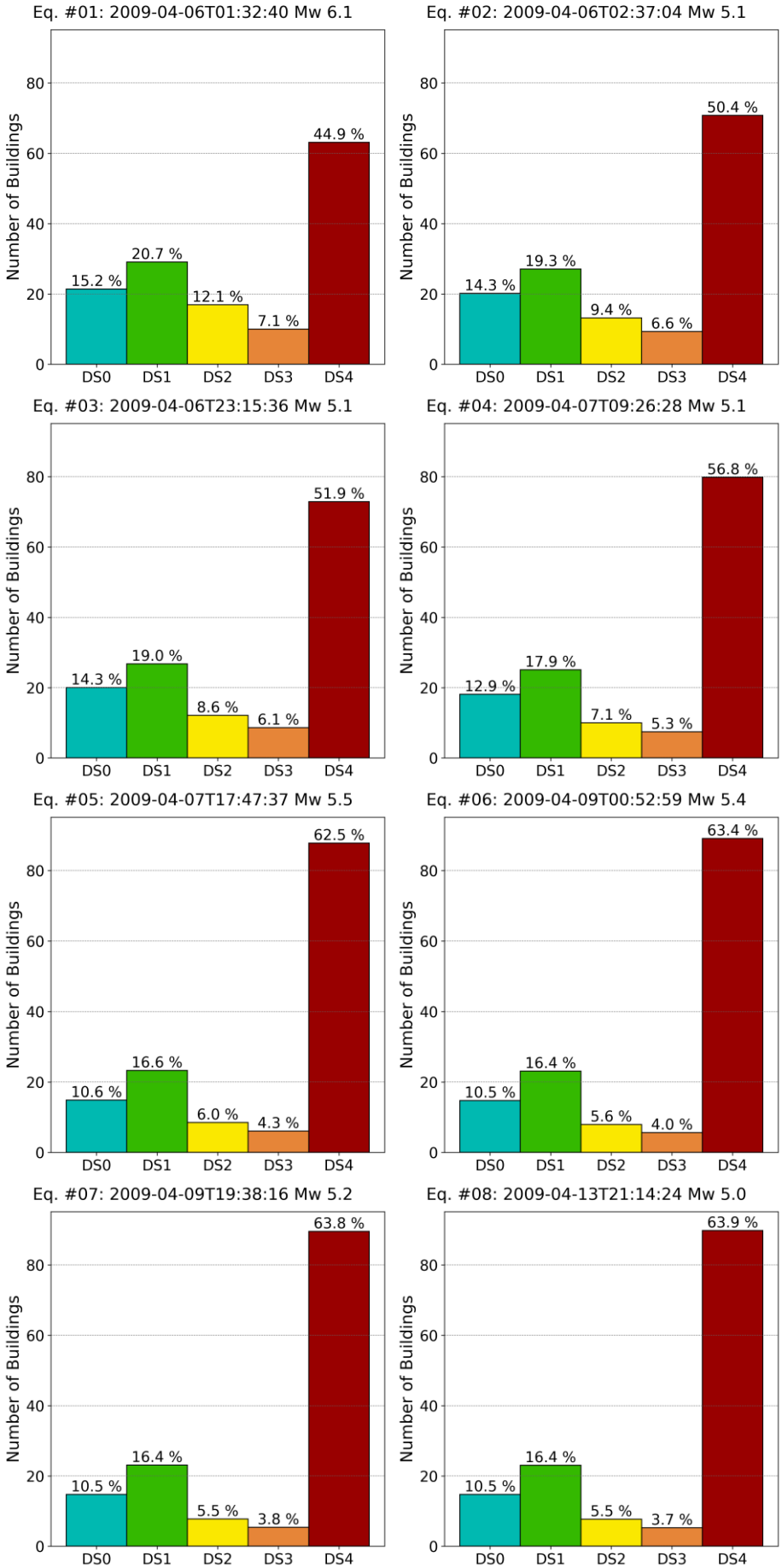

Figure 66 Expected cumulative aggregate number of buildings and probabilities per damage state at location 01 after each earthquake of interest of the 2009 L'Aquila sequence (see Table 16).

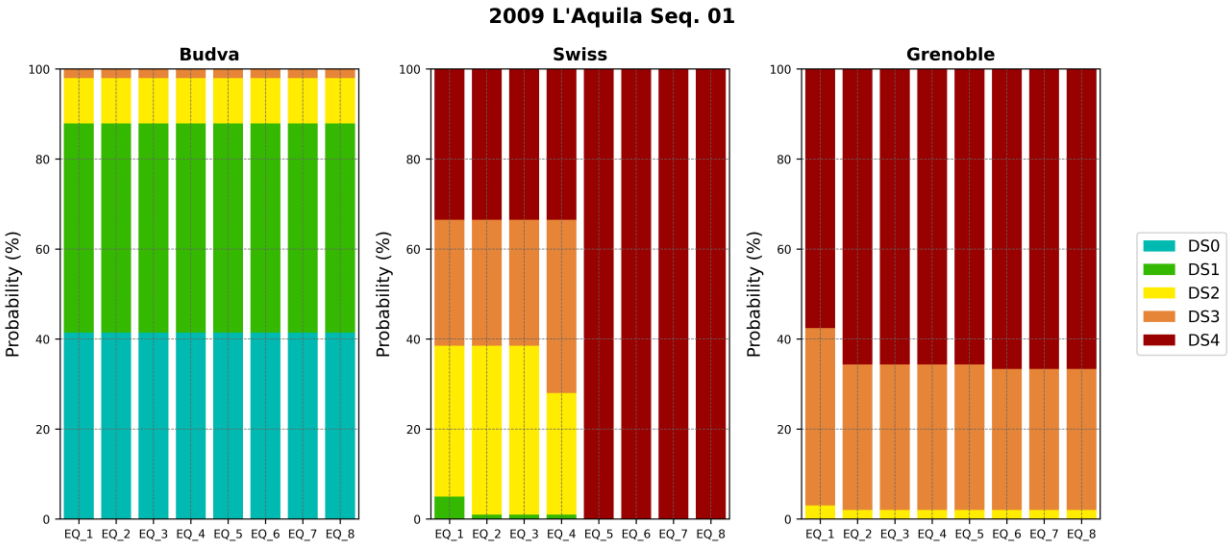

Figure 67 SHM-derived damage probabilities for each of the three monitored buildings at location 01 after each of the eight earthquakes of the 2009 L'Aquila sequence.

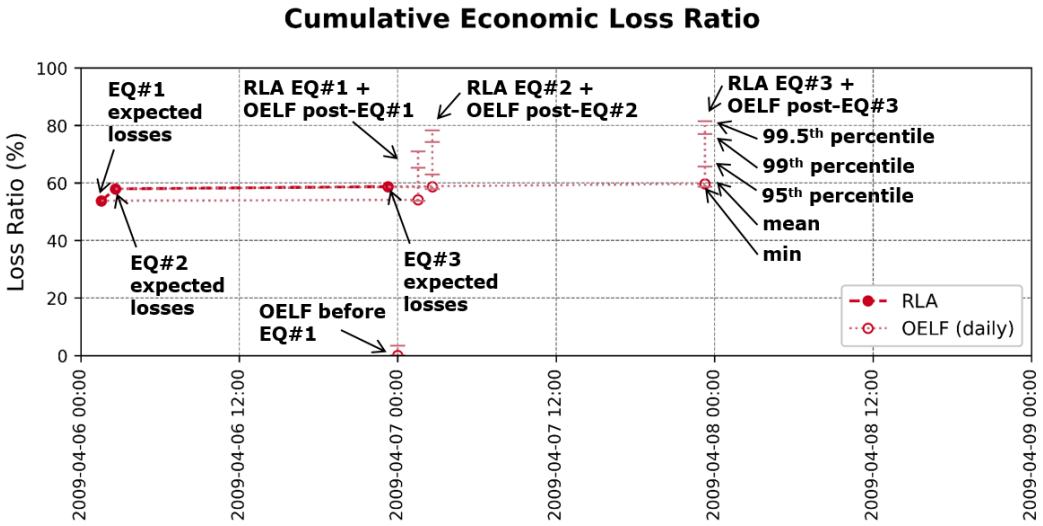

Figure 68 Cumulative economic loss ratios after the first three shocks of the 2009 L'Aquila sequence for which RLAs were conducted, and subsequent 24-hour seismicity forecasts (OELF, depicted at the end of the 24-hour periods).

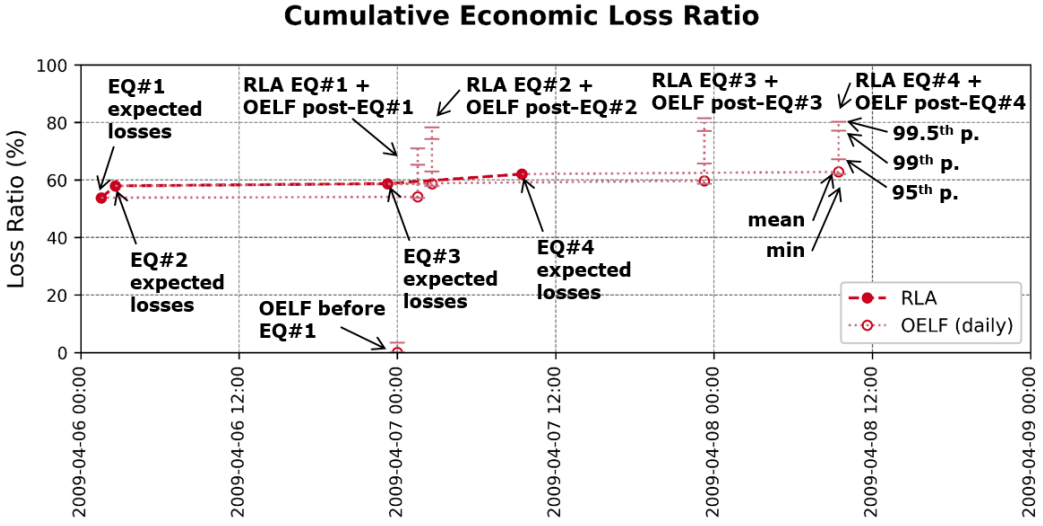

Figure 69 Cumulative economic loss ratios after the first four shocks of the 2009 L'Aquila sequence for which RLAs were conducted, and subsequent 24-hour seismicity forecasts (OELF, depicted at the end of the 24-hour periods).

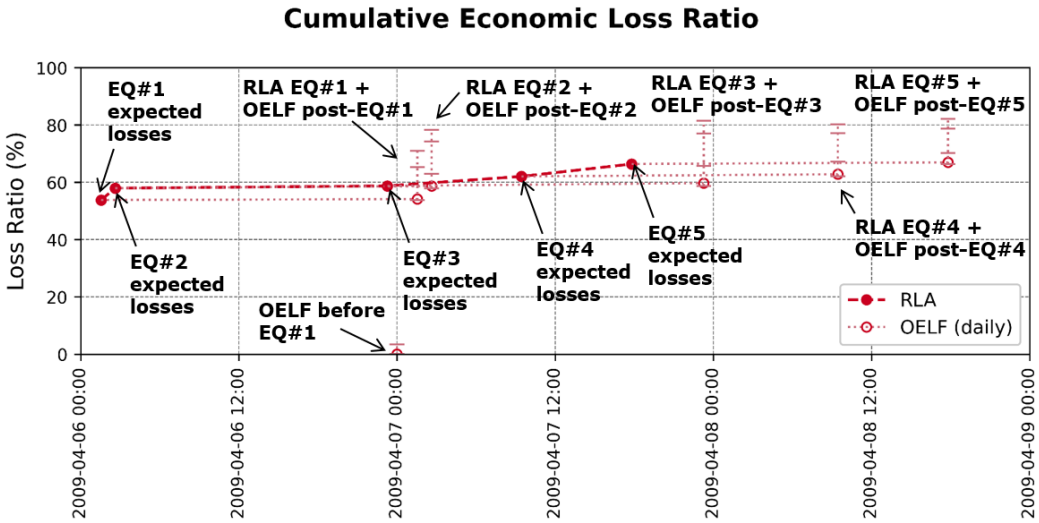

Figure 70 Cumulative economic loss ratios after the first five shocks of the 2009 L'Aquila sequence for which RLAs were conducted, and subsequent 24-hour seismicity forecasts (OELF, depicted at the end of the 24-hour periods).

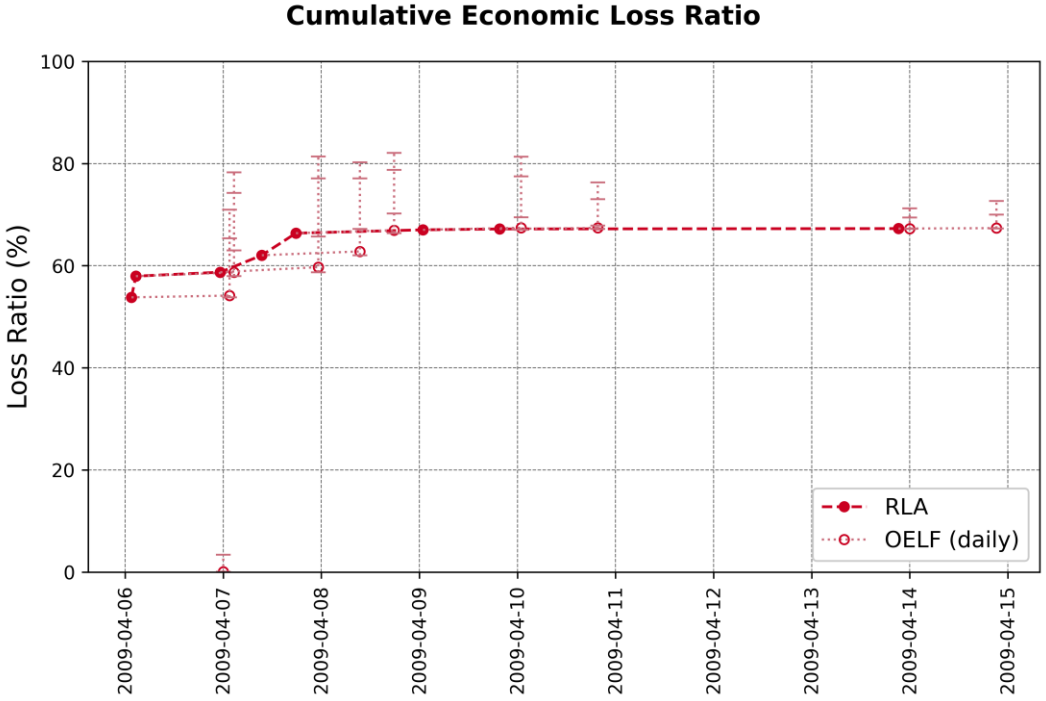

Figure 71 Cumulative economic loss ratios after all eight shocks of the 2009 L'Aquila sequence for which RLAs were conducted, and subsequent 24-hour seismicity forecasts (OELF, depicted at the end of the 24-hour periods). Vertical error bars show, in order from bottom to top, minimum, mean, 95th, 99th and 99.5th percentiles of loss ratio associated with each OELF.

Figure 72 shows the relative contribution of each earthquake in the sequence to the overall expected economic loss ratio. As can be observed, most of the losses are caused by the first shock (64 million EUR, 53.8% of the total value of the building stock) but the subsequent four earthquakes do contribute significantly to further losses building up, reaching up to 82.9 million EUR (69.6% of the total value of the building stock).

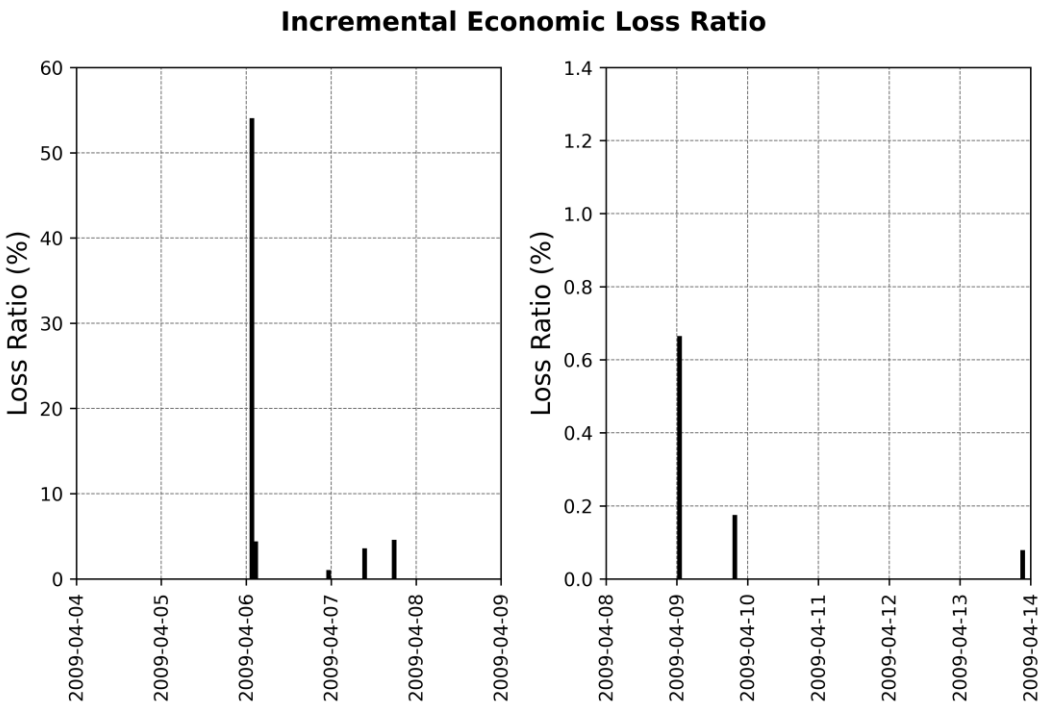

Figure 72 Incremental economic loss ratios after all eight shocks of the 2009 L'Aquila sequence for which RLAs were conducted (note the different scales used for the vertical axes).

Figure 73 and Figure 74 show the evolution of the damage probability per tile and instrumented building, while Figure 75 shows the expected economic loss ratios after the first, third, fourth and eighth shocks.

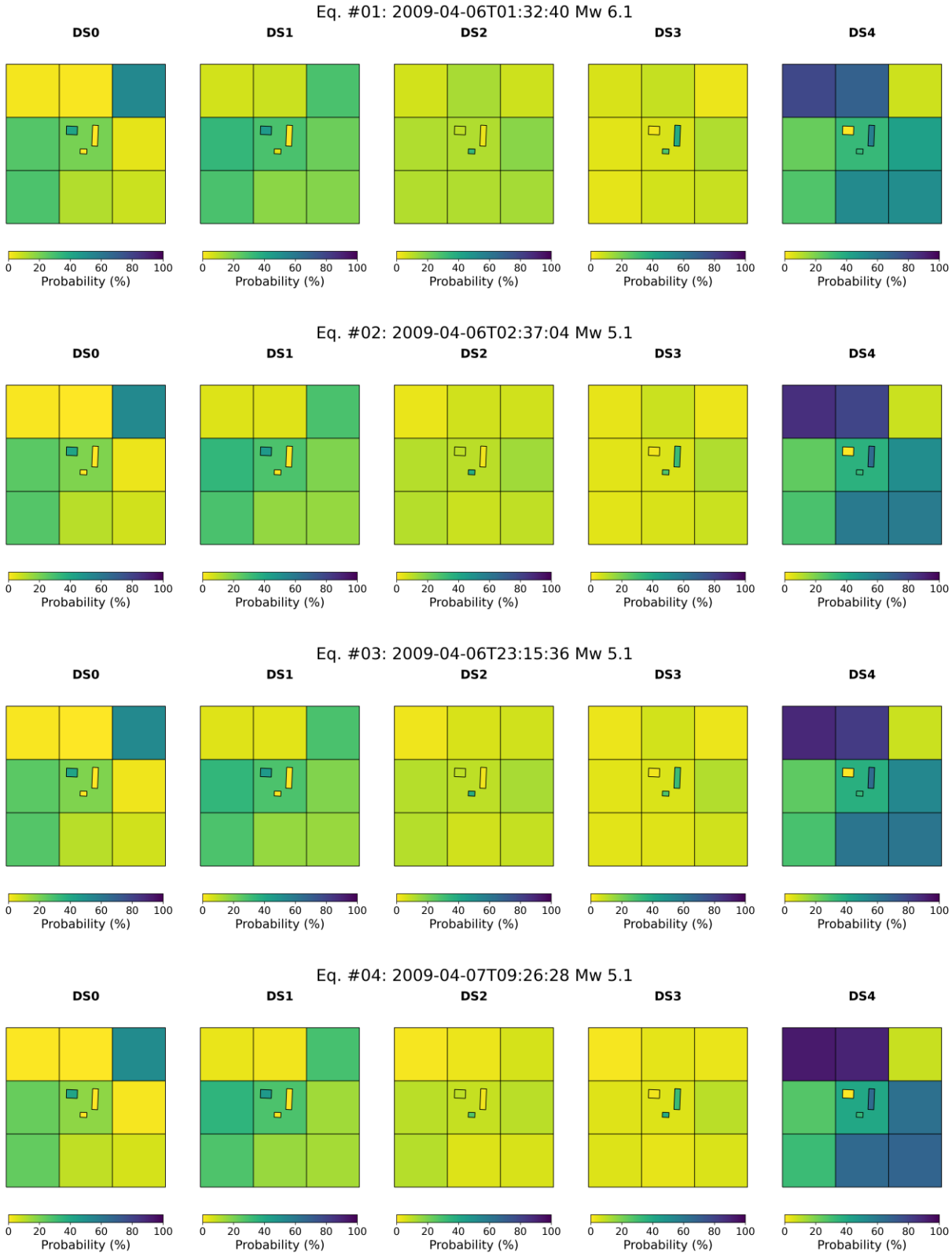

Figure 73 Expected cumulative probabilities of each damage state for each exposure tile and monitored building at location 01 after each of the first four shocks of interest of the 2009 L'Aquila sequence.

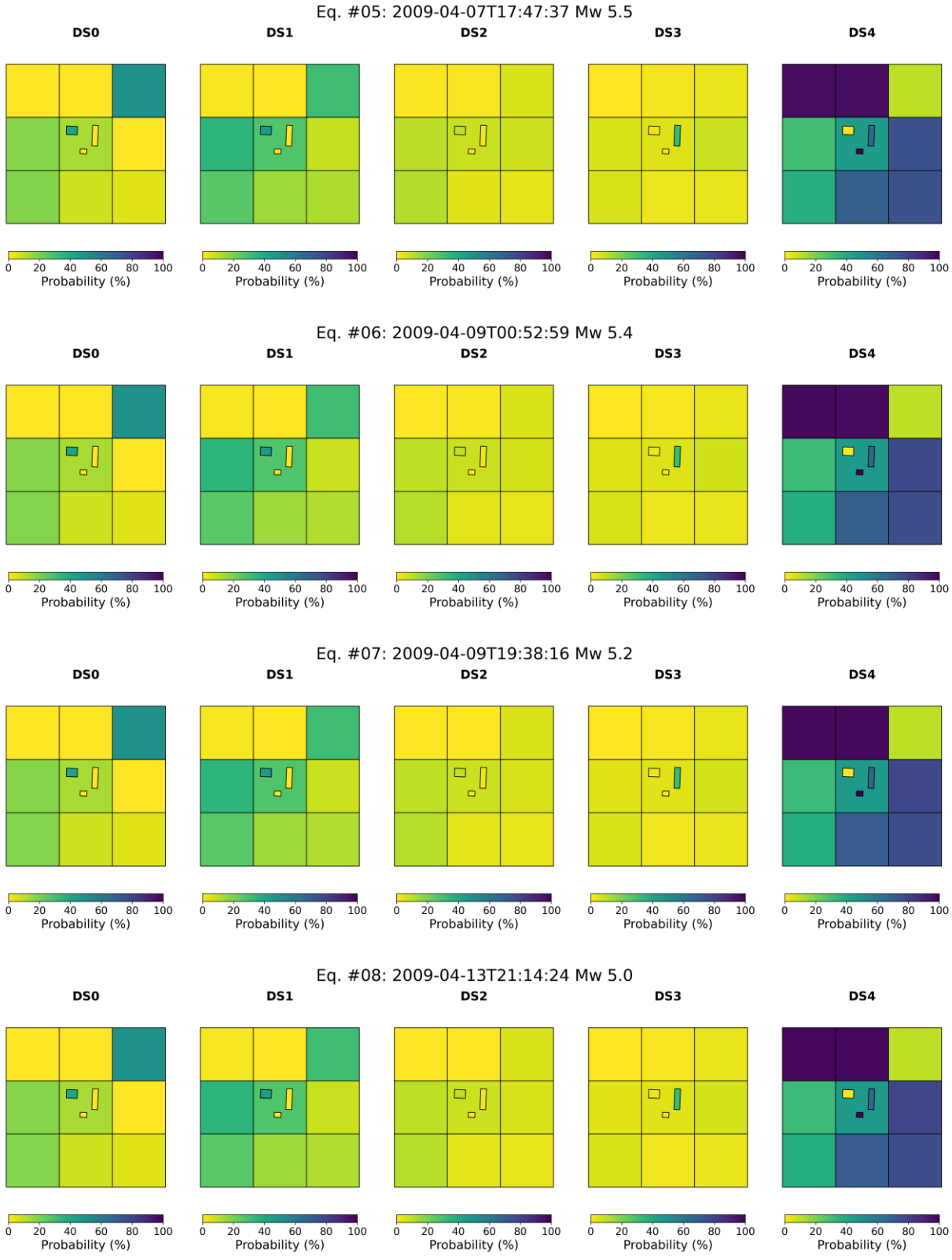

Figure 74 Expected cumulative probabilities of each damage state for each exposure tile and monitored building at location 01 after each of the last four shocks of interest of the 2009 L'Aquila sequence.

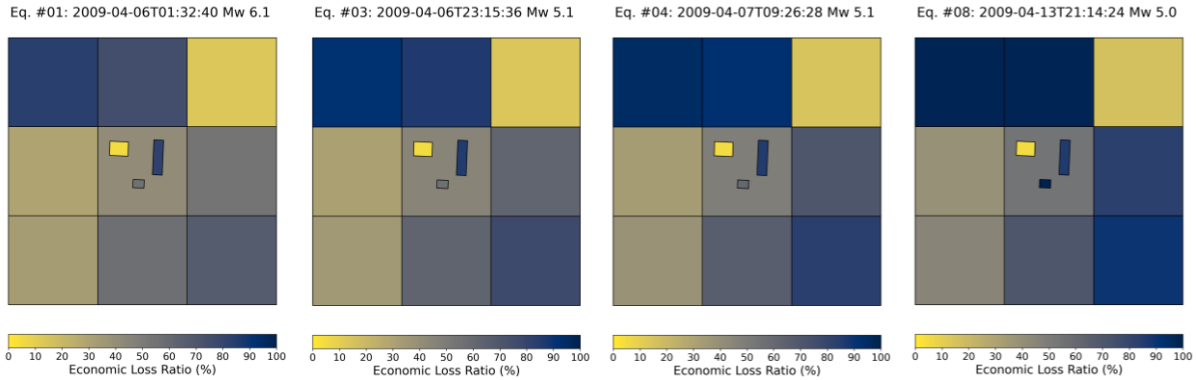

Figure 75 Expected economic loss ratios per tile and instrumented building after the first, third, fourth and eight earthquakes of the 2009 L'Aquila sequence for which RLAs were carried out.

5.3 Case-study 2: 2016-2017 Central Italy sequence at location 12

Similarly to the previous one, this case-study starts with a 1-day seismicity forecast generated at 00:00:00 UTC on 24 August 2016, a bit over an hour and a half before the first shock with moment magnitude of 5 and above of the 2016-2017 Central Italy sequence (see Table 17). A concentration of seismicity can be observed in this forecast over what would become the rupture of the Mw 6.0 and further north and north-west of it, as shown in Figure 76 (magnitude distribution shown in plot on the left of Figure 77). The forecast includes a Mw 6.8 directly to the north of the epicentre of the Mw 6.0 that did occur, a Mw 6.1, and six earthquakes in the range Mw 5.8-6.0 around the area. The mean expected economic loss ratio calculated starting from the assumption of an undamaged building portfolio is 0.01%, and only 29 out of the 10,000 stochastic event sets produce losses larger than zero (running OELF for earthquakes with Mw ≥ 5).

The first earthquake with Mw ≥ 5.0 to take place is the Mw 6.0 of 24 August 2016 at 01:36 UTC. The damage resulting from it is not very different from that resulting from the Mw 6.1 L'Aquila main shock, particularly regarding the buildings aggregated in the tiles (compare Figure 78 against Figure 56). However, the SHM-derived damage probabilities for the monitored buildings shown in Figure 79 are substantially different from those in Figure 57: the Budva hotel and Grenoble City Hall are expected to suffer less damage with the first earthquake of the Central Italy sequence (at location 12) than with the L'Aquila main shock (at location 01), while the Swiss building presents larger probabilities of DS3 and DS4 with the first earthquake of the Central Italy sequence (at location 12). For the building stock as a whole, the probability of DS4 is slightly lower in this case than for L'Aquila (at location 01), but the overall distribution of damage probabilities is very similar (compare Figure 80 against Figure 58).

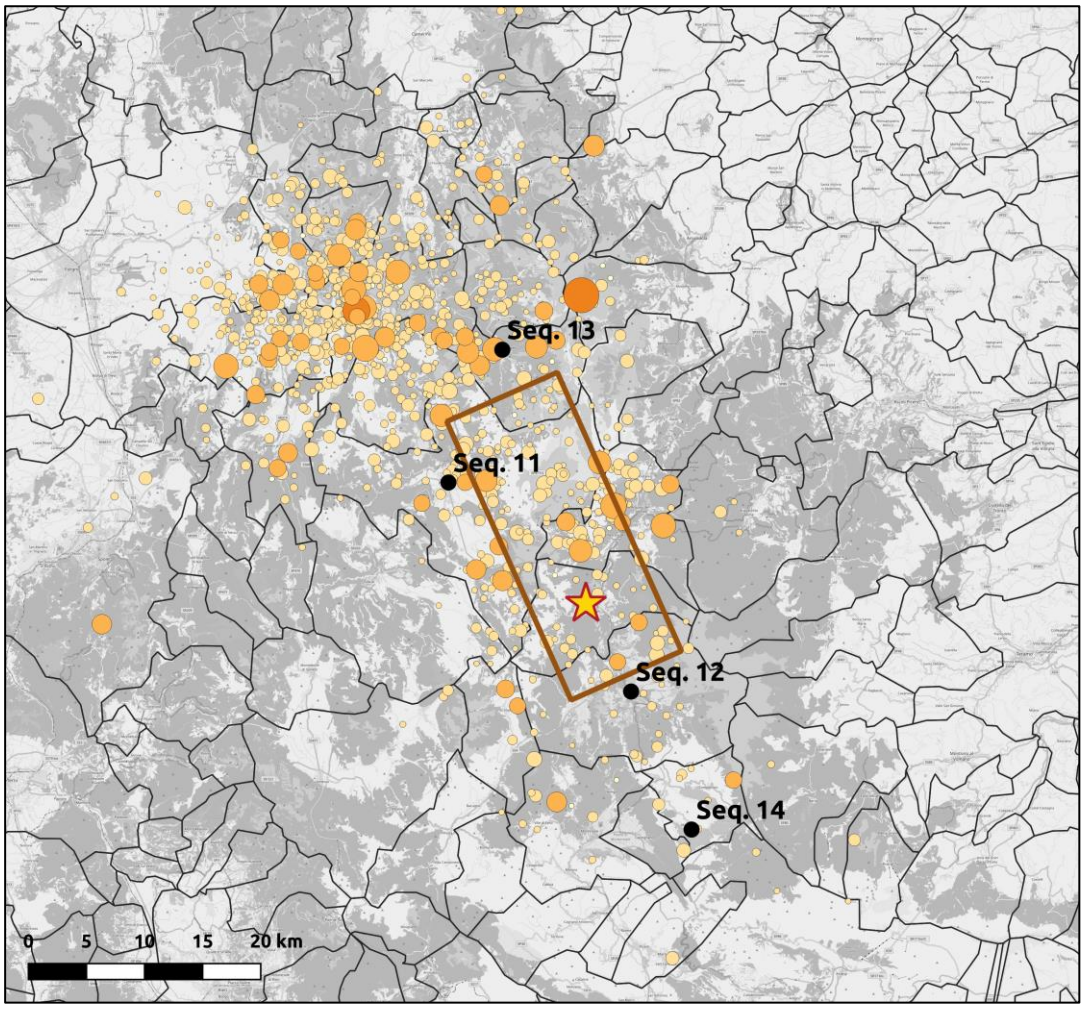

Figure 76 One-day seismicity forecast (10,000 realisations, Mw ≥ 3.99) around the towns of Norcia and Amatrice generated at 00:00:00 of 24 August 2016, around 96 minutes before the Mw 6.0 shock of that same day (yellow star, rupture in brown). Background: OpenStreetMap.

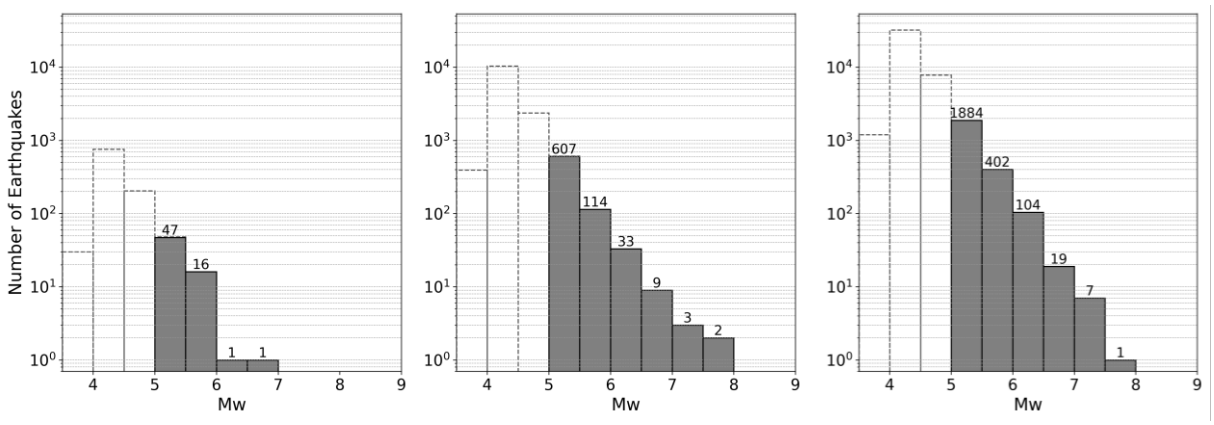

Figure 77. Number of earthquakes per magnitude bin of the daily forecast generated at 00:00 UTC (left), after the first shock (centre) and after the second shock (right) of 24 August 2016. Dotted bars show the complete forecasts (Mw≥3.99) while filled bars show the forecasts filtered for the running of OELF calculations at location 01 (Mw≥5.0, 200 km maximum epicentral distance).

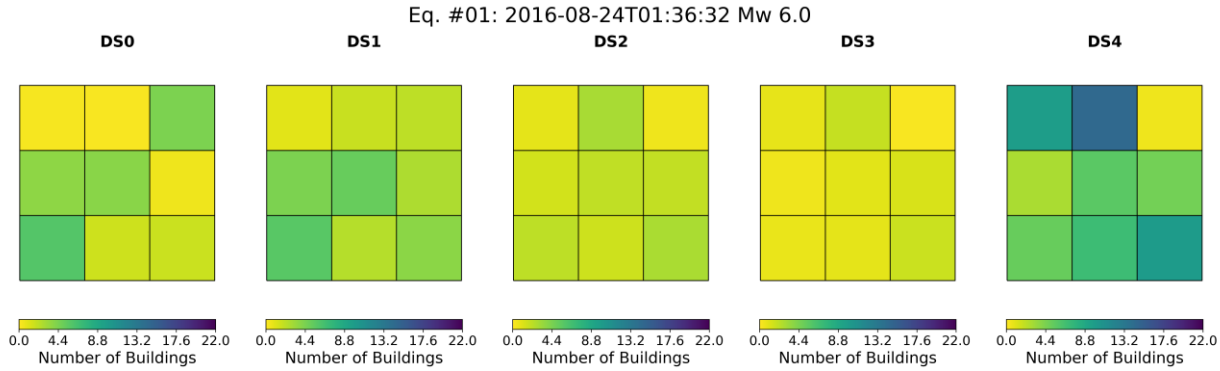

Figure 78 Expected number of buildings per damage state in each exposure tile at location 12 due to the Mw 6.0 first Mw≥5 shock of the 2016-2017 Central Italy sequence.

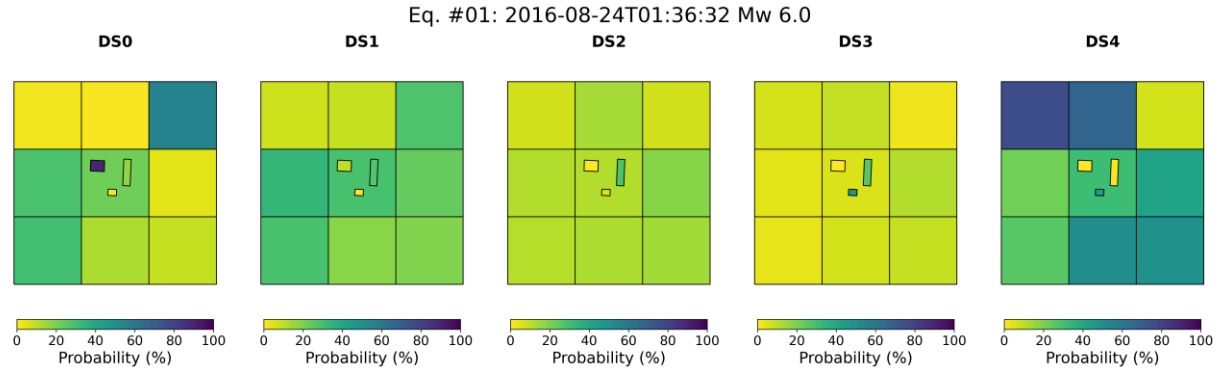

Figure 79 Expected probabilities of each damage state for each exposure tile and monitored building at location 12 due to the Mw 6.0 first Mw≥5 shock of the 2016-2017 Central Italy sequence.

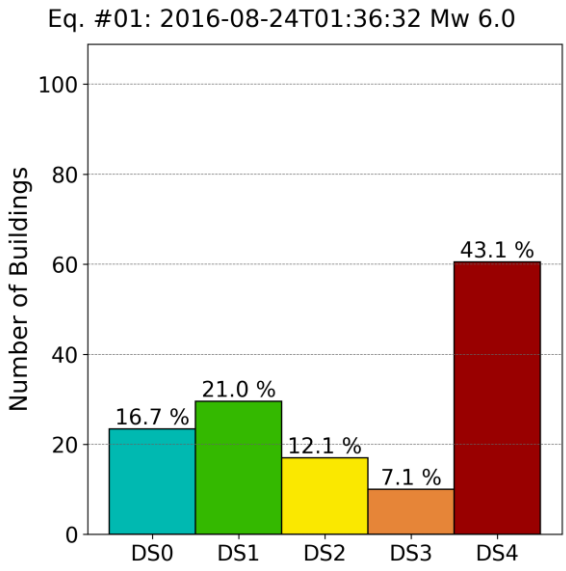

Figure 80 Expected aggregate number of buildings and probabilities per damage state at location 12 due to the Mw 6.0 first Mw≥5 shock of the 2016-2017 Central Italy sequence.

The expected absolute economic loss after this first earthquake is around 48 million EUR, which is 40.1% of the total value of all buildings in the exposure model, and substantially smaller than that calculated after the main shock of the first case-study, due mostly to the change in the damage probabilities of the three instrumented buildings. The distribution of the economic losses across different tiles and buildings is depicted in Figure 81.

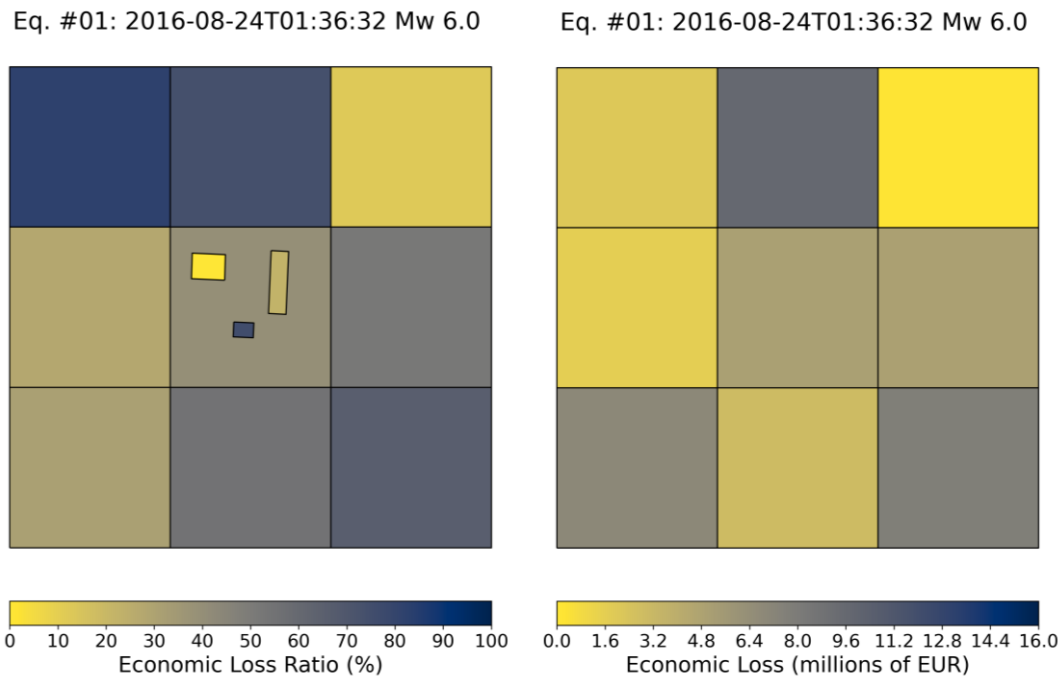

Figure 81 Expected economic loss ratios (left) and economic loss in EUR (right, only tiles) due to the Mw 6.0 first shock of the 2016-2017 Central Italy sequence at location 12.

The expected human casualties are not very different for this case-study with respect to the previous one either: 54.34 people (2.91% of the census occupants) are expected to suffer from injuries of severity 1, which require only basic medical aid in the field, while 10.66, 0.44 and 6.82 people (0.57%, 0.02% and 0.37% of the census occupants, respectively) are expected to suffer from injuries of severity 2 (non-life-threatening but requiring medical technology), 3 (immediately life-threatening) and 4 (instantaneously killed or mortally injured). This is due not only to the similarities in terms of the expected damage distribution but also to the fact that both earthquakes occurred during the night time, and the buildings for which larger differences are observed in the damage probabilities are the Budva hotel and the Grenoble City Hall, whose occupancy factor at night time is around 4% of the census number of occupants (the reader is reminded that hotel guests are not modelled in this proof of concept). As in the case of Figure 60, larger human casualty ratios are expected in tiles with a larger proportion of masonry structures than in those populated mostly with reinforced concrete moment-resisting frames (see Figure 82).

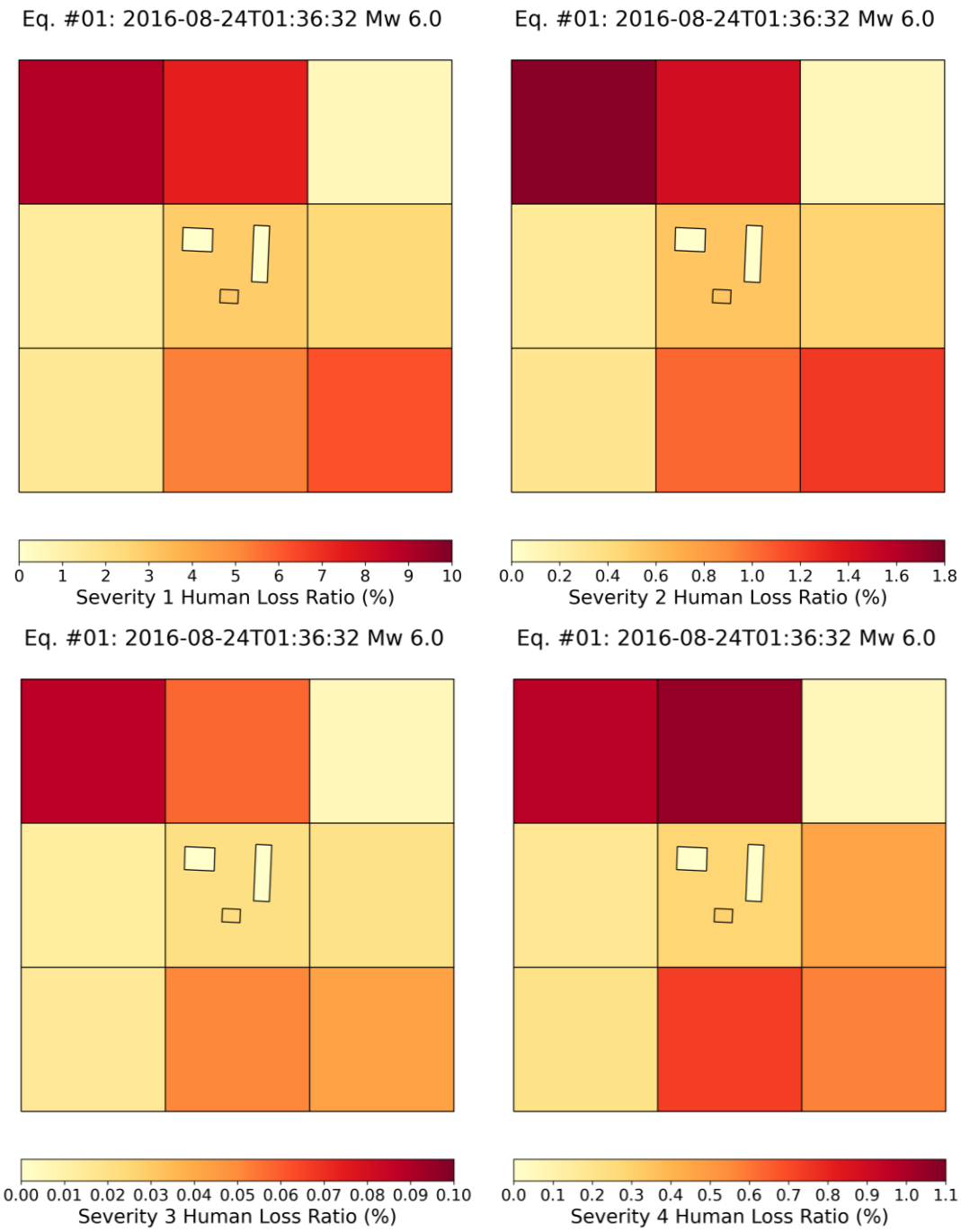

Figure 82 Expected ratios of census occupants injured with different severity levels due to the Mw 6.0 first shock of the 2016-2017 Central Italy sequence at location 12.

As before, the occurrence of this first shock of interest leads to the calculation of a seismicity forecast for the coming 24 hours, whose epicentres around the area affected by the Mw 6.0 event are shown in Figure 83 and whose magnitude distribution is depicted in the central plot of Figure 77. The mean expected cumulative economic loss due to these 10,000 realisations of seismicity is around 48.5 million EUR, which is 40.7% of the total value of all buildings in the exposure model and represents only a 0.61% increase with respect to the expected economic loss after the first real shock. Individual stochastic sets of seismicity predict up to 117 million EUR of economic loss, which is 98.4% of the total value of the building stock, with the 99th percentile of OELF economic losses being around 67.4 million EUR (56.6%).

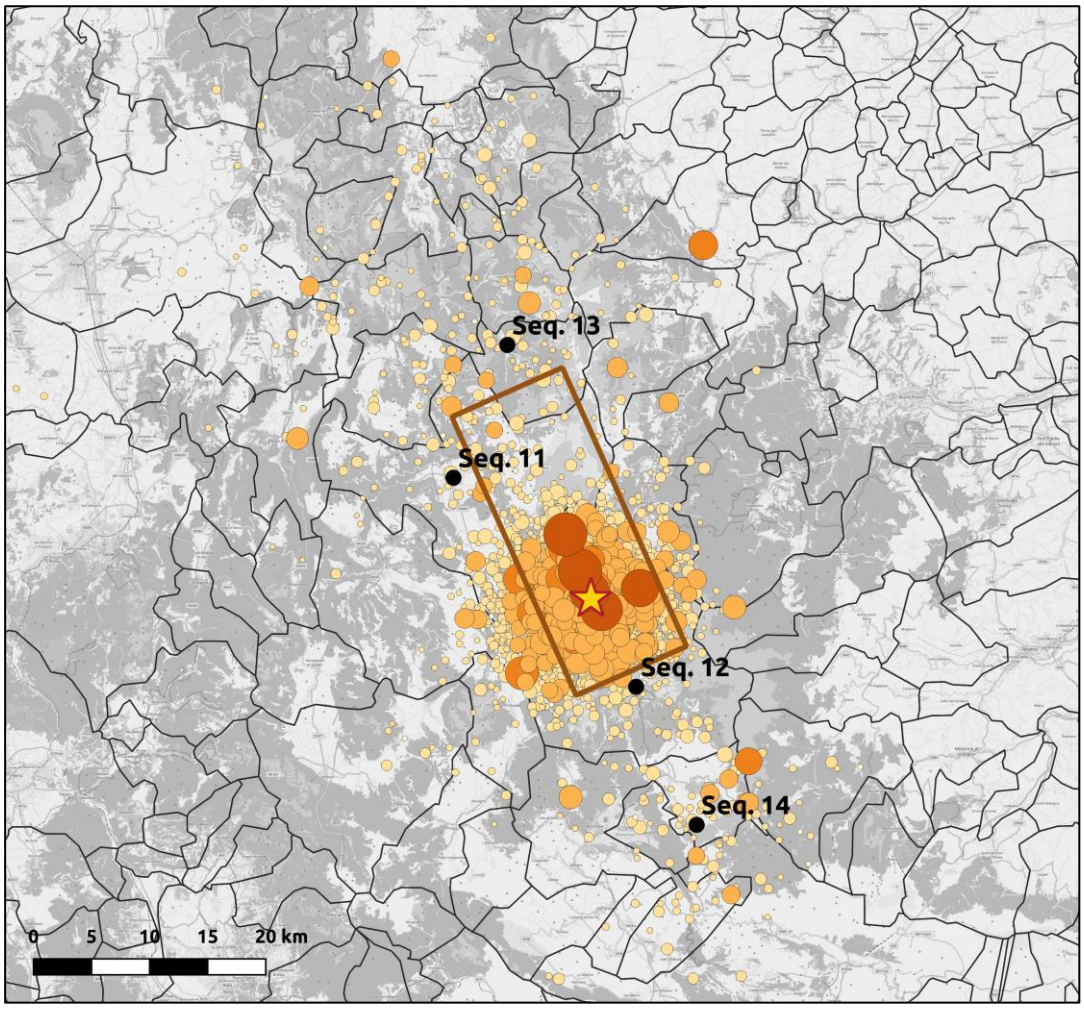

Figure 83 One-day seismicity forecast (10,000 realisations, Mw ≥ 3.99) around the towns of Norcia and Amatrice generated right after the Mw 6.0 earthquake of 24 August 2016 at 01:36 (yellow star, rupture in brown). Background: OpenStreetMap.

As the time span of the seismicity forecast is 24 hours, no additional human casualties are predicted due to the update in the number of occupants in the buildings after the first shock and the minimum seven days for inspection defined in Table 6. However, and in contrast with the case of the L'Aquila sequence for which occupants were present only for the first RLA and first OELF, occupants are allowed back into the buildings (by the timelines defined in section 3.9.2) at two points in time during the Central Italy sequence: in between the second and third earthquakes (i.e., in between 24 August and 26 October 2016), and in between the fifth and sixth earthquakes (i.e., in between 30 October 2016 and 18 January 2017). This is reflected in the RLAs for earthquakes number 3 and 6 as well as OELFs number 4 and 8 including occupants in buildings (see RLA-OELF timeline in Figure 53). Figure 84 through Figure 87 depict the incremental human casualty ratios for each severity level after each RLA. The total number of occupants for the whole building stock is 1334.75 people for the first earthquake (night time), 291 people for the third earthquake (transit time) and 171 people for the sixth earthquake (day time). As the ratios are so small and the number of occupants decreases drastically for earthquakes number 3 and 6, the initial casualties of 54.34 (2.91%) people for severity 1, 10.66 (0.57%) people for severity 2, 0.44 (0.02%) for severity 3, and 6.82 (0.37%) people for severity 4 only increase to 54.92 (2.94%), 10.72 (0.57%), 0.44 (0.02%), and 6.82 (0.37%) by the end of the sequence.

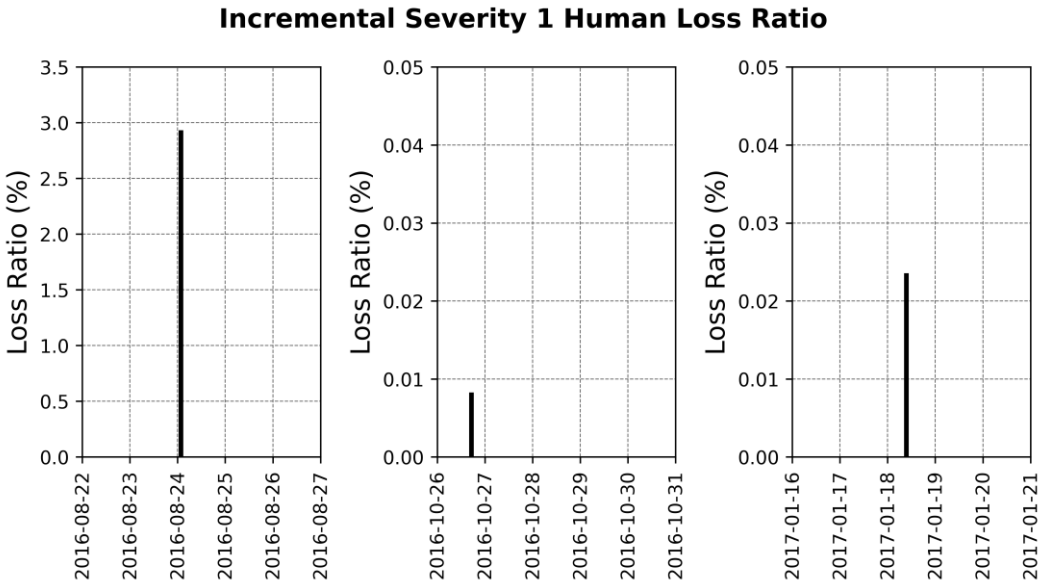

Figure 84 Incremental severity 1 human casualty ratios at location 12 after all nine shocks of the 2016-2017 Central Italy sequence for which RLAs were conducted (different vertical scales used).

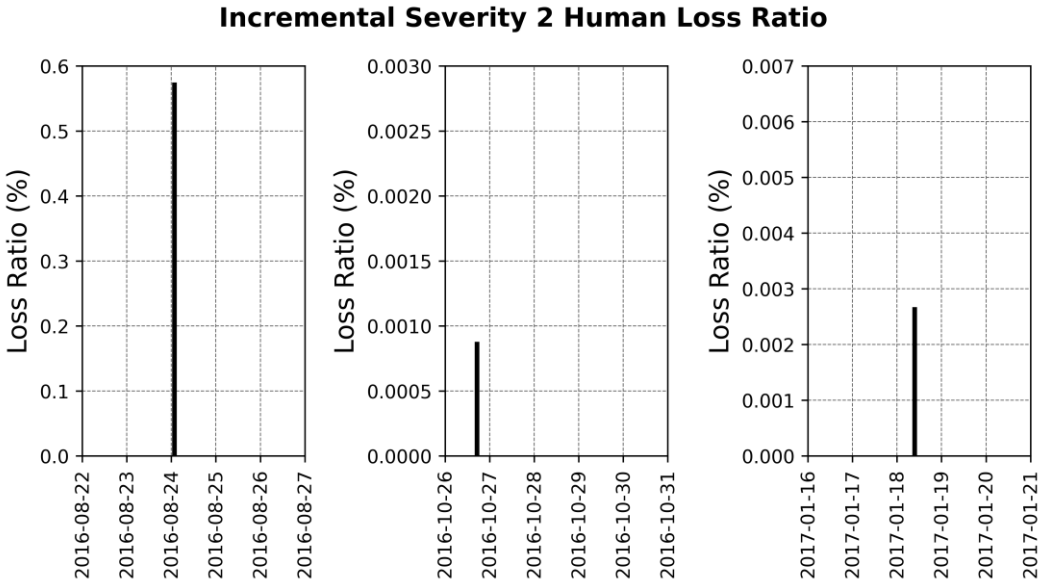

Figure 85 Incremental severity 2 human casualty ratios at location 12 after all nine shocks of the 2016-2017 Central Italy sequence for which RLAs were conducted (different vertical scales used).

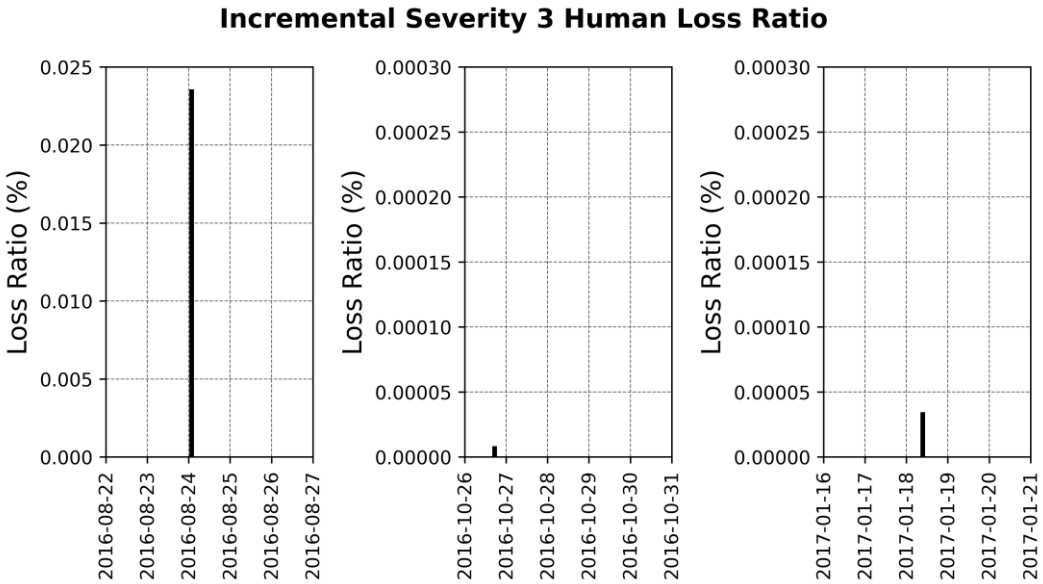

Figure 86 Incremental severity 3 human casualty ratios at location 12 after all nine shocks of the 2016-2017 Central Italy sequence for which RLAs were conducted (different vertical scales used).

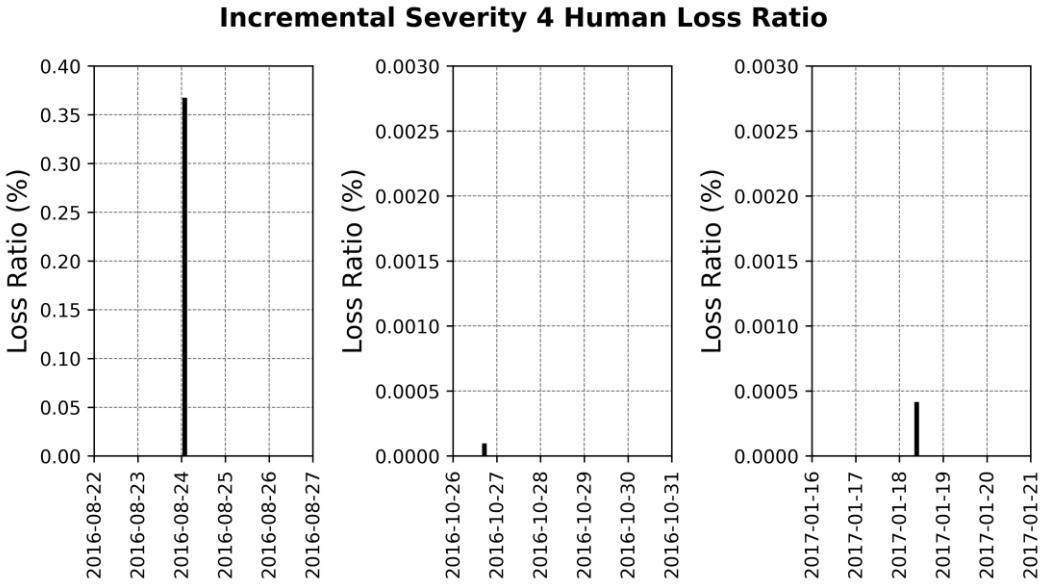

Figure 87 Incremental severity 4 human casualty ratios at location 12 after all nine shocks of the 2016-2017 Central Italy sequence for which RLAs were conducted (different vertical scales used).

As the sequence progresses, a fundamental difference with respect to the L'Aquila case analysed in the previous section becomes evident: there are three main points in time in which the damage and economic losses increase significantly, while in L'Aquila most of the damage and losses occur during the first earthquakes of the sequence and the later ones have a reduced influence on the final outcome. The fifth earthquake, the strongest in the sequence (Mw 6.5), causes an important jump in the proportion of buildings expected to suffer from DS4, which increases from 48.8% to 64.4%, as depicted in Figure 88, which consequently results in a jump in the expected losses from around 51.9 million (43.5% of the total building stock) to 66.9 million EUR (56.2%), as shown in Figure 89 and Figure 90 in terms of cumulative values and in Figure 91 in terms of incremental contributions from each earthquake. All these show a significant increase in damage and losses after the seventh shock (Mw 5.5) as well: expected economic losses rise from 68.0 million to 73.8 million EUR, which is from 57.1% to 62.0% of the value of the total building stock. The influence of the fifth shock is

clear in the SHM-derived damage probabilities for the three monitored buildings, while the seventh appears to have less of an impact (Figure 92).

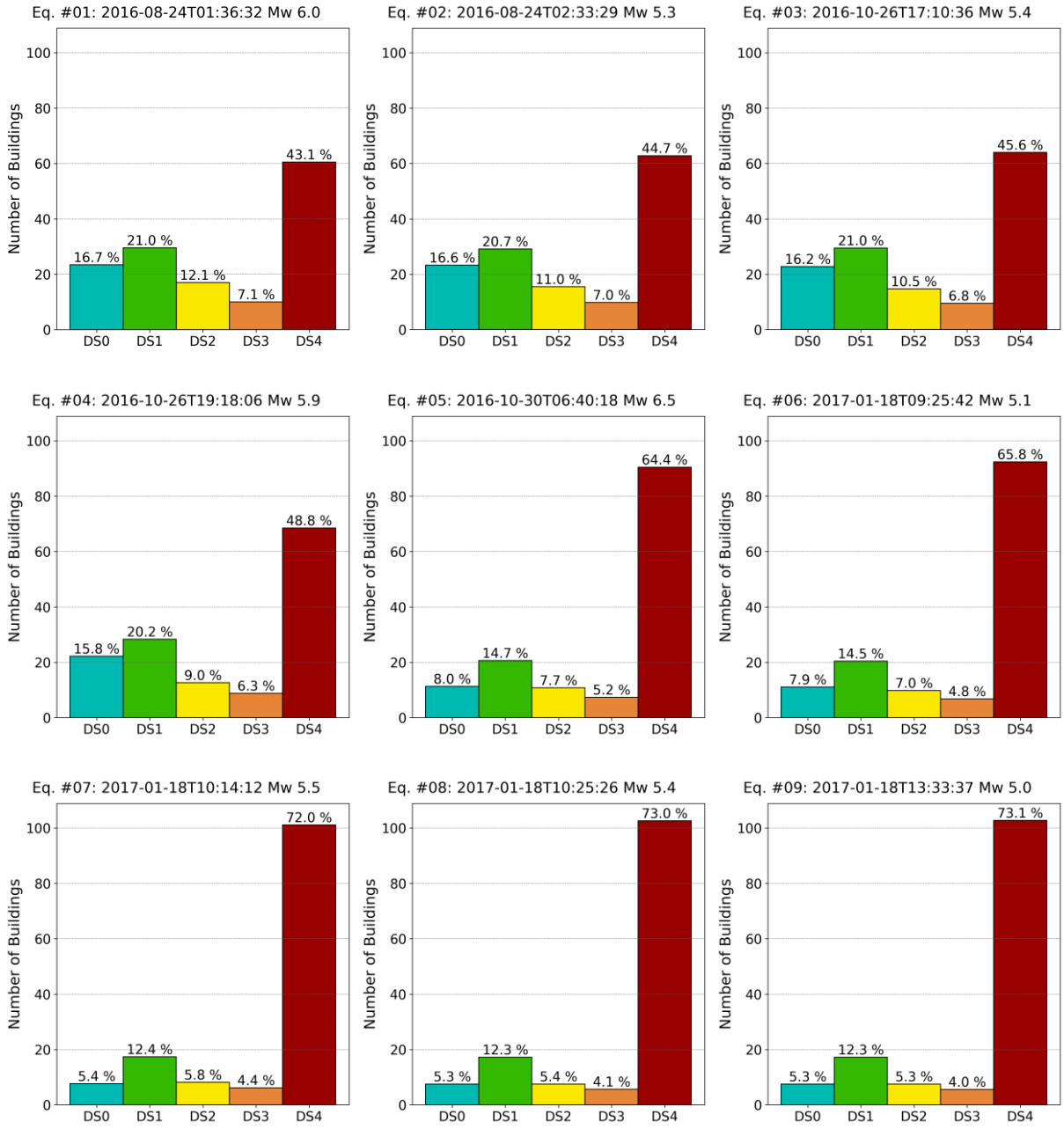

Figure 88 Expected cumulative aggregate number of buildings and probabilities per damage state at location 12 after each earthquake of interest of the 2016-2017 Central Italy sequence (see Table 17).

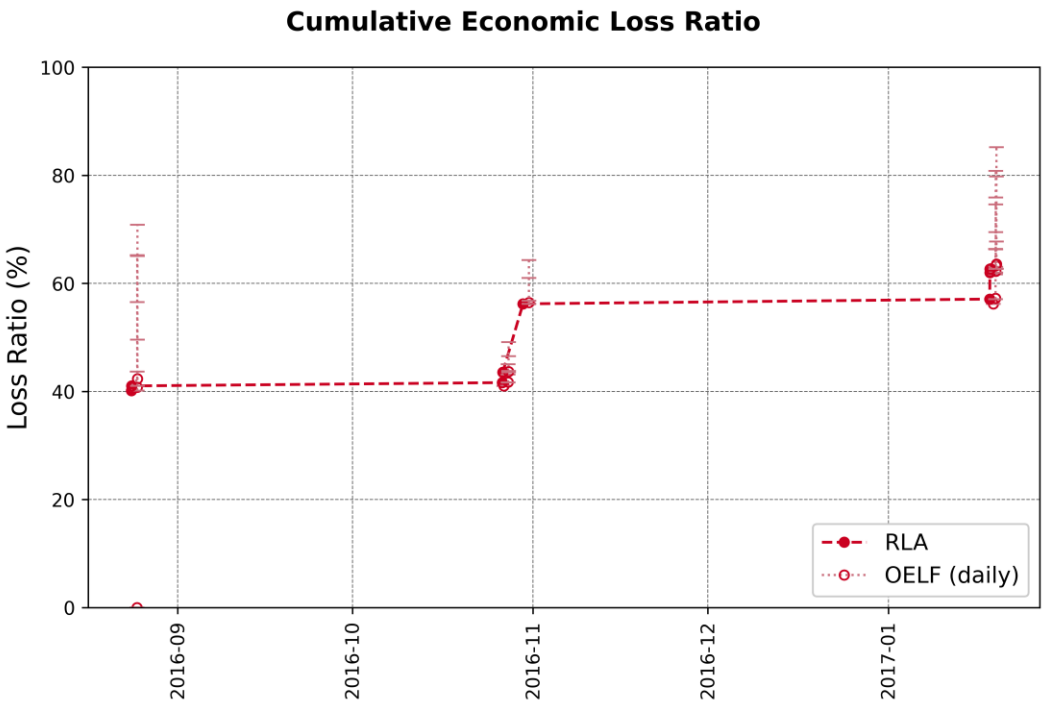

Figure 89 Cumulative economic loss ratios at location 12 after all nine shocks of the 2016-2017 Central Italy sequence for which RLAs were conducted, and subsequent 24-hour seismicity forecasts (OELF, depicted at the end of the 24-hour periods). Vertical error bars show, in order from bottom to top, minimum, mean, 95th, 99th and 99.5th percentiles of loss ratio associated with each OELF. See details in Figure 90.

Figure 90 allows to look into more detail at what happens within each of the three clusters of earthquakes in the sequence (August 2016, October 2016, January 2017) in terms of expected economic losses after each RLA and OELF. In general, the jumps in losses observed after carrying out each RLA only seem to be captured by the upper percentiles of the OELFs, whose mean expected values tend to be low, except at the beginning of the sequence (see first sub-plot in Figure 90).

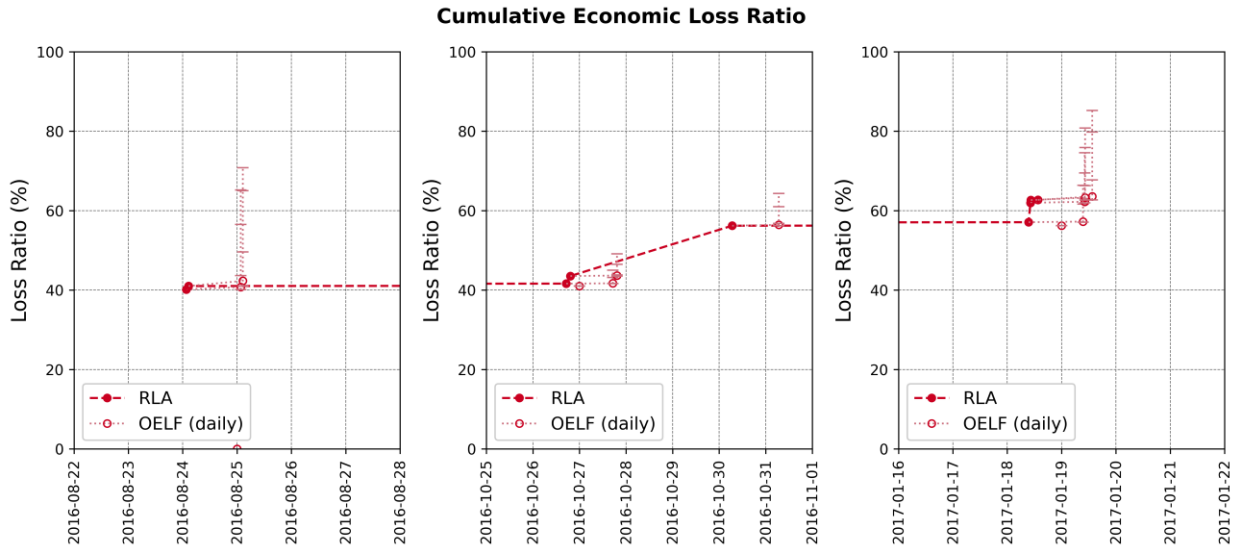

Figure 90 Cumulative economic loss ratios: zoom-ins onto the three clusters of earthquakes shown in Figure 89.

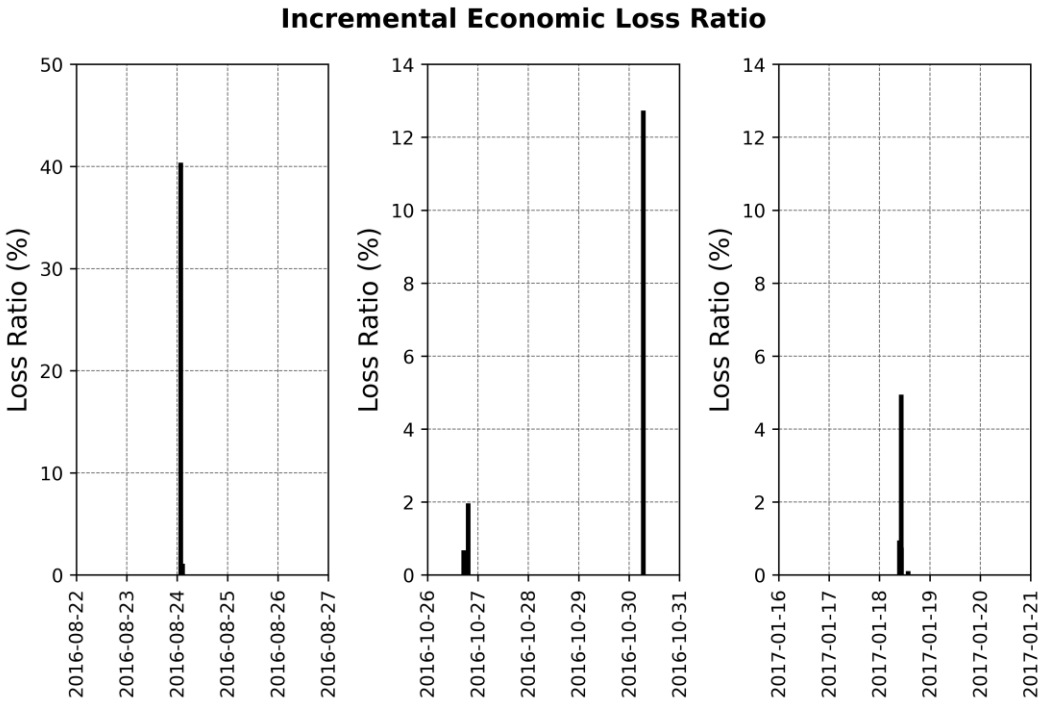

Figure 91 Incremental economic loss ratios at location 12 after all nine shocks of the 2016-2017 Central Italy sequence for which RLAs were conducted (note the different scales used for the vertical axes).

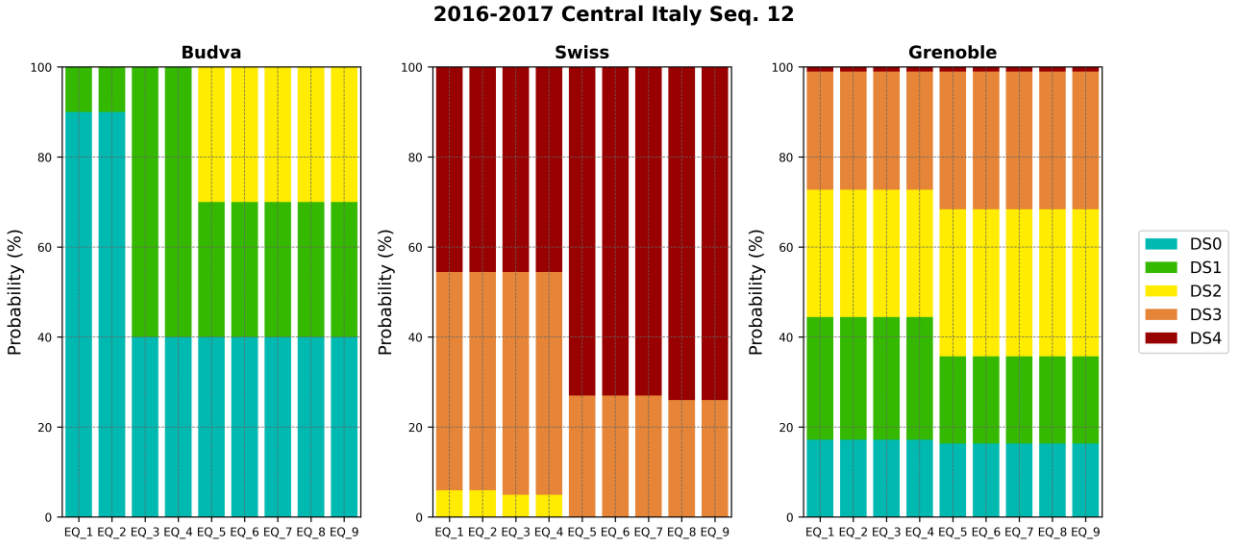

Figure 92 SHM-derived damage probabilities for each of the three monitored buildings at location 12 after each earthquake of interest of the 2016-2017 Central Italy sequence.

Figure 93 and Figure 94 show the evolution of the damage probability per tile and instrumented building, while Figure 95 shows the expected economic loss ratios after the first, fourth, fifth and ninth shocks.

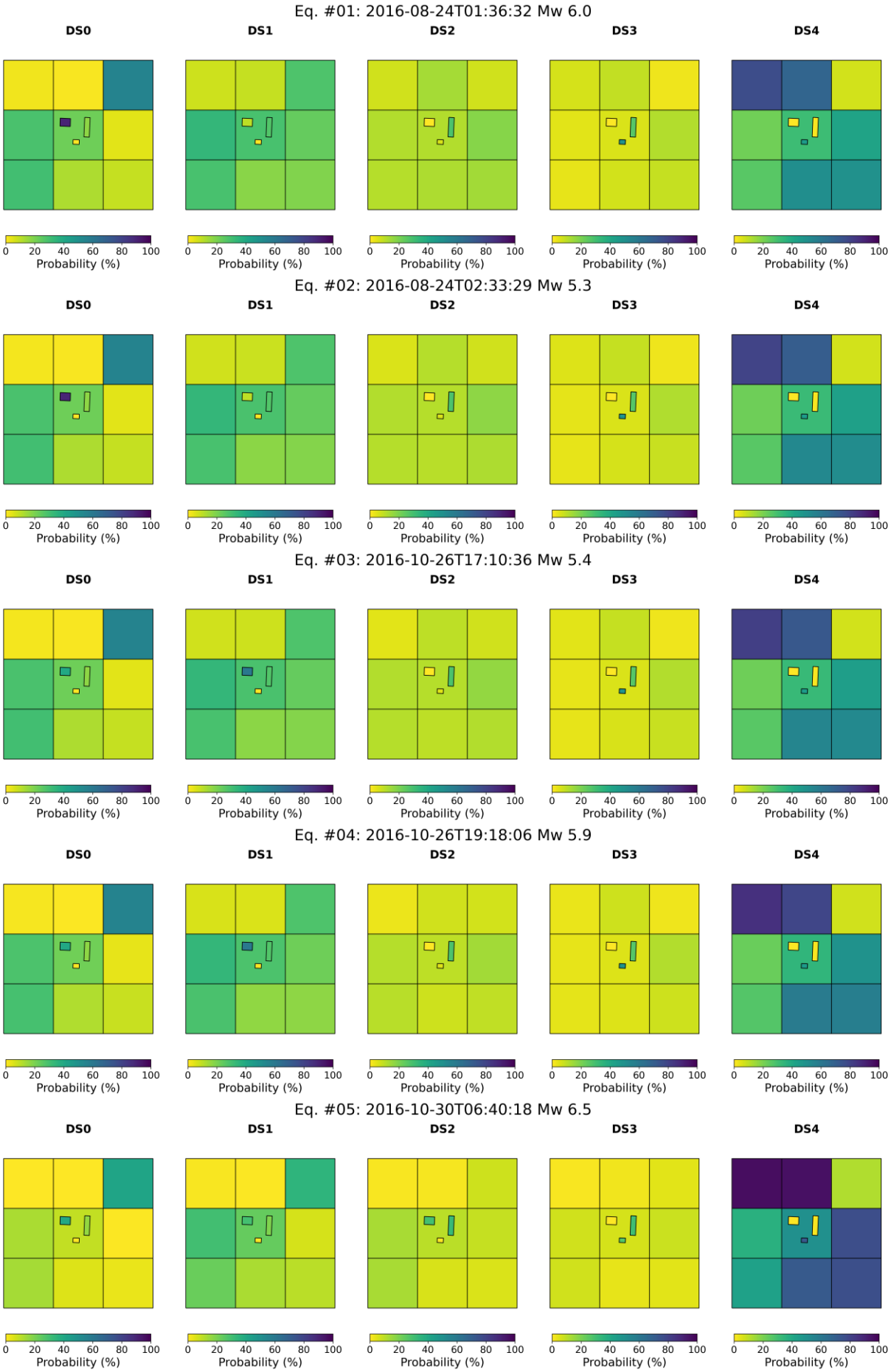

Figure 93 Expected cumulative probabilities of each damage state for each exposure tile and monitored building at location 12 after each of the first five shocks of interest of the 2016-2017 Central Italy sequence.

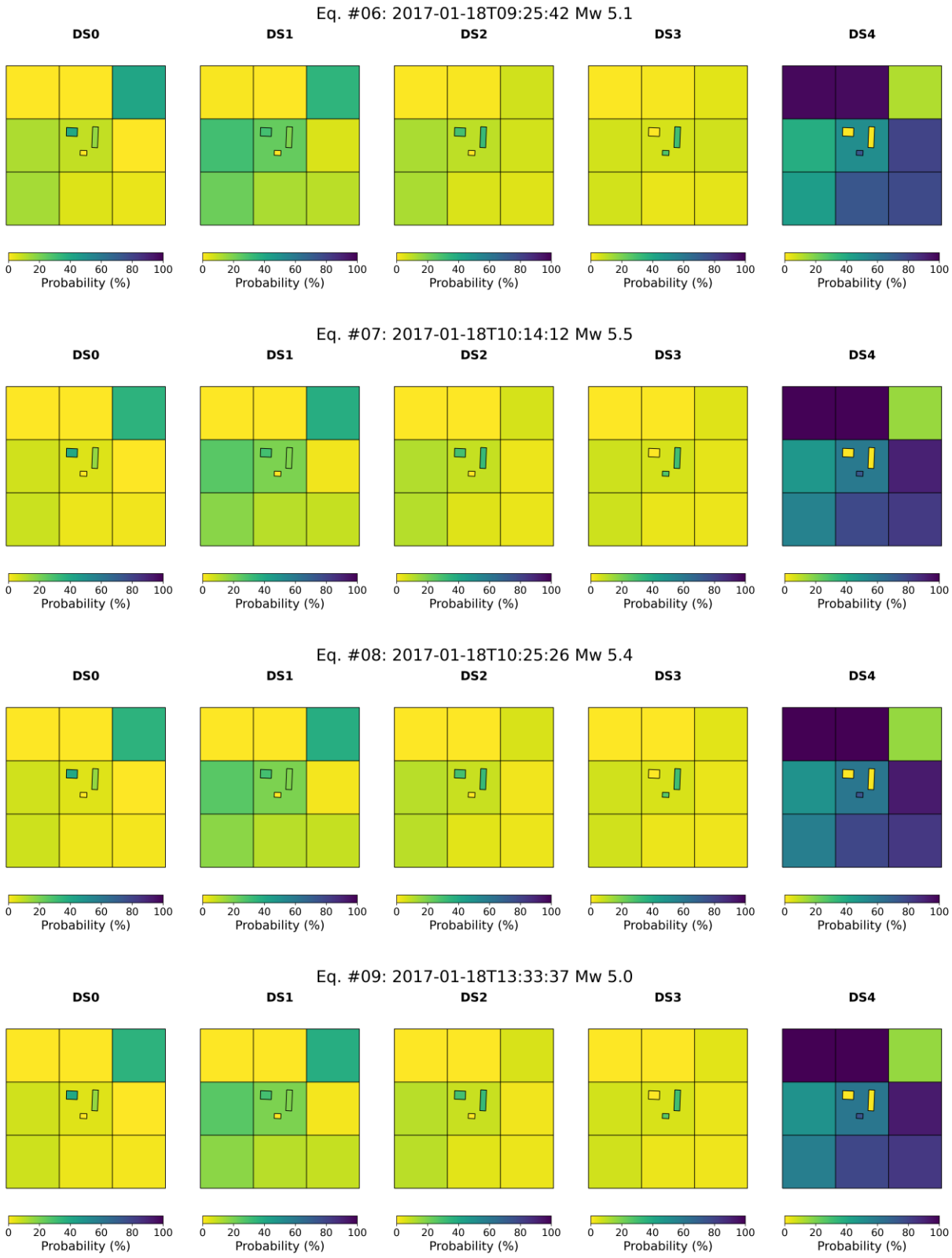

Figure 94 Expected cumulative probabilities of each damage state for each exposure tile and monitored building at location 12 after each of the last four shocks of interest of the 2016-2017 Central Italy sequence.

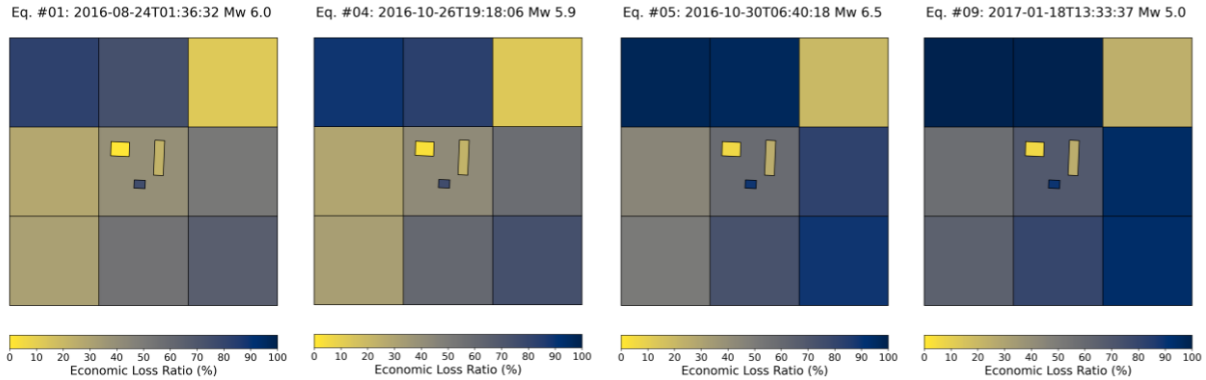

Figure 95 Expected economic loss ratios per tile and instrumented building after the first, fourth, fifth and ninth earthquakes of the 2016-2017 Central Italy sequence for which RLAs were carried out.

5.4 Case-study 3: 2016-2017 Central Italy sequence at location 14

Though focusing on the same earthquakes and seismicity forecasts as case-study number 2, this third case-study is of interest because it shows a different evolution of damage by virtue of the location of the exposed building stock. Location 14 refers to the town of Mascioni, around 13 km south-south-east of Amatrice (location 12, case-study 2) and, consequently, further away from earthquakes 1 through 5, but closer to earthquakes 6 through 9 (see Figure 51). This positioning results in over half of the building stock expected to not suffer any damage due to the first four earthquakes, but more severe damage starting to build up from the fifth earthquake (Mw 6.5, the strongest in the sequence) onward, as depicted in Figure 96. The number of buildings expected to suffer from DS4 more than doubles from around 10 after the fourth earthquake to around 24 after the fifth earthquake, and then increases to 34 after the sixth, makes a larger jump to 57 after the seventh earthquake (Mw 5.5), and then increases to around 67 and finally 69 after the last two events. By the end of the sequence, the damage scenario is worse in case-study 2.

The spatial distribution of the evolution of damage can be observed in Figure 97 and Figure 98. Which tiles result in more or less damage does not differ much from those of case-study 2, which means that the vulnerability of the different building classes in the tiles dominates the spatial distribution of damage more than the overall distance with respect to the earthquake ruptures. This is expectable, given the short distances between different tiles.

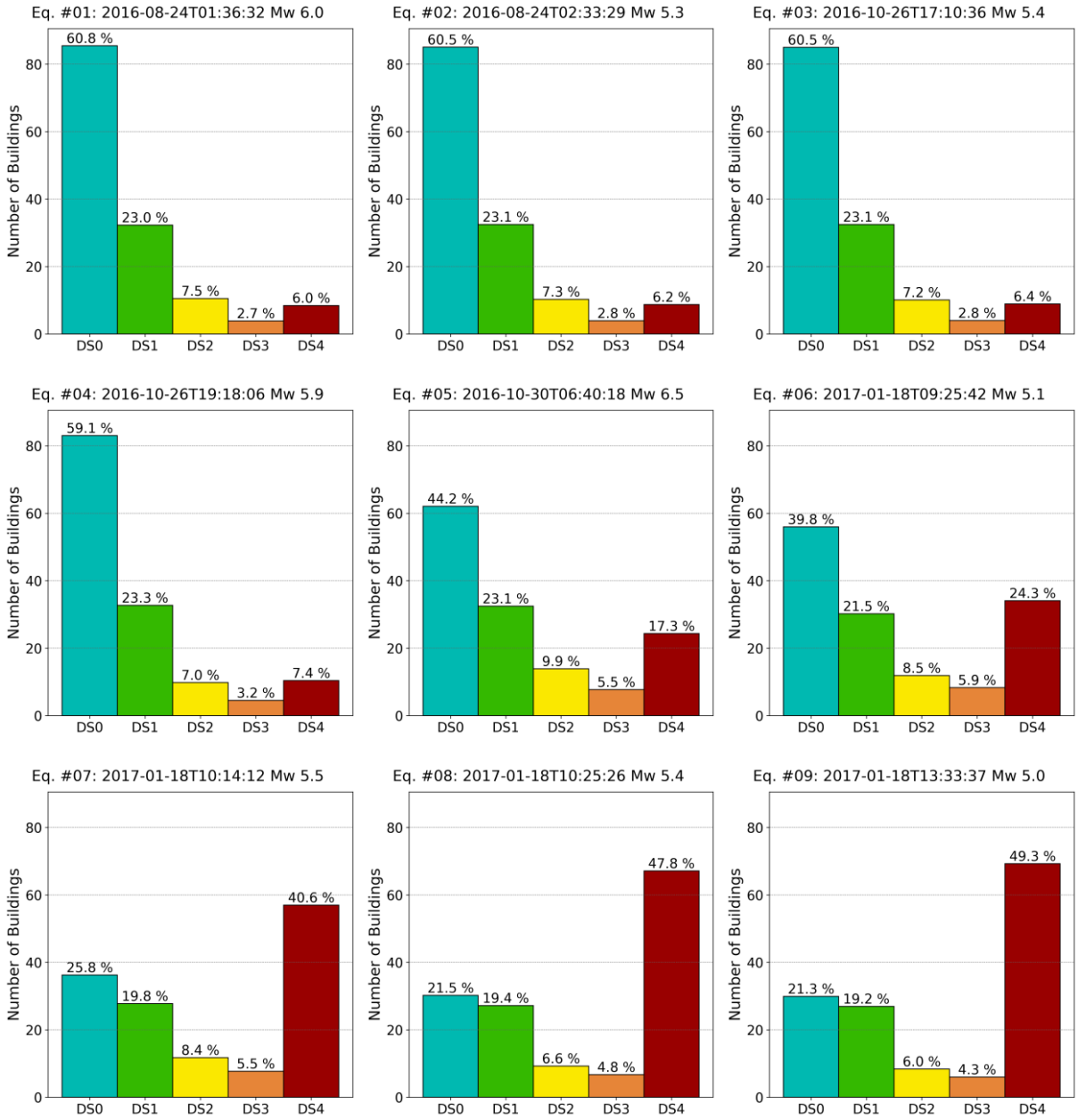

Figure 96 Expected cumulative aggregate number of buildings and probabilities per damage state at location 14 after each earthquake of interest of the 2016-2017 Central Italy sequence (see Table 17).

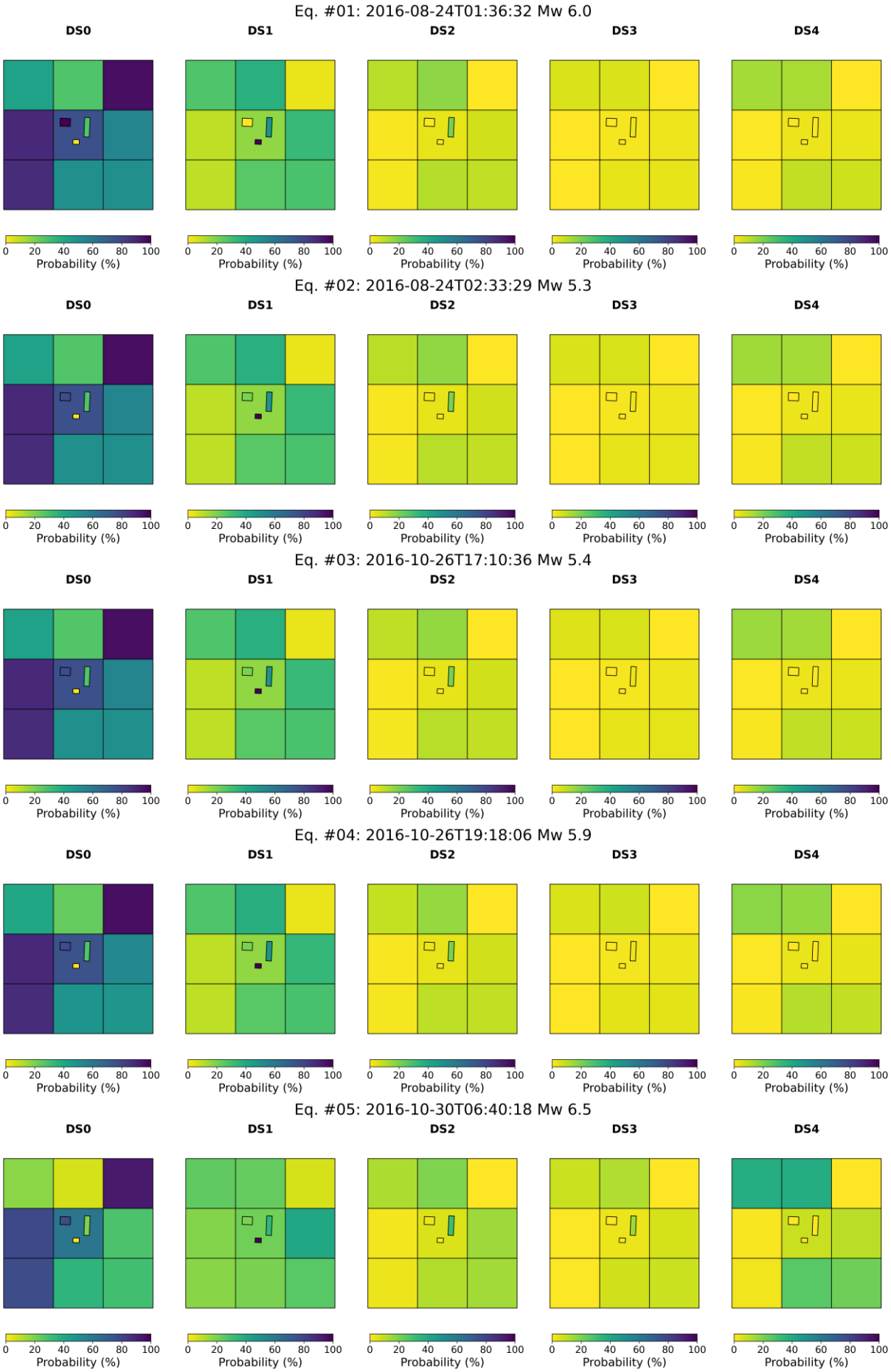

Figure 97 Expected cumulative probabilities of each damage state for each exposure tile and monitored building at location 14 after each of the first five shocks of interest of the 2016-2017 Central Italy sequence.

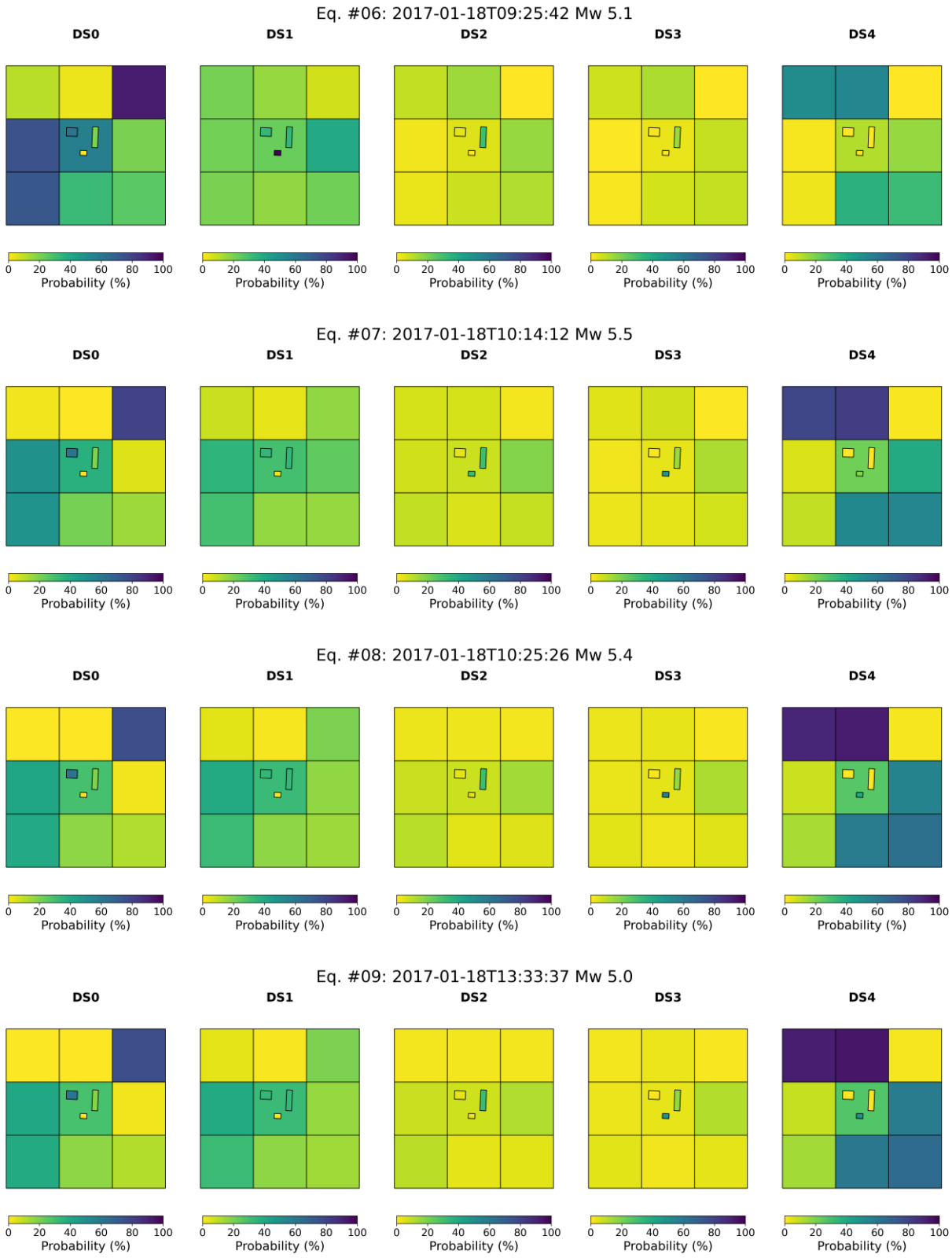

Figure 98 Expected cumulative probabilities of each damage state for each exposure tile and monitored building at location 14 after each of the last four shocks of interest of the 2016-2017 Central Italy sequence.

The SHM-derived probabilities of damage for the three monitored buildings are also different from those obtained for case-study 2. All three buildings show better performances in location 14 (case-study 3). It is interesting that the strongest shock (earthquake 5) does not seem to have an impact on the Budva hotel and the Swiss building, as it did in case-study 2) and it is the seventh earthquake (Mw 5.5) that results in more significant damage probabilities for the Swiss building, but does not seem to affect so much the outcome for the Budva hotel and the Grenoble City Hall.

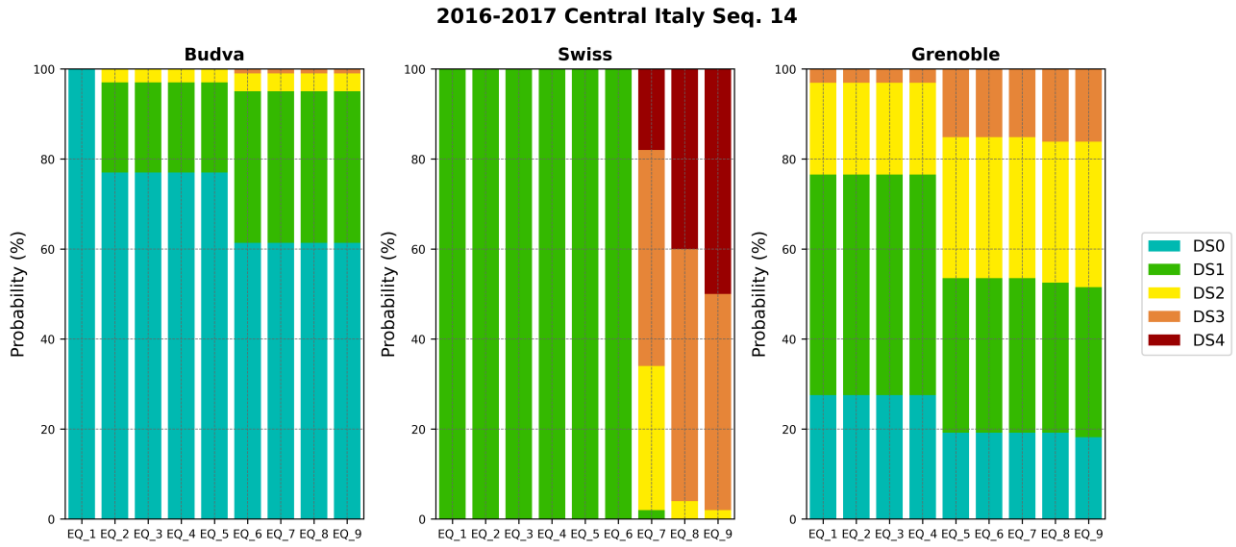

Figure 99 SHM-derived damage probabilities for each of the three monitored buildings at location 14 after each earthquake of interest of the 2016-2017 Central Italy sequence.

The difference in terms of the evolution of damage between case-studies 2 and 3 is naturally reflected in differences in the evolution of the expected economic losses. The overall pattern of three distinct steps in the plots of the cumulative economic loss ratio is maintained in case-study 3, though the relative contribution of each step changes (compare Figure 100 vs. Figure 89, and Figure 101 vs Figure 90). The larger contribution of the last cluster of earthquakes of January 2017 is apparent in the third plot of Figure 101. The incremental contributions of each earthquake are depicted in Figure 102 (compare against Figure 91).

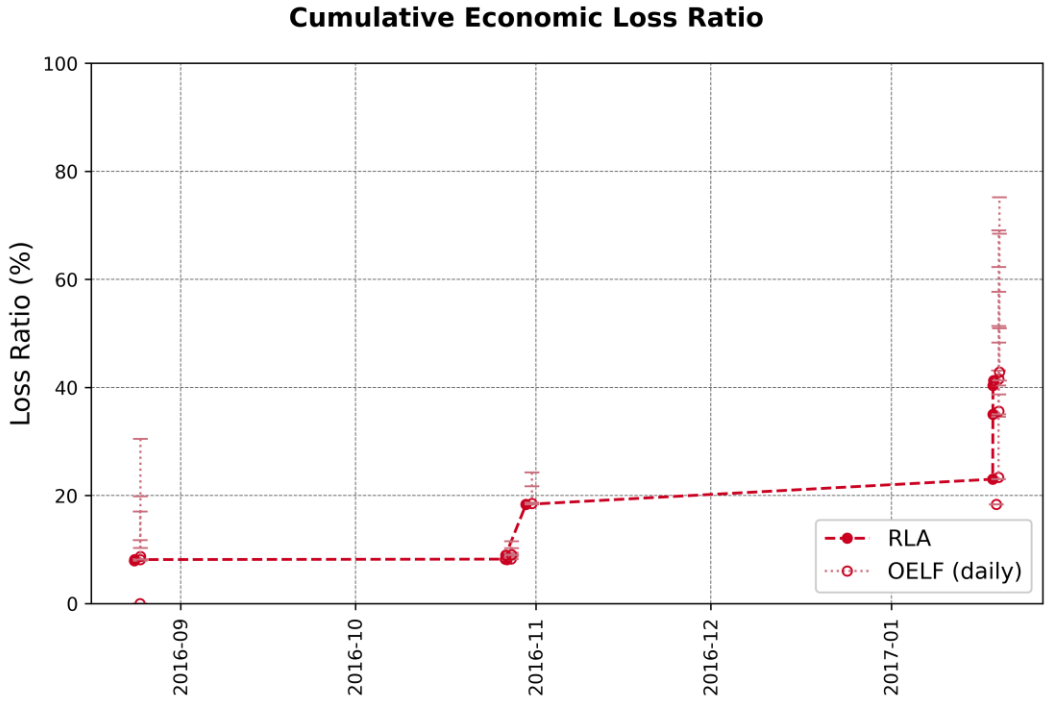

Figure 100 Cumulative economic loss ratios at location 14 after all nine shocks of the 2016-2017 Central Italy sequence for which RLAs were conducted, and subsequent 24-hour seismicity forecasts (OELF, depicted at the end of the 24-hour periods). Vertical error bars show, in order from bottom to top, minimum, mean, 95th, 99th and 99.5th percentiles of loss ratio associated with each OELF.

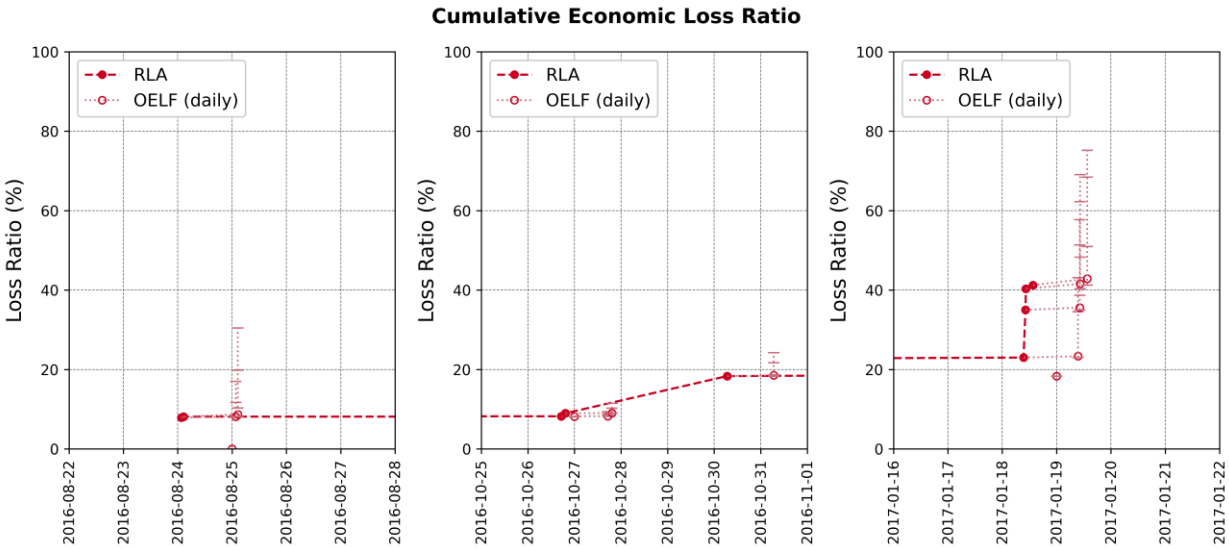

Figure 101 Cumulative economic loss ratios: zoom-ins onto the three clusters of earthquakes shown in Figure 100.

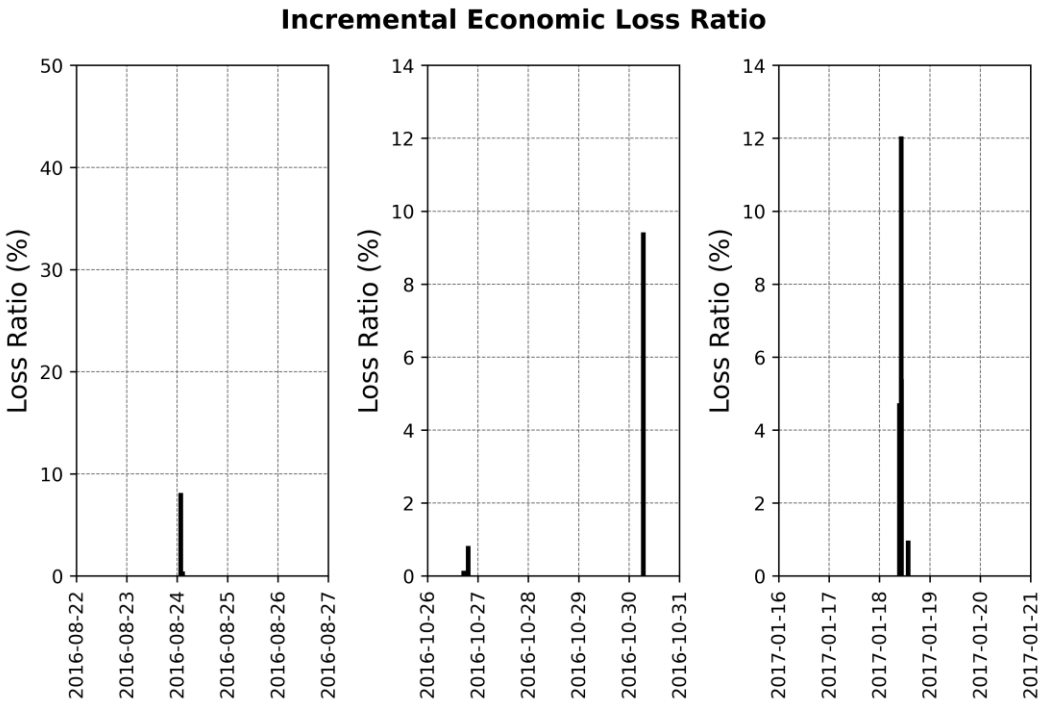

Figure 102 Incremental economic loss ratios at location 14 after all nine shocks of the 2016-2017 Central Italy sequence for which RLAs were conducted (note the different scales used for the vertical axes).

Due to the lower damage levels at the beginning of the sequence, the number of occupants present in buildings at the time the third and sixth earthquakes hit is larger than for case-study 2: 643 people for the third earthquake (against 291) and 353 people for the sixth earthquake (against 171). This, however, does not result in a larger number of injuries or deaths. In case-study 3, the casualties due to the first earthquake are much fewer than in case-study 2: 8.97 (0.48%) people with severity 1, 1.68 (0.09%) people with severity 2, 0.065 (0.003%) people with severity 3, and 0.99 (0.053%) people with severity 4. However, and as shown in Figure 103 through Figure 106, the individual contribution of the last earthquakes is larger than in case-study 2, and the final expected casualties amount to 9.87 (0.53%) people with severity 1, 1.81 (0.097%) people with severity 2, 0.069 (0.004%) people with severity 3, and 1.04 (0.056%) people with severity 4.

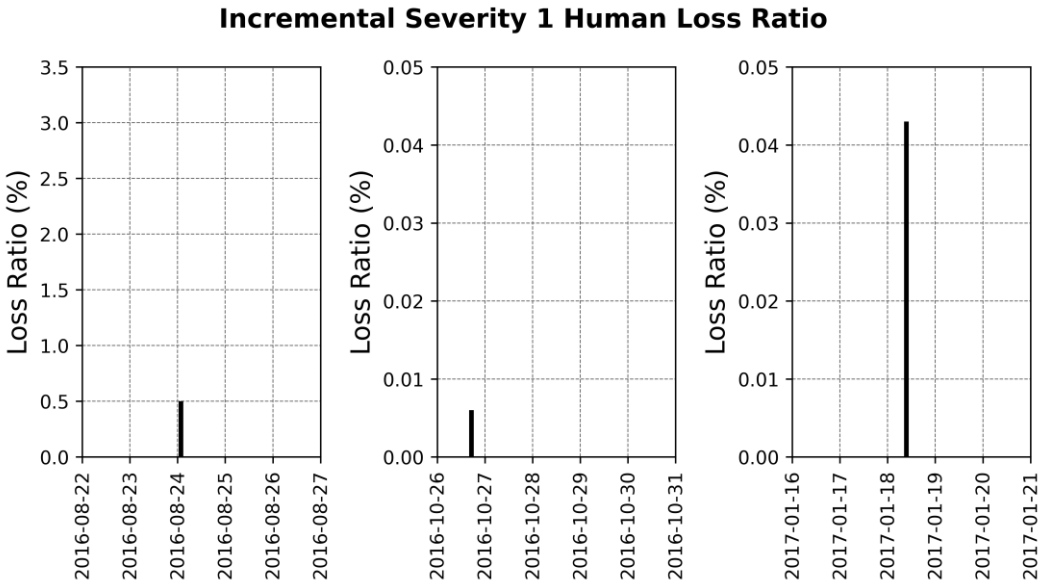

Figure 103 Incremental severity 1 human casualty ratios at location 14 after all nine shocks of the 2016-2017 Central Italy sequence for which RLAs were conducted (different vertical scales used).

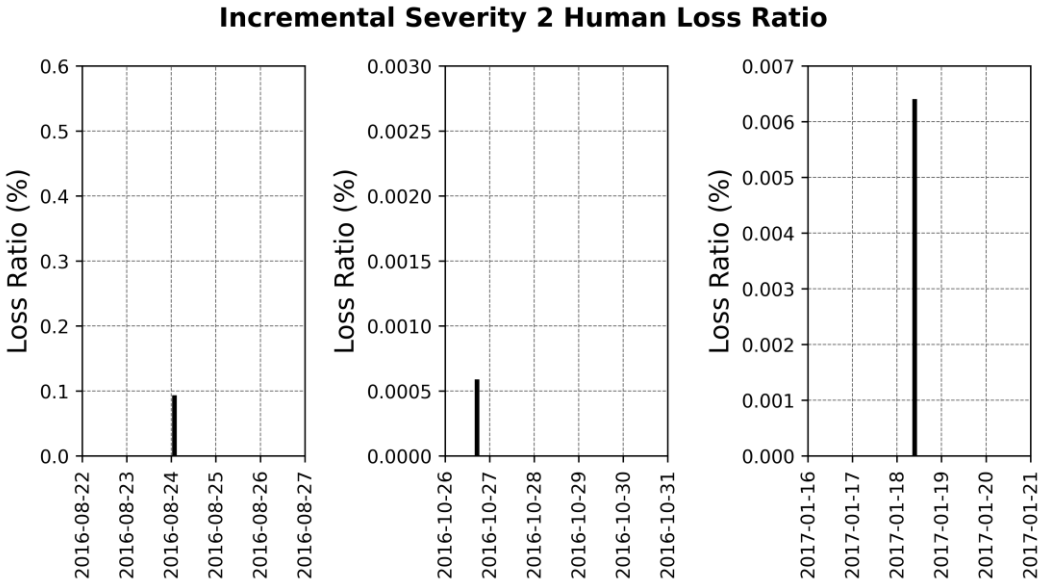

Figure 104 Incremental severity 2 human casualty ratios at location 14 after all nine shocks of the 2016-2017 Central Italy sequence for which RLAs were conducted (different vertical scales used).

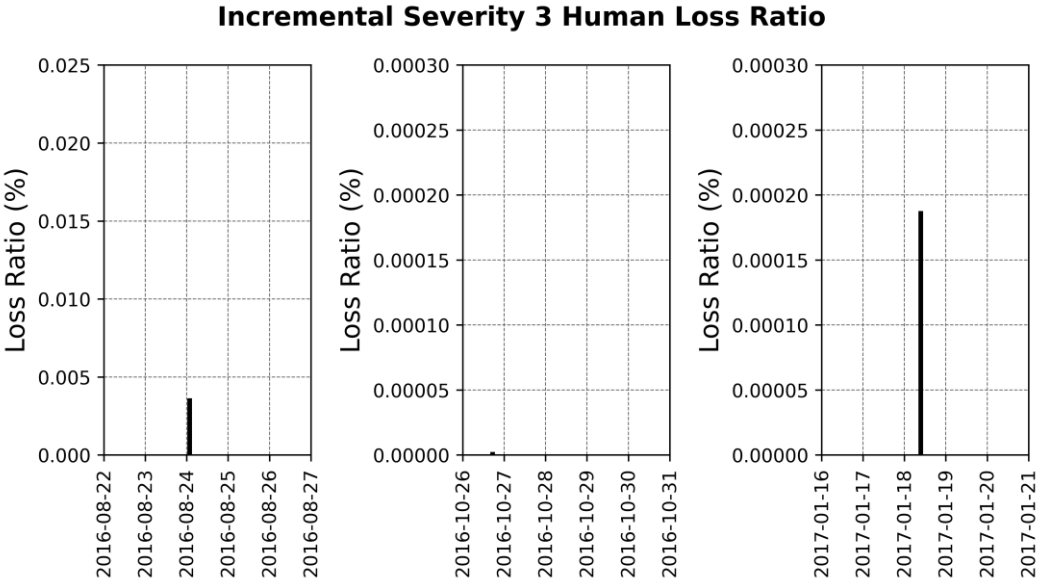

Figure 105 Incremental severity 3 human casualty ratios at location 14 after all nine shocks of the 2016-2017 Central Italy sequence for which RLAs were conducted (different vertical scales used).

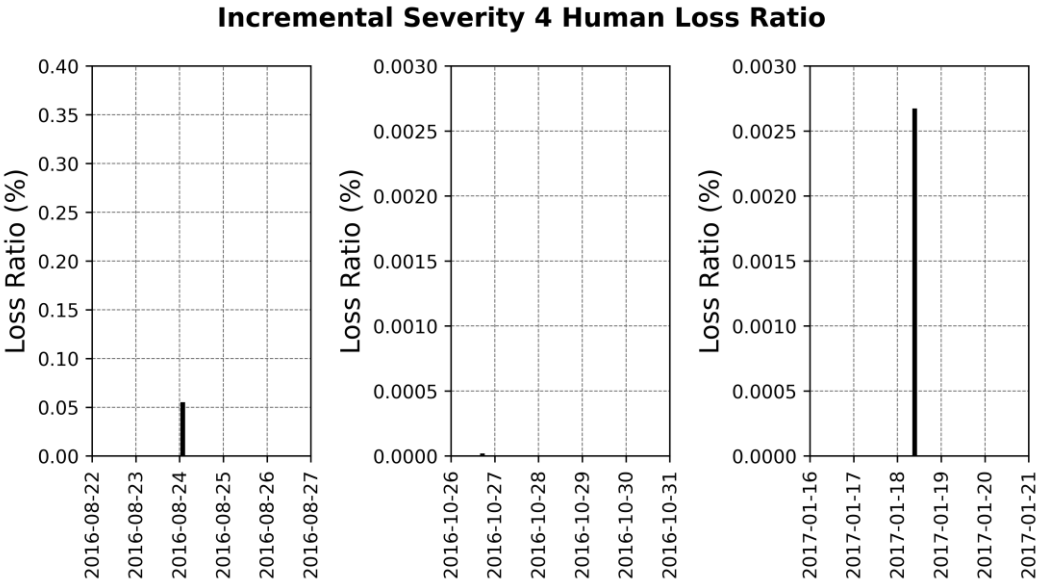

Figure 106 Incremental severity 4 human casualty ratios at location 14 after all nine shocks of the 2016-2017 Central Italy sequence for which RLAs were conducted (different vertical scales used).

5.5 Some observations on the seven case-studies

Having run three case-studies for the 2009 L'Aquila sequence and four case-studies for the 2016-2017 Central Italy one using the same building stock translated onto different locations allows us to see some interesting aspects on the evolution of cumulative damage in seismic sequences. In this sub-section we focus on economic losses as a proxy for expected damage aggregated across all structures. Figure 107 and Figure 108 depict the cumulative economic loss ratios for the case-studies of each sequence.

It is noticeable that the trajectories of cumulative economic loss ratios for the three L'Aquila locations appear, broadly speaking, as vertical translations from one another (Figure 107), while those for the four Central Italy locations (Figure 108) differ more from one another in terms of the relative magnitude of the jumps caused by each of the three seismicity clusters of the sequence (August 2016, October 2016, January 2017). This is dependent not only on the locations selected for the

analysis (see Figure 51) but also on the characteristics of the sequences in terms of the spatial and temporal distribution of shocks of different magnitudes, and is in agreement with observations on the evolution of surveyed macroseismic intensity at different localities during and after the Central Italy sequence (Rossi et al., 2019). As the seismicity migrates south in January 2017, it is locations 12 and 14 that see the impact of these last earthquakes while locations 11 and 13 do not see significant increases to their losses.

In the case of the L'Aquila sequence, it seems surprising that the economic losses due to the first two large shocks differ so much at locations 02 and 03 with respect to one another, given their geographical proximity. Apart from a difference in site conditions (V_{S30} of 521 m/s at location 02 and V_{S30} of 416 m/s at location 03), it is noted that the Grenoble City Hall seems to suffer from much more severe damage when subject to the accelerograms associated with location 03 than those associated with location 02, according to the SHM-based fragility models derived for the building (Figure 109). As the replacement value of the City Hall is around 20% of that of the whole building stock, its performance has a large impact in terms of the economic losses. After the first two earthquakes the individual contributions of successive shocks is similar in both locations.

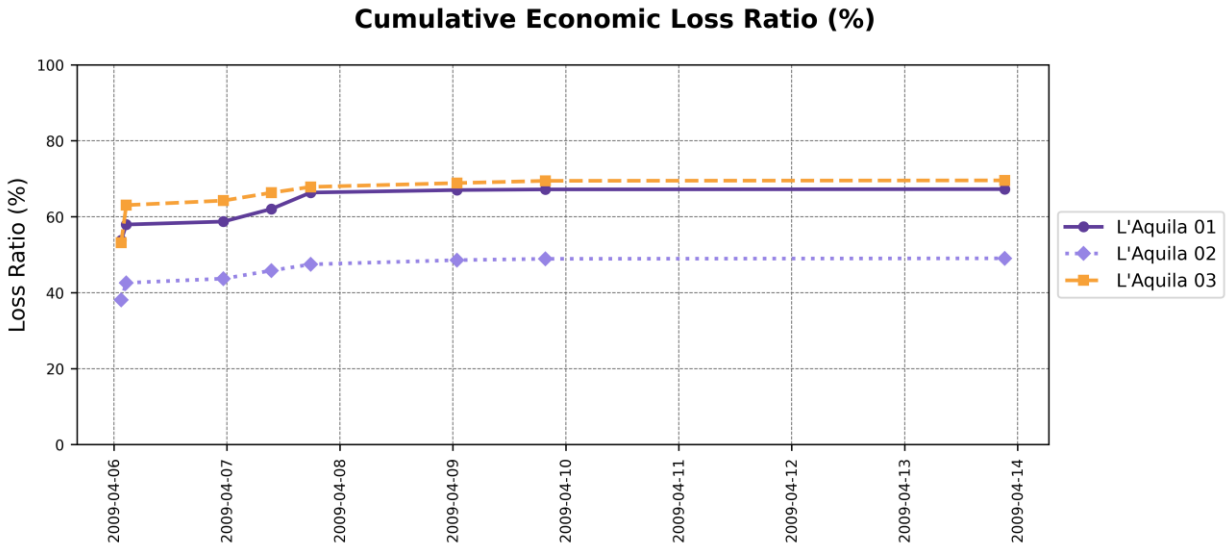

Figure 107 Cumulative economic loss ratios at the three locations analysed after all eight shocks of the 2009 L'Aquila sequence for which RLAs were conducted.

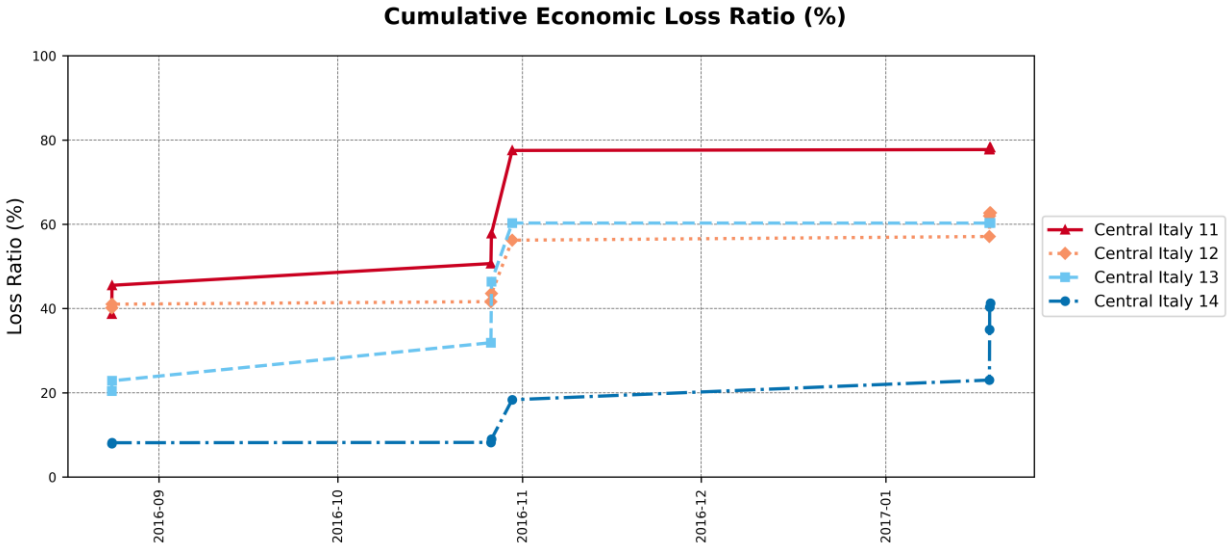

Figure 108 Cumulative economic loss ratios at the four locations analysed after all nine shocks of the 2016-2017 Central Italy sequence for which RLAs were conducted.

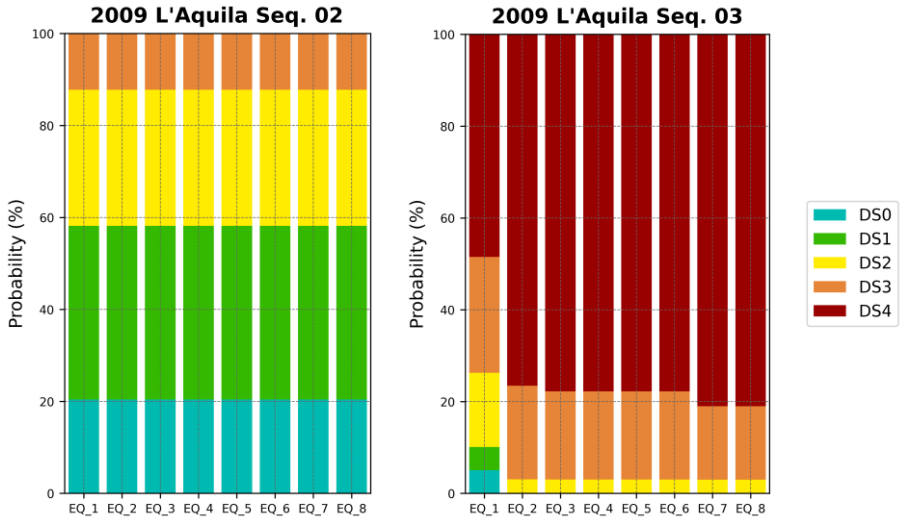

Figure 109 SHM-derived damage probabilities for the Grenoble City Hall at locations 02 and 03 after each earthquake of interest of the 2009 L'Aquila sequence.

5.6 Miscellanea

5.6.1 Running times

The running time of each rapid loss assessment with the Real-Time Loss Tools is very small in comparison to what it takes to run each operational earthquake loss forecast, and it was thus OELF that defined the overall running time of all seven case-studies. Two servers were used, with the following technical characteristics:

- Server (a): DELL PowerEdge R7425, AMD Dual EPYC 7601, 2.2GHz, 128 cores, 1TB RAM
- Server (b): Dell PowerEdge R940xa, 2 x Intel Xeon Platinum 8260 2,4 GHz, 192 cores, 755 GB RAM

With either of the two, the running times of the RLAs varied between 9 and 19 seconds per earthquake, with only one branch in the ground motion logic tree and 1,000 realisations of ground motion.

When looking at the running times of the OELFs, some additional factors need to be taken into account. Firstly, the running times reported in what follows do not include the time needed to create the seismicity forecasts themselves. Secondly, as the Real-Time Loss Tools allow the user to indicate a minimum earthquake magnitude and maximum epicentral distance below which earthquakes in the seismicity forecast are assumed to cause no damage, there is a discrepancy between the total number of earthquakes in the catalogue input files and those whose ruptures are built and which are effectively run with OpenQuake. It is these latter numbers of earthquakes per forecast that are indicated in Table 18 and Table 19, and which stem from filtering the catalogues using a minimum magnitude of 5.0 and a maximum distance of 200 km. However, all the remaining earthquakes in the catalogue do still consume some running time, as the software stores the result that they cause no damage, which is still an outcome that influences the final expected damage and loss. Similarly, when setting the *continuous_ses_numbering* parameter in the configuration file to True, the Real-Time Loss Tools assume that the total number of stochastic event sets (of seismicity) indicated as *ses_range* (10,000 in our case) is to be considered, even if not all stochastic event sets have earthquakes listed in the input catalogue. The latter can happen (and does happen) because the catalogue input files have been created for Mw of 3.99 and above, but some stochastic event sets may contain only earthquakes with magnitudes smaller than the selected threshold. When the software encounters an "empty" stochastic event set, it still carries out some actions to record that it existed and produced no additional damage. The duration times indicated in Table 18 and Table 19 include all these actions and thus correspond to how long it took to process each OELF calculation, including both earthquakes that were run in OpenQuake, earthquakes that exist in the input catalogue files

but were not run, and even earthquakes that do not exist in the input catalogue files but are still part of the forecast as stochastic event sets that are implicit in the 1-to-10,000 continuous numbering.

Table 18 Running times (in hours) and number of earthquakes run in OpenQuake for each OELF calculation of the 2009 L'Aquila sequence, using servers (a) and (b).

Date (UTC)	Time (UTC)	Seq. 01 (a)		Seq. 02 (a)		Seq. 03 (b)	
		Number	Duration	Number	Duration	Number	Duration
6 April 2009	00:00	64	0.28	64	0.27	64	0.23
6 April 2009	01:32	336	1.24	336	1.23	336	1.11
6 April 2009	02:37	1,020	3.54	1,020	3.52	1,020	3.34
6 April 2009	23:15	1,573	5.72	1,573	5.75	1,573	5.43
7 April 2009	09:26	1,367	5.28	1,367	5.26	1,367	5.03
7 April 2009	17:47	1,351	5.45	1,351	5.44	1,351	5.31
9 April 2009	00:52	1,060	4.47	1,060	4.46	1,060	4.41
9 April 2009	19:38	758	3.31	758	3.33	758	3.35
13 April 2009	00:00	243	1.19	243	1.19	243	1.18
13 April 2009	21:14	319	1.52	319	1.52	319	1.52
Total		8,091	32.00	8,091	31.96	8,091	30.91

Table 19 Running times (in hours) and number of earthquakes run in OpenQuake for each OELF calculation of the 2016-2017 Central Italy sequence, using servers (a) and (b).

Date (UTC)	Time (UTC)	Seq. 11 (a)		Seq. 12 (b)		Seq. 13 (a)		Seq. 14 (b)	
		Number	Duration	Number	Duration	Number	Duration	Number	Duration
24 Aug 2016	00:00	65	0.28	65	0.23	66	0.29	65	0.23
24 Aug 2016	01:36	768	2.63	768	2.41	768	2.64	768	2.38
24 Aug 2016	02:33	2,417	8.57	2,417	8.15	2,417	8.57	2,417	8.16
26 Oct 2016	00:00	164	0.82	105	0.51	164	0.82	75	0.40
26 Oct 2016	17:10	695	2.76	662	2.47	695	2.77	655	2.47
26 Oct 2016	19:18	1,483	5.91	1,428	5.47	1,483	5.97	1,426	5.43
30 Oct 2016	06:40	2,980	12.50	2,980	12.63	2,980	12.66	2,980	12.56
18 Jan 2017	00:00	26	0.29	27	0.24	26	0.30	27	0.24
18 Jan 2017	09:25	419	2.06	419	2.03	419	2.03	419	2.04
18 Jan 2017	10:14	800	3.78	800	3.92	800	3.78	800	3.91
18 Jan 2017	10:25	1,899	9.11	1,899	9.77	1,899	9.09	1,899	9.71
18 Jan 2017	13:33	2,765	14.16	2,765	15.41	2,765	14.08	2,765	15.30
Total		14,481	62.87	14,335	63.24	14,482	62.99	14,296	62.82

As can be observed from Table 18 and Table 19, both the number of earthquakes and the duration of each OELF calculation are very variable. Some of the durations are manageable, while some others render the idea of a daily OELF somewhat impractical, as the time span of the forecast begins to be largely consumed by the time it takes to run it. This is the case of the forecasts after the 30 October 2016 earthquake and after the last shock of 18 January 2017, which took over 12 hours and 14-15 hours to run, respectively. It is thus clear that a full-scale RLA-OELF system would need to focus on optimisation of these running times. Based on the experience acquired while developing the Real-Time Loss Tools, it is quite likely that a large gain could be obtained by implementing these calculations directly within OpenQuake, not only because it would avoid the need to carry out certain

checks and the building of calculation files and structures (writing/reading to/from disk, input validation, etc.) each time OpenQuake is called, but also because OELF calculations could be parallelised per stochastic event set, as each of them starts from the "current" damage state of the buildings and health status of their occupants, but is in fact independent from all other sets. The current version of the Real-Time Loss Tools, which has been developed as a demonstration to better define the specifications and workflow of the system, runs one stochastic event set at a time, as it allows for OpenQuake to take all the cores it can to run each individual calculation.

5.6.2 Minimum magnitude for OELF

All the case-studies presented herein were run using a minimum magnitude of 5.0 for OELF, and consequently assuming that earthquakes with magnitudes below the 5.0 threshold do not cause additional damage. This assumption was motivated mainly by time constraints but is not necessarily true, as it is ground motions, exposure and vulnerability that define the occurrence of damage, not magnitude in itself, and there has been broad proof that smaller magnitude earthquakes are capable of causing damage and loss of life (see, for example, Nievas et al., 2020).

In order to evaluate the potential impact of this decision on the results obtained, we ran the first three calculation triggers of the 2009 L'Aquila sequence at location 01 (i.e. case-study 1, section 5.2) using three different minimum magnitudes (5.0, 4.5 and 4.0) and compared the resulting mean economic losses, which are shown in Table 20 and Table 21 (note that these results assume perfect inter-period correlation of the spectral ordinates, as opposed to all other calculations presented, which use the model of Jayaram and Baker (2009) to account for this correlation). The first three triggers comprise an initial OELF (carried out assuming a fully undamaged building stock), the RLA of the main shock, and an OELF after the main shock (with initial damage stemming from the RLA). As can be observed, changes in the mean economic losses are significant in the case of the first seismicity forecast, for which the losses are very low for most of the stochastic events sets in the forecast, but are quite small in the case of the second forecast, which already starts with an expected mean economic loss of 64.12 million EUR resulting from the RLA for the Mw 6.1 main shock.

Table 20 Cumulative absolute economic losses (in thousands of EUR) calculated with the seismicity forecast of 6 April 2009 at 00:00 UTC with different thresholds of minimum magnitude (building stock initially undamaged).

Case	Mean	84th p.	90th p.	95th p.	99th p.	99.5th p.	Max.
Mw ≥ 5.0	87	0	0	0	0	5,971	64,530
Mw ≥ 4.5	120	0	0	0	2,661	7,036	64,530
Mw ≥ 4.0	134	0	0	133	2,683	7,133	64,855

Table 21 Cumulative absolute economic losses (in thousands of EUR) calculated with the seismicity forecast of 6 April 2009 at 01:32 UTC with different thresholds of minimum magnitude (building stock damaged by the Mw 6.1 main shock).

Case	Mean	84th p.	90th p.	95th p.	99th p.	99.5th p.	Max.
Mw ≥ 5.0	64,561	64,122	64,122	64,122	79,057	85,491	112,119
Mw ≥ 4.5	64,821	64,122	66,069	68,241	79,600	85,779	112,307
Mw ≥ 4.0	65,059	65,417	66,418	68,564	79,848	85,656	112,392

These results suggest that the use of 5.0 as a magnitude threshold to run the OELF calculations in this proof of concept has not had a significant impact in the results obtained. This conclusion should, however, not be generalised, given the limited scope of the comparison (which focused only on two OELF calculations) and the fact that it is only based on a reduced number of building classes. A full-scale RLA and OELF system should give detailed consideration to this matter.

6. Concluding remarks

The coding of the Real-Time Loss Tools as a demonstration to better define the specifications and workflow of an integrated RLA-SHM-OELF system, as well as its application to the case-studies presented herein, has helped pave the way for enhanced interactions across the different areas of expertise involved. The possibility to look and explore a large integration chain throws light on the value as well as expectations for each individual component and the way it relates to all other aspects of a broader, more encompassing model. We have not explored all aspects of a full-scale implementation, but we would like to summarise in what follows some of the main outcomes of this process.

The transition of the seismicity forecasting community from the traditional generation of earthquake rates to generating outputs in terms of large numbers of earthquake catalogues (i.e., stochastic realisations of seismicity) is aligned with the way the implementation of probabilistic risk calculations has evolved in the OpenQuake-engine, moving from the traditional approach of integrating hazard curves with vulnerability models towards the use of stochastic event sets sampled from the input source model. Such an approach enables us to account for correlations and conditional dependencies that would otherwise become intractably complex in a classical risk framework (e.g. spatial and inter-period correlation of ground motions, integration of uncertainties in finite rupture properties), including those that may be avenues of future developments (e.g., temporal dependencies of between-event residuals; Bindi et al., 2018).

Within the context of OELF, this transition comes with the need to generate ruptures associated with the forecasted earthquakes. In the Real-Time Loss Tools we have approached this as a post-processing of the seismicity forecasts (given in terms of date, time, magnitude and epicentral location) by which we sample rupture properties (strike, dip, rake, dimensions of the rupture) from available seismic source models (similarly to Papadopoulos et al., 2020). However, one could wonder if a future generation of operational earthquake forecasts could integrate this directly to the forecasting model, or might even be able to directly output ruptures that are compatible with the tectonics of the region and the dynamics of ruptures succeeding each other in a small temporal window (e.g., Field et al., 2017). In this sense, the rupture-based OELF framework is readily adaptable to allow for the integration of realisations of seismicity emerging from physics-based rupture simulators (e.g., Milner et al., 2022).

Running times for operational earthquake loss forecasting calculations based on earthquake catalogues and the stochastic generation of earthquake ruptures clearly pose a challenge. Having been developed as a demonstration to define the specifications and workflow of such a system and not as a direct operational implementation, we believe the Real-Time Loss Tools can now be used in interactions with the OpenQuake-engine developers, with a view to getting OELF one day implemented in OpenQuake in a manner that resolves the efficiency challenges. We hope that the existence of this prototype workflow will facilitate such interactions, as well as any other discussions within the scientific community aimed at identifying matters that require further research and/or development.

In this sense, the use of the Real-Time Loss Tools is not limited to any of the specific inputs used for the present proof of concept. Different models from those discussed herein can be used for seismicity forecasting, building/population exposure, ground motion, site amplification, fragility (both ground motion-based and SHM-based), economic and human consequences, as long as they are adequately formatted as described in chapter 4. Some alternative models might already exist (e.g., other seismicity forecasting models developed as part of RISE Task 3.3), while others might still need to be developed. The need for extensive databases of state-dependent fragility models that cover a broad range of building classes (ideally, all those of the European Seismic Risk Model ESRM20) is apparent, and so is the need for data and models for the timelines that evolve after an earthquake and affect the displacement and future location of people, due to damage inspections, repairs, recovery in hospital, etc. A significant step in this direction has been undertaken as

part of RISE Task 4.3, with the development of the OpenQuake Recovery and Rebuilding Effort software (OQ-RRE; RISE Deliverable 4.4; Reuland et al., 2022a). It is our hope that future developments of the Real-Time Loss Tools and the OpenQuake Recovery and Rebuilding Effort software lead to a full integration of all these aspects of earthquake resilience.

To conclude, we would like to encourage the earthquake engineering and engineering seismology research community to explore the Real-Time Loss Tools and all the individual components integrated in this work. By implementing these methods in open-source code, we hope to have facilitated the wider application and understanding of these developments and to have set in place a framework through which future innovations could eventually find their way into deployment.

7. Acknowledgements

The authors would like to thank Francesco Visini for providing the files of the Italian MA4 source model of Visini et al. (2022).

8. References

Aghagholizadeh M, Massumi A (2016) A new method to assess damage to RCMRFs from period elongation and Park–Ang damage index using IDA. International Journal of Advanced Structural Engineering 8:243-252. https://doi.org/10.1007/s40091-016-0127-8.

Astorga A, Guéguen P (2023) On the value of weak-to-moderate earthquake data recorded in buildings. Submitted to Bull. Seism. Soc. Am.

Akkar S (2021) Earthquake Physical Risk/Loss Assessment Models and Applications: A Case Study on Content Loss Modeling Conditioned on Building Damage. In: Akkar S., Ilki A., Goksu C., Erdik M. (eds) Advances in Assessment and Modeling of Earthquake Loss. Springer Tracts in Civil Engineering. Springer, Cham. https://doi.org/10.1007/978-3-030-68813-4_10

Baker JW, Cornell CA (2006) Spectral shape, epsilon and record selection. Earthq Eng Struct Dyn 35:1077–1095. https://doi.org/10.1002/eqe.571

Baltzopoulos G, Baraschino R, Iervolino I, Vamvatsikos D (2018) Dynamic analysis of single-degree-of-freedom systems (DYANAS): a graphical user interface for OpenSees. Engineering Structures 177:395–408. https://doi.org/10.1016/j.engstruct.2018.09.078.

Baraschino R, Baltzopoulos G, Iervolino I (2022). A note on peak inelastic displacement as a proxy for structural damage in seismic sequences. XIX ANIDIS Conference, Seismic Engineering in Italy. Structural Integrity Procedia.

Batista e Silva F, Freire S, Schiavina M, Rosina K, Marin M, Ziemba L, Craglia M, Koomen E, Lavalle C (2020) Uncovering temporal changes in Europe's population density patterns using a data fusion approach. Nat Commun 11:4631. https://doi.org/10.1038/s41467-020-18344-5

Bayliss K, Naylor M, Illian J, Main IG (2020) Data-Driven Optimization of Seismicity Models Using Diverse Data Sets: Generation, Evaluation, and Ranking Using Inlabru. Journal of Geophysical Research: Solid Earth 125(11): e2020JB020226. https://doi.org/10.1029/2020JB020226

Bayliss K, Naylor M, Kamranzad F, Main I (2022) Pseudo-prospective testing of 5-year earthquake forecasts for California using inlabru. Natural Hazards and Earth System Sciences 22(10): 3231-3246. https://doi.org/10.5194/nhess-22-3231-2022

Bindi D, Pacor F, Luzi L, Puglia R, Massa M, Ameri G, Paolucci R (2011) Ground motion prediction equations derived from the Italian strong motion database. Bulletin of Earthquake Engineering 9:1899-1920. https://doi.org/10.1007/s10518-011-9313-z

Bindi D, Cotton F, Spallarossa D, Picozzi M, Rivalta E (2018) Temporal Variability of Ground Shaking and Stress Drop in Central Italy: A Hint for Fault Healing? Bulletin of the Seismological Society of America 108(4):1853–1863. doi: https://doi.org/10.1785/0120180078

Blagojević N, Didier M, Stojadinović B (2022) Quantifying component importance for disaster resilience of communities with interdependent civil infrastructure systems. Reliability Engineering & System Safety 228:108747. https://doi.org/10.1016/j.ress.2022.108747

Bodenmann L, Reuland Y, Stojadinovic B (2021) Dynamic updating of building loss predictions using regional risk models and conventional post-earthquake data sources. In: Proceedings of the 31st European Safety and Reliability Conference (ESREL 2021):1411-1418.

Bommer JJ, Crowley H (2017) The purpose and definition of the minimum magnitude limit in PSHA calculations. Seismological Research Letters 88(4):1097-1106. https://doi.org/10.1785/0220170015

Bogoevska S, Spiridonakos M, Chatzi E, Dumova-Jovanoska E, Höffer R (2017) A Data-Driven Diagnostic Framework for Wind Turbine Structures: A Holistic Approach. Sensors 17(4):720. https://doi.org/10.3390/s17040720

Böse M, Heaton TH, Hauksson E (2012) Real-time Finite Fault Rupture Detector (FinDer) for large earthquakes. Geophysical Journal International 191(2): 803 – 812 https://doi.org/10.1111/j.1365-246X.2012.05657.x

Böse M, Smith DE, Felizardo C, et al. (2018) Finder v.2: Improved real-time ground-motion predictions for M2 – M9 with seismic finite-source characterization. Geophysical Journal International 212: 725 – 724 https://doi.org/10.1093/gji/ggx430

Brzev S, Scawthorn C, Charleson AW, Allen L, Greene M, Jaiswal K, Silva V (2013) GEM building taxonomy version 2.0. GEM Technical Report 2013-02 V1.0.0. Pavia, Italy: GEM Foundation.

Chioccarelli E, Pacifico A, Iervolino I (2022) Operational earthquake loss forecasting for Europe. RISE Project Deliverable 4.3.

Clinton JF, Heaton TH (2002) Potential advantages of a strong-motion velocity meter over a strong-motion accelerometer. Seismological Research Letters 73(3):332-342. https://doi.org/10.1785/gssrl.73.3.332

Cochran E, Lawrence J, Christensen C, Chung A (2009) A novel strong-motion seismic network for community participation in earthquake monitoring, IEEE Instrumentation & Measurement Magazine 12(6):8–15. https://doi.org/10.1109/MIM.2009.5338255

Cosenza E, Del Vecchio C, Di Ludovico M, Dolce M, Moroni C, Prota A, Renzi E (2018) The Italian guidelines for seismic risk classification of constructions: technical principles and validation. Bulletin of Earthquake Engineering 16:5905–5935. https://doi.org/10.1007/s10518-018-0431-8

Crowley H, Despotaki V, Rodrigues D, Silva V, Toma-Danila D, Riga E, Karatzetzou A, Fotopoulou S, Zugic Z, Sousa L, Ozcebe S, Gamba P (2020a) Exposure model for European seismic risk assessment. Earthquake Spectra 36(1_suppl):252-273. https://doi.org/10.1177/8755293020919429.

Crowley H, Dabbeek J, Despotaki V, Rodrigues D, Martins L, Silva V, Romão, X, Pereira N, Weatherill G, Danciu L (2021a) European Seismic Risk Model (ESRM20), EFEHR Technical Report 002, V1.0.1, 84 pp, https://doi.org/10.7414/EUC-EFEHR-TR002-ESRM20

Crowley H, Despotaki V, Silva V, Dabbeek J, Romão X, Pereira N, Castro JM, Daniell J, Veliu E, Bilgin H, Adam C, Deyanova M, Ademović N, Atalic J, Riga E, Karatzetzou A, Bessason B, Shendova V, Tiganescu A, Toma-Danila D, Zugic Z, Akkar S, Hancilar U (2021b) Model of seismic design lateral force levels for the existing reinforced concrete European building stock. Bulletin of Earthquake Engineering 19:2839-2865. https://doi.org/10.1007/s10518-021-01083-3.

Crowley H, Dabbeek J, Ozcebe S, Bossu R, Finazzi F, Cauzzi C, Danciu L, Papadopoulos A, Han M, Mizrahi L, Michelini A, Faenza L, Lauciani V (2023) Report on the Development of RLA, EEW and OEF at European Scale. RISE Project Deliverable 6.5.

Danciu L, Nandan S, Reyes C, Basili R, Weatherill G, Beauval C, Rovida A, Vilanova S, Sesetyan K, Bard P-Y, Cotton F, Wiemer S, Giardini D (2021) The 2020 update of the European Seismic Hazard Model – ESHM20: Model Overview. EFEHR Technical Report 001 v1.0.0. https://doi.org/10.12686/a15

De Martino G, Di Ludovico M, Prota A, Moroni C, Manfredi G, Dolce M (2017) Estimation of repair costs for RC and masonry residential buildings based on damage data collected by post-earthquake visual inspection. Bulletin of Earthquake Engineering 15:1681-1706. https://doi.org/10.1007/s10518-016-0039-9.

Desprez C, Kotronis P, Mazars J (2011) Analyse et Réduction de la Vulnérabilité Sismique d'une Structure Existante en Béton Armé: renforcement par TFC. In 8ème Colloque National de l'Association Française de Génie Parasismique, No. paper 96, pp. 383-389.

Desprez C, Kotronis P, Mazars J (2015) Seismic vulnerability assessment of a RC structure before and after FRP retrofitting. Bulletin of Earthquake Engineering 13:539-564. https://doi.org/10.1007/s10518-014-9621-1

Didier M, Broccardo M, Esposito S, Stojadinovic B (2018) A compositional demand/supply framework to quantify the resilience of civil infrastructure systems (Re-CoDeS). Sustainable and Resilient Infrastructure 3(2): 86-102. https://doi.org/10.1080/23789689.2017.1364560

Di Ludovico M, De Martino G, Prota A, Manfredi G, Dolce M (2021) Damage Assessment in Italy, and Experiences After Recent Earthquakes on Reparability and Repair Costs, In: Akkar S, Ilki A, Goksu C, Erdik M (eds) Advances in Assessment and Modeling of Earthquake Loss. Springer Tracts in Civil Engineering. Springer, Cham. https://doi.org/10.1007/978-3-030-68813-4_4.

Dolce M, Di Bucci D (2018) The 2016–2017 central Apennines seismic sequence: analogies and differences with recent Italian earthquakes. In: Recent Advances in Earthquake Engineering in Europe: 16th European Conference on Earthquake Engineering, Thessaloniki, Greece, 2018 (pp. 603-638). Springer International Publishing. https://doi.org/10.1007/978-3-319-75741-4_26

Earle PS, Wald DJ, Jaiswal KS, Allen TI, Hearne MG, Marano KD, Hotovec AJ, Fee J (2009) Prompt Assessment of Global Earthquakes for Response (PAGER): A System for Rapidly Determining the Impact of Earthquakes Worldwide. U.S. Geological Survey Open-File Report, no. 2009–1131, https://doi.org/10.3133/ofr20091131.

Erdik M (2021) Earthquake Risk Assessment from Insurance Perspective. In: Akkar S, Ilki A, Goksu C, Erdik M (eds) Advances in Assessment and Modeling of Earthquake Loss. Springer Tracts in Civil Engineering. Springer, Cham. https://doi.org/10.1007/978-3-030-68813-4_6

European Court of Auditors (2018) Office accommodation of EU institutions – Some good management practices but also various weaknesses. Special report 34/2018. Publications Office of the European Union, Luxembourg. https://doi.org/10.2865/896619.

Federal Emergency Management Agency (FEMA), 2003. HAZUS-MH Technical Manual, Washington, D.C.

Field E, Porter K, Milner K (2017) A Prototype Operational Earthquake Loss Model for California Based on UCERF3-ETAS – A First Look at Valuation. Earthquake Spectra 33(4):1279-1299. https://doi.org/10.1193/011817eqs017m

Gerstenberger M, McVerry G, Rhoades D, Stirling M (2014) Seismic hazard modeling for the recovery of Christchurch. Earthquake Spectra 30(1):pp.17-29. https://doi.org/10.1193/021913EQS037M

Goda K (2012) Nonlinear response potential of Mainshock-Aftershock sequences from Japanese earthquakes. Bulletin of the Seismological Society of America 102(5):2139–2156. https://doi/org/10.1785/0120110329.

Goda K (2015) Record selection for aftershock incremental dynamic analysis. Earthquake Engineering & Structural Dynamics 44:1157–1162. https://doi.org/10.1002/eqe.2513.

Goggins J, Broderick BM, Basu B, Elghazouli AY (2007) Investigation of the seismic response of braced frames using wavelet analysis. Structural Control Health Monitoring: The Journal of the International Association for Structural Control and Monitoring and of the European Association for the Control of Structures 14(4):627–648. https://doi.org/10.1002/stc.180

Goulet JA, Michel C, der Kiureghian A (2015) Data-driven post-earthquake rapid structural safety assessment. Earthquake Engineering & Structural Dynamics 44(4): 549–562. https://doi.org/10.1002/eqe.2541

Guéguen P, Langlais M, Garambois S, Voisin C, Douste-Bacqué I (2017) How sensitive are site effects and building response to extreme cold temperature? The case of the Grenoble's (France) City Hall building. Bulletin of Earthquake Engineering 15:889-906. https://doi.org/10.1007/s10518-016-9995-3

Guéguen P, Guattari F, Aubert C, Laudat T (2020) Comparing direct observation of torsion with array-derived rotation in civil engineering structures. Sensors 21(1):142. https://doi.org/10.3390/s21010142

Guéguen P, Astorga A, Langlais M (2023). Amplitude-frequency noise models for seismic building monitoring in a weak-to-moderate seismic region. Submitted to Seism. Res. Letters.

Guerrini G, Graziotti F, Penna A, Magenes G (2017) Improved evaluation of inelastic displacement demands for short-period masonry structures. Earthq Eng Struct Dyn 46:1411–1430. https://doi.org/10.1002/eqe.2862

Gulia L, Wiemer S (2019) Real-time discrimination of earthquake foreshocks and aftershocks. Nature 574(7777:pp.193-199. https://doi.org/10.1038/s41586-019-1606-4

Holland A (2003) Earthquake data recorded by the MEMS accelerometer: Field testing in Idaho, Seismological Research Letters 74(1):20-26. https://doi.org/10.1785/gssrl.74.1.20

Hong HP, Goda K (2007) Orientation-dependent ground-motion measure for seismic-hazard assessment. Bulletin of the Seismological Society of America 97(5):1525-1538. https://doi.org/10.1785/0120060194

Iaccarino AG, Guéguen P, Picozzi M, Ghimire S (2021). Earthquake early warning system for structural drift prediction using machine learning and linear regressors. Frontiers in Earth Science 9:666444. https://doi.org/10.3389/feart.2021.666444.

Iervolino I, Chioccarelli E, Giorgio M, Marzocchi W, Zuccaro G, Dolce M, Manfredi G (2015) Operational (short-term) earthquake loss forecasting in Italy. Bulletin of the Seismological Society of America 105:2286–2298. https://doi.org/10.1785/0120140344

Iervolino I, Giorgio M (2015) Stochastic modeling of recovery from seismic shocks. 12th International Conference on Applications of Statistics and Probability in Civil Engineering (ICASP12), Vancouver, Canada, July 12-15. https://dx.doi.org/10.14288/1.0076088

Iervolino I, Giorgio M, Chioccarelli E (2016) Markovian modeling of seismic damage accumulation. Earthquake Engineering & Structural Dynamics 45(3):441-461. https://doi.org/10.1002/eqe.2668

Iervolino I, Giorgio M (2022) Holistic Modelling of Loss and Recovery for the Resilience Assessment to Seismic Sequences. Findings:37210. https://doi.org/10.32866/001c.37210

Jaiswal KS, Wald DJ (2010) Development of a semi-empirical loss model within the USGS Prompt Assessment of Global Earthquakes for Response (PAGER). Proceedings of the 9th US and 10th Canadian Conference on Earthquake Engineering: Reaching Beyond Borders, July 25-29, 2010, Toronto, Canada. https://earthquake.usgs.gov/static/lfs/data/pager/Jaiswal_Wald_2010_Semi.pdf

Jayaram N, Baker JW (2009) Correlation model for spatially-distributed ground-motion intensities. Earthquake Engineering and Structural Dynamics 38(15):1687-1708. https://doi.org/10.1002/eqe.922

Jordan T, Chen YT, Gasparini P, Madariaga R, Main I, Marzocchi W, Papadopoulos G, Yamaoka K, Zschau J (2011) Operational Earthquake Forecasting: State of Knowledge and Guidelines for Implementation. Annals of Geophysics 54(4). https://doi.org/10.4401/ag-5350

Jordan TH, Marzocchi W, Michael AJ, Gerstenberger MC (2014) Operational earthquake forecasting can enhance earthquake preparedness. Seismological Research Letters 85(5):955-959. https://doi.org/10.1785/0220140143

Katsanos EI, Sextos AG (2015) Inelastic spectra to predict period elongation of structures under earthquake loading. Earthquake Engineering & Structural Dynamics 44(11):1765-1782. https://doi.org/10.1002/eqe.2554.

Lagomarsino S, Giovinazzi S (2006) Macroseismic and mechanical models for the vulnerability and damage assessment of current buildings. Bulletin of Earthquake Engineering 4:415–443. https://doi.org/10.1007/s10518-006-9024-z

Lanzano G, Luzi L, Pacor F, Felicetta C, Puglia R, Sgobba S, D'Amico M (2019) A Revised Ground-Motion Prediction Model for Shallow Crustal Earthquakes in Italy. Bull Seismol. Soc. Am. 109(2):525–540. https://doi.org/10.1785/0120180210

Lilienkamp H, Bossu R, Cotton F, Finazzi F, Landès M, Weatherill G, von Specht S (2023) Utilization of crowdsourced felt reports to distinguish high-impact from low-impact earthquakes globally within minutes of an event. The Seismic Record, in press.

Lin JF, Li XY, Wang J, Wang LX, Hu XX, Liu JX (2021) Study of building safety monitoring by using cost-effective MEMS accelerometers for rapid after-earthquake assessment with missing data. Sensors 21(21):7327. https://doi.org/10.3390/s21217327

Lolli B, Randazzo D, Vannucci G, Gasperini P (2020) The HOmogenized instRUmental Seismic catalog (HORUS) of Italy from 1960 to present. Seismological Research Letters 91(6):3208-3222. https://doi.org/10.1785/0220200148

Luco N, Bazzurro P, Cornell CA (2004) Dynamic versus static computation of the residual capacity of a mainshock-damaged building to withstand an aftershock. 13th World Conference on Earthquake Engineering, Vancouver, B.C., Canada, August 1-6, 2004.

Mai PM, Thingbaijam KKS (2014) SRCMOD: An online database of finite-fault rupture models. Seismological Research Letters 85(6): 1348 – 1357 https://doi.org/10.1785/0220140077

Martakis P, Reuland Y, Chatzi E (2021) Amplitude-dependent model updating of masonry buildings undergoing demolition. Smart Structures and Systems 27(2):157–172. https://doi.org/10.12989/SSS.2021.27.2.157

Martakis P, Reuland Y, Imesch M, Chatzi E (2022) Reducing uncertainty in seismic assessment of multiple masonry buildings based on monitored demolitions. Bulletin of Earthquake Engineering 20(9): 4441–4482. https://doi.org/10.1007/s10518-022-01369-0

Martakis P, Reuland Y, Stavridis A, Chatzi E (2023) Fusing damage-sensitive features and domain adaptation towards robust damage classification in real buildings. Soil Dynamics and Earthquake Engineering 166:107739. https://doi.org/10.1016/j.soildyn.2022.107739

Martins L, Silva V (2021) Development of a fragility and vulnerability model for global seismic risk analyses. Bulletin of Earthquake Engineering 19(15):6719–6745. https://doi.org/10.1007/S10518-020-00885-1

Martins L, Silva V, Crowley H, Cavalieri F (2021) Vulnerability Modeller's Toolkit, an Open-Source Platform for Vulnerability Analysis. Bulletin of Earthquake Engineering 19:5691-5709. https://doi.org/10.1007/s10518-021-01187-w

Marzocchi W, Lombardi AM, Casarotti E (2014) The establishment of an operational earthquake forecasting system in Italy. Seismol Res Lett 85:961–969. https://doi.org/10.1785/0220130219

Marzocchi W, Iturrieta P, Falcone G (2022) A new generation of OEF models. RISE Project Deliverable 3.3.

McKenna F, Fenves GL, Scott MH, Jeremic B (2000) Open System for Earthquake Engineering Simulation (OpenSees), Pacific Earthquake Engineering Research Center, University of California, Berkeley, CA.

Meletti C, Marzocchi W, D'Amico V, Lanzano G, Luzi L, Martinelli F, Pace B, Rovida A, Taroni M, Visini F, MPS19 Working Group (2021) The New Italian Seismic Hazard Model (MPS19). Annals of Geophysics 64(1). https://doi.org/10.4401/ag-8579

Mena Cabrera B, Nievas C, Crowley H, Papadopoulos A, Boese M, Chioccarelli E, Reuland Y, Chatzi E (2023) Good-practice report on risk-cost-benefit in terms of socio-economic impact. RISE Project Deliverable 4.7.

Michael AJ, McBride SK, Hardebeck JL, Barall M, Martinez E, Page MT, van der Elst N, Field EH, Milner KR, Wein AM (2020) Statistical seismology and communication of the USGS operational aftershock forecasts for the 30 November 2018 Mw 7.1 Anchorage, Alaska, earthquake. Seismological Research Letters 91(1):153-173. https://doi.org/10.1785/0220190196

Michel C, Guéguen P (2010) Time-frequency analysis of small frequency variations in civil engineering structures under weak and strong motions using a reassignment method. Structural health monitoring 9(2):159-171. https://doi.org/10.1177/1475921709352146.

Michel C, Guéguen P, El Arem S, Mazars J, Kotronis P (2010) Full-scale dynamic response of an RC building under weak seismic motions using earthquake recordings, ambient vibrations and modelling. Earthquake Engineering & Structural Dynamics 39(4):419-441. https://doi.org/10.1002/eqe.948.

Mikael A, Gueguen P, Bard PY, Roux P, Langlais M (2013) The analysis of long-term frequency and damping wandering in buildings using the random decrement technique. Bulletin of the Seismological Society of America 103(1):236-246. https://doi.org/10.1785/0120120048.

Milner KR, Shaw BE, Field EH (2022) Enumerating plausible multifault ruptures in complex fault systems with physical constraints. Bulletin of the Seismological Society of America 112(4):1806-1824. https://doi.org/10.1785/0120210322

Naylor M, Serafini F, Lindgren F, Main I (2023) Bayesian modelling of the temporal evolution of seismicity using the ETAS.inlabru R-package. Frontiers in Applied Mathematics and Statistics, special issue Physical and Statistical Approaches to Earthquake Modeling and Forecasting. https://doi.org/10.3389/fams.2023.1126759

Nazari N, van de Lindt JW, Li Y (2015) Effect of Mainshock-Aftershock Sequences on Woodframe Building Damage Fragilities. Journal of Performance of Constructed Facilities 29(1). https://doi.org/10.1061/(ASCE)CF.1943-5509.0000512.

Neely JS, Stein S (2021) Why do continental normal fault earthquakes have smaller maximum magnitudes? Tectonophysics 809:228854. https://doi.org/10.1016/j.tecto.2021.228854

Nievas CI, Sullivan T (2018) A multidirectional conditional spectrum. Earthquake Engineering & Structural Dynamics 47(4):945-965. https://doi.org/10.1002/eqe.3000

Nievas CI, Bommer JJ, Crowley H, van Elk J (2020) Global occurrence and impact of small-to-medium magnitude earthquakes: a statistical analysis. Bulletin of Earthquake Engineering 18(1):1-35. https://doi.org/10.1007/s10518-019-00718-w

Organisation for Economic Cooperation and Development (OECD) (2023) Length of hospital stay (indicator). doi: 10.1787/8dda6b7a-en (accessed on 6 January 2023).

Orlacchio M (2022) The effects of seismic sequences on seismic hazard and structural vulnerability. PhD Thesis. University of Naples Federico II, Naples, Italy.

Orlacchio M, Chioccarelli E, Baltzopoulos G, Iervolino I (2021) State-dependent seismic fragility functions for Italian reinforced concrete structures: preliminary results. In: 31st European Safety and Reliability Conference (ESREL).

Pagani M, Monelli D, Weatherill G, Danciu L, Crowley H, Silva V, Henshaw P, Butler L, Nastasi M, Panzeri L, Simionato M, Vigano D (2014) OpenQuake engine: An open hazard (and risk) software for the global earthquake model. Seismological Research Letters 85(3):692-702. https://doi.org/10.1785/0220130087

Papadopoulos A N, Bazzurro P (2020) Exploring probabilistic seismic risk assessment accounting for seismicity clustering and damage accumulation: Part II. Risk analysis. Earthquake Spectra 37(1):386-408. https://doi.org/10.1177/8755293020938816

Papadopoulos A N, Bazzurro P, Marzocchi W (2020) Exploring probabilistic seismic risk assessment accounting for seismicity clustering and damage accumulation: Part I. Hazard analysis. Earthquake Spectra 37(2):803-826. https://doi.org/10.1177/8755293020957338

Péquegnat C, Guéguen P, Hatzfeld D, Langlais M (2008) The French accelerometric network (RAP) and national data centre (RAP-NDC). Seismological Research Letters 79(1):79-89. https://doi.org/10.1785/gssrl.79.1.79

Péquegnat C, Schaeffer J, Satriano C, Pedersen H, Touvier J, Saurel JM et al. (2021). RÉSIF-SI: A distributed information system for French seismological data. Seismological Research Letters, 92(3), 1832-1853. https://doi.org/10.1785/0220200392

Perrault M, Guéguen P, Aldea A, Demetriu S (2013) Using experimental data to reduce the single-building sigma of fragility curves: case study of the BRD tower in Bucharest, Romania. Earthquake Engineering and Engineering Vibration 12(4):pp.643-658. https://doi.org/10.1007/s11803-013-0203-z.

Petruzzelli F, Iervolino I (2021) NODE: a large-scale seismic risk prioritization tool for Italy based on nominal structural performance. Bulletin of Earthquake Engineering 19:2763–2796. https://doi.org/10.1007/s10518-021-01093-1

Pittore M, Haas M, Silva V (2020) Variable resolution probabilistic modeling of residential exposure and vulnerability for risk applications. Earthquake Spectra 36(1_suppl):321-344. https://doi.org/10.1177/8755293020951582.

Pittore M, Wieland M, Errize M, Kariptas C, Gungor I (2015) Improving Post-Earthquake Insurance Claim Management: A Novel Approach to Prioritize Geospatial Data Collection. International Journal of Geo-Information 4(4):2401-2427. https://doi.org/10.3390/ijgi4042401

Popovic N, Pejović J (2023) Seismic Performance Evaluation Of Existing RC High-Rise Building In Montenegro. Proceedings of the 2nd Croatian Conference on Earthquake Engineering - 2CroCEE, Zagreb, Croatia, March 22 to 24, in print.

Powell G H (2007) Detailed Example of a Tall Shear Wall Building: Using CSI's PERFORM 3D Nonlinear Dynamic Analysis: Nonlinear Modeling, Analysis and Performance Assessment for Earthquake Loads. Computers & Structures Incorporated.

Raghunandan M, Liel AB, Luco N (2015) Aftershock collapse vulnerability assessment of reinforced concrete frame structures. Earthquake Engineering & Structural Dynamics 44(3):419–439. https://doi.org/10.1002/eqe.2478.

RAP-RESIF. (2023). French Accelerometric Network, https://rap.resif.fr/. Last access: January 2023.

Reinoso E, Jaimes MA, Esteva L (2017) Estimation of life vulnerability inside buildings during earthquakes. Structure and Infrastructure Engineering 14(8):1140-1152. https://doi.org/10.1080/15732479.2017.1401097.

RESIF-DC. (2023). Résif Seismological data portal. http://doi.org/10.17616/R37Q06.

RESIF.RAP. (1995). RESIF-RAP French Accelerometric Network. RESIF - doi:10.15778/resif.ra

Reuland Y, Lestuzzi P, Smith IFC (2019a) A model-based data-interpretation framework for post-earthquake building assessment with scarce measurement data. Soil Dynamics and Earthquake Engineering 116:253–263. https://doi.org/10.1016/j.soildyn.2018.10.008

Reuland Y, Lestuzzi P, Smith IFC (2019b) Measurement-based support for post-earthquake assessment of buildings. Structure and Infrastructure Engineering 15(5):647–662. https://doi.org/10.1080/15732479.2019.1569071

Reuland Y, Martakis P, Chatzi E (2021) Damage-sensitive features for rapid damage assessment in a seismic context. In: Proceedings of the International Conference on Structural Health Monitoring of Intelligent Infrastructure 2021 (pp. 613-619). International Society for Structural Health Monitoring of Intelligent Infrastructure (ISHMII).

Reuland Y, Bodenmann L, Blagojevic N, Stojadinovic (2022a) Development of RRE forecasting services in OpenQuake. RISE Project Deliverable 4.4.

Reuland Y, Martakis P, Chatzi E (2022b) The use of structural health monitoring for rapid loss assessment. RISE Project Deliverable 4.5.

Reuland Y, Martakis P, Chatzi E (2023) A Comparative Study of Damage-Sensitive Features for Rapid Data-Driven Seismic Structural Health Monitoring. Applied Sciences 13(4):2708. https://doi.org/10.3390/app13042708

Romão X, Castro JM, Pereira N, Crowley H, Silva V, Martins L, Rodrigues, D (2019) European physical vulnerability models. SERA Project Deliverable 26.5. Available online at: http://static.seismo.ethz.ch/SERA/JRA/SERA_D26.5_Physical_Vulnerability.pdf

Rossi A, Tertulliani A, Azzaro R, Graziani L, Rovida A, Maramai A, Pessina V, Hailemikael S, Buffarini G, Bernardini F, Camassi R (2019) The 2016–2017 earthquake sequence in Central Italy: macroseismic survey and damage scenario through the EMS-98 intensity assessment. Bulletin of Earthquake Engineering 17:2407-2431. https://doi.org/10.1007/s10518-019-00556-w

Ruiz-García J (2012) Mainshock-aftershock ground motion features and their influence in building's seismic response. Journal of Earthquake Engineering 16(5):719–737. https://doi.org/10.1080/13632469.2012.663154.

Russo E, Felicetta C, D Amico M, Sgobba S, Lanzano G, Mascandola C, Pacor F, Luzi L (2022) Italian Accelerometric Archive v3.2 - Istituto Nazionale di Geofisica e Vulcanologia, Dipartimento della Protezione Civile Nazionale. doi:10.13127/itaca.3.2

Ryu H, Luco N, Uma SR, Liel AB (2011). Developing fragilities for mainshock-damaged structures through incremental dynamic analysis. Proceedings of the Ninth Pacific Conference on Earthquake Engineering, 14-16 April 2011, Auckland, New Zealand. Paper number 225.

Safak E, Clinton J (2022) Performance-based early warning systems in Europe. RISE Project Deliverable 4.6.

Schiavina M, Freire S, Rosina K, Ziemba L, Marin Herrera M, Craglia M, Lavalle C, Kemper T, Batista e Silva F (2020) ENACT-POP R2020A - ENACT 2011 Population Grid.European Commission, Joint Research Centre (JRC). PID: http://data.europa.eu/89h/347f0337-f2da-4592-87b3-e25975ec2c95. https://doi.org/10.2905/347F0337-F2DA-4592-87B3-E25975EC2C95.

Schorlemmer D, Beutin T, Cotton F, Garcia Ospina N, Hirata N, Ma KF, Nievas C, Prehn K, Wyss M (2020) Global Dynamic Exposure and the OpenBuildingMap – A big-data and crowd-sourcing approach to exposure modeling. EGU General Assembly 2020 Conference Abstracts (p. 18920). https://doi.org/10.5194/egusphere-egu2020-18920

Schorlemmer D, Cotton F, Delattre F, Evaz Zadeh T, Kriegerowski M, Lingner L, Oostwegel L, Prehn K, Shinde S (2023) An open, dynamic, high-resolution dynamic exposure model for Europe. RISE Project Deliverable 2.13.

Serafini F, Lindgren F, Naylor M (2023) Approximation of bayesian Hawkes process models with Inlabru. Submitted to Envirometrics. arXiv preprint: https://doi.org/10.48550/arXiv.2206.13360

Shahi SK, Baker JW (2014) NGA-West2 models for ground motion directionality. Earthquake Spectra 30(3):1285-1300. https://doi.org/10.1193/040913EQS097M

Silva V, Crowley H, Pagani M, Monelli D, Pinho R (2014) Development of the OpenQuake engine, the Global Earthquake Model's open-source software for seismic risk assessment. Natural Hazards 72:1409-1427. https://doi.org/10.1007/s11069-013-0618-x

Silva V, Horspool N (2019) Combining USGS ShakeMaps and the OpenQuake-engine for damage and loss assessment. Earthquake Engineering and Structural Dynamics 486:634-652. https://doi.org/10.1002/eqe.3154

Silva V, Brzev S, Scawthorn C, Yepes C, Dabbeek J, Crowley H (2022) A building classification system for multi-hazard risk assessment. International Journal of Disaster Risk Science 13(2):161-177. https://doi.org/10.1007/s13753-022-00400-x

SISmalp (2023) Service de surveillance de la Sismicité des Alpes. https://sismalp.osug.fr. Last access: February 2023.

Sivori D, Cattari S, Lepidi M (2022) A methodological framework to relate the earthquake-induced frequency reduction to structural damage in masonry buildings. Bulletin of Earthquake Engineering 20(9): 4603–4638. https://doi.org/10.1007/s10518-022-01345-8

Spence R (ed) (2007) Earthquake Disaster Scenario Predictions and Loss Modelling for Urban Areas. LESSLOSS Report No. 2007/07.

Swiss Federal Statistical Office (2022) Housing conditions. Available online at: https://www.bfs.admin.ch/bfs/en/home/statistics/construction-housing/dwellings/housing-conditions.html (last accessed 3 February 2023).

Taroni M, Marzocchi W, Schorlemmer D, Werner MJ, Wiemer S, Zechar JD, Heiniger L, Euchner F (2018) Prospective CSEP evaluation of 1-day, 3-month, and 5-yr earthquake forecasts for Italy. Seismological Research Letters 89(4):1251-1261. https://doi.org/10.1785/0220180031

Thompson EM, Worden CB (2018) Estimating Rupture Distances without a Rupture. Bulletin of the Seismological Society of America 108(1):371–379. https://doi.org/10.1785/0120170174

Trevlopoulos K, Guéguen P (2016). Period elongation-based framework for operative assessment of the variation of seismic vulnerability of reinforced concrete buildings during aftershock sequences. Soil Dynamics and Earthquake Engineering 84:224–237. https://doi.org/10.1016/j.soildyn.2016.02.009

Trevlopoulos K, Guéguen P, Helmstetter A, Cotton F (2020) Earthquake risk in reinforced concrete buildings during aftershock sequences based on period elongation and operational earthquake forecasting. Structural Safety 84:101922. https://doi.org/10.1016/j.strusafe.2020.101922

Tyagunov S, Grünthal G, Wahlström R, Stempniewski L, Zschau J (2006) Seismic risk mapping for Germany. Natural Hazards and Earth System Sciences 6:573-586. https://doi.org/10.5194/nhess-6-573-2006

Vamvatsikos D, Cornell CA (2001) Incremental Dynamic Analysis. Earthquake Engineering and Structural Dynamics 31(3):491–514. https://doi.org/10.1002/eqe.141

Vamvatsikos D, Cornell CA (2004) Applied incremental dynamic analysis. Earthquake Spectra 20(2):523–553. https://doi.org/10.1193/1.1737737.

Vanin F, Penna A, Beyer K (2020a) Equivalent-Frame Modeling of Two Shaking Table Tests of Masonry Buildings Accounting for Their Out-Of-Plane Response. Frontiers in Built Environment 6. https://doi.org/10.3389/fbuil.2020.00042

Vanin F, Penna A, Beyer K (2020b). A three-dimensional macroelement for modelling the in-plane and out-of-plane response of masonry walls. Earthquake Engineering & Structural Dynamics 49(14): 1365–1387. https://doi.org/10.1002/eqe.3277

Villar-Vega M, Silva V (2017) Assessment of earthquake damage considering the characteristics of past events in South America. Soil Dynamics and Earthquake Engineering 99:86–96. https://doi.org/10.1016/j.soildyn.2017.05.004

Ville de Grenoble, Département Ressources Humaines et Numériques, Direction Gestion des Ressources Humaines, Service Relations Sociales et Suivi de la Masse Salariale (2021) Bilan social 2021. Available online at: https://www.grenoble.fr/cms_viewFile.php?idtf=28091&path=Bilan-social-2021-Ville-de-Grenoble.pdf (last accessed: 3 February 2023).

Visini F, Meletti C, Rovida A, et al. (2022) An updated area-source seismogenic model (MA4) for seismic hazard of Italy. Natural Hazards and Earth System Sciences 22: 2807-2827 https://doi.org/10.5194/nhess-22-2807-2022

Weatherill G, Crowley H, Roullé A, Tourlière B, Lemoine A, Gracianne C, Kotha SR, Cotton F (2022) Modelling site response at regional scale for the 2020 European Seismic Risk Model (ESRM20). Bulletin of Earthquake Engineering 21:665-714. https://doi.org/10.1007/s10518-022-01526-5

Weber B, Becker J, Hanka W, Heinloo A, Hoffmann M, Kraft T, Pahlke D, Reinhardt J, Saul J, Thoms (2007) SeisComP3—Automatic and interactive real time data processing. Geophys. Res. Abstr. 9(09):219.

Wells DL, Coppersmith KJ (1994) New Empirical Relationships among Magnitude, Rupture Length, Rupture Width, Rupture Area and Surface Displacement. Bulletin of the Seismological Society of America 84(4):974–1002.

Worden CB, Wald DJ, Allen TI, Lin K, Garcia D, Cua G (2010) A revised ground-motion and intensity interpolation scheme for ShakeMap. Bulletin of the Seismological Society of America 100(6):3083-3096. https://doi.org/10.1785/0120100101

Worden CB, Thompson EM, Baker JW, Bradley BA, Luco N, Wald DJ (2018) Spatial and Spectral Interpolation of Ground-Motion Intensity Measure Observations. Bulletin of the Seismological Society of America 108(2):866–875. https://doi.org/10.1785/0120170201

Worden CB, Thompson EM, Hearne m, Wald DJ (2020) ShakeMap Manual Online: technical manual, user's guide, and software guide, U. S. Geological Survey. http://cbworden.github.io/shakemap/. https://doi.org/10.5066/F7D21VPQ

Yeo GL, Cornell CA (2009) Building life-cycle cost analysis due to mainshock and aftershock occurrences. Structural Safety 31(5):396-408. https://doi.org/10.1016/j.strusafe.2009.01.002

Yepes-Estrada C, Silva V, Valcárcel J, Acevedo AB, Tarque N, Hube MA, Coronel G, Santa María H (2017) Modeling the residential building inventory in South America for seismic risk assessment. Earthquake Spectra 33(1):299-322. https://doi.org/10.1193/101915eqs155dp.